Exploring the Neutron Substructure with Advanced Polarized Helium-3 Targets

(Or: How I Learned to Stop Worrying
and Love Spectroscopy)

Christopher James Jantzi
B.Sc Physics, University of Washington, 2015

A thesis presented for the degree of
Doctor of Philosophy in Physics

Department of Physics
University of Virginia
United States
July 31, 2024

Abstract

As we seek to understand the smallest, physical aspects of our universe, we cannot simply rely on our senses to probe the world around us as we did in the past. The smallest physical elements of our universe behave in strange, probabilistic ways and are completely invisible to the naked eye/ear/etc. So, we design clever experiments (such as scattering experiments) to probe these minute realms. Then, just as with the larger, observable world, we devise models and equations to describe what we think is happening. Due to the nature of the physical universe at the quantum scale and with the aid of symmetries such as Lorentz invariance, we can write down equations that describe the scattering, but the expressions contain functions, which we call "form factors" and "structure functions", that we cannot compute from first principles. We can, however, formulate models that make predictions for these functions. By comparing our predictions with the observed data, we can gain insight into the validity of our models and thus a better physical understanding of what is happening at these minuscule scales.

Studying the constituents *inside* of the nucleus of an atom adds another layer of difficulty if we can't remove those components from the nucleus. This is the case with the neutron. When not bound in the nucleus with protons and other neutrons, the neutron will decay into a proton after about 15 minutes. So, we're forced to study the neutron while it is still bound in the nucleus of an atom such as helium-3 (^{3}He). For the last 1,000 years (rounding up), our group has developed high quality, polarized ^{3}He targets made of an aluminosilicate glass. These targets are made in order to perform experiments at Jefferson Lab (JLab), experiments which let us determine the form factors and structure functions of the neutron by scattering polarized electrons from polarized neutrons (or rather polarized ^{3}He). The specific experiments reported on in this thesis push the bounds of our understanding of the internal structure of the neutron.

Good science is often about pushing experimental techniques to a new level. Toward that goal we study our polarized ^{3}He targets both to advance the technology and to choose the best ones for our experiments. We do this using a process called nuclear magnetic resonance (NMR) to gauge the maximum polarization of a target and how fast the polarization decays with time. While these tests primarily provide us information that make analysis of our experimental scattering data possible, they also let us determine whether or not a target-cell is useful or even, dare I say, of spectacular quality. Our latest targets utilize a novel convection design allowing ^{3}He to be polarized and quickly moved in front of the electron-beam, making it possible to use larger targets with higher electron-beam currents than ever before. This means more electrons scatter and we get more data. *And* by studying our targets in detail prior to using them in our experiments, we have found techniques to take effects which could have been detrimental to target quality and turn them to our advantage! It's a real case of making lemonade out of lemons.

We also use laser spectroscopy to study the absorption lines of alkali-metals in the target (potassium and rubidium, specifically). We add these alkali-metals to our target to facilitate polarizing the ^{3}He. We can use the measurement of these pressure broadened absorption lines to determine the ^{3}He density inside of the target with great precision. Historically, we understood the width of these lines would be dependent on the temperature of the target. Specifically, if I raise the temperature, the width should get bigger. I found that was not the case, which was very confusing at first, though very exciting now that I realize the data are self-consistent and suggestive of unexpected behaviour.

This thesis details the development of high quality, glass, polarized ^{3}He targets for the 2020 A_1^n/d_2^n and 2023 G_E^n experiments, which utilized the first ^{3}He convection targets and broke records in target quality. This thesis also covers the initial development of metal windows for the next-generation of ^{3}He target-cells. Finally, this thesis documents the temperature dependence of the width of potassium (K) and rubidium (Rb) absorption lines as measured with laser spectroscopy.

Acknowledgements

Wow. So here we are at the end. Well, the beginning for you, dear reader. There's a lot of people to thank, but they all rock, so please read on!

When I left the Navy at 32, I took two classes to complete my associates degree, still trying to figure out what I wanted to do with my life. In the first class, Intro to Political Science, I met my love, Bailey Nickel. In the second class, Intro to Astrobiology, I met my other love, physics. I was fortunate enough to have a great teacher, David Fong, whose enthusiasm for teaching matched a fascination with science (and not just science fiction) I didn't even realize I had. Professor Fong is one of those people in a fandom that love it so much they want to welcome everyone else in. Not a gatekeeper, not Lording his knowledge over you, but the best kind of fan: the welcoming kind. Professor Fong introduced me to quarks (more than just a hilarious Star Trek character) and Bailey pointed out that when I talked about quarks, she'd never seen me so excited (unless I was talking about music). And so, having never taken a physics class in my life, I decided I'd major in it! Professor Fong, thank you so much for sharing your enthusiasm and knowledge. You literally changed the course of my life (for the better).

Thank you to friends like MM1/SS Joel Davies (Port and Starborad Aux Aft, Baby!), to Elana Voigt for company on the long ferry rides and in the UW physics department, to Matt Roberts and the rest of my first year study group, to Sumudu Katugampola for all the guidance in my early days in the lab, to Josh Nothnagle for excellent sandwiches (and energetic conversations), to Raymond Deuel for over three decades of friendship and for pulling me out of my shell in middle school, and to my sister Angie, the Boris to my Natasha.

Thank you Cloudkicker for your "Unending" album, Sithu Aye for your "Invent the Universe" album (and it's remaster). Thank you Jimmy Eat World, Tool, Trifonic, and a hundred other artists. And thank you to Robert Evans and crew at the "Behind the Bastards" podcast. You folks are the soundtrack to my science.

A major thank you to Kent Paschke, whose continued guidance after I switched to Gordon's lab was invaluable. A thank you to Xiaochao Zheng for timely and helpful edits on my ramblings herein. And to Gordon Cates, whose lab became a second home in the best possible way. I built **all** the things, Gordon! How *cool* is *THAT*? Who else gets to *do* that!?!

Finally, thanks to my family. First to mi novia, mi amor, Bailey Nickel. You truly are the other half of me, my co-op partner for life, and I don't know where I'd be without you. And lastly to Avaline Pearl Jannic, my amazing, brilliant, wonderful child. You are the future, Squeak, and I am privileged to be here at the start. *Oh the places you'll go...*

"Anything you want to do, you can learn to do better in college."

– My mother, Debbie Marie Jantzi neé Cushman, on the merits of pursuing a degree in Music Composition rather than simply "becoming a rock star". Love you most, Mom.

"You're an idiot."

– My father, Thomas John Jantzi, responding to my plan to simply "become a rock star". Indeed, this was a general refrain to many of my plans. You ain't so bad either, Dad.

"Men have called me mad; but the question is not yet settled, whether madness is or is not the loftiest intelligence – whether much that is glorious – whether all that is profound – does not spring from disease of thought – from moods of mind exalted at the expense of the general intellect."

– Excerpt from "Eleonora" by Edgar Allen Poe, 1842.

Contents

1 A beginning... 1

2 The Proton Spin Crisis and the Fallout 4
- 2.1 A breakdown of total nucleon spin . . . 6
- 2.2 Functions for describing the interior of a nucleon . . . 8
- 2.3 An effective, single neutron target . . . 12

3 Recent Measurements of A_1^n/d_2^n and G_E^n Experiments at JLab 14
- 3.1 Measuring A_1^n and d_2^n . . . 15
- 3.2 Previous Measurements of A_1^n and d_2^n . . . 17
- 3.3 The Recent A_1^n Measurement for JLab (2019-2020) . . . 19
  - 3.3.1 The HMS and SHMS Spectrometers and Kinematic Settings . . . 21
- 3.4 The Recent d_2^n Measurement for JLab (2020) . . . 21
- 3.5 Measuring G_E^n . . . 23
- 3.6 Previous Measurements of G_E^n . . . 25
- 3.7 The Recent G_E^n Measurement for JLab (2022-2023) . . . 27

4 Polarized ^{3}He Target Cells 30
- 4.1 Geometry: Past and Present . . . 31
- 4.2 Production . . . 32
  - 4.2.1 Minimizing contaminants inside the target . . . 33
  - 4.2.2 Filling the target-cell . . . 34
- 4.3 Polarimetry Measurements . . . 39
  - 4.3.1 AHSEOP . . . 39
  - 4.3.2 The NMR and EPR Apparatus . . . 41
  - 4.3.3 I built this system (on rock and roll) . . . 43
  - 4.3.4 Temperatures . . . 44
  - 4.3.5 NMR AFP Tests . . . 44
  - 4.3.6 Simulated beam tests . . . 56
- 4.4 Results . . . 57
  - 4.4.1 Characterization Results . . . 58
  - 4.4.2 Influence of Variations in Production on Characterization Results . . . 60
  - 4.4.3 Directional Dependence of Maximum Polarization and Lifetime . . . 66
  - 4.4.4 Metal End-Windows . . . 71
- 4.5 Conclusions . . . 76

4.5.1 Production Variables . . . 76
4.5.2 Hysteresis Effects and the Merits of Degaussing . . . 77
4.5.3 Metal End Windows . . . 77

5 Interferometry and Spectroscopy Measurements 78
5.1 Interferometry: An introduction to window/wall measurements . . . 78
5.2 Interferometry: Experimental Setup . . . 79
5.2.1 Taking a Window Thickness Measurement . . . 82
5.3 Interferometry: Data Analysis . . . 82
5.4 Interferometry: Results . . . 84
5.5 Spectroscopy: Introduction to pressure broadening . . . 88
5.5.1 Natural Linewidth and Doppler Broadening . . . 88
5.5.2 Pressure / Collisional Broadening . . . 89
5.5.3 Additional broadening mechanisms . . . 90
5.6 Spectroscopy: Experimental Setup . . . 90
5.7 Spectroscopy: Data Analysis . . . 95
5.7.1 My Forebears: The Lorentzian Fit . . . 98
5.7.2 Reinventing the Wheel: The pseudo-Voigt Profile . . . 102
5.7.3 The Rabbit Hole: Misadventures when considering all isotopes and hyperfine levels . . . 103
5.7.4 An Act of Desperation: The Integral Fit . . . 106
5.7.5 Finding ^{3}He Density from Spectroscopic Data . . . 108
5.7.6 Finding the Ratio of Alkali Densities from Spectroscopy Data . . . 110
5.7.7 Extrapolating Alkali Density to High Temperatures with Vapor Pressure Curves . . . 112
5.8 Spectroscopy: Results . . . 116
5.9 Spectroscopy: Conclusions . . . 125
5.9.1 Systematic Issues Resolved . . . 125
5.9.2 Differences Between the Ti:Sapphire system and the Diode Laser System 127
5.9.3 Differences Between the W&M system and the UVa System . . . 127
5.9.4 Final Thoughts . . . 128

6 ...and an ending. 129
6.1 The future of A_1^n, d_2^n, and G_E^n Measurements: The Next Stage in ^{3}He Targets . . . 129
6.2 The Future of Spectroscopic Measurements in Cates Group: A Tantalizing Mystery 130
6.3 The End of the Line . . . 130

A Data Tables of Chapter 4 131

B Data Tables of Chapter 5 137

List of Figures

2.1 From reference [4], the paper reporting results for SLAC's E-4 experiment. From that paper: $[\sigma/\sigma_{Mott}]$ in GeV^{-1} vs q^2 for $W = 2, 3$ and 3.5 GeV. The lines drawn through the data are meant to guide the eye. Also shown is the cross section for elastic e-p scattering divided by σ_{Mott}, calculated for $\theta = 10°$, using the dipole form factor. The relatively slow variation with q^2 of the inelastic cross section compared with the elastic cross section is clearly shown. 5

2.2 Results from the landmark 1988 EMC experiment which spawned the Proton Spin Crisis. Left: The asymmetry A_1^p plotted vs. x along with results from SLAC [26] (reference [9]) and SLAC [27] (reference [10]) with a curve modelled from reference [11]. Right: $xg_1^p(x)$ plotted vs. x and $\int_{x_m}^1 dx$ plotted vs. x_m with a marker showing the Ellis-Jaffe prediction for $\int_{x_m}^1 dx$ at $x = 0$, a sum rule that assumes the strange quarks in the nucleon are unpolarized. 6

2.3 Two images showing the evolving complexity of our picture of the inside of a nucleon. 7

2.4 Probable spin states for the ^{2}H and ^{3}He nuclei ground states. 12

3.1 Interactions measured in studying A_1^n and d_2^n. 15

3.2 Existing world data for A_1^n and d_2^n from reference [29]. 20

3.3 An elastic collision between an electron and the neutron in a ^{3}He nucleus (adapted from reference [18]). 23

3.4 Targets used in G_E^n measurements at MAMI. Left: The target used in the exploratory experiment (reference [36]) and the A3 collaboration experiment (reference [18]) as detailed in Becker *et al.* ([18]). Right: The target used by the A1 collaboration [37] and the follow up experiment which measured both G_E^n and A_y^o [38]. 27

3.5 World data for G_E^n-I. 28

4.1 A comparison of the relative sizes of the three target designs discussed: (a) diffusion, (b) Bastille Day, and (c) coathanger models. Actual targets varied only slightly from these designs. The Bastille Day design also employed a small bulb meant to assist in pNMR measurements. 31

4.2 Target windows before they were made into a target. 33

4.3 A convection target attached to the manifold. The bellows was attached to the gas handling system. 34

4.4 Attaching a target to the gas handling system. 35

4.5 On the left, a target in the Mollie. On the right, Al Tobias prepares the same target for fill, then pull off. The metal piece in his hand will protect the pumping chamber from the heat of the hand torch during the pull off process. 36
4.6 A visual depiction of how Rb was polarized during Spin-Exchange Optical Pumping. 40
4.7 Mounting a target on the oven base. 41
4.8 A diagram of the NMR/EPR apparatus. The *purple* lines are the signal driving the NMR RF field, the *green* lines are the modulated signal driving the EPR RF coils, the *red* lines trace the signal from the PC pickup coils, the *blue* lines trace the signal from the TC pickup coils, and the *yellow* lines trace the signal from the EPR photodiode. Grad Student Illustrated by Jorge Cham, Illustrator, PhD Comics (jorge@phdcomics.com) 42
4.9 Pictures of the old and new NMR/EPR systems. RF coils in 4.9a are the small, white ones pictured near the top and bottom of the oven. The same coils are present in 4.9b as well as an additional set of coils made of aluminum bicycle tire frames. The RF coils in 4.9c are dark gray. The joints in 4.9d are pinned mortise and tenon joints and are secured via friction rather than screws or nails. 44
4.10 For time in seconds, a full up-sweep and down-sweep in the lab frame comparing orientation of a single spin (red arrow) with holding-field (black arrow). 45
4.11 Examples of the two tests that comprise target characterization with the NMR/EPR apparatus. The y-axis defines the polarization (figure 4.11a) or amplitude in mV (figure 4.11b) of the *pumping chamber only* (blue line). The target chamber (red line) is plotted only to show that the two chambers are mixing at a reasonable rate as indicated by the two lines rising or falling synchronously. 46
4.12 A typical three-point plot using 1-hour, 2-hour, and 8-hour spin-downs. 47
4.13 Impedance Matching Circuits 49
4.14 Finding the equivalent circuit using Thèvenin's theorem. 50
4.15 A circuit diagram of the AΦ box. 52
4.16 The steps of an EPR calibration. 53
4.17 PI box circuit diagram. 54
4.18 An example of a calibration constant using two NMR measurements (NMR_A and NMR_B) and two frequency shifts (P_{12} and P_{34}). Percent polarization, field, and frequency shift were calculated using equations found in [45], [48], and [49]. . . . 55
4.19 Variables in target production (x-axis) vs. max. percent target pol. (y-axis) for A_1^n/d_2^n 62
4.20 Variables in target production (x-axis) vs. max. percent target pol. (y-axis) for G_E^n at 91 kHz 63
4.21 Variables in target production (x-axis) vs. max. percent target pol. (y-axis) for G_E^n at 154 kHz 64

4.22 An explanation of orientations used in testing G_E^n-II targets at UVa (not to scale). The JLab system is similar to this, but not exactly the same. The arrow defines the direction of the holding field. The black box on the target chamber is an arbitrary indicator meant to break the symmetrical look of the targets in the diagram. Usually, a small paper name tag was affixed externally to the target, off-center, along the length of the target chamber. This was used to define final orientation O2(O4) from initial orientation O1(O3). The box around the pumping chamber is the oven, of course. 66
4.23 Relaxation rates, Γ, for the pumping chamber (above) and target chamber (below) in hr^{-1} for the initial (black circle) and final (diamond) positions. All spin-downs at initial positions were performed with RF ≈ 154kHz. For final positions, red diamonds indicate RF ≈ 154 kHz, blue diamonds indicate RF ≈ 91 kHz, and green diamonds indicate RF ≈ 91 kHz, though these green final measurements (and their corresponding initial measurement) were taken after the target was degaussed. Data used in making this figure can be found in table 4.6. 68
4.25 On the left, a description of the regions assigned during degaussing (image credit: Jacob Koenemann). On the right, Pristine (P) and Tiger (T) relaxation rates summarized from table 4.6. Circles are measurements in the initial position with RF ≈ 154 kHz. Diamonds are measurements in the final position. Red diamonds indicate RF ≈ 154 kHz, blue diamonds indicate RF ≈ 91 kHz, and green diamonds indicate RF ≈ 91 kHz. Green final measurements (and their corresponding initial measurement) were taken after the target was degaussed. Initial measurements for the post-degaussing data are colored green strictly for emphasis; these measurements were taken at RF ≈ 154 kHz as with all initial measurements described in this and the previous section. 70
4.26 Design of a test cell (Lazarus) for the prototype metal end-windows. 72
4.28 Prototype MK-I and MK-II windows after being electropolished. 75
4.29 Luminosity in units of $10^{34} \cdot cm^{-2} \cdot s^{-1}$ from eight different experiments. Data (and sources) are summarized at the top of appendix A and in table A.1, but are taken from references [29], [45], [53], [62], [63], and [64]. Experiments here are color-coded: saGDH (orange), G_E^n-I and G_E^n-II (red), d_2^n-I and d_2^n-II (blue), A_1^n-I and A_1^n-II (purple), and Transversity (green). Note that the saGDH (orange) targets are Rb-only rather than a hybrid K-Rb mixture. Targets from Fulla (purple) and to the right of Fulla represent the experiments presented in this thesis. Targets to the left of Fulla are diffusion targets. All targets were used in beam and polarization results are from papers pertaining to their respective experiments. 76

5.1 Experimental setup for measuring wall/window thickness. Grad Student Illustrated by Dr. Jorge Cham, Illustrator, PhD Comics (jorge@phdcomics.com) . . 79
5.2 Analyzing the constructive interference pattern of the reflected beam 81
5.3 Positioning a target for window measurements. 83

5.4 Definitions of wall and window designations seen in A_1^n-II and d_2^n-II targets in this chapter. Positions along walls were designated by a side and a number position, i.e. L2 indicates the second position on the left side. Front, back, left, and right are assigned relative to the pNMR bulb. 85
5.5 A pressure broadened line profile. The shaded area is the kernal. It is the width of the FWHM and centered on the central frequency, ν_0. The remaining portions of the line are the wings. 89
5.7 Experimental setup for measuring pressure broadened absorption lines. Grad Student Illustrated by Dr. Jorge Cham, Illustrator, PhD Comics (jorge@phdcomics.com) 91
5.8 Variance in reflected and transmitted beam intensity through the Thorlabs Non-Polarizing Beamsplitter Cube. Shaded gray area represents range of operation for the laser used in this measurement. Data for these plots can be found on the Thorlabs website. The part number for the NPBS is listed in the footnotes. . . . 92
5.9 A typical example of spectroscopy data (in red) and a typical fit (in black). . . . 95
5.10 Examples of rubidium data (in red) and a typical fit (in black). Differences between the fit and the data (residuals) are shown in blue in the lower figure of each image. 99
5.11 Example of potassium data (in red) and a typical fit (in black) for target-cell Florence. Differences between the fit and the data (residuals) are shown in blue in the lower figure of each image. 101
5.12 A comparison of the Lorentzian (left) and pseudo-Voigt fits for a RbD2 line measured at 155°C 103
5.14 A comparison of the Lorentzian fit (left) and a full Lorentzian fit accounting for all possible hyperfine transitions for a RbD2 line measured at 155°C 107
5.15 Maximum attenuation vs. temperature (in °C) of absorption lines for all target cells scanned at high power. From left to right, plots are Rb D1, Rb D2, K D1, and K D2. Colors are for the following runs: Brianna Run 1 (blue), Florence Run 2 (red), Fulla Run 1 (purple), Fulla Run 2 (green), Fulla Run 5 (cyan), Noah Run 1 (deep pink), Sandy II Run 1 (gold), Sandy II Run 2 (pink), and Wayne Run 1 (chocolate). 117
5.16 Maximum attenuation vs. temperature (in °C) of absorption lines for all Kappa cells scanned at high power. From left to right, plots are Rb D1, Rb D2, K D1, and K D2. Colors are for the following runs: Kappa 1 Run 2 (blue), Kappa 2 Run 1 (red), Kappa 3 Run 1 (purple), Kappa 4 Run 1 (green), and Kappa 4 Run 2 (cyan). 117
5.17 Maximum attenuation vs. temperature (in °C) of absorption lines for all target cells scanned at low power. From left to right, plots are Rb D1, Rb D2, K D1, and K D2. Colors are for the following runs: Austin Run 1 (blue), Big Brother Run 1 (red), Brianna Run 2 (purple), Butterball Run1 (green), Butterball Run 2 (cyan), Dutch (deep pink), Florence Run 3 (gold), Florence Run 4 (pink), Florence Run 5 (chocolate), Fulla Run 6 (rosy brown), Tommy Run 1 (teal), and Wayne Run 2 (Dodger blue). 118

5.18 Maximum attenuation vs. temperature (in °C) of absorption lines for all Kappa cells scanned at low power. From left to right, plots are Rb D1, Rb D2, K D1, and K D2. Colors are for the following runs: Kappa 2 Run 2 (blue), Kappa 3 Run 2 (red), Kappa 3 Run 3 (purple), Kappa 3 Run 4 (green), Kappa 4 Run 3 (cyan), Kappa 4 Run 4 (deep pink) and Kappa 5 Run 1 (gold). 118
5.19 FWHM (GHz) vs. temperature (in °C) for TARGET and KAPPA cell Rb D-lines measured at LOW POWER. 119
5.20 Average FWHM/Density (GHz/Amagats) vs. temperature (in °C) for TARGET cell absorption lines measured at HIGH POWER. Starting from upper left, plots are Rb D1, Rb D2, K D1, and K D2. 120
5.21 Average FWHM/Density (GHz/Amagats) vs. temperature (in °C) for KAPPA cell absorption lines measured at HIGH POWER. Starting from upper left, plots are Rb D1, Rb D2, K D1, and K D2. 120
5.22 Average FWHM/Density (GHz/Amagats) vs. temperature (in °C) for TARGET cell absorption lines measured at LOW POWER. Starting from upper left, plots are Rb D1, Rb D2, K D1, and K D2. 121
5.23 Average FWHM/Density (GHz/Amagats) vs. temperature (in °C) for KAPPA cell absorption lines measured at LOW POWER. The gray circles represent Kappa 5, the only Rb-only cell for which I gathered data. Starting from upper left, plots are Rb D1, Rb D2, K D1, and K D2. 121
5.24 Results for run 1 (high power, bottom) and run 2 (low power, top) of target-cell Wayne for each of the 4 absorption lines. of low power tests for Wayne. On the left, attenuation plotted against temperature (°C). On the right, FWHM (GHz) plotted against temperature. 123
5.25 Results of low power test, Florence Run 4, with error bars reflecting combined error from all measurements at that temperature for each of the 4 absorption lines: RbD1 (blue), RbD2 (red), KD1 (purple), and KD2 (green). On the left, attenuation plotted against temperature (°C). On the right, FWHM (GHz) plotted against temperature. 124

List of Tables

3.1 Kinematic settings for the recent A_1^n measurement (from reference [32]). Production times listed are planned production times and are only an estimate. . . 21

3.2 Kinematic settings for the recent d_2^n measurement (from reference [33]). Targets used in this experiment were Brianna, Tommy, and Austin. 22

3.3 A summary of the information for previous experiments presented in this section. Information in this table comes from the following references: E-142 [25], E-154 [34], HERMES [27], A_1^n-I [14], g_1^n [28], and d_2^n-I [29]. Target length for g_1^n taken from Solvignon's thesis [35]. Information for A_1^n-II and d_2^n-II are average values for targets that were used in-beam for those experiments. Information on those targets is presented in chapter 4. Effective luminosity ($\mathcal{L}^{eff}$) is calculated for the entire target at room temperature as opposed to only the TC at operating temperature (as is done in table A.1) and using the largest values of beam current. The equation for effective luminosity can be found in chapter 4, equation 4.1. . . 22

3.4 Kinematic settings for the recent G_E^n-II measurement.[39] 29

3.5 A summary of the information for previous experiments presented in this section. Information in this table comes from the following references: Pilot [36], A3 [18], A1 [37], G_E^n/A_y^os [38], and G_E^n-I [40]. Information for G_E^n-II are average values for targets that were used in-beam for those experiments. Information on those targets is presented in chapter 4. Effective luminosity ($\mathcal{L}^{eff}$) is calculated for the entire target at room temperature as opposed to only the TC at operating temperature (as is done in table A.1). The equation for effective luminosity can be found in chapter 4, equation 4.1. 29

4.1 Physical Characteristics of A_1^n-II and d_2^n-II target-cells. TC wall thickness measurements with an asterisk (*) were measured via ultrasonic interferometry at JLab. All others were measured with laser interferometry at UVa. See chapter 5 for further details. 37

4.2 Physical Characteristics of G_E^n-II target-cells. TC wall thickness measurements with an asterisk (*) were measured via ultrasonic interferometry at JLab. All others were measured with laser interferometry at UVa. See chapter 5 for further details. 38

4.3 Effective luminosity at operating temperature, $\mathcal{L}^{eff}(T_{op})$ (equation 4.1), for **target chamber** of all targets used in beam for the 2020 A_1^n/d_2^n experiments and the 2023 G_E^n experiment. FOM are in units of $10^{34}\cdot cm^{-2}\cdot s^{-1}$ similar to reference [53]. Scaling to operating temperature detailed in section 4.5 and figure 4.29 in that section. 57
4.4 Polarimetry results from tests performed at UVa for A_1^n targets as measured in the pumping chamber (PC). [1]There is no error on Sandy-II maximum lifetime as the single spin-down consisted of only two data points. D.Rate is the measurement rates for the multiple spin-downs that were used to find the adjusted lifetime or the single measurement rate which found the maximum lifetime. . . . 58
4.5 Polarimetry results for G_E^n targets as measured in the pumping chamber (PC). JLab results are preliminary as analysis is still ongoing. The rate and RF frequency listed in columns 3 and 4 were the settings which yielded the maximum lifetime in column 5. Similarly, the laser power and RF frequency listed in columns 6 and 7 were the settings which yielded the maximum polarization in column 8. 59
4.6 Relaxation rates in units of hr^{-1} for G_E^n-II targets in their initial orientation (Initial) and rotated 180° in their final position (Final). Error from multiple spin down measurements added in quadrature. (Post) indicates measurements taken post-degaussing. All data are from spin downs with convection on, taken consecutively, and with measurements at 2 hour intervals with the following exceptions: (1) Pristine's Initial is an average of 2 and 4 hour intervals, (2) Hunter's Final is an average of 1 and 2 hour intervals, (3) Tiger (B) Final is an average of 2, 4, and 8 hour intervals, and (4) Ginger (B) measurements were not taken consecutively. Ginger was measured in O3 at 154 kHz then O4 at 154 kHz, resulting in Ginger (A). RF was then lowered to 91 kHz, resulting in the Ginger (B) final measurement; both Ginger (A) and (B) share the same initial measurement. 69

5.1 Window thickness (μm) for A_1^n and d_2^n target-cells as measured using laser interferometry. 85
5.2 Target wall thickness (mm) for A_1^n-II and d_2^n-II target-cells measured with laser (Las.) ultrasonic (U.So.) interferometry. Laser interferometry measurements were performed at UVa. Uncertainty for laser interferometry measurements were on the order of 10^{-4}mm. Ultrasonic interferometry measurements were performed at JLab. Uncertainty for ultrasonic interferometry measurements are ±0.05mm. 86
5.3 Window thickness (μm) for G_E^n target-cells as measured using laser interferometry. Mechanical measurements (Mech.) were performed by Mike Souza. The 3-Pt and 9-Pt measurements are the 3-point and 9-point measurements described in section 5.2.1. 87
5.4 Natural line width and Doppler width (in GHz) for applicable rubidium (Rb) and potassium (K) D-Lines. Doppler width calculated for $T = 373K$ 88
5.5 Scan Ranges for applicable rubidium (Rb) and potassium (K) D-Lines 94

5.6 Shift from the mean freq. of the D1 and D2 lines for all stable isotopes of Rb and K . . . 104
5.7 FWHM (in GHz) for Rb lines of two targets using three different Lorentzian fits: a single Lorentzian (eq. 5.10), a sum of 4 Lorentzians (eq. 5.12), or a sum of 20 Lorentzians (described in this section). . . . 106
5.8 Oscillator strengths for Rb lines (ref [71] and [72]) and K lines (ref [75]) . . . 111
5.9 Results from Averett *et al.* at the College William and Mary for target-cell Florence. I do not know if power here refers to the power from the laser or the power of the laser going through the pumping chamber. . . . 122
5.10 A comparison of FWHM/density (GHz/amagats) for absorption lines of Kappa-cells measured at low power with FWHM/density for those same lines taken at 80°C from Romalis *et al.* and Kluttz *et al.* . . . 125

A.1 Comparison of Effective Luminosity in units of $10^{34} \cdot \mathrm{cm}^{-2} \cdot \mathrm{s}^{-1}$ from several eras of target production across 8 experiments. ^{3}He Den. is fill density at room temperature and is scaled to operating temperature using equation A.1. . . . 132
A.2 Two tables showing the data displayed in 4.19 as well as the longest measured lifetime for each target. . . . 134
A.3 The data displayed in 4.21 as well as the longest measured lifetime for each target. Triveline, Autobahn, and Talisker were excluded from the plots because they did not have EPR calibrations. . . . 135
A.4 The data displayed in 4.20 as well as the longest measured lifetime for each target. Triveline, Autobahn, and Talisker were excluded from the plots because they did not have EPR calibrations. . . . 136

B.1 Austin - Low Power Spec. Results (Fitted) . . . 138
B.2 Austin - Low Power Spec. Results (Integrated) . . . 138
B.3 Big Brother - Low Power Spec. Results (Fitted) . . . 140
B.4 Big Brother - Low Power Spec. Results (Integrated) . . . 140
B.5 Brianna - High Power Spec. Results (Fitted) . . . 142
B.6 Brianna - High Power Spec. Results (Integrated) . . . 142
B.7 Brianna - Low Power Spec. Results (Fitted) . . . 144
B.8 Brianna - Low Power Spec. Results (Integrated) . . . 144
B.9 Butterball - Low Power Spec. Results (Fitted) . . . 146
B.10 Butterball - Low Power Spec. Results (Integrated) . . . 147
B.11 Dutch - Low Power Spec. Results (Fitted) . . . 149
B.12 Dutch - Low Power Spec. Results (Integrated) . . . 149
B.13 Florence - High Power Spec. Results (Fitted) . . . 151
B.14 Florence - High Power Spec. Results (Integrated) . . . 151
B.15 Florence - Low Power Spec. Results (Fitted) . . . 153
B.16 Florence - Low Power Spec. Results (Integrated) . . . 154
B.17 Fulla - High Power Spec. Results (Fitted) . . . 157
B.18 Fulla - High Power Spec. Results (Integrated) . . . 158
B.19 Fulla - Low Power Spec. Results (Fitted) . . . 161
B.20 Fulla - Low Power Spec. Results (Integrated) . . . 161

B.21 Kappa 1 - High Power Spec. Results (Fitted) . . . 162
B.22 Kappa 1 - High Power Spec. Results (Integrated) . . . 162
B.23 Kappa 2 - High Power Spec. Results (Fitted) . . . 164
B.24 Kappa 2 - High Power Spec. Results (Integrated) . . . 164
B.25 Kappa 2 - Low Power Spec. Results (Fitted) . . . 166
B.26 Kappa 2 - Low Power Spec. Results (Integrated) . . . 167
B.27 Kappa 3 - High Power Spec. Results (Fitted) . . . 169
B.28 Kappa 3 - High Power Spec. Results (Integrated) . . . 169
B.29 Kappa 3 - Low Power Spec. Results (Fitted) . . . 170
B.30 Kappa 3 - Low Power Spec. Results (Integrated) . . . 173
B.31 Kappa 4 - High Power Spec. Results (Fitted) . . . 176
B.32 Kappa 4 - High Power Spec. Results (Integrated) . . . 176
B.33 Kappa 4 - Low Power Spec. Results (Fitted) . . . 178
B.34 Kappa 4 - Low Power Spec. Results (Integrated) . . . 178
B.35 Kappa 5 - Low Power Spec. Results (Fitted) . . . 180
B.36 Kappa 5 - Low Power Spec. Results (Integrated) . . . 180
B.37 Noah - High Power Spec. Results (Fitted) . . . 181
B.38 Noah - High Power Spec. Results (Integrated) . . . 181
B.39 Noah - Low Power Spec. Results (Fitted) . . . 182
B.40 Noah - Low Power Spec. Results (Integrated) . . . 182
B.41 Sandy II - High Power Spec. Results (Fitted) . . . 183
B.42 Sandy II - High Power Spec. Results (Integrated) . . . 183
B.43 Savior - High Power Spec. Results (Fitted) . . . 185
B.44 Savior - High Power Spec. Results (Integrated) . . . 185
B.45 Tommy - Low Power Spec. Results (Fitted) . . . 186
B.46 Tommy - Low Power Spec. Results (Integrated) . . . 186
B.47 Wayne - High Power Spec. Results (Fitted) . . . 188
B.48 Wayne - High Power Spec. Results (Integrated) . . . 188
B.49 Wayne - Low Power Spec. Results (Fitted) . . . 190
B.50 Wayne - Low Power Spec. Results (Integrated) . . . 190

Chapter 1

A beginning...

"*In the beginning the Universe was created.*
This has made a lot of people very angry and been widely regarded as a bad move." [1]

Oh, where to begin? Perhaps, before I brief you on the rest of the thesis (don't worry, it's the very next paragraph), I should state my intentions plainly: I hope I don't bore you. More specifically, I hope this work does not conform to the tone of regular scientific literature. That is to say, I hope I can deliver this information with the same rigor, detail, and unflinching commitment to honesty we all deserve from scientific research, but with, perhaps, 10% more whimsy. Levity is sorely lacking in scientific communication, wouldn't you agree? Perhaps just as my research is a tiny step forward in our broader understanding of the subjects herein, this thesis could be a tiny step forward in making scientific communication a little more interesting (and, dare I say it, more accessible).

But that's just my personal opinion on the subject and you're not here for *that*! *You're* here for the ***science***. So, moving on.

This thesis chronicles my work with three experiments at Jefferson Laboratory which utilized polarized, ^{3}He targets to investigate the internal structure of the neutron. I will only touch on the experiments I was directly involved with that also involved my targets (sorry, PREX-II, but you are the subject of a thesis I will never have the pleasure of writing)[1]. These would be the A_1^n and d_2^n experiments which ran at Jefferson Lab (JLab) from late 2019 to early 2020 and the G_E^n experiment which ran at JLab during 2023. I'll delve into the physics these experiments were investigating, how these experiments were performed, and what questions we expected to address. Results of these experiments are still a number of months or years down the line and I will not be reporting on them at length in this thesis; I'd like to graduate soon, being currently near the end of my ninth year in grad school!

As my primary job during these experiments was to characterize polarized ^{3}He target-cells, the development of these targets will be one of the primary topics of this thesis. I'll detail my work with the UVa Spin Physics Group, building and characterizing target-cells as well as developing the next generation of targets. There were a few fun mysteries that arose during

[1]Prior to working with Gordon Cates and the Spin Physics Group, I was also fortunate enough to work with Kent Paschke for a year and left the PREX-II experiment with his blessing. I did sit shifts at JLab for that experiment, which was a pleasant coda to the work I'd done with Kent.

the production of the G_E^n cells and there have always been questions about what elements of filling a target go into making a high quality target-cell. I've tried my best to separate science from superstition regarding these production variables. Also, of course, I report on the vast improvement in the targets from those used in previous experiments. The targets made for the 2023 G_E^n experiment represent a significant increase in target quality over all previous experiments *including* the A_1^n and d_2^n experiments a scant few years before.

The other major focus of this thesis will be laser spectroscopy and interferometry. I was originally brought into this group to design and build an updated spectroscopy and interferometry system so we could do "pressure-broadening measurements" and measure the thickness of glass windows (with *lasers*...which is *rad*). And while I've achieved that goal in that the system definitely provides high quality data with a very high signal to noise ratio, the results have always skewed from what we expected. Consistently. While the pessimist in me initially suspected incompetence on my part[2], I have no reason to disbelieve the results. It's just...a *very* interesting trend in the data, one that seems to match historical data at benchmark t– you know what? I don't want to spoil it any further. I've done my level best to chronicle my efforts in building the new spectroscopy system, to explain the many attempts at reconciling the data with the theory, and, in the end, to show unequivocally that there's something happening here...and what it is...ain't exactly clear.[3]

Lastly (or perhaps firstly if you're looking at chapter order), I'll put all of this work in historical context. Here, I outline the difficult work of understanding what is happening inside of neutrons and protons. I joked with my wife that I'm essentially writing a book report, but perhaps that's not an unfitting metaphor. I touch on everything from our initial ideas about the internal structure of nucleons to Murray Gell-Mann, Finnegan's Wake, and finally to the results of the 1988 EMC experiment, which showed us just how little we actually knew. The findings of the EMC experiment resulted in what we called the "Proton Spin Crisis", although I've heard it downgraded to the "Proton Spin Problem". But look, we did not call the issue "The Proton Spin Inconvenience" or "The Proton Spin Kerfuffle", we called it "The Proton Spin *Crisis*" because we understood, in that moment, how much our knowledge was *lacking*. And that's fantastic! What an opportunity to learn! And we *did* learn. We soldiered on and kept looking, leading to the next 40 years of fascinating research, a whole slew of PhDs along the way, and eventually this humble thesis of mine, which I hope will be a worthy addition: a small brick with which to build our collective knowledge.

[2] ...which is probably just the clinical depression, frankly.

[3] The wording here is *absolutely* an allusion to reference [2], a great song by the supergroup *Buffalo Springfield*.

At the time of this writing, this thesis is incomplete. In fact, I haven't written the next chapter! Don't worry, I'm sure it'll be done by the time *you* get there. If not, skip to the ones that *are* done, would ya?[4] But before I get to the "book report", I wanted to get this small introduction out of the way. My dear dear reader, I hope you enjoy my thesis. I hope some of my words make you laugh or at least chortle to yourself. And if you're one of the next generation of graduate students or even some soul in the far flung future, I hope you find this thesis useful.

Your Friend in Time,[5]

(Hopefully) Dr. Christopher James Jantzi, April 4th, 2024

[4]Honestly, unless you're Gordon Cates or Xiaochao Zheng, I don't expect you to be reading this chapter prior to the thesis being done and if you are . . . why? You've *got* to have better things to do than proofread. Go away now. Shoo! SHOO!

[5]A reference to the *Back to the Future* film series. Dr. Emmett Brown signed his letter this way when writing his time displaced friend, Marty, 70 years in the future. For more information, watch the end of *Back to the Future: Part II* and/or the beginning of *Back to the Future: Part III*, Directed by Robert Zemeckis, Performances by Michael J. Fox, Christopher Lloyd, Thomas F. Wilson, and Lea Thompson, Amblin Entertainment and Universal Pictures, 1989 and 1990, respectively.

Chapter 2

The Proton Spin Crisis and the Fallout

In 1969, a fundamental shift in our understanding of the nucleon occurred with one of SLAC's very first experiments. E-4 was meant as a shakedown of the systems at "the Monster"[3], an affectionate nickname for the still new accelerator, which could accelerate electrons to higher energies than any accelerator before it, reaching beam energies of up to 50 GeV with Q^2 up to 4 $(\mathrm{GeV}/c)^2$. It was also a test of a few fundamental hypotheses about the nucleon such as the existence of a nucleon core. At the time, a widespread notion of what the internal nucleon structure looked like was a hard core with a soft shell. Imagine the plum pudding model of the atom except with one giant plum and not a lot of pudding and you've got it.

The results were surprising in that for larger invariant mass, W, what was seen was only a weak dependence[4][5] on four-momentum transfer squared, q^2, as you can see from figure 2.1. This was not what was expected if the electrons were elastically scattering from a core with a finite radius. Instead, the electrons seemed to be scattering off of point-like objects. Luckily, in a paper published five years earlier, Murray Gell-Mann argued we could model the nucleon as three *purely mathematical* particles to describe the interior of the nucleon. He theorised there would be three of these things and decided to call them "quarks" after a line from *Finnegan's Wake*: "— Three quarks for Muster Mark!"[1]. The word had no meaning, like many words in *Finnegan's Wake*. So...why not?

Gell-Mann's theory wasn't taken seriously at the time as a description of physical particles. Gell-Mann himself concluded that paper by stating, "A search for stable quarks [...] at the highest energy accelerators would help to reassure us of the non-existence of real quarks"[6]. Maybe he was being cautious with his language or maybe he didn't think the quark could be a real particle, I don't know, but his paper went on to make predictions about how these mathematical entities would behave were they physical particles, predictions that match how we've observed real quarks behave. As an example, he predicted one quark (presumably u or d, in his words) would be stable and the other would decay into it, which we now recognize as the mechanism for neutron decay, wherein a d-quark decays to a u-quark.

One prediction held that 100% of a nucleon's spin angular momentum would come from the spin and orbital angular momentum of the constituent quarks[7]. But how to test it? Well, in

[1] James Joyce wrote a truly wild poem. "Three quarks for Muster Mark! Sure he hasn't got much of a bark And sure any he has it's all beside the mark" and that goes on for half a page before getting to made up words like "hattajocky". Seriously, start from any page and read the whole thing around back to that page and it makes as much sense as starting from the beginning. Intentionally.

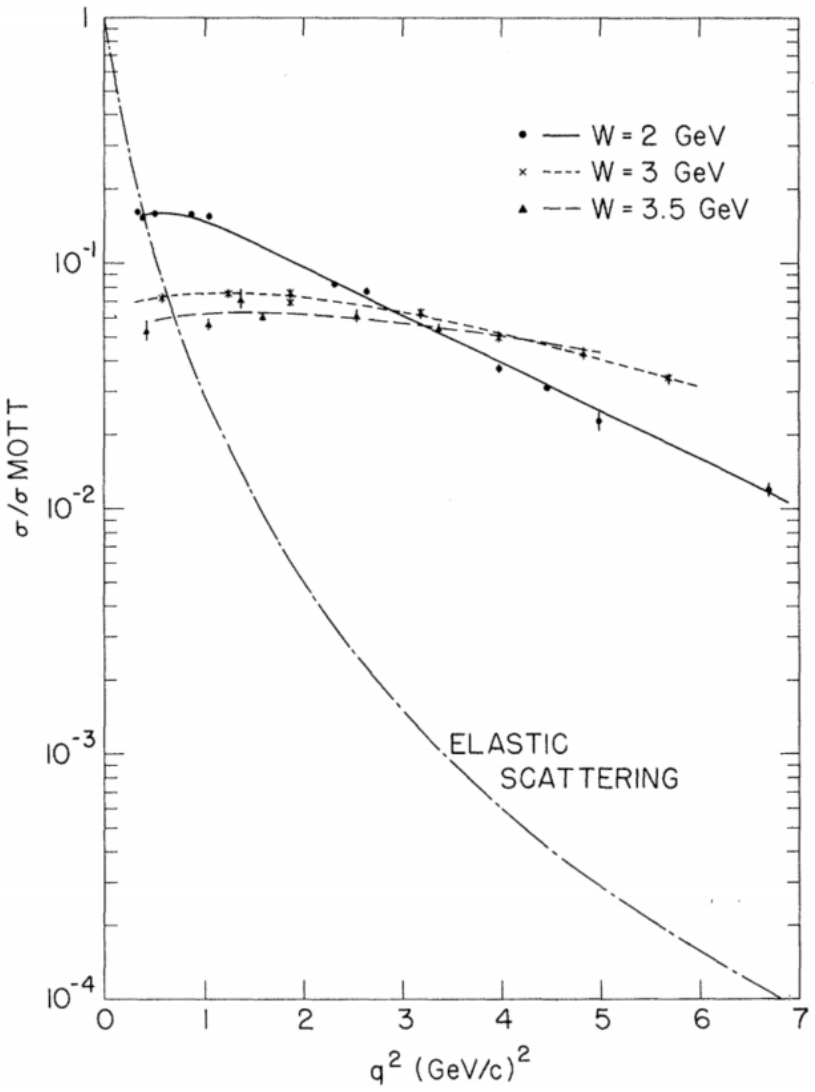

Figure 2.1: From reference [4], the paper reporting results for SLAC's E-4 experiment. From that paper: $[\sigma/\sigma_{Mott}]$ in GeV^{-1} vs q^2 for $W = 2, 3$ and 3.5 GeV. The lines drawn through the data are meant to guide the eye. Also shown is the cross section for elastic e-p scattering divided by σ_{Mott}, calculated for $\theta = 10°$, using the dipole form factor. The relatively slow variation with q^2 of the inelastic cross section compared with the elastic cross section is clearly shown.

the late 1970's, Vernon Hughes was homeless. Rather, his experiment was. Hughes had developed the first polarized electron sources for SLAC and led the first spin structure experiments. Despite the initial positive reception to his latest research proposals, SLAC discontinued his research. Hoping to continue his work (scattering polarized electrons off of polarized protons[8]), he needed a new home. And although his experiments would eventually make a return to SLAC, he currently found a home for his experiments with the European Muon Collaboration (EMC) located at the *Conseil Européen pour la Recherche Nucléaire*, better known . . . as CERN[2].

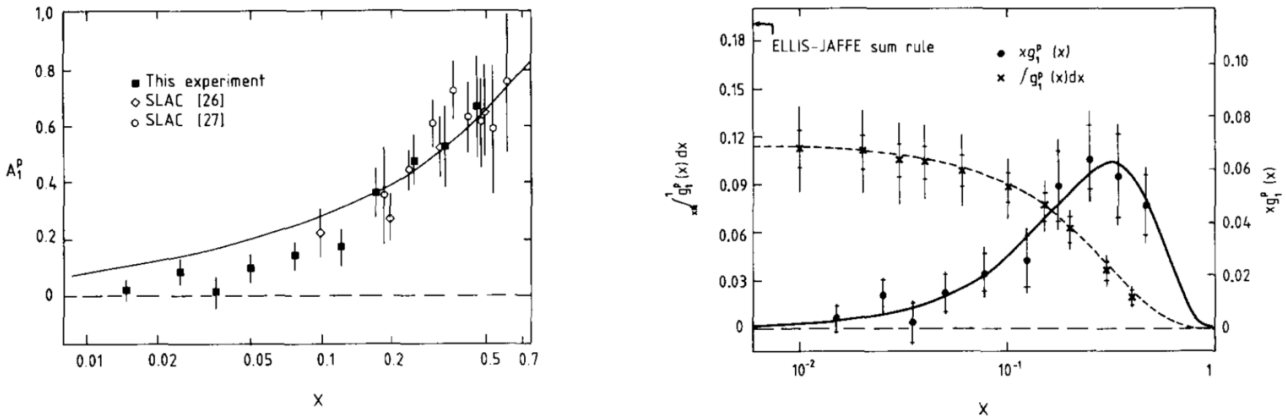

Figure 2.2: Results from the landmark 1988 EMC experiment which spawned the Proton Spin Crisis. Left: The asymmetry A_1^p plotted vs. x along with results from SLAC [26] (reference [9]) and SLAC [27] (reference [10]) with a curve modelled from reference [11]. Right: $xg_1^p(x)$ plotted vs. x and $\int_{x_m}^1 dx$ plotted vs. x_m with a marker showing the Ellis-Jaffe prediction for $\int_{x_m}^1 dx$ at $x = 0$, a sum rule that assumes the strange quarks in the nucleon are unpolarized.

Through the 1980's, the European Muon Collaboration (EMC) set out to better understand the internal structure of the proton using even higher energy muons with Q^2 up to 70 $(\mathrm{GeV}/c)^2$. Hughes led the EMC in a new direction, continuing his work from SLAC in experiments with both polarized and unpolarized protons which showed that the spin of the polarized proton was not concentrated in its valence quarks [12]. With a landmark paper in 1988 (reference [13]), the EMC collaboration reported the spin carried by these quarks only accounted for $(12 \pm 14)\%$ of total nucleon spin! This 1988 result came to be known as the "Proton Spin Crisis".

Since 1988, constructing a complete picture of nucleon spin structure has become one of the most important questions in nuclear physics today. We've since found the constituent quarks carry 20% to 30% of total nucleon spin[14], but there is still work to be done.

2.1 A breakdown of total nucleon spin

So where does the nucleon spin come from if it's not simply from the spin of the constituent quarks? Our understanding is that total nucleon spin comes from the spin *and* orbital angular

[2]And queue the fanfare and queue the applause. I mean, it's *CERN*. That's a pretty big deal, even now, 70 years after it's founding!

momentum of *all* of the elements of the hadronic system, summed up nicely in the Jaffe-Manohar decomposition formula (reference [15]):

$$\frac{1}{2} = \frac{1}{2}\Delta\Sigma + \Delta G + L_q + L_g \tag{2.1}$$

where $(1/2)\Delta\Sigma$ is the spin of the quarks, ΔG is the spin of the gluons, L_q is the orbital angular momentum of the quarks, and L_g is the orbital angular momentum of the gluons.

Of course, this summation rule isn't the same for both types of nucleons. All of the terms on the right hand side of the equation are necessarily different as protons and neutrons have different flavors of valence quarks and, unfortunately, we can only study the nucleons as a whole rather than studying the properties of the constituent parts as well as how they interact; color confinement prevents us from removing the constituent parts of the nucleon and isolating them for study. All is not lost, though. The difference between a proton and a neutron is the flavor of a single quark: a proton is two up-quarks and one down-quark (uud) while a neutron is one up-quark and two down-quarks (udd). The two nucleons are connected through "flavor" or "isospin" symmetry, so studying both nucleons and comparing the results allows us to determine the motion of both up and down quarks.

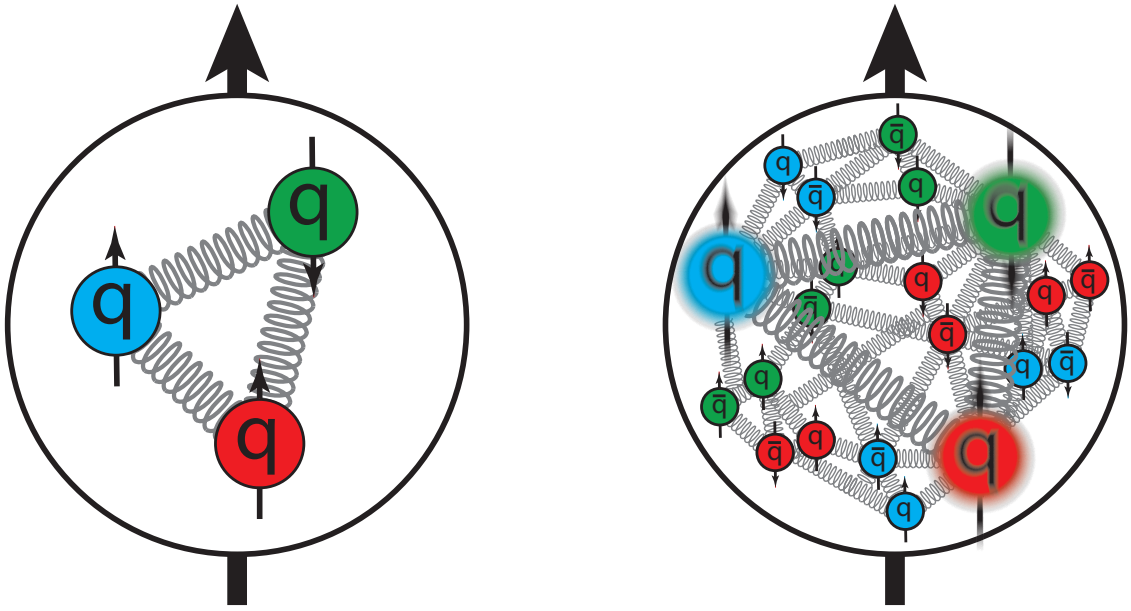

(a) An early, simple interpretation consisting of the constituent quarks and the gluons holding them together.

(b) A complex, modern interpretation consisting of the quark-antiquark sea, a multitude of gluon interactions, and the "constituent quarks" shown as large, fuzzy quarks.

Figure 2.3: Two images showing the evolving complexity of our picture of the inside of a nucleon.

Experiments at SLAC, including the early work of Vernon Hughes and measuring the quark spin and orbital angular momentum, continued on at JLab using polarized NH_3, ND_3, and ^3He. Much later, measurements at the Relativistic Heavy Ion Collider (RHIC) and CERN

have shed some light on the gluon spin term, ΔG, showing that this contribution to total spin is "sizeable" (reference [16]) at about 26%, though with large uncertainties. Coupled with the knowledge that the quark spin, $(1/2)\Delta\Sigma$, contributes about 30%, the hazy picture of internal proton structure is much clearer than in 1988. Indeed, one term in equation 2.1 whose contribution to total spin remains *quite* hazy is the orbital angular momentum contribution of the quarks. That is one of the focuses of the A_1^n experiment discussed in chapter 3 as well as upcoming measurements at the planned Electron-Ion Collider (EIC).

A further complication arises when studying the spin and orbital angular momentum terms for the quark. On average, each of these nucleons contains three quarks, which we call "valence quarks" (as in what we all learned in Elementary Particles 101, see figure 2.3a). As seems with everything *else* in quantum mechanics, the truth is much more complex. In reality, the quark content of a nucleon consists of a bubbling quark-antiquark sea where quark-antiquark pairs form from gluons that split, quickly annihilate, and revert to gluons (figure 2.3b) *as well as* an average of three valence quarks. So, the spin and orbital angular momentum terms in equation 2.1 contain not only the spin and angular momentum contribution from the three valence quarks, but also the spin and angular momentum of the quark-antiquark sea.

One region where we can effectively study the valence quark contribution, i.e. where the contribution from the sea quarks is small, is the large x region, also know as the "valence quark region". Here, where there are scarce sea quarks (and gluons), we can examine the spin contribution from the valence quarks independently.

2.2 Functions for describing the interior of a nucleon

When testing theoretical models, two types of functions are useful to describe the internal, electromagnetic structure of the nucleon. Much of this section will be paraphrasing several chapters of reference [17], especially chapters 6, 7, and 16. Equations in this section were sourced from those chapters as I found the explanation of these concepts by Povh *et al.* to be very helpful.[3]

The first functions are "form factors". Roughly speaking, these describe the electromagnetic spatial distribution of the partons inside the nucleon[18]. They can be directly related back to the cross section for scattering an electron from a nucleon via the Rosenbluth formula (page 77 of [17]):

$$\left(\frac{d\sigma}{d\Omega}\right) = \left(\frac{d\sigma}{d\Omega}\right)_{Mott} \cdot \left[\frac{G_E^2(Q^2) + \tau G_M^2(Q^2)}{1+\tau} + 2\tau G_M^2(Q^2)\tan^2\frac{\theta}{2}\right] \tag{2.2}$$

where G_E and G_M are the electric and magnetic form factors of the nucleon, respectively. $(d\sigma/d\Omega)_{Mott}$ is the Mott scattering cross section. Finally, $\tau = Q^2/4M^2c^2$ where Q is the four-momentum transfer from the electron to the nucleon, M is the nucleon mass, and c is speed of light in a vacuum, as usual.

[3] I have recently learned some people dislike Povh. To that derision, I offer a word of advice. It's better to find an author whose explanation, perhaps with less math or more analogy, makes sense to *you*. Don't waste your precious time bludgeoning yourself with a 500-page textbook hoping the head trauma will allow knowledge to pass to your brain through osmosis.

The form factors G_E and G_M are measured by elastically scattering leptons from the nucleon and they are both solely dependent on Q^2. Determining these form factors at different Q^2 gives us information about the radial distributions of electric charge (G_E) and magnetic field (G_M) inside the nucleon. In the limit where $Q^2 \to 0$, G_E becomes the charge of the nucleon and G_M becomes the magnetic moment of the nucleon:

$$\begin{aligned} G_E^p &= e & G_E^n &= 0 \\ G_M^p &= +2.793\mu_N & G_M^n &= -1.913\mu_N \end{aligned}$$

where $\mu_N = e\hbar/2M_p$ is the nuclear magneton, e is the elementary charge, M_p is the rest mass of the proton, and $\hbar$ is the reduced Planck's constant.

Historically, form factors were measured using the Rosenbluth separation method [18], but at high values of Q^2, the cross-section is dominated by the magnetic form factor, making the extraction of the electric form factor difficult. For many years, it was believed that G_E^p and G_M^p were of comparable size at high Q^2, though the data supporting this idea came with relatively large errors. However, using double polarization techniques, Jones *et al.*[19] discovered the ratio G_E^p/G_M^p actually *decreased* nearly linearly with Q^2! This discovery was a primary motivator for the measurement of G_E^n/G_M^n, a central part of the work presented here. Double polarization techniques will be discussed more in chapter 3.

The second type of functions are called "structure functions". Again roughly speaking, these describe the momentum distribution of the partons inside the nucleon[18]. As with form factors, structure functions can be related back to the scattering cross section; structure functions serve the same role in deep inelastic scattering (DIS) as form factors do in elastic scattering with a few addenda. First, we are no longer scattering from the nucleon as a whole. Instead, in DIS, we scatter from the quarks themselves. As a consequence, these functions are dependent not just on Q^2, but also dependent on the Lorentz-invariant "Bjorken scaling variable", x, defined in equation 2.3. x can be interpreted as the fraction of the nucleon momentum carried by the struck quark in the infinite momentum frame.

We define both x and another Lorentz-invariant variable, y, in the usual way:

$$\begin{aligned} x &= \frac{Q^2}{2M(E-E')} = \frac{Q^2}{2M\nu} \\ y &= \left(1 - \frac{E'}{E}\right)_{lab} \end{aligned} \tag{2.3}$$

where $Q^2 = 4EE'\sin^2(\theta/2)$ is momentum-transfer squared (neglecting the mass of the electron), M is the nucleon mass, E is the energy of the incoming electron, E' is the energy of the outgoing electron, $\nu = E - E'$, and θ is the scattering angle.

The second important difference between the form factor cross-section from equation 2.2 and the cross-section for these structure functions is a consequence of what the structure functions

are describing: momentum distribution of the quarks *within* the nucleon. Again, this is encapsulated in the structure functions by including their dependence on x. Models that include or don't include quark orbital angular momentum (OAM), for instance, will make dramatically different predictions for how these structure functions will behave in the high-x region[14], allowing us to take measurements at a variety of x-values and ideally begin to distinguish between these models.

For a target and electron with no polarization, the structure functions are denoted $F_1(x, Q^2)$ and $F_2(x, Q^2)$. These are measured by inelastically scattering non-polarized electrons from a non-polarized nucleon. The cross section for these spin independent structure functions is written in the following way (page 91 of reference [17]):

$$\left(\frac{d^2\sigma}{dQ^2\,dx}\right) = \frac{4\pi\alpha^2\hbar^2}{Q^4}\left[y^2F_1(x,Q^2) + \left(\frac{1-y}{x} - \frac{My}{2E}\right)F_2(x,Q^2)\right] \tag{2.4}$$

where y and x are as defined in equation 2.3 and $\alpha \approx 1/137$ is the *fine structure constant*.

Both structure functions in equation 2.4 relate back to the simple momentum distribution of the quarks[4], both valence quarks and sea quarks, by taking a sum of these distributions weighted by the square of the quark charge:

$$\begin{aligned} F_1(x,Q^2) &= \frac{1}{2}\sum_{q=u,d,s} z_q^2[q_{\text{val}}(x,Q^2) + q_{\text{sea}}(x,Q^2) + \overline{q}_{\text{sea}}(x,Q^2)] \\ F_2(x,Q^2) &= 2x \cdot F_1 \end{aligned} \tag{2.5}$$

where z_q is the charge for the type of quark normalized to the elementary charge: 2/3 for up-quarks, -1/3 for down- and strange-quarks[5]. The summation is done for up-, down-, and strange-quarks (and antiquarks). Each $q(x, Q^2)$ function is the parton distribution function (PDF) for a particular quark and the "val" and "sea" subscripts denote the valence and sea quarks, respectively. Finally, the q_{val} term for strange quarks is, in principle, zero and thus ignored in the case of the proton and neutron.

For a target and electron-beam (or muon-beam) which are polarized with respect to the electron-beam direction, the spin dependent structure functions are g_1 and g_2. These relate to how the spin of the quarks are aligned with respect to the spin of the nucleon (see eqn. 2.8 below), again measured by inelastically scattering electrons from the nucleon. The cross section is...a little more complicated than equation 2.4. We actually have to consider a combination of two cross sections. With both the electron and nucleon longitudinally polarized, we consider the cross section where the electron-beam polarization and target polarization are parallel and the cross section where the two are anti-parallel. With that in mind, we have the following cross section (from page 271 of reference [17]):

[4] As a consequence of quark spin being 1/2.[17]

[5] Approximations based on the parton-model approximation.

$$\left(\frac{d^2\sigma_{LL}}{dQ^2\,dx}\right) = \frac{8\pi\alpha^2\hbar^2 y}{Q^4}\left[\left(1-\frac{y}{2}-\frac{yxMc^2}{2E}\right)g_1(x,Q^2)-\frac{xMc^2}{E}g_2(x,Q^2)\right] \tag{2.6}$$

where all terms are as defined in equation 2.4 save for the cross section, σ_{LL}, which is defined in the following way:

$$\sigma_{LL} = \frac{1}{2}\left(\sigma^{\rightarrow}_{\Rightarrow} - \sigma^{\rightarrow}_{\Leftarrow}\right) \tag{2.7}$$

where $\Rightarrow$ and $\Leftarrow$ are the polarization direction of the target, $\rightarrow$ is the polarization direction of the beam, and the cross section when the two are parallel or anti-parallel are described by $\sigma^{\rightarrow}_{\Rightarrow}$ and $\sigma^{\rightarrow}_{\Leftarrow}$, respectively.

As with F_1 and F_2, g_1 can be related back to some sort of quark distributions, albeit this time the distribution of quark helicity:

$$g_1(x,Q^2) = \frac{1}{2}\sum_{q=u,d,s} z_q^2[\Delta q_{\text{val}}(x,Q^2) + \Delta q_{\text{sea}}(x,Q^2) + \Delta\overline{q}_{\text{sea}}(x,Q^2)] \tag{2.8}$$

where Δq denote the helicity distributions rather than momentum distributions of the quarks, but otherwise the equation mirrors equation 2.5.

According to references [14], [17], and [20], g_2 does not have a simple interpretation based on quark distributions. However, we can decompose it into a term wholly dependent on g_1 and another term that encapsulates the quark-gluon correlations:

$$g_2(x,Q^2) = g_2^{WW}(x,Q^2) + \bar{g}_2(x,Q^2) \tag{2.9}$$

where $\bar{g}_2(x,Q^2)$ contains the quark-gluon correlations and $g_2^{WW}(x,Q^2)$ is the "twist-2" term derived by Wandura and Wilczek and is defined as follows:

$$g_2^{WW}(x,Q^2) = -g_1(x,Q^2) + \int_x^1 \frac{g_1(x,Q^2)}{y}dy \tag{2.10}$$

As for what a twist term is, let me explain following the conventions of reference [21] and [22]. First, we perform a perturbative expansion of the matrix elements of the parton operators in terms of λ/Q^2. Here, $Q^2 = -q^2 = -(p-p')^2$ is the four-momentum transfer squared, also known as the four momentum of the exchanged, virtual particle. λ is a non-perturbative scaling factor (for massless QCD). A twist-expansion is one in which we choose an energy scale such that $\lambda/Q^2 \ll 1$ and thus the quarks approach the approximation of a free quark; we choose an energy scale such that higher order terms can be neglected, rendering elements of QCD calculable which would normally be *in*calculable in a perturbative expansion.

2.3 An effective, single neutron target

Lone protons effectively do not decay. So, if we want to study the proton, ^{1}H is the optimal choice. If we make a target from the nucleus of deuterium (^{2}H), commonly called a deuteron, we can compare the results from studying the deuteron to the results from studying ^{1}H and learn something about bound nucleons.

Unfortunately, no such options exist for a neutron; we can't find a single nucleon target for the neutron like we can for the proton with ^{1}H. An isolated neutron, removed from the nucleus of an atom, has an average lifetime of about 15 minutes (reference [17]). We are therefore forced to study the neutron while bound in a nucleus. This leaves two natural choices for target: deuterium (^{2}H) and helium-3 (^{3}He). Either could (theoretically) be used as an effective, single neutron target so long as we mathematically correct for the inclusion of one or two pesky protons. While both are used to study the internal structure of the neutron, there are certain advantages to using one or the other.

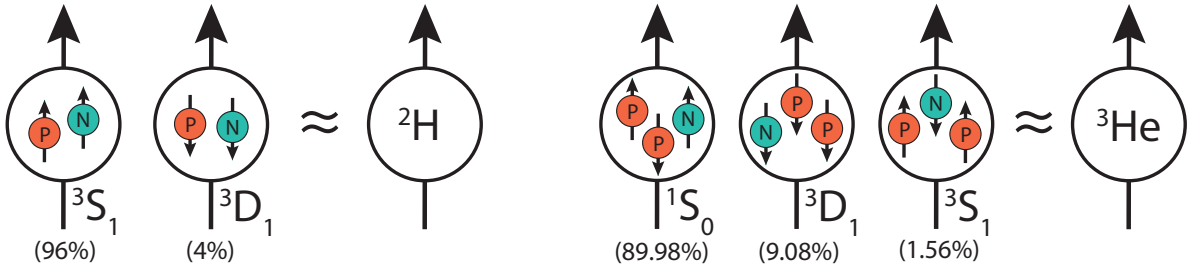

(a) The ^{2}H nucleus **(b)** The ^{3}He nucleus

Figure 2.4: Probable spin states for the ^{2}H and ^{3}He nuclei ground states.

As you can see from figure 2.4a, one advantage of using ^{2}H is that the spins of the two nucleons are always aligned in the ground state; the ground state is dominated by an S-state with a small admixture of a D-state. In fact, 96% of the time, the nucleus holds all of the polarization and we have $m_s = +1$. Few things could be so certain in life, let alone in quantum mechanics! Now the bad news. The spin is always $S = 1$. The spins of the nucleons are inextricably linked. The result is that uncertainties in the proton structure functions will add uncertainty to our measurements of the neutron.

And now we come to the target for which we're all here: ^{3}He. Looking at figure 2.4b, you can see that $\approx 90\%$ of the ground state wavefunction is comprised of $^1S_0$. This state is space-symmetric and spin-isospin anti-symmetric, leading to no magnetic moment for the "like" nucleons (protons) as they are constrained to a spin singlet[23]. ^{3}H has a similar feature: the neutrons are in a spin singlet in the $^1S_0$ state. So, what's this mean? While the like nucleons are wrapped up together, cancelling each other's magnetic moment and thus their spin, the dissimilar nucleon carries the spin of the entire nucleus! So, if you want to study the spin of a neutron, ^{3}He is your best choice for an "isolated" neutron.

And now, my favorite part: experiments. Let's talk about throwing tiny things at slightly

less tiny things and seeing what shakes out!!! FOR SCIENCE!!!

Chapter 3

Recent Measurements of A_1^n/d_2^n and G_E^n Experiments at JLab

The experiments I worked directly on were all performed at Jefferson Lab (JLab) between late 2019 and late 2023. The A_1^n and d_2^n measurements were performed consecutively in JLab's Hall C and G_E^n was measured much later in Hall A. This chapter will focus on the "intellectual ancestors" of each experiment. I'll focus primarily on experiments that used the same type of target (comprised of polarized ^{3}He) and the same type of beam (comprised of polarized electrons). In this way, I hope to highlight just how big a step each of these experiments were in furthering our knowledge of physics.

The recent experiments that I will discuss ran during the following periods:

- The A_1^n measurement I participated in ran in Hall C, began November 18, 2019 and ran (regardless of issues with the oncoming global pandemic) until March 13, 2020.
- The d_2^n measurement, which also ran in Hall C, began immediately following A_1^n...and was shut down after 1-2 weeks (due to said global pandemic). As soon as the lab opened up again on August 1, 2020, we continued (albeit in masks and PPE). We finished measurements on September 21, 2020.
- The G_E^n measurement began September 21, 2022, exactly two years after d_2^n ended[1]. The run that included G_E^n was finished on November 29, 2023.

A complete picture of A_1^n and d_2^n can only be made by taking measurements at many values of the Bjorken scaling variable, x, defined back in equation 2.3. Additionally, while the Q^2 dependence of A_1^n is small, the Q^2 dependence of d_2^n is not fully understood and is of considerable interest. So d_2^n measurements needed to be taken at many values of Q^2 as well. G_E^n is strictly dependent on Q^2 and progress to a complete picture of this form factor comes from making measurements at many values of Q^2. In the coming sections, I'll use these metrics to explain how each succeeding experiment clarified and added to the complete picture of these functions.

[1] I am just realizing the time gap between these experiments as I write this and realizing just how much the pandemic set me back: I should've graduated before G_E^n.

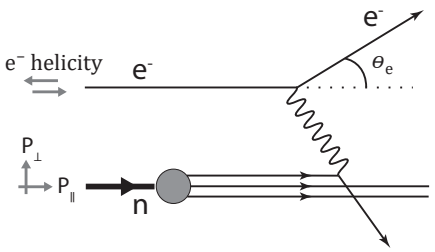

(a) An inelastic collision between an electron and the quark in a neutron.

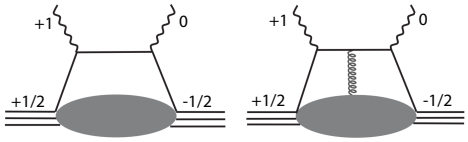

(b) Twist-2 and -3 contributions to virtual Compton scattering. Both of these contribute to g_2^n.

Figure 3.1: Interactions measured in studying A_1^n and d_2^n.

3.1 Measuring A_1^n and d_2^n

We should probably start by defining both A_1^n and d_2^n. As you may have noticed, neither of these are form factors or structure functions as were discussed back in section 2.2. Let's start by talking about what these two things *are* and work our way to relating them to structure functions.

A_1 is the helicity asymmetry of the virtual photons (γ^*) that are exchanged between the incoming lepton and the nucleon, often simplified as the "virtual photon asymmetry". A_1 is defined as follows:

$$A_1(x, Q^2) \equiv \frac{\sigma_{1/2} - \sigma_{3/2}}{\sigma_{1/2} + \sigma_{3/2}} \tag{3.1}$$

where $\sigma_{1/2}$ ($\sigma_{3/2}$) is the total photo-absorption cross section for the $\gamma^* - N$ system with total spin projection of $1/2$ ($3/2$).

These asymmetry terms can be related back to a ratio of structure functions. Namely, we can relate A_1 to a linear combination of the polarized structure functions, g_1 and g_2, divided by one of the non-polarized structure functions, F_1, like so:

$$A_1(x, Q^2) = \frac{g_1(x, Q^2) - \gamma^2 g_2(x, Q^2)}{F_1(x, Q^2)} \approx \frac{g_1(x, Q^2)}{F_1(x, Q^2)}$$
$$\text{where} \quad \gamma^2 = \frac{4M^2x^2}{Q^2} \tag{3.2}$$

where the final approximation (valid only for leading order F_1 and g_1 according to reference [24]) is appropriate for the high Q^2 region as γ^2 is inversely proportional to Q^2.

Furthermore, taking the Q^2 evolution of both g_1 and F_1 to the leading order and next-to-leading order terms, we find the Q^2 dependence in the two structure functions are the same;

the Q^2 dependence in these first two terms cancel exactly when taking their ratio. Hence, to leading order and next to leading order, A_1^n would appear to be independent of Q^2.

d_2 is the "twist-3" matrix element of the neutron, as was discussed in section 2.2. In more general terms, d_2^n reflects the response of the color, electric, and magnetic fields to the polarization of the nucleon. d_2 features heavily in Lattice QCD and provides a particularly clean observable with which to test the theory. From reference [20], we can describe d_2 in terms of the quark-gluon correlation term mentioned in section 2.2 as follows:

$$\begin{aligned} d_2(x,Q^2) &= 3\int_0^1 x^2 \bar{g}_2(x,Q^2)dx \\ d_2(x,Q^2) &= \int_0^1 x^2\left[2g_1(x,Q^2)+3g_2(x,Q^2)\right]dx \end{aligned} \tag{3.3}$$

So, how do we measure these? Well, it seems we need to measure these structure functions, g_1 and g_2. We measure the asymmetry of the electron-neutron collision (given the the virtual photon's longitudinal polarization) for both parallel and perpendicular cross sections, relate them back to g_1 and g_2, and solve for A_1^n and d_2^n! Confused? You won't be after the next ~~episode of Soap!~~[2] couple paragraphs.

Both the A_1^n and d_2^n measurements are double polarized, fixed target experiments. That is, the electron-beam and the target are both polarized. The relative polarization of the target and beam are either perpendicular or parallel to one another; the orientation of the target polarization is changed while the electron-beam remains longitudinally polarized. Also, following equation 3.1, the electron spin direction can be changed between parallel and anti-parallel. This leads us to the following asymmetries:

$$\begin{aligned} A_\parallel &= \frac{\sigma_{\downarrow\Uparrow}-\sigma_{\uparrow\Uparrow}}{\sigma_{\downarrow\Uparrow}+\sigma_{\uparrow\Uparrow}} \\ A_\perp &= \frac{\sigma_{\downarrow\Rightarrow}-\sigma_{\uparrow\Rightarrow}}{\sigma_{\downarrow\Rightarrow}+\sigma_{\uparrow\Rightarrow}} \end{aligned} \tag{3.4}$$

where the arrows on the σ terms denote the electron polarization ($\downarrow$ or $\uparrow$) and the target polarization ($\Uparrow$ or $\Rightarrow$).

We can now relate g_1 and g_2 to the asymmetries, $A_\parallel$ and $A_\perp$. From appendix A of reference [14], we have the following relations:

[2] This is a reference to a television show. They ended every episode this way and episodes were *very* confusing. (SOAP. Susan Harris, USA, ABC 1977-1981)

$$g_1(x,Q^2) = \frac{F_1}{D'}\left(A_\parallel + A_\perp \tan\left(\frac{\theta}{2}\right)\right)$$
$$g_2(x,Q^2) = \frac{yF_1(x,Q^2)}{2D'\sin(\theta)}\left[A_\perp \frac{E+E'\cos(\theta)}{E'} - A_\parallel \sin(\theta)\right] \tag{3.5}$$

Bearing in mind that $R = \sigma_L/\sigma_T$ is the ratio of the longitudinal and transverse virtual photon cross sections, we define D' and ϵ as follows:

$$D' = \frac{(1-\epsilon)(2-y)}{y[1+\epsilon R(x,Q^2)]}$$
$$1/\epsilon = \left[1 + 2(1+\gamma^2)\tan^2\frac{\theta}{2}\right] \tag{3.6}$$

So, as long as we have F_1 and R from world data, we can use experimental data to extract both A_1^n and d_2^n using equations 3.2 and 3.3.

3.2 Previous Measurements of A_1^n and d_2^n

Experiment E-142 ran over a period of six weeks in November and December of 1992 at the Stanford Linear Accelerator (SLAC) and was the first measurement of both $A_\parallel^n$ and $A_\perp^n$ performed by scattering a polarized electron-beam from a polarized ^{3}He target. Average beam polarization was limited to 36% and average target polarization 33%[25]. Experiment E-154 ran during October and November of 1995 (again, at SLAC) and measured g_1^n and A_1^n using a similar method as E-142. Average beam polarization was much larger than it's predecessor, reaching approximately 82%. Target polarization remained about the same at about 38%. Beam current in both experiments was approximately 1.5 μA.

Both experiments examined a similarly wide range of average x ($0.035 < \langle x \rangle < 0.466$ for E-142 and $0.014 < \langle x \rangle < 0.564$ for E-154). They began to paint a picture of the spin structure of the neutron, the fraction of spin carried by the quarks and, perhaps most importantly, confirmed the validity of the Bjorken Sum Rule. E-154 also confirmed and refined the results of E-142 as well as extended our knowledge to a larger range of x values. However, one drawback noted at the time was that the new data "did not adequately constrain the low-x region such that the integral of g_1^n can be reliably extracted" [26].[3]

[3]Fun historical tidbit: Vernon Hughes helped develop the first polarized electron source for SLAC as discussed in chapter 2, but couldn't continue his research there. Emlyn Hughes, Vernon's son and a skilled physicist in his own right, worked as a researcher on both E-142 and E-154!

The HERMES experiment, which ran in the late 1990's at the Deutsches Elektronon-Synchrotron (DESY), was again only measuring A_1^n. However, it differed from E-142 and E-154 in a couple of significant ways. First, rather than use a polarized electron-beam, HERMES used polarized positrons. Second, they used an internal gas target, which is to say the target was enclosed in the beam line. Also, unlike the E-142 and E-154 targets, the HERMES target contained only ^{3}He rather than a target of ^{3}He with a small amount of N_2 and an alkali metal to aid in polarization (see chapter 4). Beam current came in "positron fills" where a load of polarized positrons would be injected into the ring, resulting in a current starting at 30 mA and decreasing to 10 mA over the course of about 8 hours per fill. The average target polarization was approximately 46%, but unfortunately HERMES suffered from a much lower density of polarized ^{3}He. While it's predecessors at SLAC averaged on the order of 10^{20} ^{3}He atoms/cm^3, HERMES averaged a mere 10^{13} ^{3}He atoms/cm^3. While beam polarization reached about the same as E-142 at around 55%[27] and target polarization was higher than either E-142 or E-154, the lower ^{3}He density meant the target had a much lower luminosity than it's predecessors. Luminosity is an important figure of merit which will be discussed further in section 4.1.

HERMES studied a similar range of average x values as it's predecessors ($0.033 < \langle x \rangle < 0.464$) and, as before, error bars on the largest x values remained too large to differentiate between constituent quark models. However, HERMES was a *very* important stepping stone on the path to understanding g_1^n. Not only did they confirm the results from previous experiments, but they did so using "an entirely new technique - windowless polarized internal target with pure atomic species in a positron storage ring"[27].

What we generally refer to as the A_1^n-I experiment (E99-117) ran at JLab from the beginning of June 2001 through the end of July 2001. However, they didn't just find data to extract A_1^n. They extracted A_1^n, A_2^n, g_1^n/F_1^n, and g_2^n/F_1^n! Again, a higher beam polarization of $(79.7 \pm 2.4)\%$ and a similar target polarization of $(40 \pm 1.5)\%$ led to a higher multiplicative combination of the two and thus very precise results in the high-x region[14]. Additionally, the beam current was significantly higher than previous electron experiments, with currents averaging 12 μA. The goal of this experiment was, specifically, to provide more accurate data in the largest x regions and finally distinguish between models. One way this was done was by setting both high resolution spectrometers to large scattering angles (35° and 45°) and momentum settings, doubling the statistics for each data point.

The 2001 experiment focused on only three values of x. $x = 0.33$ would confirm previous results. $x = 0.47$ matches the highest average x values reached by both HERMES and E-142. Precise data here could finally differentiate between constituent quark models. Finally, $x = 0.60$ would push the bounds of our knowledge of A_1^n, reaching higher than even E-154 (which peaked at $x = 0.564$). The experiment was a resounding success, with $x = 0.33$ agreeing very well with world data and an order of magnitude improvement in precision for data at $x > 0.4$.

The data at $x = 0.60$ "unambiguously show, for the first time, that A_1^n crosses zero around $x = 0.47$ and becomes significantly positive at $x = 0.60$" [14]. Furthermore, the $x = 0.47$ and $x = 0.60$ data points were inconsistent with pQCD models where hadron helicity was conserved, perhaps implying quark orbital angular momentum (OAM) play a larger role in the valence quark region than we initially thought.

As for their data for d_2^n, their measurements when combined with existing world data improved the precision of our overall knowledge of d_2^n by a factor of 2[14]. Results for g_2^n (as well

as A_2^n) had a precision comparable to the best world data yet measured. A resounding success by any measure.

A 2003 measurement of g_1^n at JLab, E01-012 [28], marked the first high-precision test of quark-hadron duality and again an increase in target quality. While average target polarization remained about the same as A_1^n-I (clocking in at 38±2% as compared to 40% for A_1^n), target's were longer than A_1^n and the beam current was slightly higher ($I_b = 15\mu A$), nearly doubling the figure of merit, a metric for target quality described in chapter 4. This experiment found A_1^n had limited dependence on Q^2 above $Q^2 = 2.2$ and their measurement of g_1^n would later be used in calculations of d_2^n.

In 2009 we finally had a dedicated d_2^n experiment at JLab that was somewhat short, running from February 8, 2009 to March 15, 2009. While the average target polarization for d_2^n-I was $(50.5 \pm 7.2)\%$, the average beam current (15 μA) was higher than the previous A_1^n measurement (12 μA) and the average polarization of the electron-beam was $(72.0 \pm 1.7)\%$. This experiment was able to get clear results for d_2^n with small error bars at a number of x values previous results were only able to achieve with large error bars (the range of this measurement was $0.277 < \langle x \rangle < 0.548$). It confirmed previous results of both d_2^n *and* A_1^n.

3.3 The Recent A_1^n Measurement for JLab (2019-2020)

This experiment is the first of three experiments I participated in at JLab and I'll discuss it's targets in chapter 4. For now, I present an overview.

First proposed in 2006 and taking advantage of the JLab 12 GeV upgrade, the Hall C A_1^n measurement (herein referred to as A_1^n-II) further tested various predictions of A_1^n behavior beyond $x = 0.6$ including those from the relativistic constituent quark model (RCQM) and perturbative quantum chromodynamics (pQCD) with hadron helicity (HHC) conserved as well as pQCD predictions where the quarks would have orbital angular momentum (OAM). Previous A_1^n measurements at JLab found that quark OAM may play a significant role in nucleon spin even in the valence quark region where it was predicted to decrease or even disappear completely[31].

This experiment also marked the first precision data for A_1^n at Bjorken-x values of $x > 0.78$!

The measurement consisted of scattering polarized electrons from an ≈11 GeV beam off of a polarized ^{3}He target. There were two target-cells involved, Big Brother and Dutch, and the average target polarization for the experiment was ≈58%. The average beam current during the experiment was ≈30 μA with a polarization of roughly $85.4 \pm 0.3\%$[32]. The Moller polarimeter in Hall C measured the beam polarization and provided an absolute error of $< 1\%$. To prevent damage to the targets via heat and radiation, the beam rastering system shaped the beam into a 4-4.5 mm diameter, circular cross section. This is a standard procedure for all JLab experiments utilizing the polarized ^{3}He target.

A significant difference between the targets used in this experiment versus previous experiments was the A_1^n-II targets were the first to utilize convection to move the polarized ^{3}He through the cell. I discuss these targets much more in chapter 4.

Target spin was either aligned parallel or perpendicular to the direction of the beam propagation and the spin of the electrons was alternated between left- and right-handed helicity at a frequency of 120 Hz. Actual maximum target polarization will be discussed in section 4.4.

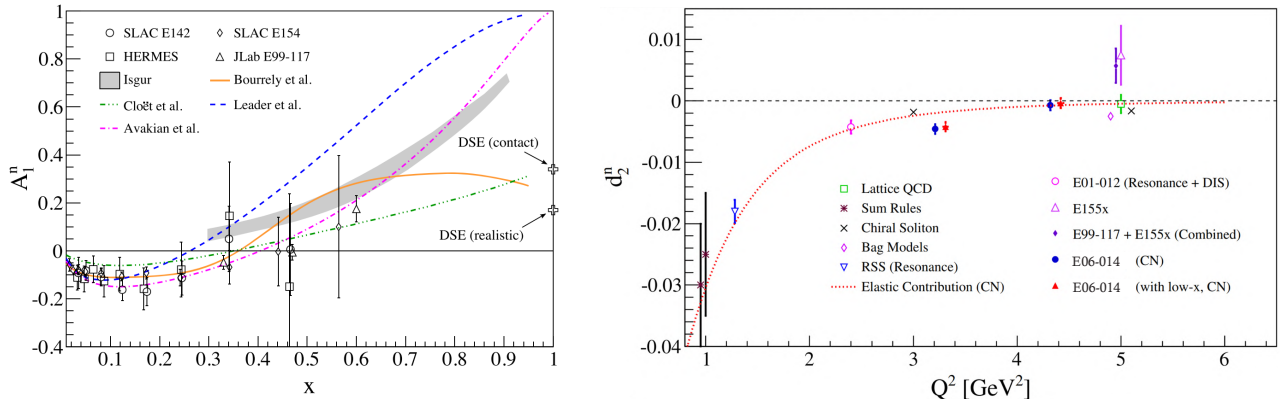

(a) World data for A_1^n as a function of x. Included experiments are SLAC's 1992 E-142 and 1995 E-154, DESY's HERMES, and JLab's previous 6 GeV A_1^n measurement from 2001, A_1^n-I (E99-117), all discussed in section 3.2. Also included are various models: a pQCD-inspired global analysis (dashed curve), a statistical quark model (solid curve), a pQCD parameter including OAM (dash-dotted curve), a CQM model (gray band), an NJL-type model (dash triple-dotted curve), and predictions from Dyson-Schwinger equation treatments (DSE) shown at x = 1. Further details about these predictions can be found in reference [29].

(b) World data for d_2^n as a function of Q^2. Included experiments are JLab's g_1^n labelled E01-012 [30] (pink circles) and d_2^n-I labelled E06-014 [29] (blue circles and red diamonds), discussed in section 3.2. Other experiments included are SLAC's E-155 experiment (purple triangles), and work by the JLab Resonance Spin Structure Collaboration (blue triangles). These are beyond the scope of this thesis as they did not involve ^{3}He targets. Additionally, data from E-155 are combined with results from the 2001 A_1^n measurement, A_1^n-I (E99-117), at JLab discussed in section 3.2 (purple diamonds). Model curves and predictions included are a QCD sum rule approach for $Q^2 \approx 1$ GeV^2 (red star), a chiral soliton model (black x's), and a bag model (violet diamonds). Lastly, a lattice QCD calculation is shown as a green square and the elastic contribution to d_2^n is shown as a red, dashed curve. This figure was adapted from reference [29] and further details can be found there.

Figure 3.2: Existing world data for A_1^n and d_2^n from reference [29].

3.3.1 The HMS and SHMS Spectrometers and Kinematic Settings

Scattered electrons were detected with the high momentum spectrometer (HMS) and super high momentum spectrometer (SHMS) whose kinematic settings are listed in table 3.1. These spectrometers utilize a gas Cherenkov detector as well as a multiple layered, lead-glass shower counter to reject high pion backgrounds. Hodoscopes trigger the DAQ to record an event and drift chambers are used for tracking.

Kine	Spec	E_b (GeV)	E_0 (GeV)	Angle (°)	Prod. Time (hrs)	Target-Cell
3	HMS	10.38	2.90	30.0	88.0	Big Brother
4	HMS	10.38	3.50	30.0	511.0	Dutch, Big Brother
B	SHMS	10.38	2.60	30.0	511.0	Dutch, Big Brother
C	SHMS	10.38	3.40	30.0	88.0	Big Brother

Table 3.1: Kinematic settings for the recent A_1^n measurement (from reference [32]). Production times listed are planned production times and are only an estimate.

3.4 The Recent d_2^n Measurement for JLab (2020)

The d_2^n measurement we refer to as d_2^n-II piggybacked on the 2020 A_1^n measurement as it used a very similar setup as A_1^n-II. It was also the second of three experiments I worked on at JLab and I'll definitely discuss the d_2^n targets as well...but not until chapter 4.

Prior to this measurement, though, the entire target apparatus was rotated such that the holding field was positioned perpendicular to the propagation of the electron-beam. This was done primarily to accommodate the new positions of the HMS and SHMS for measuring d_2^n. The d_2^n measurement would only place modest demands on the spectrometers and would be an excellent test of the new target system at moderate luminosities before being deployed to Hall A for the G_E^n measurement. Three target-cells were used: Brianna, Tommy, and Austin. This d_2^n measurement focused on measuring the spin structure functions, g_1^n and g_2^n, over the kinematic range of $0.2 < x < 0.95$ with $2.5 < Q^2 < 7(GeV^2/c^2)$. Beam current was also ≈ 30 μA, average beam polarization was $\approx 85 \pm 0.3$ %, and average target polarization was $\approx 45 \pm 3$ % [33].

Similar to the A_1^n measurement, the d_2^n measurement was a fixed target, double polarization experiment; d_2^n-II measured both asymmetries in the scattering cross section when the target polarization was parallel to the beam polarization and when the two were perpendicular with one another. Kinematic measurements are listed in table 3.2. With an already established value of F_1^n, both g_1^n and g_2^n could be extracted from the asymmetries $A_\parallel$ and $A_\perp$.

g_2 is among the cleanest, higher twist observables we could measure and all of this information allows for a calculation of d_2^n at truly constant Q^2 values of $Q^2 = 3$, 4, and 5. The precision with which these values were measured, combined with explicit information on the Q^2 evolution of d_2^n provide a strict test of Lattice QCD.

HMS Production					
Setting	P_0 (GeV/c)	Angle (°)	x	Q^2	W
A	4.2	13.5	0.207	2.414	3.178
B	4.2	16.4	0.305	3.554	2.993
C	4.0	20.0	0.418	5.018	2.806
SHMS Production					
Setting	P_0 (GeV/c)	Angle (°)	x	Q^2	W
X	7.5	11.0	0.527	2.866	1.859
Y	6.4	14.5	0.565	4.240	2.036
Z	5.6	18.0	0.633	5.701	2.046

Table 3.2: Kinematic settings for the recent d_2^n measurement (from reference [33]). Targets used in this experiment were Brianna, Tommy, and Austin.

		I_b	P_b	P_t	^{3}He Den.	TC Len.	$\mathcal{L}^{eff}$
Exp.	Year	μA	%	%	atoms/cm^3	cm	10^{34}cm^{-2}s^{-1}
E-142	1992	1.5	36.0	33	2.33E+20	29.83	0.709
E-154	1995	2	82.0	38	1.10E+20	30.00	0.595
HERMES	1995	10k-30k	55.0	46	8.25E+13	40.00	0.013
JLab A_1^n-I	2001	12	79.7	40	2.31E+20	25.00	6.930
JLab g_1^n	2003	15	71.4-84.9	38	3.20E+20	40	17.304
JLab d_2^n-I	2009	15	63.0-79.0	50.5	2.13E+20	38.40	19.525
JLab A_1^n-II	2020	30	85.4	58	1.86E+20	39.88	46.650
JLab d_2^n-II	2020	30	85.0	45	1.99E+20	39.84	35.551

Table 3.3: A summary of the information for previous experiments presented in this section. Information in this table comes from the following references: E-142 [25], E-154 [34], HERMES [27], A_1^n-I [14], g_1^n [28], and d_2^n-I [29]. Target length for g_1^n taken from Solvignon's thesis [35]. Information for A_1^n-II and d_2^n-II are average values for targets that were used in-beam for those experiments. Information on those targets is presented in chapter 4. Effective luminosity ($\mathcal{L}^{eff}$) is calculated for the entire target at room temperature as opposed to only the TC at operating temperature (as is done in table A.1) and using the largest values of beam current. The equation for effective luminosity can be found in chapter 4, equation 4.1.

3.5 Measuring G_E^n

Hey, good news! We already defined G_E^n back in chapter 2! We're already off to a smashing[4] start over that *last* section.

So, let's jump to the obvious first question: what are we *actually* measuring. Well, *quelle surprise*, this is another double polarized, fixed target experiment, utilizing a polarized electron-beam and a polarized ^{3}He target. And again, we'll be measuring an asymmetry in scattering cross sections.

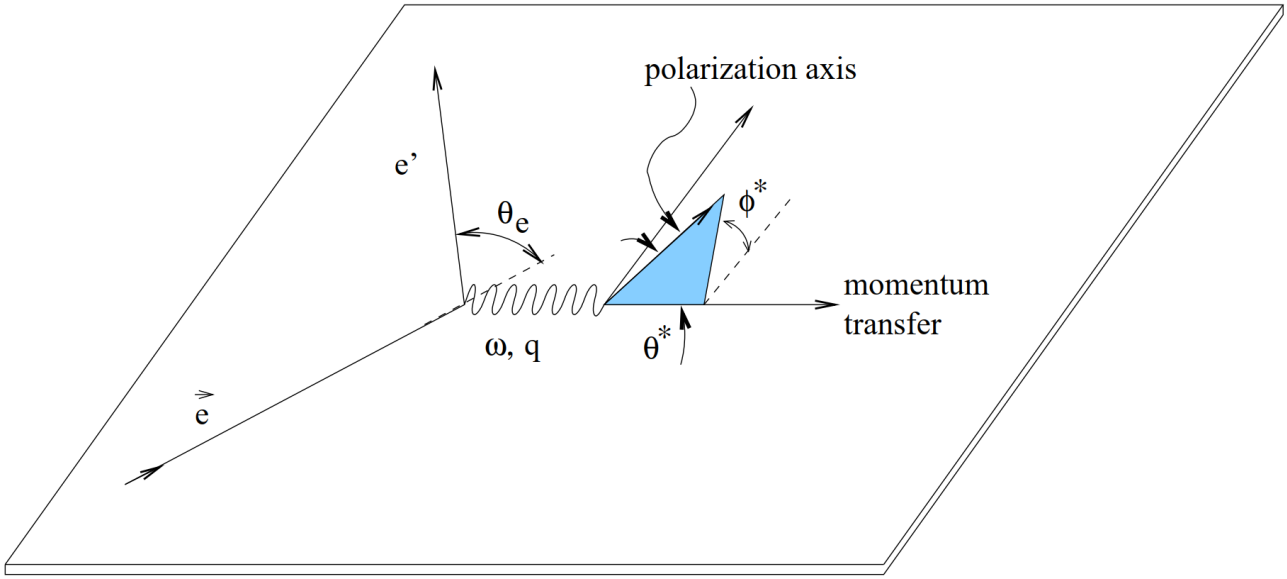

Figure 3.3: An elastic collision between an electron and the neutron in a ^{3}He nucleus (adapted from reference [18]).

Following reference [18], let's start by defining the geometry of the measurement (seen in figure 3.3). The plane is defined by the scattering angle of the electron, θ_e. θ^* is the angle between the direction of target polarization and direction of momentum transfer, $\overrightarrow{q}$. So, for $\theta^* = 0°$, we have the momentum transfer and target polarization parallel to one another and for $\theta^* = 90°$, the momentum transfer and target polarization are perpendicular to one another. We'll call an asymmetry in the parallel orientation A_S. This should be having a familiar ring to it after section 3.1. We'll call an asymmetry in the perpendicular orientation A_I. I've refrained from calling these $A_\parallel$ and $A_\perp$ as the angle here is between the target polarization and momentum transfer rather than beam propagation.

The total asymmetry for scattering longitudinally polarized electrons from polarized *free* neutrons at rest is given by the following:

[4]Pun slightly intended. I mean, roughly speaking, we're smashing polarized electrons into polarized neutrons in these experiments, although I generally reserve the term "smashy physics" for high energy physics.

$$\begin{aligned} A &= P_e P_n V \frac{a \sin\theta^* \cos\phi^* (G_E^n)(G_M^n) + b \cos\theta^* (G_M^n)^2}{c(G_E^n)^2 + d(G_M^n)^2} \\ &= A_I \sin\theta^* \cos\phi^* + A_S \cos\theta^* \end{aligned} \tag{3.7}$$

where P_e is the polarization of the electron-beam and P_n is the polarization of the neutron. V is the dilution factor. θ^* is the angle between the direction of momentum transfer and direction of target polarization and ϕ^* is the azimuthal angle about the momentum transfer such that $\phi^* = 0$ and $\phi^* = 180$ both correspond to the polarization being in the scattering plane (see figure 3.3). Recalling $\tau = Q^2/(2M)^2$, constants $a - d$ are described in equation 3.8:

$$\begin{aligned} a &= -2\sqrt{\tau(1+\tau)} \tan(\vartheta_e/2) \\ b &= -2\tau\sqrt{1 + \tau + (1+\tau)^2 \tan^2(\vartheta_e/2)} \tan(\vartheta_e/2) \\ c &= 1 \\ d &= \tau + 2\tau(1+\tau)\tan^2(\vartheta_e/2) \end{aligned} \tag{3.8}$$

where ϑ_e is the electron scattering angle in the lab frame as defined above.

There is an advantage to taking measurements in either the parallel or perpendicular orientation. Let's examine the explicitly perpendicular and parallel orientation cases:

$$\begin{aligned} A(90^\circ) = A_I &= P_e P_n V_I \frac{a G_E^n G_M^n}{c(G_E^n)^2 + d(G_M^n)^2} \approx \frac{a}{d} P_e P_n V \frac{G_E^n}{G_M^n} \\ A(0^\circ) = A_S &= P_e P_n V_S \frac{b (G_M^n)^2}{c(G_E^n)^2 + d(G_M^n)^2} \approx \frac{b}{d} P_e P_n V \end{aligned} \tag{3.9}$$

where V_I and V_S are the dilution factors for the A_I and A_S cases, respectively. The final approximation is made assuming $G_E^n \ll G_M^n$. Which it is. Good assumption.

Finally, if we were so inclined, we could take the ratio of the asymmetry terms and do a little rearranging to find a ratio of just the G_E^n and G_M^n terms in the following way:

$$\frac{a}{b}\frac{G_E^n}{G_M^n} = \frac{(P_e P_n V)_S}{(P_e P_n V)_I}\frac{A_I}{A_S} \tag{3.10}$$

Taking this ratio limits uncertainties due to beam polarization, neutron polarization, and the dilution factor but at the sacrifice of devoting part of the beam-time to A_S and overall larger statistically uncertainties, both of which make the exercise not worth the time for high Q^2. While early experiments measured both asymmetries (A_I and A_S), it's not entirely necessary to measure both to find the ratio of G_E^n to G_M^n if you can reliably measure P_e, P_b, and V. With that in mind, let's define A_I another way.

In the geometry defined in figure 3.3, equations 3.7 and 3.8 can be interpretted as follows: the "magnetic dipole-dipole amplitude (g) changes signs with respect to helicity reversal whereas the electric Coulomb amplitude (f) remains unchanged"[18]. Thus, we can define the cross sections of the helicity states "+" and "-" as follows:

$$\sigma^{\pm} \approx |f \pm g|^2 = |f|^2 \pm 2\Re(f^* g) + |g|^2 \tag{3.11}$$

where only the real part of the interference term, $|f^* g|$, is taken.

The interference term, $|f^* g|$, can further be sussed out by taking the following asymmetry, which is equal to A_I:

$$A_I = \frac{\sigma^+ - \sigma^-}{\sigma^+ + \sigma^-} = \frac{2\Re(f^* g)}{|f|^2 + |g|^2} \tag{3.12}$$

In this asymmetry, the small effect of Coulomb scattering from the neutron is enhanced by the large magnetic one.[18]

3.6 Previous Measurements of G_E^n

The first measurement of A_I and A_S using a polarized ^{3}He target began in earnest with an experiment by the A3 Collaboration at the Mainz Microtron (MAMI) at the Johannes Gutenberg University in 1994 (the experiment in reference [18]). However, this was preceded by an exploratory experiment in the early 1990s that was no less important. Indeed, the pilot experiment performed at MAMI by Meyerhoff *et al.* (reference [36]) was seen as a proof of concept experiment for the larger one performed by the A3 Collaboration in 1994.

Before the exploratory experiment, we had limited understanding of G_E^n from other types of measurements, but with quite a few caveats[36]. For $Q^2 \approx 0\,\mathrm{GeV}^2$, thermal neutron scatter from atomic electrons described a charge radius which, in turn, had a slope proportional to the derivative of G_E^n with respect to Q^2. For $0.2 \leq Q^2 \leq 0.6\,\mathrm{GeV}^2$, elastic electron-deuteron scattering found G_E^n, but the results were model dependent. Finally, for ranges of $1.75 \leq Q^2 \leq 4\,\mathrm{GeV}^2$, quasi-elastic scattering between electrons and deuterons provided values for G_E^n. While these were not model dependent, they relied on using Rosenbluth separation. Why would that matter? Well, an issue using a deuteron as a target is that the cross section contains an interference term proportional to $G_E^n \cdot G_E^p$. To quote Rohe, *et al.*: "Sufficient sensitivity to G_E^n can be obtained only through observables which depend on interference terms in which the small contribution of G_E^n is amplified by another, dominating amplitude."[37]

Basically, it's difficult to separate the G_E^n and G_E^p contributions due to the electromagnetic structure of the deuteron. Fortunately, the advances to beam technology allowed the folks at MAMI to conduct an exploratory experiment [36] to show the viability of a double polarization experiment using polarized ^{3}He as a target. While the experiment was limited to one kinematic

point ($Q^2 = 0.31\,\mathrm{GeV}^2$) and polarization of both the beam and the target limited (32% and 38%, respectively), this experiment successfully showed we could use spin observables to investigate the electromagnetic structure of the neutron.

The work by Meyeroff *et al.* was quickly followed up by the A3 collaboration experiment at MAMI by Becker *et al.*[18]. This experiment expanded the range of Q^2 over which G_E^n had been measured using polarized ^{3}He as a target to $0.27 \leq Q^2 \leq 0.5\,\mathrm{GeV}^2$, but MAMI also did something far more interesting[5]. Previous experiments showed a discrepancy between values of G_E^n found when using a deuteron target versus using polarized ^{3}He. To explore this discrepancy, a measurement of G_E^n was performed using a deuteron target with the same setup as the experiment performed by Becker *et al.* This allowed researchers to test the discrepancy in results between deuteron and ^{3}He targets. Rarely do we get such an experiment in accelerator physics and certainly not in the business of crafting targets: the ability to take data using the exact same equipment and setup and simply changing out the target. And most importantly, they showed the discrepancy persisted, even in their carefully crafted, dual experiment. And if that all sounds pretty exciting, I'm sorry, because that's the last I'll be discussing an experiment using a deuteron target. Focus, dear reader, there's so much more to talk about!

The target used in these first two ^{3}He experiments deserves some discussion considering the length and breadth of chapter 4 and how dissimilar the target used in these first two experiments was. Rather than the self-contained targets we would use for later G_E^n measurements at JLab as well as many of the experiments discussed in section 3.1, this target was attached to a larger system allowing the gas in the target to be removed and polarized away from the electron-beam (see the left image in figure 3.4). Here's how the system worked. The gas was first polarized at a low pressure of about 1 mbar. It was then pressurized to 1 bar and pumped into the target cell while simultaneously being mixed with a small concentration of N_2 ($\approx 10^{-4}$ N_2 to ^{3}He). When the target was evacuated, the gas was run through a getter purifier to remove the N_2 before being cycled back into the pumping chambers and polarized again. The entire gas recycling time was approximately 50 minutes[18]. Target and beam polarization were improved between the exploratory experiment and the larger A3 Collaboration work in 1994: average beam polarization rose from 32% to 41.5% and average target polarization rose from 38% to as high as 49%.

Shortly after the A3 collaboration at MAMI made their measurement of G_E^n for $0.27 \leq Q^2 \leq 0.5\,\mathrm{GeV}^2$, the A1 collaboration[37] made a measurement at a higher kinematic point ($Q^2 = 0.67\,\mathrm{GeV}^2$) *and* with a completely different target (see on the right in figure 3.4). This target was essentially a small sphere with two cylindrical extensions where the beam could pass through. Interestingly, the target needed to be polarized in another lab then installed in the beamline. As such, average target polarization in beam was lower than previous experiments (32%) even though beam polarization was significantly higher (70%). Unfortunately, this experiment yielded a result with significant error bars. Thus, another experiment was conducted by Bermuth *et al.*[38] using the same setup and target as the A1 collaboration. This was, in part, to confirm the A1 collaboration's results, again measuring both A_I and A_S just as previous measurements at MAMI. In addition to measuring A_I and A_S, they also made a measurement of A_y^o, defined as follows:

[5] Well, far more interesting in *my* opinion.

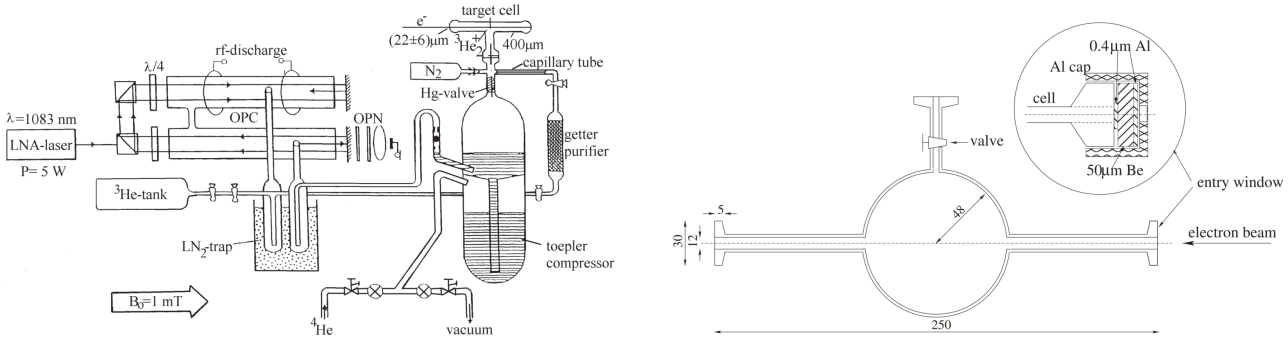

Figure 3.4: Targets used in G_E^n measurements at MAMI. Left: The target used in the exploratory experiment (reference [36]) and the A3 collaboration experiment (reference [18]) as detailed in Becker *et al.* ([18]). Right: The target used by the A1 collaboration [37] and the follow up experiment which measured both G_E^n and A_y^o [38].

$$A^o_{y(e,e'n)} = \frac{1}{P_t}\frac{N^{\uparrow} - N^{\downarrow}}{N^{\uparrow} + N^{\downarrow}} \tag{3.13}$$

where $N^{\uparrow(\downarrow)}$ are the normalized ^{3}He(e,e'n) events and the arrows indicate target polarization direction, which is perpendicular to the scattering plane. P_t is, as usual, the target polarization.

Unlike the G_E^n measurements, the A_y^o measurement was made with a polarized target but an *un*polarized beam. This was also only measured for $Q^2 = 0.37\,\mathrm{GeV}^2$, the kinematic point already measured by both the exploratory experiment and the A3 collaboration. Importantly, the overall G_E^n/A_y^o experiment confirmed the previous result at $Q^2 = 0.67\,\mathrm{GeV}^2$. Target polarization was improved over the A1 Collaboration measurement from a few years before (rising from 32% to 35.6%) as well as beam polarization (now 78.8%), at least for the A_I and A_S measurements.

Finally, in 2006, a measurement of G_E^n was made at JLab. Unlike previous experiments, this experiment only measured the perpendicular asymmetry, A_I. It was again a double polarized experiment, though this time using targets similar to those discussed in chapter 4 and, again, with both improved beam polarization (84.37%) and target polarization (45.7%). This experiment more than doubled the range over Q^2 in which we had measured G_E^n up to $Q^2 = 3.41\,\mathrm{GeV}^2$! The targets used in this experiment were also roughly twice as long as the targets used at MAMI, leading to a significantly higher luminosity.

3.7 The Recent G_E^n Measurement for JLab (2022-2023)

And here it is. The third and final experiment I made targets for (yes, discussed in chapter 4, just as the others). Before we dive into the targets, let's talk about the larger experiment first.

The 2022-2023 Hall A measurement of G_E^n, which we refer to as G_E^n-II, nearly tripled the range of Q^2 values for which G_E^n had been measured *and* with a higher precision than ever before! Not only that, but if the error in the ratio G_E^n/G_M^n could be kept below 20%, the accuracy would be comparable to data for G_E^p/G_M^p for the first time! Unfortunately, the

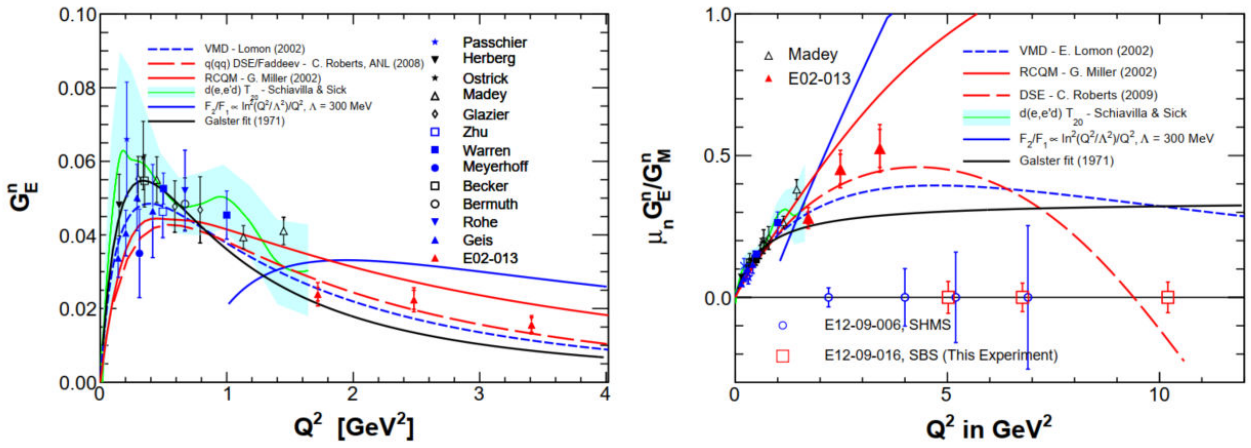

Figure 3.5: World data for G_E^n-I.

analysis will take some time, so I cannot report on whether we reached that goal, but I will report on preliminary information about the beam polarization, target polarization, and other factors involved in analysis that we *do* know now that the measurement is complete.

First, briefly recall from equation 3.9 that we can write A_I as follows:

$$\begin{aligned} A_I &\approx \frac{a}{d} P_e P_n V \frac{G_{En}}{G_{Mn}} \\ &= (P_e P_n V) \frac{-2\sqrt{\tau(1+\tau)}\tan(\vartheta_e/2)}{\tau + 2\tau(1+\tau)\tan^2(\vartheta_e/2)} \frac{G_{En}}{G_{Mn}} \end{aligned} \tag{3.14}$$

where τ is only a function of Q^2 ($\tau = Q^2/(2M)^2$) and all other variable are known from the experiment.

As you can see from table 3.4, measurements were performed at 3 kinematic points: $Q^2 = 3.0\,\mathrm{GeV}^2$, $Q^2 = 6.8\,\mathrm{GeV}^2$, and $Q^2 = 9.8\,\mathrm{GeV}^2$. The beam current was roughly 45 μA and held a consistent polarization between 80-86% as measured by the Hall A Moller polarimeter. As A_I is roughly proportional to the ratio of G_E^n/G_M^n (as you can see from equation 3.14), given knowledge of Q^2, the beam polarization P_e, the target polarization P_n, and the dilution factor V, one can extract G_E^n from only A_I so long as we know G_M^n to a good approximation. Fortunately, we have good values for G_M^n. *Un*fortunately, those values have a large error (20%) for G_M^n measurements over $Q^2 = 10\,\mathrm{GeV}^2$, so the data found in this experiment will require more accurate measurements of G_M^n over $Q^2 = 10\,\mathrm{GeV}^2$ to accurately calculate G_E^n/G_M^n in that range.

The target design used in this experiment was what will be described in chapter 4 as a "coathanger" design. It represents a significant step in target development for many, *many* reasons which I'll discuss further in chapter 4. Suffice it to say, the only important things to

note are that, like A_1^n-II and d_2^n-II, this target was also a convection target[6] and frankly that's only important here when comparing *this* G_E^n measurement (G_E^n-II) to the *last* G_E^n measurement at JLab (G_E^n-I) because the previous measurement did not use a convection target!

Kine	Q^2	p_e	p_N	E_b
	$(\text{GeV/c})^2$	(GeV/c)	(GeV/c)	(GeV)
2	3.00	2.69	2.37	4.29
3	6.83	2.73	4.51	6.37
4	9.82	3.21	6.11	8.45

Table 3.4: Kinematic settings for the recent G_E^n-II measurement.[39]

Kine	BB Ang	BB Dis	SBS Ang	SBS Dis	HCal Ang	HCal Dist
	(°)	(m)	(°)	(m)	(°)	(m)
2	29.5	1.63	34.7	2.8	34.7	17
3	36.5	1.63	22.1	2.8	21.6	17
4	35.0	1.63	18.0	2.8	18.0	17

		Q^2	I_b	P_b	P_t	^{3}He Den.	TC Len.	$\mathcal{L}^{eff}$
Exp.	Year	$(GeV/c)^2$	μA	%	%	atoms/cm^3	cm	10^{34}cm^{-2}s^{-1}
Pilot	1993	0.31	10.0	32.00	38.00	10^{18}	22.0	0.020
A3	1995	0.27 - 0.5	7.5	41.50	47.00	10^{18}	22.0	0.023
A1	1997	0.67	10.0	70.00	32.00	10^{18}	25.0	0.016
G_E^n/A_y^o	2000	0.37/0.67	10.0	78.80	35.60	10^{18}	25.0	0.020
G_E^n-I	2006	1.72/2.48/3.41	8.0	84.37	45.70	10^{20}	38.7	7.998
G_E^n-II	2023	3.0/6.83/9.82	45.0	86.00	44.68	10^{20}	60.0	63.692

Table 3.5: A summary of the information for previous experiments presented in this section. Information in this table comes from the following references: Pilot [36], A3 [18], A1 [37], G_E^n/A_y^os [38], and G_E^n-I [40]. Information for G_E^n-II are average values for targets that were used in-beam for those experiments. Information on those targets is presented in chapter 4. Effective luminosity ($\mathcal{L}^{eff}$) is calculated for the entire target at room temperature as opposed to only the TC at operating temperature (as is done in table A.1). The equation for effective luminosity can be found in chapter 4, equation 4.1.

[6] In fact, the original plan for the other experiments did not call for convection targets and it's only in developing a better target for *this* experiment that we were able to use convection targets for those experiments.

Chapter 4

Polarized ^{3}He Target Cells

I don't think one could overstate the importance of studying the internal structures of nucleons. The behaviour of the quark-gluon quantum soup is at the very edge of human knowledge. And while I'd argue a deeper knowledge of the universe is, in and of itself, a worthy goal, I'm sure someone could explain the practical applications better than I can. I *can* explain why we study neutrons specifically. The difference between a proton and a neutron is the behaviour of an up versus a down quark for a proton or a neutron, respectively. By studying the internal structure of both nucleons and by combining our findings, we isolate the up/down quark, unlocking knowledge of a world smaller than we've ever studied before.

But there's the rub: we need to study *both* nucleons. Quite unlike the proton, accurate studies of spin-dependent observables in the neutron are hampered slightly by the neutron's stubborn refusal to exist longer than a few minutes outside of an atom (about 15 minutes according to [17], page 279). If you'd like to know why we specifically use polarized ^{3}He as a target, I suggest section 2.3. As for why we always work to improve our target-cells, increasingly detailed measurements require more *polarized* ^{3}He. So, a target-cell with a longer lifetime holds polarization longer and a target-cell that can achieve higher total polarization means there are more polarized ^{3}He nuclei providing targets for the electron-beam. In short: to get increasingly detailed measurements, we need increasingly better targets.

As you can see from tables 3.3 and 3.5, our target-cells are higher quality than any that have come before. In this chapter, I'll discuss the process of making and characterizing these remarkable target-cells.

4.1 Geometry: Past and Present

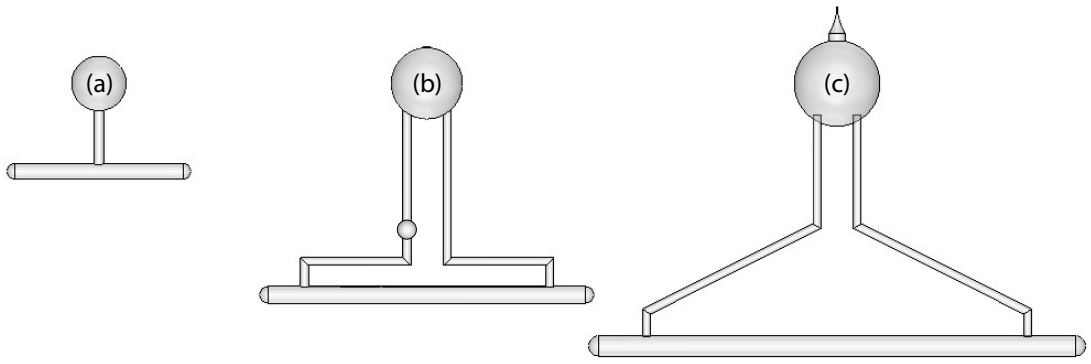

Figure 4.1: A comparison of the relative sizes of the three target designs discussed: (a) diffusion, (b) Bastille Day, and (c) coathanger models. Actual targets varied only slightly from these designs. The Bastille Day design also employed a small bulb meant to assist in pNMR measurements.

Our ^{3}He target-cells were made of blown glass. We often used GE-180, an aluminosilicate-glass. Newer targets were blown out of Corning 1720, another aluminosilicate-glass, due to the scarcity of GE-180. The size and features of the glass ^{3}He targets have changed dramatically even in the short time I've worked in the field, but they all had the same three core elements as you can see in figure 4.1. First, a pumping chamber (PC) that was roughly spherical, where the gas was polarized using circularly polarized light (to be discussed further in section 4.3). Second, a target chamber (TC) that was roughly cylindrical, where an electron-beam would pass through. The windows in the ends of the target chamber were a fraction of a millimeter thick (see section 5.1). And finally, connecting the two chambers was a transfer tube (or tubes in the case of targets (b) and (c) in figure 4.1). The transfer tube(s) let the gas in the two chambers mix.

Various models of target-cell can be seen in figure 4.1, with the oldest design used in almost all of the experiments described in chapter 3 on the left. These targets used diffusion to move the polarized ^{3}He between the two chambers. An updated design in the middle of figure 4.1 were used in the A_1^n-II measurement described in section 3.3 and the d_2^n-II measurement described in section 3.4. These were the first targets to utilize convection which allowed the chambers to mix much faster; convection allowed us to consistently maintain a higher density of polarized gas in the target chamber, minimizing loss of polarization due to interactions with the electron-beam. This design also incorporated a small bulb on the transfer tube to aid in pNMR measurements. Finally, the target on the right was the design used in the G_E^n-II measurement described in section 3.7. Combined with the redesign of the target chambers such that they could accommodate larger beam cross sections, we were able to significantly increase our luminosity (equation 4.1) over the luminosity of the diffusion targets and even the first generation of convection targets.

Luminosity is commonly described by the following equation:

$$\mathcal{L}^{eff} = \mathcal{L}\, P_{He}^2 = I_b\, \rho_t\, l_t\, P_{He}^2 \tag{4.1}$$

where $\mathcal{L}$ is the usual luminosity for a fixed target experiment, defined as the product of the beam current, I_b, the target density, ρ_t, and the target length, l_t. P_{He} is the polarization of the ^{3}He interacting with the beam.

Each iteration of cell design was made because we were always aiming to improve the luminosity of the target. Normally, luminosity is proportional to how many collisions one can get in a set amount of time (usually per second), but we also scaled our luminosity by the square of the polarization of the helium. We called this figure of merit "effective luminosity". I define both in equation 4.1. If one needed to rate a target's usefulness, luminosity and effective luminosity are great barometers.

To increase luminosity, we could (to some extent) control the shape of the target and the polarization of the ^{3}He. As I said, earlier targets (figure 4.1 (a)) relied on diffusion to move polarized gas between chambers. This caused polarization gradients when the two chambers mixed due to both the electron-beam and the natural decay of polarization (aka relaxation). The "Bastille Day" design (shown in figure 4.1 (b)) largely eliminated those gradients by letting us mix the two chambers very quickly. I'm saying largely here simply because I'm *sure* there was *some* polarization loss due to mixing. The Bastille Day design was larger than previous designs (thus more ^{3}He) and added a second transfer tube to accommodate fast mixing through convection. Care was taken to achieve fast, consistent mixing of the two chambers through convection without sacrificing polarization through either wall relaxation *or* by limiting the interaction time between the ^{3}He and alkali metals in the pumping chamber (a process of polarization I discuss in section 4.3).

Finally, the coat hanger design (figure 4.1 (c)) saw the transfer tubes...bend! This both shortened the transfer tubes and meant less exposure of the PC to radiation from the electron-beam since the two chambers were further apart. Not a big enough innovation for you? Well, fine! The coat hanger design had a TC that was significantly longer (about 50% longer than the Bastille Day design)! *More* you say!?! The coat hanger targets could also withstand a much higher beam current; they were designed to withstand double the beam. With these factors combined, the coat hanger design had a much higher luminosity than all previous designs.

4.2 Production

The glass target-cells and associated pieces were fabricated offsite by Mike Souza, formerly of Princeton University, renowned as "the second best scientific glass blower in the world" (citation: Mike Souza). Why second best, you may ask? Well, to quote the same source, "People will argue with you if you say you're the best, but nobody's going to argue for second place." What follows is my broad understanding of how he worked his magic.

Mike started with off-the-shelf glass tubing (the aluminosilicate-glass mentioned at the top of section 4.1). He blew several end windows at a time, each attached to a fitting, with a central thicknesses ranging from 120 μm to 170 μm (which Mike determined with a mechanical micrometer). These were made in large batches and sent to us for pressure testing up to 20 atmospheres. The windows that survived the pressure test were initially measured using interferometry (detailed thoroughly in chapter 5, starting in section 5.1). This was no longer necessary once we developed a reliable, repeatable technique to create windows with an acceptable shape. The windows were then sent back to Mike so he could incorporate them into a

(a) A fresh set of windows

(b) A window mounted for pressure testing

Figure 4.2: Target windows before they were made into a target.

target-cell.

To make a target-cell, Mike began by forming the pumping chamber (PC), target chamber (TC), and transfer tubes (TT) separately. He gauged the thickness of the glass structures he shaped by the amount of tubing he fed in; we knew the stock tube thickness and how long they were, which meant we only needed to tell Mike how many tubes to use for a *very* accurate thickness of the PC, TC, and TT. He also created a t-section that he attached to the top of the target chamber. Mike made additional components to be assembled on site, including a retort and additional tubing to connect the target to our gas system. Before sending the target to us, he attached the the t-section to the top of the pumping chamber, the transfer tubes to the bottom of the pumping chamber, and the target chamber to the other end of the transfer tubes. The target was also cured[1] prior to transferring the cell to us.

When the target-cell was received, the manifold pieces were assembled in-house and attached to a gas handling system (which would, surprise surprise, handle the gas and convey it from a bottle to the target). The assembled unit is what appears in figure 4.3 with the bellows being the piece that attached to the gas handling system.You can find pictures of actual targets in figures 4.4a and 4.4b. An ampule of the alkali mixture was broken open and immediately dropped into the retort and the top of the retort was fused shut (figures 4.3 and 4.4c), completely sealing the target and manifold save for it's single connection to the gas system.

4.2.1 Minimizing contaminants inside the target

Next, the target was put under vacuum. While under vacuum, the target was baked at high temperature for a number of days to remove as many contaminants as possible. Parts that could not fit into the oven, such as the retort, were flame baked with an oxy-fuel welding torch (herein referred to as a "hand torch"). This was where a hand torch was run near the glass but not close enough or hot enough to melt the glass.

[1] "Curing" can mean many things. For example, concrete drying is the same as concrete curing and curing meats is a way to preserve them using salt to draw out the moisture. In the case of the glass targets, curing means a process of heating the glass and allowing it to cool and rest at room temperature.

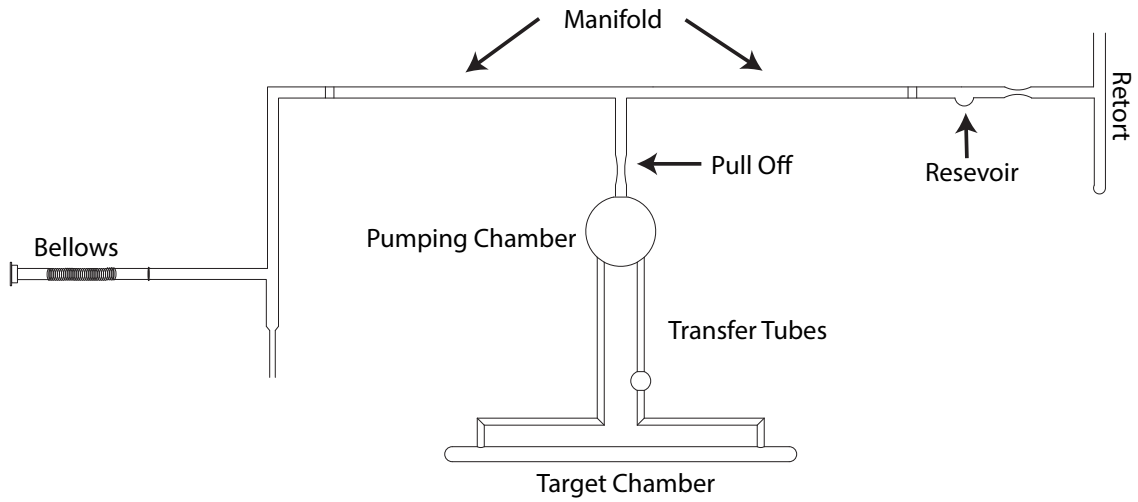

Figure 4.3: A convection target attached to the manifold. The bellows was attached to the gas handling system.

Following the discovery of contamination inside "Tiger", a G_E^n target-cell, the targets were also put through what we referred to as an "O_2 bake". The target was filled with a mixture of gases comprised mostly of oxygen. The target was then baked for approximately two days at a temperature ranging from 380°C to 400°C. In this oxygen rich environment, any remaining detritus was hopefully burned off. The gas mixture in the target was removed and refreshed four times a day during this process. This baking procedure was one production factor I was able to investigate to see if varying temperatures or baking times affected overall target quality (see section 4.4.2).

Ultimately, we think the contamination in Tiger may have been *inside* the glass itself. Still, the quest for cleaner targets is Sisyphean. Thus, Huong Nguyen oversaw and implemented a retrofit of the gas handling system. One major change to the system was the order of gas system components that the gas passed through during a fill. During the A_1^n/d_2^n era, the gas was moved through a cold trap and then into the calibrated volume. Once the gas was pumped out of the fill gap between the calibrated volume and the target, the gas in the calibrated volume was bled through the fill gap and into the target itself. It was possible contaminants in either the fill gap or the calibrated volume could migrate into the target. To eliminate this possibility, the gas was now fed into the calibrated volume first. From there, it was bled through the cold trap and immediately into the target. In addition to the oxygen bake, this reordering hopefully ensured the gas was as clean as possible before entering the target-cell.

4.2.2 Filling the target-cell

After the bake out, we finally filled the target. We started by driving the alkali mixture from the retort and into the reservoir via distillation. The retort was then removed by heating the constriction near the retort and slowly pulling the retort away. The vacuum pulled the constriction closed, ensuring the interior of the target remained isolated from the surrounding

(a) A target, shortly after receiving it, pieces in position.

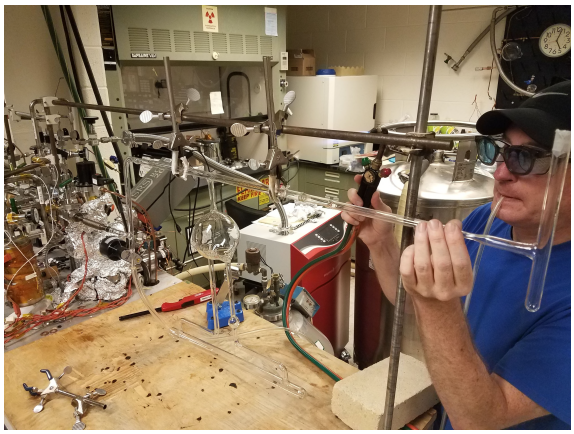

(b) Al Tobias assembling the various parts using a technique called "butt welding".

(c) A sealed retort sealed with an ampule of Rb inside.

Figure 4.4: Attaching a target to the gas handling system.

atmosphere. Then, the alkali was distilled into the pumping chamber. A hand torch was used to heat up the alkali metal into a vapor and damp paper towels wrapped around sections of the manifold were used to steer the alkali mixture into the pumping chamber; damp paper towels were placed at the t-section above the pumping chamber, on the chamber itself, and between the t-section and the gas handling system to limit the amount of alkali that could reach the gas handling system. Only a small amount of alkali is needed for the polarization process (see section 4.3).

With the gas system and target still under vacuum, the target/manifold was isolated (via a valve) at the point it connected to the gas handling system. A soupçon of nitrogen (N_2) was fed through a cold trap containing liquid nitrogen (LN_2), which removed impurities from the gas system itself. The gaseous N_2 was fed out of the cold trap and into a calibrated volume. The calibrated volume was isolated. Slowly, the valve between the manifold and the gas system was opened and N_2 was bled into the target. And again, this order was changed for G_E^n targets (where the gas flowed out of the calibrated volume and *then* through the cold trap and into the target). We knew the volume of the calibrated volume, the volume of the target-cell, and we knew the pressure once we equalized the two. Knowing these volumes and pressure gave us enough information to determine exactly how much nitrogen we'd put in the cell, which we measured in amagats.[2]

The target was then isolated. The entire gas system was again put under vacuum and we pumped out the excess N_2. The cold trap LN_2 was replaced with liquid helium (LHe). Our dewar (which we called the "Mollie" for some reason, see figure 4.5) was large enough to accommodate a cold trap line *and* submerge the target chamber in LHe, which forced the N_2 to condense and settle into the target chamber. The density of the ^{3}He also increased due to the temperature (though it did not change states). After a fill, the pressure at these cryogenic temperatures was less than 1 atm, which was critical in removing the target-cell from

[2]An "amagat" is an archaic unit of volumetric density which, converted to modern, more sophisticated (or at least SI) units is roughly 44.615 mol/m^3.

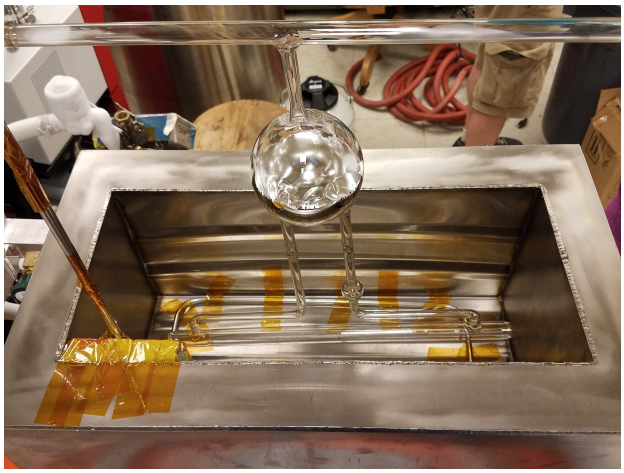
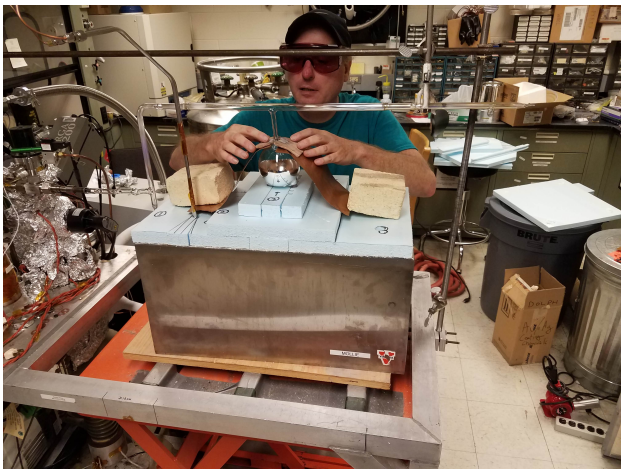

Figure 4.5: On the left, a target in the Mollie. On the right, Al Tobias prepares the same target for fill, then pull off. The metal piece in his hand will protect the pumping chamber from the heat of the hand torch during the pull off process.

the attached manifold (but I'm getting ahead of myself).

We added ^{3}He to the target in the same way we added N_2. The system was pumped out. In the case of the A_1^n/d_2^n targets, ^{3}He was then fed into the cold trap and contaminants were allowed some time to "freeze out" before the valve to the calibrated volume was opened. After isolating the calibrated volume, the valve that led into the target/manifold was slowly opened and the gas equalized. The pressures were noted and the target was isolated again. The process was repeated until we reached the desired pressure (and thus the desired density of ^{3}He, usually around 7 amagats).

Finally, the cell was "pulled off". There was another constriction built into the glass connecting the pumping chamber to the glass manifold (labelled as "pull off" in figure 4.3). This constriction was heated and the manifold slowly pulled away from the pumping chamber. Because the pressure inside the manifold-cell system was below one atmosphere, the glass collapsed inward, sealing both the manifold and target. Once the manifold and target were separated and allowed to heat to room temperature, the gas in the glass manifold and the calibrated volume were used to determine the final pressure and amount of ^{3}He in the target. The density was also calculated and the two numbers were reconciled (and agreed well). The ^{3}He density could also be confirmed using pressure broadening measurements, but more on that later in chapter 5, but do keep in mind I said "could" rather than "was". That's what we in the business call *foreshadowing*....

The remaining LHe in the cold trap was allowed to vaporize. The target was left overnight to heat back up to room temperature; slowly heating the target back to room temperature minimized the risk of stress fractures forming in the glass which could have ultimately led to a small explosion and a very sad team of physicists who had spent 2-4 weeks prepping and filling the target. Tables 4.1 and 4.2 contain the physical characteristics of all the targets that did not suffer that fate (read: were filled successfully).

	Exp.	^{3}He Den.	N_2 Den.	Volumes (mL)			TC Win.	TC Wall	TC Len.	TC Dia.
Target Name		(amg)	(torr)	PC	TC	TT	μm	mm	in.	in.
Savior		7.380	92.06	313.07	110.11	31.34			15.750	0.861
Fulla	A_1^n	6.332	91.70	337.26	104.00	29.73	136.016	1.416	15.875	0.837
Florence		6.958	91.66	335.77	113.18	29.50			15.563	0.876
Noah		7.292	95.78	298.20	110.99	30.48			16.000	0.8505
Brianna	A_1^n/d_2^n	6.938	95.93	289.53	99.88	26.97	129.598	1.403*	15.551	0.83
Elle		7.280								
Sandy-II		7.460								
Phoenix		7.140	95.86	284.41	100.86	31.07			15.700	0.81
Zoe		7.890								
Dutch	A_1^n	7.759	94.69	297.15	111.87	32.52	138.981	1.334	15.625	0.8725
Wayne		7.313	93.73	312.30	112.00	32.77			15.725	0.868
Tommy	d_2^n	7.760					141.206	1.399*		
Zhou		7.350								
Big Brother	A_1^n	6.992	89.52	293.82	100.76	32.60	119.683	1.428	15.750	0.8285
Columbus		7.650								
Austin	d_2^n	7.498	93.75	305.87	106.46	37.92	146.995	1.369	15.686	0.85
Yixin		7.540								
Butterball		7.608	93.30	304.62	95.44	28.55	151.690	1.530	15.611	0.8125
Chout		7.153	88.76	314.06	99.73	32.70			15.721	0.826

Table 4.1: Physical Characteristics of A_1^n-II and d_2^n-II target-cells. TC wall thickness measurements with an asterisk (*) were measured via ultrasonic interferometry at JLab. All others were measured with laser interferometry at UVa. See chapter 5 for further details.

	^{3}He Den.	N_2 Den.	Volumes (mL)			TC Wall	TC Len.	TC Dia.
Target Name	(amg)	(torr)	PC	TC	TT	mm	in.	in
Talisker	0.801	2.41	546.73	196.64	40.55			
Triveline	6.424	90.91	526.33	204.34	42.45			
Ukraine	6.894	91.11	580.47	199.76	39.13		23.250	0.916
Autobahn	6.711	89.57	615.31	197.55	48.70		23.250	0.912
Tiger	7.011	90.06	485.72	207.46	34.97		23.244	0.931
Pristine	7.150	90.61	530.62	199.68	53.10		23.631	0.909
Hunter	7.387	90.80	306.17	160.90	44.87	1.50	23.401	0.863
Walter	6.388	90.39	455.14	202.58	41.15		23.339	0.920
Windmill	6.993	90.70	437.70	191.22	36.62	1.43	23.750	0.895
Fringe	6.711	90.13	462.16	201.20	40.21	1.43	23.670	0.917
Chicago	6.890	91.28	432.13	199.87	50.04	1.51	23.755	0.913
Mekong	5.745	90.13	421.81	179.32	41.00	1.50	23.593	0.872
Ginger	6.489	89.29	430.16	184.44	41.64	1.42	23.695	0.879
Christin	6.829	89.76	430.70	195.63	41.08	1.52	23.876	0.902
Donya	6.882	92.55	331.18	208.93	43.34		23.536	0.934
Barbie	6.931	90.13	323.65	193.63	43.33		23.600	0.903
Juna	5.395	89.16	412.53	205.33	43.44			

Table 4.2: Physical Characteristics of G_E^n-II target-cells. TC wall thickness measurements with an asterisk (*) were measured via ultrasonic interferometry at JLab. All others were measured with laser interferometry at UVa. See chapter 5 for further details.

4.3 Polarimetry Measurements

There were two systems we used to characterize the targets. The first was the NMR (nuclear magnetic resonance) and EPR (electron paramagnetic resonance) system. In this section, I'll discuss the NMR/EPR system, how it worked, and how it was upgraded. The other system will be discussed in chapter 5, but the "spin-ups" and "spin-downs" performed with the NMR/EPR system were our bread and butter. Figure 4.8 shows a wiring schematic of the NMR and EPR systems on the left and right side of the diagram, respectively.

To perform a spin-up or spin-down, the pumping chamber was placed in a convection oven with the transfer tubes and target chamber hanging below. A spin-up and spin-down were both measurements of the target polarization taken over time, usually over a number of days. In a spin-up, we heated the oven and polarized the target while taking measurements at designated time intervals (every two, three, or four hours, say). In a spin-down, we allowed the polarization to decay naturally and took measurements, again, at designated intervals.

4.3.1 AHSEOP

The target-cells contained the alkali metal mixture mentioned in section 4.2 which was central to polarizing the ^{3}He gas. In the SLAC and early JLab era (discussed heavily in chapter 2), targets only contained rubidium. Since then, it was determined a mixture of potassium (K) *and* rubidium (Rb) would greatly improve polarization of the ^{3}He, both the rate of polarization and the maximum polarization. A ratio of 6 ± 1 for K vapor to Rb vapor was found to be optimal (references [41] and [42]). Vapor density was controlled by heat: we put the pumping chamber in an oven and heated it up (more on that in section 4.3.2)

We polarized the ^{3}He nuclei through a three step process called Alkali Hybrid Spin-Exchange Optical Pumping (AHSEOP). It's a mouthful.

The Rb was polarized using circularly polarized light tuned to the Rb D1 spectral line (at approximately 794.760 nm) [43]. Normally, selection rules for the excited electron allow the quantum number related to Zeeman splitting (m_f for hyperfine state F) to change by $\Delta m_f = 0, \pm 1$ and (independently) $\Delta F = 0, \pm 1$. Circularly polarized light changes those rules depending on the direction of the circular polarization and the direction at which the alkali is polarized. In our lab, when polarizing the target from one direction, the laser's direction of propagation was the same as the direction of the alkali polarization: both were aligned with the main magnetic field. In this case, the quantum number m_F is forced to change by $\Delta m_f = -1$ for clockwise circular polarization or $\Delta m_f = +1$ for counter-clockwise circular polarization ([44], [45]). These rules reverse if the direction of beam propagation is anti-aligned with that of the magnetic field (and thus the alkali polarization); when polarizing a target from two sides, the circular polarization for each beam needed to be opposite else each beam would be depopulating the state the other beam was populating!

The electron decay follows the same selection rules F and m_f naturally follow (see figure 4.6a) if it were to emit a photon, but we try to avoid that as the emitted photon would hinder polarization. This is where the nitrogen comes into play. Because N_2 has many internal degrees of freedom, collisions between Rb and N_2 allow the electron to decay without emitting a photon. Once in the ground state, the electrons are excited again with the caveat that $\Delta m_F = -1(+1)$ for clockwise (counter-clockwise) circularly polarized light. This cycle continues until

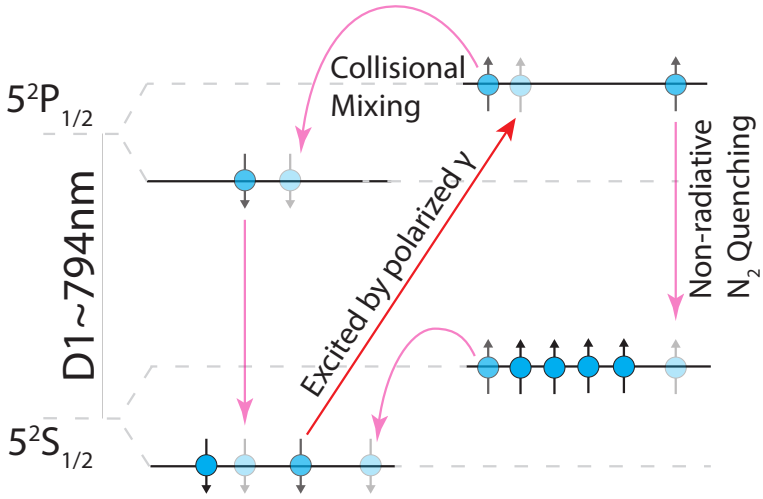

(a) A simplified diagram of SEOP showing the path of the Rb electrons to their final, polarized state. The bright red line indicates the path an electron can take when absorbing a photon (CCW in this case). The magenta lines show the various paths the electron can take back to the ground state.

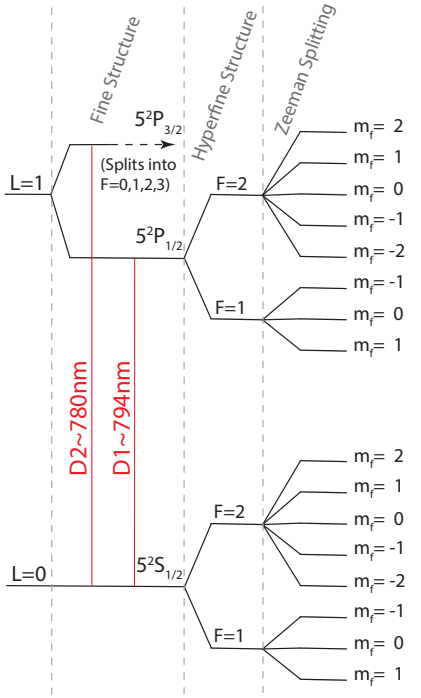

(b) The L=0 and L=1 energy levels of rubidium, split into the Fine Structure (spin-orbit coupling), Hyperfine Structure (electron-nucleus interaction), and energy levels from Zeeman splitting (affect of the magnetic field).

Figure 4.6: A visual depiction of how Rb was polarized during Spin-Exchange Optical Pumping.

the electron reaches the ground state $F = 2$ with quantum number $m_F = -2$ ($m_F = +2$) for clockwise (counter-clockwise) circularly polarized light. Like Thanos, it is inevitable[3]. Some decay from this heavily populated state will naturally occur through collisional mixing, but the electron will soon find itself back in the $m_F = -2$ ($m_F = +2$) state. It's easy to see if we look at figure 4.6b closely. Say we're using CCW circularly polarized light. Once an electron decays to the $F = 2, m_f = 2$ ground state, it cannot absorb another photon because it cannot move $\Delta m_f = +1$. It's only way out is moving to an $m_f = 1$ ground state, where it will again be pumped to the $m_f = 2$ excited state...and round and round it goes.

But all we've done so far was polarize Rb. The polarization of the Rb electrons quickly comes to equilibrium with the polarization of the K electrons through rapid spin-exchange. The K electrons then exchange *their* spin with the ^{3}He nucleus through hyperfine interactions. To a lesser extent, the polarized Rb electrons also interact with the ^{3}He nucleus through hyperfine interactions (otherwise, how would the old, Rb-only targets of the E-142 era and early JLab work). And thus, after all that work, we get polarized ^{3}He nuclei.

4.3.2 The NMR and EPR Apparatus

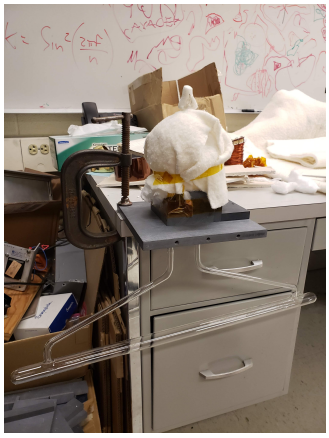

(a) Target mounted in the base of the oven

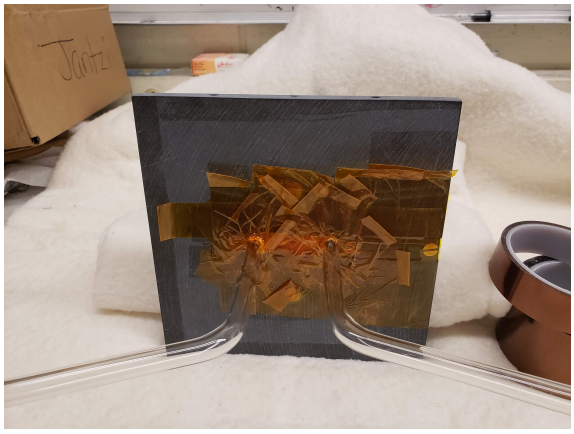

(b) Underside of the oven base, the hole sealed with Kapton tape and aluminosilicate insulation

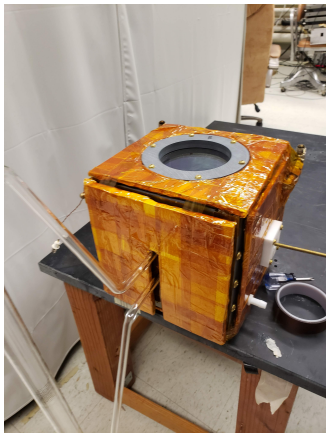

(c) Base of the oven installed and insulated

Figure 4.7: Mounting a target on the oven base.

Any test began by mounting the target in the oven (mentioned at the top of this section and pictured in figure 4.7c). The target was first mounted to the oven base, then the base inserted into the oven. Great care was taken to ensure the base was leak tight before mounting the oven in the testing apparatus.

The oven was built of half-inch thick alumino-cilicate plates[4] and insulated with a fibrous, flexible mat of polycrystalline alumina fiber[5]. It was heated by forced air convection. A frame

[3] *Avengers: Endgame*, Directed by Anthony Russo and Joe Russo, Performances by Robert Downey Jr., Chris Evans, Mark Ruffalo, Chris Hemsworth, Scarlett Johansson, Jeremy Renner, and many others, Marvel Studios, 2019

[4] p/n 8479K58 alumina-silicate ceramic, McMaster-Carr, Robbinsville, NJ

[5] p/n D9201, Alumina Mat, Zircar Ceramics, Florida, NY

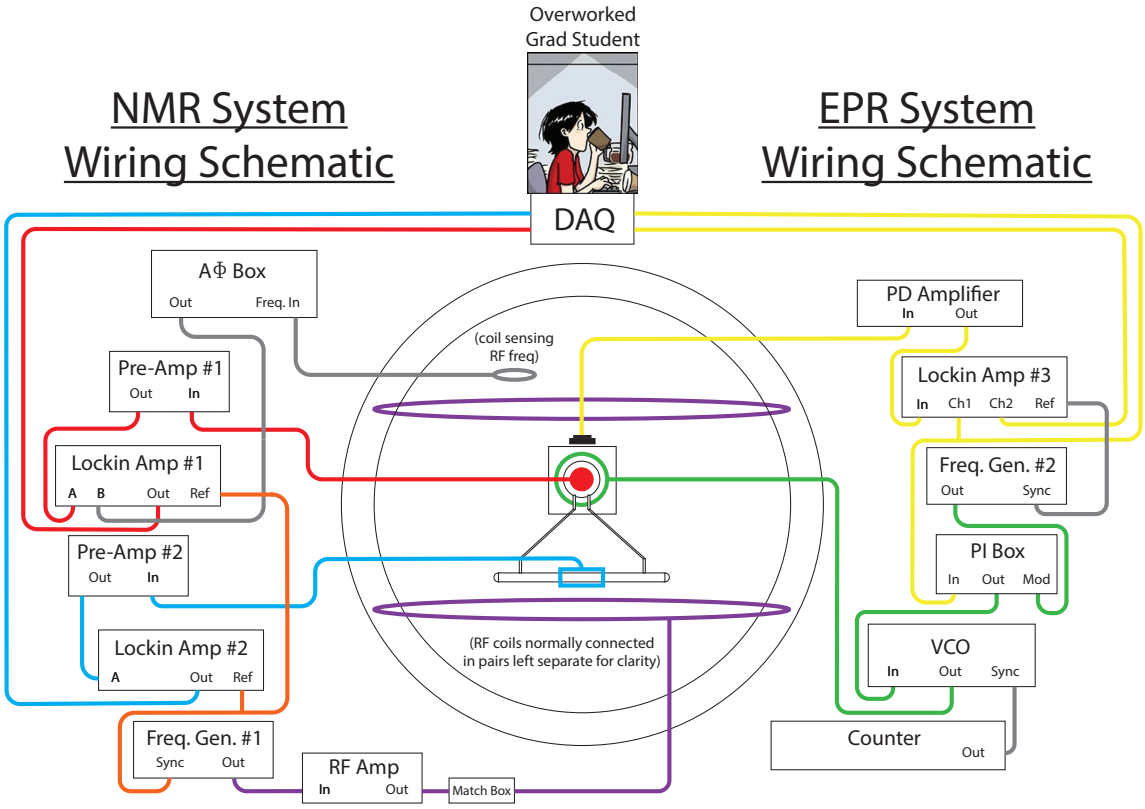

Figure 4.8: A diagram of the NMR/EPR apparatus. The *purple* lines are the signal driving the NMR RF field, the *green* lines are the modulated signal driving the EPR RF coils, the *red* lines trace the signal from the PC pickup coils, the *blue* lines trace the signal from the TC pickup coils, and the *yellow* lines trace the signal from the EPR photodiode. Grad Student Illustrated by Jorge Cham, Illustrator, PhD Comics (jorge@phdcomics.com)

held the oven near the center of a large holding-field, maintained by two very large coils[6] placed in a Helmholtz configuration (the large, black rings in figure 4.8) and connected to a voltage controlled power supply[7]. A smaller set of coils provided an RF field (the purple ovals in figure 4.8). They were driven by a function generator[8] fed through an RF amplifier[9] and centered on the oven as well. A yet smaller set of coils *inside* of the oven were placed very close to the pumping chamber (red circles, figure 4.8) and mounted on movable, brass rods that extended out of the oven. These cleverly named coils[10] picked up the signal from the pumping chamber during our tests and sent the signal to a pre-amp[11], then a lock-in amplifier[12], and finally the DAQ[13] to interface with the computer. A secondary set of pickup coils was placed on the target chamber near the center of its length (the blue coils in figure 4.8). Like the pumping chamber pickup coils, these were fed though a pre-amp[14] and a lock-in amplifier[15]. Finally, a small resistance heater[16], powered by a variable transformer[17], was wrapped around one of the transfer tubes very close to the bottom of the oven. This heater induced convection inside the cell, expediting the transfer of gases between the two chambers.

4.3.3 I built this system (on rock and roll)

In the fall of 2021, I upgraded the NMR/EPR system to accommodate much larger targets. Unfortunately, a lot of this work needed to done at night to avoid transmission of COVID-19, but I had a healthy collection of rock and roll to keep me company. I removed everything except the holding-field coils. Great care was taken to limit the amount of metal in the new system to minimize field inhomogeneities. I constructed a wooden frame to replace the metal and rubber frame holding the old oven and RF coils in place. Most of the wooden joints in the new frame were held together by pinned mortise and tenon joints (figure 4.9d), which don't require nails or screws (but did require a rubber mallet and excessive profanity). Two long metal L brackets (visible in figure 4.9c) were the only large pieces of metal in the system and were necessary as they could both support the oven's weight and withstand its temperatures. The old RF coils, wrapped on a bicycle wheel rim, were replaced with plastic frames and were significantly larger (the large, dark gray, flattened rings in 4.9c). They were also on plastic hinges so the coils could easily be moved in and out of position (which was useful when we removed the oven). While the oven was larger than the previous oven, it maintained fundamentally the same design and used the same alumina-silicate ceramic plates as the old oven (which were already non-magnetic).

[6] Helmholtz Coils, 67" Custom, Milhous Company, Amhearst VA
[7] ATE 100-10DMG, Linear Power Supply, Kepco Power, Flushing NY
[8] Agilent 33250A, 80 MHz function / arbitrary waveform generator, Agilent Technologies, Santa Clara CA
[9] 1040L, Broadband Power Amplifier, Electronics and Innovation Ltd., Rochester NY
[10] Yes, they were simply called pickup coils. Yes, I was using "clever" sarcastically.
[11] SR560, Low Noise Amplifier, Stanford Research Systems, Sunnyvale CA
[12] SR860, 500 kHz DSP Lock-in Amp., Stanford Research Systems, Sunnyvale CA
[13] BNC-2090A, Rack Mounted Terminal Block, National Instruments, Austin TX
[14] SR560, Low Noise Amplifier, Stanford Research Systems, Sunnyvale CA
[15] SR124, 200 kHz Analogue Lock-in Amp., Stanford Research Systems, Sunnyvale CA
[16] Kapton Heater Kit, 1.5 x 4.5 in., Omega Engineering, Norwalk CT
[17] 3PN116B, Powerstat Autotransformer Variac, Superior Electric Company, Bristol CT

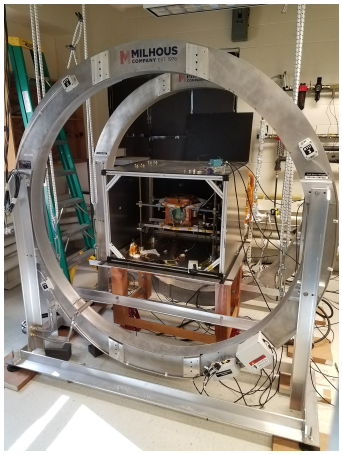

(a) The previous NMR/EPR system.

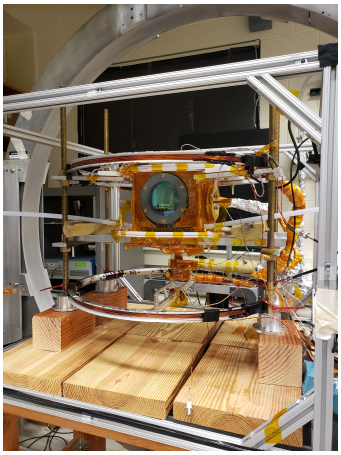

(b) The previous NMR/EPR system, modified.

(c) The upgraded NMR/EPR system.

(d) Wooden joints.

Figure 4.9: Pictures of the old and new NMR/EPR systems. RF coils in 4.9a are the small, white ones pictured near the top and bottom of the oven. The same coils are present in 4.9b as well as an additional set of coils made of aluminum bicycle tire frames. The RF coils in 4.9c are dark gray. The joints in 4.9d are pinned mortise and tenon joints and are secured via friction rather than screws or nails.

4.3.4 Temperatures

For a spin-up, the pumping chamber was heated to around 235°C using forced air convection. You may have noticed that 235°C is quite a bit higher than the melting points of either rubidium ($\approx$ 90°C) or potassium ($\approx$ 64°C). The temperature of the oven was determined by the desired number density of the alkali vapor. While 235°C had been the benchmark temperature for performing a spin-up, oven temperatures ranged from 220°C to as high as 255°C for targets using an alkali mix, though rubidium (Rb) only targets were always tested at 170°C. At the time of this writing, Rb-only targets were made to test the gas system or new target cell designs; Rb-only targets were not production cells to be used at JLab.

4.3.5 NMR AFP Tests

Target polarization was measured using an NMR technique called adiabatic fast passage (AFP) where we flip the ^{3}He spins from being aligned with the holding-field to anti-aligned and finally back to aligned (figure 4.10). Here's how it works. With the holding-field on, we started by polarizing the gas through AHSEOP. Next, we turned on an RF field with a frequency slightly higher than the Larmor frequency of the ^{3}He nuclei. Then, we performed an "up sweep" which means we increased the holding-field strength such that the Larmor frequency of the ^{3}He passed through resonance with the RF field. Finally, we performed a "down sweep" which (you may have guessed) means we decreased the holding-field strength, again passing the Larmor frequency through resonance with the RF field frequency. While figure 4.10 shows a sweep of eight seconds (four seconds up, four seconds down), this was not typical. I used eight seconds because it breaks up nicely into nine pictures. Further, the time we took to sweep the field

up or down wasn't as important as the rate at which we swept the field. For example, when performing a test for a Larmor frequency near 154 kHz, the field would be swept from 37-57G in 4 seconds (a rate of 5G/s). For tests with a Larmor frequency around 91 kHz, the field was swept from 23-33G in 2 seconds (the same rate of 5 G/s).

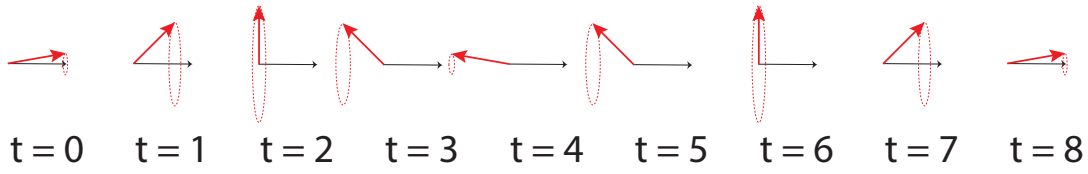

Figure 4.10: For time in seconds, a full up-sweep and down-sweep in the lab frame comparing orientation of a single spin (red arrow) with holding-field (black arrow).

I note here that this procedure was how we took an AFP for spin-ups and spin-downs. The procedure was slightly different for an EPR measurement, which I will be discuss in section 4.3.5.

So, what's physically happening during a sweep? Using the conventions of Rabi, Ramsey, and Schwinger[46], we can describe the effective magnetic field experienced by the ^{3}He in the frame rotating at the Larmor frequency about the direction of the holding field as follows:

$$\mathbf{H}_{er} = H_1\mathbf{i} + (H_0 - \omega/\gamma)\mathbf{k} \tag{4.2}$$

where H_0 is the strength of the holding-field, H_1 is the strength of the RF field, ω is the angular speed of the rotating frame, and γ is the gyromagnetic ratio of the ^{3}He.

For a sweep up, we increased the holding-field strength, H_0, through resonance and continued increasing until the field was once again off resonance. At resonance, the contribution of the effective field in the $\mathbf{k}$ direction reduced to zero and the spins aligned to the RF field. As the holding-field increased further, passing out of resonance, there was a sign change in the $\mathbf{k}$ contribution of the field. The spins again aligned to the holding-field, only now pointed anti-parallel to the field. A down sweep was the same process but reversed (illustrated in figure 4.10). As the spins of the ^{3}He passed through the plane perpendicular to the holding-field (leading through time stamps $t = 2$ sec and $t = 6$ sec in figure 4.10), a signal (in mV) was picked up through the appropriately named "pickup coils" on the pumping chamber and target chamber (see figure 4.8).

Spin-ups, spin-downs, three-point plot

As I said before, spin-ups and spin-downs were the bread and butter of target characterization. A spin-up was performed by heating the oven to temperatures discussed in section 4.3.4, using lasers to polarize the target using AHSEOP (discussed in section 4.3.1), and taking AFP measurements at a set interval (say every 2 hours, every 4 hours, every 6 hours, etc), charting the target-cell's increasing polarization with time. The data points were then fit to the following equation:

$$P(t) = (P_0 - P_\infty)e^{-(\gamma_{se}+\Gamma)\,t} + P_\infty \tag{4.3}$$

where P_0 is the initial polarization, P_∞ is the saturation polarization, γ_{se} is the total spin-exchange rate with both alkali species, Γ is the total relaxation rate due to every factor that is *not* spin-exchange, and t is time. P_∞ can further be defined as:

$$P_\infty = P_A \frac{\gamma_{se}}{\gamma_{se} + \Gamma} \tag{4.4}$$

where $P_A \approx 100\%$ is the alkali polarization and all other variables are as in equation 4.3.

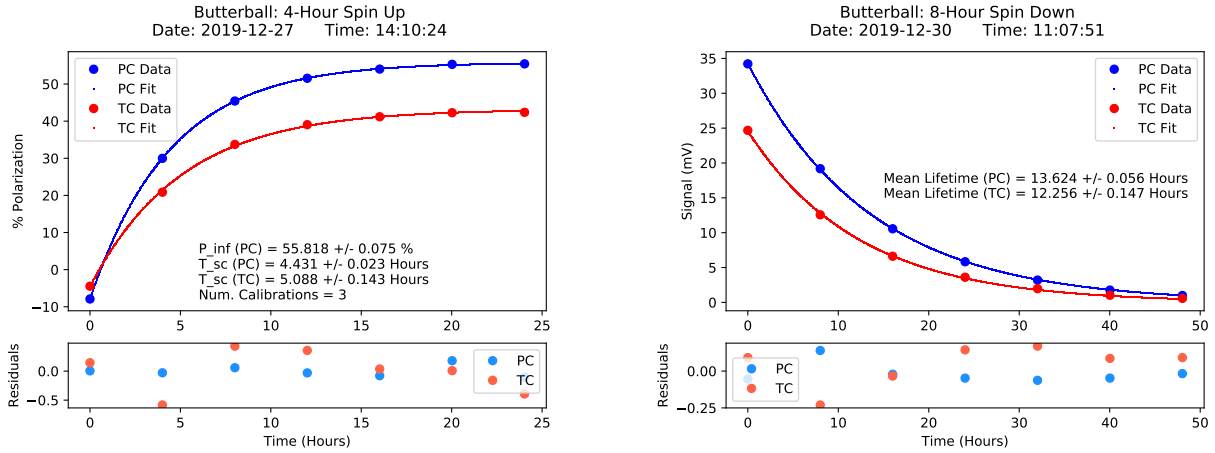

(a) A typical spin-up, 4-hour interval.

(b) A typical spin-down, 8-hour interval

Figure 4.11: Examples of the two tests that comprise target characterization with the NMR/EPR apparatus. The y-axis defines the polarization (figure 4.11a) or amplitude in mV (figure 4.11b) of the *pumping chamber only* (blue line). The target chamber (red line) is plotted only to show that the two chambers are mixing at a reasonable rate as indicated by the two lines rising or falling synchronously.

The goal of performing a spin-up was to find the saturation polarization, P_∞. The rate of relaxation, Γ, also carried important information and will be discussed further at the end of this section. The example in figure 4.11a shows a 4-hour spin-up.

A spin-down was performed when the oven was cool and the cell was well polarized. Similar to a spin-up, we took AFP measurements at a set interval (say every 2 hours, every 4 hours, every 6 hours, etc). The data were then fit to a simple exponential decay:

$$P(t) = P_0 e^{-t \cdot \Gamma_{cold}} \tag{4.5}$$

where P_0 is the initial polarization, Γ_{cold} is the spin relaxation rate (inverse of mean lifetime), and t is time.

There was a third test that was equally important called a three-point plot, which combined the results of several spin-downs to find an intrinsic lifetime for a target. The spin-ups told us maximum polarization and the spin-downs told us the mean lifetime for that spin-down. However, this mean lifetime for a given spin-down was a combination of the intrinsic lifetime of the target and of the polarization lost due to taking an AFP measurement.

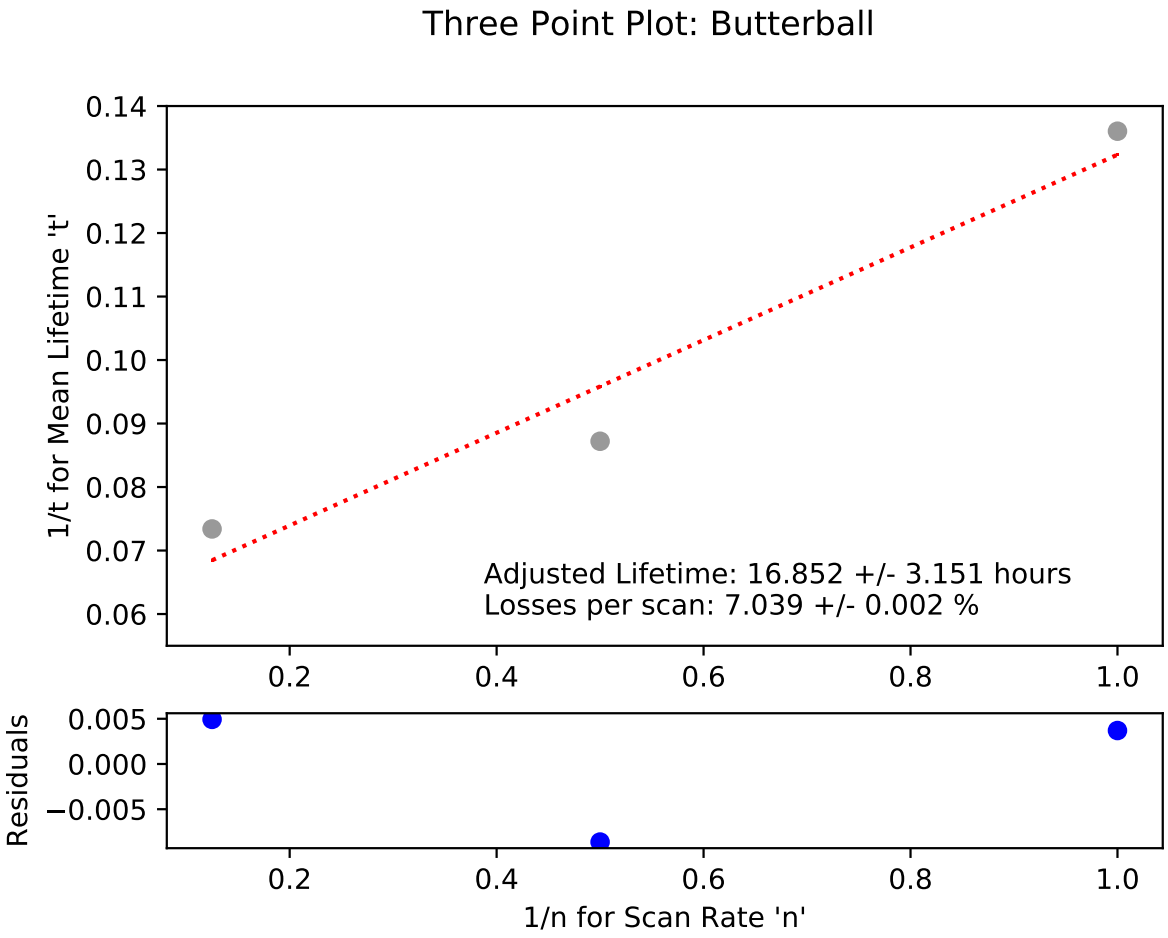

Figure 4.12: A typical three-point plot using 1-hour, 2-hour, and 8-hour spin-downs.

To separate the polarization decay due to taking an AFP measurement from the natural decay due to the target-cell simply existing, we start by considering the total relaxation rate of the polarization in the target and thus the total lifetime of the target polarization:

$$\Gamma = \Gamma_{AFP} + \Gamma_{cell}$$
$$\Gamma = {}^{1}\!/_{\tau} = n \cdot \Gamma_{AFP}^{1hr} + {}^{1}\!/_{\tau_{cell}} \tag{4.6}$$

where $\Gamma = 1/\tau$ is the total relaxation rate, τ is the total lifetime, Γ_{AFP} is the relaxation due to AFP measurements related to this lifetime, Γ_{AFP}^{1hr} is the relaxation rate if AFP measurements were only taken once per hour, n is the sampling rate (in measurements per hour), $\Gamma_{cell} = 1/\tau_{cell}$ is the intrinsic relaxation rate of the target which includes wall relaxation and collisional relaxation, and $\tau_{cell} = 1/\Gamma_{cell}$ is the intrinsic lifetime of the target.

The intrinsic lifetime of the target, τ_{cell}, is a constant. From a spin-down, we have both the lifetime, τ, and the sampling rate, n, for that spin-down, but those would only constitute one data point for the linear equation, 4.6. So, several spin-downs were taken at different sampling rates, usually consisting of a spin-up between each one (because if you're going to be polarizing the target, you might as well take more data, in my opinion). For a "three-point plot", we perform at least three spin-downs, giving us three data points for equation 4.6 and allowing us to solve for the two constants: intrinsic lifetime, τ_{cell}, and relaxation rate per AFP sweep per hour, Γ_{AFP}^{1hr}, which will become important in section 4.3.6.

Maximizing fields, minimizing leakage, and getting the most bang for our buck.

To function efficiently and produce the strongest field, the RF coils needed to be driven at their natural resonant frequency. Making coils that naturally resonate at the frequency we wanted was about as likely as me discovering Bigfoot: sure, there's a minute possibility, but I'm not going to stake my career on it. There's also the added complication that we needed the coils to resonate at three completely different frequencies. We used a 42 kHz field during an EPR calibration, but used either a 91 kHz field or a 154 kHz field for the tests described in section 4.3.5. Why we use two different RF field strengths for regular AFP measurements and a third one for EPR calibrations will be detailed in section 4.4. For now, let's discuss how.

An impedance matching L-network circuit will solve the issue. So let's build one! Z_1 in figure 4.13a will be our RF coil. Let's assume for a moment that $Z_1 = A + jB$, where A and B are the real and imaginary parts of the Z_1 impedance, respectively. Following the same steps as in reference [47], we can find general solutions for X_s and X_p by first finding the equivalent impedance to the circuit involving the L-network and the coil:

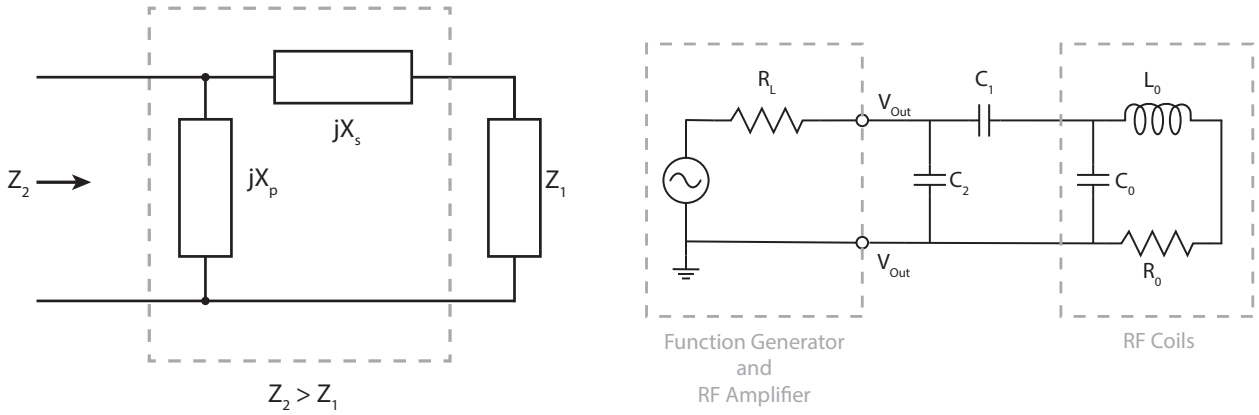

(a) An L-network, where input resistance desired was Z_2. If the circuit represented by Z_1 only has an inductor, then either X_s or X_p *must* be a capacitor. The reverse was also true. Adapted from reference [47].

(b) Matchbox circuit used to manipulate resonant frequency of the RF coils. R_L is the load resistance from the RF amplifier, C_1 and C_2 are the capacitors of the L-network, and L_0, R_0, and C_0 are the inductance, resistance, and capacitance of the RF coils, respectively.

Figure 4.13: Impedance Matching Circuits

$$Z_{in}^{-1} = [(A+jB)+jX_s]^{-1} + [jX_p]^{-1} = \frac{A+jB+jX_s+jX_p}{(A+jB+jX_s)(jX_p)} = \frac{A+j(B+X_s+X_p)}{-X_p(B+X_s)+j(AX_p)}$$

$$Z_{in} = \frac{-X_p(B+X_s)+j(AX_p)}{A+j(B+X_s+X_p)} = \frac{AX_p^2+j(A^2X_p+(B+X_s)(B+X_s+X_p)}{A^2+(B+X_s+X_p)^2} \tag{4.7}$$

where the final form of equation 4.7 was found by making the denominator real (multiplying both the denominator and numerator by the complex conjugate of the denominator).

Let's next set $X_s = {}^{-1}/_{\omega C_1}$ and $X_p = {}^{-1}/_{\omega C_2}$ so we can match figure 4.13b. Lastly, we set $Im(Z_{in}) = 0$ and $Re(Z_{in}) = Z_2 = R_L$, where R_L is the load resistance of the RF amplifier and function generator. We can now solve these two equations for C_1 and C_2, finding the following:

$$C_1 = \frac{1}{\omega(B-\sqrt{A(R_L-A)})} \qquad C_2 = \sqrt{\frac{R_L-A}{A\omega^2R_L^2}} \tag{4.8}$$

where, $\omega = 2\pi f$ is the desired resonant frequency of the coils and R_L is the load resistance of the RF amplifier and function generator. A and B are still the real and imaginary parts of the RF coil impedance (respectively) mentioned above.

With the older system and it's smaller coils, we modeled the coils as an inductor in line with a resistor, making $A = R_0$ and $B = \omega L_0$. Oh, for simpler days. Unfortunately, the size

of the new coils meant we needed a more robust equivalent circuit to account for the larger resistance and self-capacitance. I adopted a common equivalent circuit where, in addition to the series inductor and resistor, there was a capacitor running in parallel to them (see the RF coil in figure 4.13b).

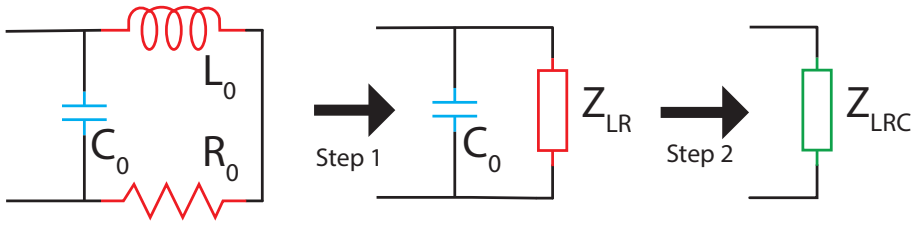

Figure 4.14: Finding the equivalent circuit using Thèvenin's theorem.

We can find the impedance of the new equivalent circuit using Thèvenin's theorem and the steps in figure 4.14:

$$
\begin{aligned}
Z_{LR} &= Z_R + Z_L = R_0 + j\omega L_0 \\
Z_{LRC}^{-1} &= Z_{LR}^{-1} + Z_C^{-1} = \frac{1}{R_0 + j\omega L_0} + j\omega C_0 = \frac{(1-\omega^2 L_0 C_0) + j(\omega R_0 C_0)}{R_0 + j\omega L_0} \\
Z_{LRC} &= \frac{R_0 + j\omega L_0}{(1-\omega^2 L_0 C_0) + j(\omega R_0 C_0)} = \frac{R_0 + j\omega[L_0 + C_0(R_0^2 - \omega^2 L_0^2)]}{(1-\omega^2 L_0 C_0)^2 + (\omega R_0 C_0)^2}
\end{aligned}
\tag{4.9}
$$

where L_0, R_0, and C_0 are the inductance, resistance, and capacitance of the RF coils, respectively, and ω is the target frequency. We finally have values we can plug into equation 4.8:

$$
A = \frac{R_0}{(1-\omega^2 L_0 C_0)^2 + (\omega R_0 C_0)^2} \qquad B = \frac{\omega[L_0 - C_0(R_0^2 + \omega^2 L_0^2)]}{(1-\omega^2 L_0 C_0)^2 + (\omega R_0 C_0)^2} \tag{4.10}
$$

where (finally) A and B are the real and imaginary parts of the coil impedance defined in terms of the physical characteristics of the coils and load themselves. I'd also like to note that should $C_0 = 0$, we recover $A = R_0$ and $B = \omega L_0$ just as we had in our series model for the old NMR system.

Three matching circuits, which we call "matchboxes", were made for the RF coils, one for each of the frequencies at which we operated. A fourth matchbox between the pumping chamber pickup coils and their pre-amp (red coils and wires on figure 4.8) was sometimes used to filter out unwanted resonances in the incoming signal.

The resonant frequency of the circuit for the RF coils in figure 4.13b was also slightly different from the standard $\omega = \sqrt{1/LC}$ due to the new equivalent model for the RF coils.

Thankfully Kaiser already worked that out. Equation 5.30 of reference [47] was the resonant frequency for such a circuit and reads as such:

$$\omega_0 = \sqrt{\frac{1}{LC} - \left(\frac{R}{L}\right)^2} \tag{4.11}$$

where ω_0 is the resonant frequency, f_0, multiplied by 2π. L, R, and C are the inductance, resistance, and capacitance of the RF coils, respectively.

Another issue arose from the larger coils: heat changes resistance. There was a lot more current than the old coils so there was a noticeable difference in heat. As you can see from equation 4.11, that means the resonant frequency drifted *over time* as the coils heated and the resistance increased. This issue was actually resolved by the gray, sensing coil in figure 4.8 and a little patience (more on the sensing coil in a moment). We simply set the RF frequency a little higher than what our matchbox was tuned to and gave the system a little time to warm up before taking a measurement. The frequency shift usually settled down within 60 seconds. The sensing coil in figure 4.8 was plugged into the final piece of the setup I want to talk about: the AΦ box.

The signal from the ^{3}He we were trying to see was at the same frequency as the RF field, which was obviously problematic. There were very effective steps we took to minimize RF leakage into our pickup coils. The first and simplest step was to adjust the angle of the pickup coils with respect to the RF coils. As I mentioned in section 4.3.2, they were mounted on a movable brass rod whose fulcrum was near the oven wall. The rod was long enough that it provided a lever arm for adjusting the angle of the coil with respect to the normal vector from the wall it was mounted on. Watching the signal from the pickup coils on a scope, the procedure was as simple as moving the coil around until the signal was small. Additionally, the distance between the coil and the target could be adjusted by twisting the rod, but this was done during installation, wasn't useful for minimizing leakage, and I just wanted to mention because I thought it was pretty neat.

It wasn't possible to eliminate all of the leakage by adjusting the angle of the pickup coils. The leakage was further reduced by generating a sinusoidal signal that resembled our RF field. We then fed this signal into the differential input of the lock-in amplifier which received our pickup coil signal: subtract the manufactured signal from the pickup coil signal *et voilà*, we had a signal comprised of a lone, ^{3}He polarization signal. The sinusoidal signal was generated with the AΦ box in figure 4.8 and whose circuit is displayed in figure 4.15.

The sensing coil in figure 4.8 tracked the amplitude and frequency of the RF field as well as any phase shifts in the RF field that occurred as the RF coils warmed up. The frequency and phase were fed into the "Ref. Freq. In" connection in figure 4.15. The AΦ box produced a sinusoidal signal with the same frequency and relative phase as the RF field. The phase and amplitude of the outgoing signal were adjustable via three circuits and their potentiometers (knobs). The amplitude was adjustable via the circuit labelled "Gain" in figure 4.15 and the phase was adjustable using either the "Lead" or "Lag" circuits in the same diagram. A switch immediately to the right of the "Lead" and "Lag" circuits in figure 4.15 allowed us to choose a phase that either led or lagged behind the phase received from the reference frequency coil.

A stationary set of pickup coils (the blue ones in figure 4.8) gathered data for the target

chamber, but as of the time of this writing, a second AΦ box has not been integrated into this system. Due to their position in the RF field, leakage is less of an issue.

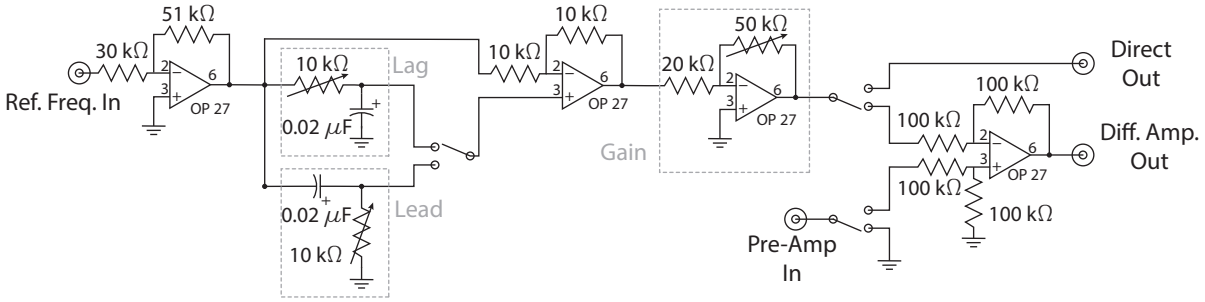

Figure 4.15: A circuit diagram of the AΦ box.

The end result of these noise cancellation and signal amplification efforts was the ability to detect a clean signal with a very high signal-to-noise ratio on measurements from the pickup coils on the order of a single microvolt (1 μV).

Measuring a shift in Zeeman splitting through EPR

AFP measurements provided a signal that was proportional to polarization but measured in mV. However, the signal in mV didn't tell us how much polarized gas we had in the target cell. To translate our signal from millivolts to a percentage of total polarization, we performed an "EPR calibration". This technique, based in EPR (hence the clever name), was sensitive to the effective magnetic field caused by the polarized ^{3}He as seen by the alkali-metal atoms. Given cell characteristics logged during the target's fill (including the ^{3}He density), this effective magnetic field was easily translated into units of percent polarization. By taking an AFP measurement close in time to an EPR calibration, we could correlate a signal in mV to the percent polarization of the ^{3}He at that time. The AFP measurements in this procedure were exactly as described in section 4.3.5.

The tests described in section 4.3.5 were done at an RF frequency of about 154 kHz and later at about 91 kHz. This corresponds to a Larmor frequency from a holding-field strength of about 47.5 G and 28 G, respectively. Unfortunately, these correspond to EPR frequencies up to about 41 MHz (for the 47.5 G field). We simply could not run enough current through our EPR RF coils to achieve a strong RF field at those frequencies. Therefore, AFP measurements were taken at their normal holding-field strength and EPR measurements were taken at a much lower field, 13 G, which corresponded to an EPR frequency on the order of 9 MHz. To ensure minimal time between the AFP measurements and the EPR calibration, the appropriate matchboxes (discussed in section 4.3.5) were placed near one another to accommodate fast switching when changing the frequency of the main RF field.

A photodiode[18] was placed over the window at the top of the oven prior to the start of testing. To isolate light from the Rb D2 line (the transition between the $5P_{3/2}$ to the $5S_{1/2}$ states), a 780 nm filter[19] was placed over the photodiode.

[18]UDT PIN 10D, Photodiode, OSI Optoelectronics, Hawthorne CA
[19]FB-780-10, Bandpass Filter, Thorlabs, Newton NJ

We began the procedure by polarizing the target until it reached saturation polarization as described in section 4.3.5. Then, we took one AFP measurement at the same holding-field and RF frequency settings we wished to calibrate. Following that, we lowered the holding-field to 13 G.

As the laser light pumps the Rb-electrons from the $5S_{1/2}$ state to the $5P_{1/2}$ state (see section 4.3.1), some Rb-electrons move from the $5P_{1/2}$ to the $5P_{3/2}$ state due to collisional mixing. While most of the Rb-electrons that decay from the $5P_{3/2}$ to the $5S_{1/2}$ state do so through non-radiative quenching (via interactions with the N_2), some small fraction will decay by emitting a photon, specifically a photon at ≈780 nm. These represented most of the photons detected by the photodiode. The current generated by the photodiode was fed through a PD amplifier[20] before being fed into a lock-in amplifier[21].

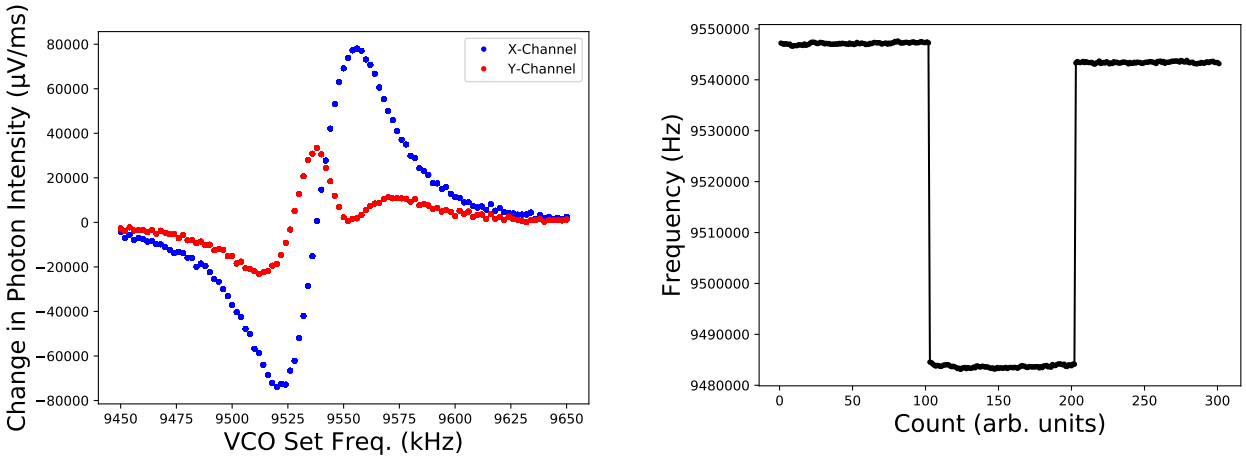

(a) A typical FM sweep.

(b) The well-shaped EPR frequency shift of ^{39}K.

Figure 4.16: The steps of an EPR calibration.

Next, we needed to know the energy splitting between the appropriate $4S_{1/2}$ hyperfine states; we wanted to know what frequency with which to drive a pair of coils (EPR RF field coils) in an effort to maximize mixing in the ground states of potassium which would in turn depolarize more Rb-electrons and allow more Rb-electrons to be excited to the $5P_{1/2}$, some of which would mix into the $5P_{3/2}$ state through collisions, thus increasing output of photons with $\lambda \approx 780$nm. I'll note here that we typically were interested in driving the the $m_f = -2$ to $m_f = -1$ transition in the F=2 hyperfine manifold, specifically, because K tends to be driven into the $m_f = -2$ state when we polarize the ^{3}He into the lower-energy state. To do this, we used a frequency modulated RF field driven by a voltage controlled oscillator (VCO)[22] and swept the EPR RF field frequency through the resonant frequency that corresponded to the energy difference between those two energy levels. At the same time we swept the EPR RF field frequency, we monitored the current coming from the photodiode atop the oven. The frequency

[20]PDA 200C, Photodiode Amplifier, Thorlabs, Newton NJ
[21]SR830 DSP Dual Phase Lock-In Amp., Stanford Research Systems, Sunnyvale CA
[22]Fluke 80, 50 MHz function generator, Fluke Calibrations, Everett WA

modulation came from a function generator[23] driven at 200 Hz and was fed into the previously mentioned lock-in amplifier. Referring back to figure 4.8, these are the yellow lines on the right side of the schematic. The result of this sweep was a plot showing the first derivative of the photodiode amplitude plotted against frequency (figure 4.16a).

The zero crossing on figure 4.16a marks the resonant frequency we were seeking. By setting the EPR RF field to this resonant frequency, we maximized mixing between the $4S_{1/2}$ hyperfine states, thus maximizing photon output from the target and maximizing our photodiode signal. At this point, we attached the PI box so the VCO would lock to the transition.

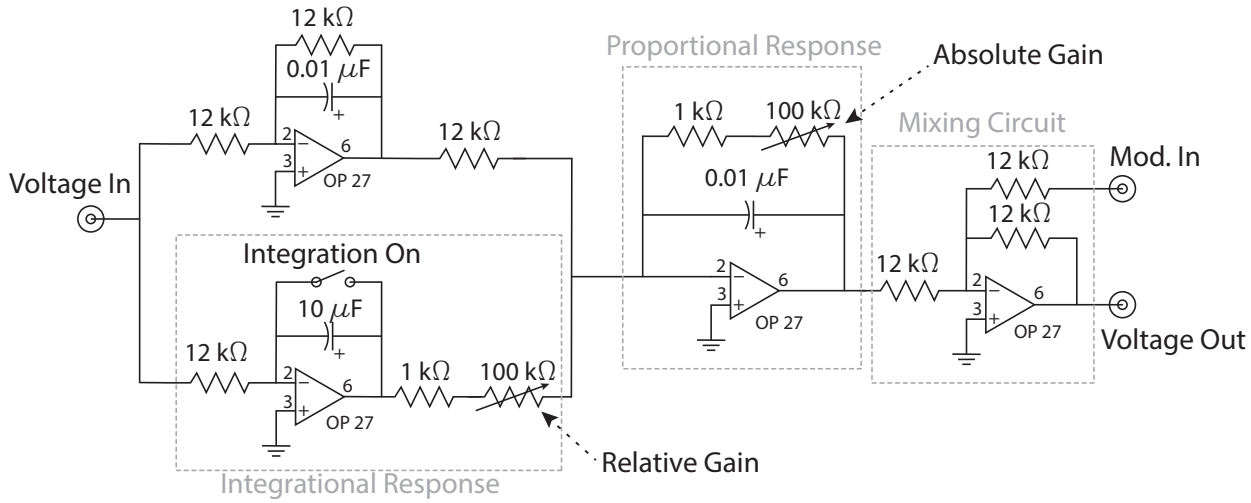

Figure 4.17: PI box circuit diagram.

In the penultimate step, we performed a spin flip while monitoring the frequency of the EPR RF field. Recall from section 4.3.5 that an AFP sweep was done by holding the RF field frequency constant and changing the holding-field strength (and thus the Larmor frequency of the ^{3}He spins). In this case, we needed to keep the holding-field strength constant, so we swept the RF field frequency from 60 kilohertz to 30 kilohertz and then (after a moment)[24] back to 60 kilohertz. This created a well-shaped plot (see figure 4.16b) where the top of the well was the frequency of the EPR RF field when the field due to ^{3}He polarization was aligned with the holding-field and the bottom of the well was the EPR RF field frequency when the field due to ^{3}He polarization was anti-aligned with the holding-field.

The shift in frequency is due to several factors. The obvious factor is the change in the total effective magnetic field cause by flipping the ^{3}He spin polarization and flipping it back. Less obvious contributions to the frequency change come from alkali-alkali spin exchange and frequency detuning of the pumping laser (caused by the changing ^{3}He polarization)[48][49], though both of these frequency shifts are of comparable size to the frequency shift caused by flipping the ^{3}He polarization. However, by flipping the ^{3}He polarization as we do, we significantly reduce their effect. The remaining frequency shift is proportional to ^{3}He polarization, ^{3}He density, and a

[23] Agilent 33250A, 80 MHz function / arbitrary waveform generator, Agilent Technologies, Santa Clara CA

[24] To be clear, "after a moment" here means we took 100 data points with the 60 kHz field, flipped the spins and took 100 data points at the 30 kHz field, then flipped the spins again and took 100 more data points at 60 kHz, yielding a clean looking well shape with lots of data points in each field strength.

dimensionless parameter, κ_0, which encapsulates our knowledge of the alkali-^{3}He spin-exchange cross section. The frequency shift seen in figure 4.16b actually relates to $2\Delta\nu_{SE}$ and with that in mind, we could relate our observed frequency shift to the percent polarization of the ^{3}He with the following equation taken from reference [49]:

$$\Delta\nu_{SE} = -\frac{8\pi}{3}\frac{g_e\mu_B\mu_{He}}{h(2I+1)}(1+\epsilon)\kappa_0[^3He]P_{He} \tag{4.12}$$

where μ_B is the Bohr magneton, g_e is the g-factor of the electron, h is Planck's constant, I is the nuclear spin, μ_{He} is ^{3}He nuclear magnetic moment, $[^3He]$ is the ^{3}He density, and P_{He} is the polarization of the ^{3}He gas. ϵ represents higher order terms which are proportional to powers of B, specific to the particular RF transition which is being driven (here, $m_F = -2$ to $m_F = -1$), and discussed further in [49] and [50].

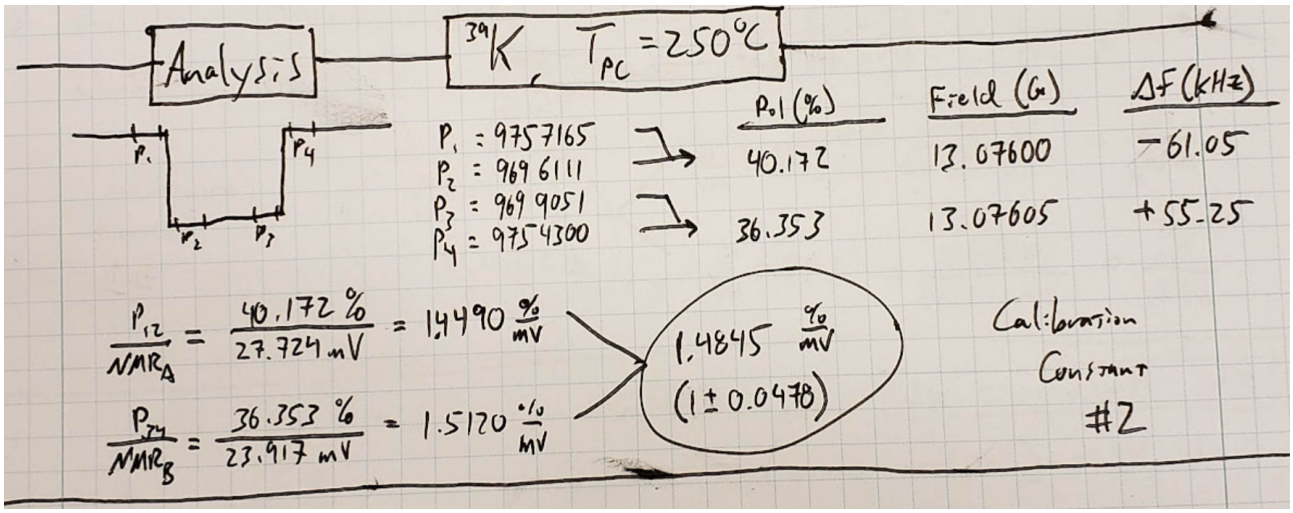

Figure 4.18: An example of a calibration constant using two NMR measurements (NMR_A and NMR_B) and two frequency shifts (P_{12} and P_{34}). Percent polarization, field, and frequency shift were calculated using equations found in [45], [48], and [49].

As the final step of our EPR calibration, we raised the holding-field back to its previous strength, the same strength we took our initial AFP measurement, and took one additional AFP measurement after the EPR spin flip. The end result of this entire procedure was two AFP measurements (in mV) and two spin flip measurements (ultimately in %). As you can see in figure 4.18, we divided the latter with the former; we divided the first AFP by the result from the sweep from 60 kHz the 30 kHz and the second AFP was divided by the sweep from 30 kHz to 60 kHz. We then averaged these two numbers. This yielded a single number with units of % per mV. This was a single calibration constant. We could multiply our spin-up data by this calibration constant to translate mV into percent of total ^{3}He polarization. However, this calibration constant was only good for these exact RF field settings. When we switched to a lower frequency field or changed the field strength, another calibration needed to be performed.

4.3.6 Simulated beam tests

In order to be useful, a target needed to maintain a high level of polarization even when faced with the depolarizing effects of the electron-beam at high currents. We can approximate the rate of spin relaxation in a cylindrical target with the following equation from reference [51]:

$$\Gamma_{Beam} = (n_a + n_m)\Gamma_i = (n_a + n_m)\frac{L\, I_b}{V\, E_{ion}^{He}}\left(\frac{dE}{dx}\right)^{He}$$
$$\Gamma_{Beam} = \left[\frac{n_a + n_m}{E_{ion}^{He}}\left(\frac{dE}{dx}\right)^{He}\right]\left(\frac{I_b}{A}\right) \tag{4.13}$$

where Γ_{Beam} is the relaxation rate due to the beam, Γ_i is the ionization rate per ^{3}He atom, n_a and n_m are the contributions to the ^{3}He depolarization due to the atomic ions ($^3He^+$) and molecular ions ($^3He_2^+$) produced by the beam interacting with the ^{3}He gas, L is the length of the cylindrical target, V is the volume of the cylindrical target (leaving A as the cross-sectional area of the target), I_b is the beam current, E_{ion}^{He} is the mean energy required to produce an ion pair, and $(dE/dX)^{He}$ is the energy loss per incident-beam particle *per* ^{3}He atom ***per*** cm^2.

Luckily, we can estimate the bracketed terms in equation 4.13 for our specific situation, namely a polarized electron-beam incident on polarized ^{3}He atoms. From reference [45] and [52]:

$$\Gamma_{Beam} = \left[5 \times 10^{-3}\frac{\text{cm}^2}{\mu\text{A hr}}\right]\left(\frac{I_b}{A}\right) \tag{4.14}$$

Comparisons to experimental data from both SLAC and JLab have shown this estimate is accurate to within 10-20%. And this equation would be all we need if our target were merely a long cylinder, but in our two chambered cells, some of the ^{3}He was obviously not in the target chamber. We can account for this by adding one more factor to the previous equation (again, from reference [52]):

$$\Gamma_{Beam}^{avg} = f_{TC}\Gamma_{Beam} = f_{TC}\left[5 \times 10^{-3}\frac{\text{cm}^2}{\mu\text{A hr}}\right]\left(\frac{I_b}{A}\right) \tag{4.15}$$

where the new factor, f_{TC}, is the fraction of the ^{3}He in the target chamber. Equation 4.15 gives us an estimate of the beam induced spin relaxation rate for the entire cell.

Looking back at equation 4.6, we already found the spin relaxation rate of an AFP measurement taken once per hour, Γ_{AFP}^{1hr}. We also have the relaxation rate due to the polarized electron-beam, Γ_{Beam}^{avg}. So, as long as we choose the appropriate sampling rate, n, we can simulate relaxation due to the electron-beam using our NMR system in the following way:

$$n \cdot \Gamma_{AFP}^{1hr} = (1\,\mathrm{hr}) \cdot \Gamma_{Beam}^{avg}$$

$$n = \frac{\Gamma_{Beam}^{avg}}{\Gamma_{AFP}^{1hr}}\,\mathrm{hrs} \tag{4.16}$$

where Γ_{Beam}^{avg} is the rate of relaxation due to the electron-beam as described in equation 4.15 and n is the aforementioned sampling rate.

4.4 Results

As emphasized earlier, the range of physics that is accessible using a polarized ^{3}He target is expanded as the figure of merit of the target is increased (eq. 4.1). The equilibrium polarization will always be limited by a competition between the rate at which ^{3}He nuclei are polarized and the rate at which they are depolarized, including depolarization due to the electron-beam. In Singh *et al.* (reference [53]) it was demonstrated that both alkali-hybrid mixtures and improved, spectrally narrowed lasers could greatly increase the spin exchange rate. Ultimately, target-cells utilizing AHSEOP are still limited by the rate at which gas polarized in the pumping chamber replaces gas depolarized by the constant bombardment of electrons in the target chamber. The convection designs shown in figure 4.1 and described in the lion's share of this chapter address that issue. We drove convection at such a rate as to maximize mixing between the chambers while not driving the alkali mixture out of the PC or driving the gas out of the PC before it can be polarized. With the rate of mixing sufficiently shorter than the rate of depolarization, the two chambers could be regarded as having the same polarization (hence no lag between the curves in figure 4.11a).

Target	Experiment	$\mathcal{L}^{eff}(\mathrm{T}_{op})$
Hunter	G_E^n-II	97.483
Windmill	G_E^n-II	93.307
Donya	G_E^n-II	86.370
Fringe	G_E^n-II	78.833
Dutch	A_1^n-II	68.129
Big Brother	A_1^n-II	62.325
Brianna	A_1^n-II / d_2^n-II	61.283
Fulla	A_1^n-II	57.668
Chicago	G_E^n-II	51.166
Tommy	d_2^n-II	40.989
Austin	d_2^n-II	39.908

Table 4.3: Effective luminosity at operating temperature, $\mathcal{L}^{eff}(\mathrm{T}_{op})$ (equation 4.1), for **target chamber** of all targets used in beam for the 2020 A_1^n/d_2^n experiments and the 2023 G_E^n experiment. FOM are in units of $10^{34} \cdot \mathrm{cm}^{-2} \cdot \mathrm{s}^{-1}$ similar to reference [53]. Scaling to operating temperature detailed in section 4.5 and figure 4.29 in that section.

The convection design also made it possible to scale up the size of the targets since gas mixing times were no longer limited by diffusion times. These larger convection-based targets, however, brought with them new issues, as detailed in section 4.4.3. As they say "mo volume, mo problems" or something to that effect (see reference [54]). Producing these targets was challenging and I try to capture here both the peaks and pitfalls of our journey creating better targets and, I think most importantly, what we learned in the process[25]. Whatever the issues

[25] I mean, it's science....it's all about what we learned along the way!

in production, the results described in this section demonstrate that the large convection-based designs enabled large increases in target figures-of-merit which ultimately leads to better *science*!

4.4.1 Characterization Results

Without further ado, I present characterization results for all 18 targets produced in service of the 2020 A_1^n/d_2^n measurements in table 4.4 and similar results for the 17 targets produced in service of the 2023 G_E^n measurement in table 4.5. Recall the design differences between these two groups of targets as explained in section 4.1. While all 35 targets in these tables were convection targets, A_1^n/d_2^n targets were the Bastille day design and G_E^n targets were the coat hanger design.

For a detailed description of the tests mentioned in this section, please refer back to section 4.3.5 for a spin-up, spin-down, or three point plot and section 4.3.6 for simulated beam tests. In the instances where the "experiment"("Kinematic Point") column in table 4.4(4.5) is left blank, these targets were never mounted at JLab and were not used in an experiment.

Target	Fill Date	D.Rate	Max/Adj. Life	Max Pol.	SBT	Exp.
		Hrs	Hrs	% or **mV**	% or **mV**	
Savior	2016-10-27	4	10.887(28)	40.145(253)		
Fulla	2018-09-07	2,4,8	17.254(144)	58.452(4.049)		A_1^n
Florence	2018-09-28	2,4,6,8	11.295(1.661)	44.802(48)		
Noah	2019-03-07	1	1.242(3)	**4.386(294)**		
Brianna	2019-03-27	8	19.889(27)	56.122(2.364)	53.849(139)	A_1^n/d_2^n
Sandy-II	2019-05-28	4	1.137[1]	25.287(125)		
Phoenix	2019-06-03	2	2.710(2)	27.411(1.223)		
Zoe	2019-08-07	2	0.989(7)	14.477(238)		
Dutch	2019-08-23	1,2,4,6	36.489(5.414)	53.930(609)	53.930(610)	A_1^n
Wayne	2019-08-31	1	2.556(6)	41.230(510)		
Tommy	2019-09-11	4	15.398(82)	59.192(648)	47.295(2)	d_2^n
Zhou	2019-09-27	1.5,3,6	9.840(29)	40.458(151)		
Big Brother	2019-10-22	2,4,8	25.063(816)	61.748(360)		A_1^n
Columbus	2019-10-23	4	4.188(10)	23.401(13)		
Austin	2019-11-08	1,2,4	19.909(401)	56.690(94)		d_2^n
Yixin	2019-11-25	4	10.104(48)	44.994(154)		
Butterball	2019-12-17	1,2,4,6,8	16.446(1.852)	56.136(114)	47.475(62)	
Chout	2020-01-13	1,4,8	9.175(21)	50.499(1.258)		

Table 4.4: Polarimetry results from tests performed at UVa for A_1^n targets as measured in the pumping chamber (PC). [1]There is no error on Sandy-II maximum lifetime as the single spin-down consisted of only two data points. D.Rate is the measurement rates for the multiple spin-downs that were used to find the adjusted lifetime or the single measurement rate which found the maximum lifetime.

Target	Fill Date	Rate	RF	Max Life	P_{laser}	RF	Max Pol.	JLab	Kin.
		Hrs.	kHz	Hrs	W	kHz	% or **mV**	%	
Talisker	2021-08-31	8	154.4	17.097(212)	80	154.4	**4.414(68)**		
Triveline	2021-12-17	4	154.7	1.302(20)	80	154.7	**8.551(9)**		
Ukraine	2022-03-23	2	154.0	6.323(20)	140	154.0	31.799(50)		
Autobahn	2022-04-25	4	154.0	1.491(38)	40	154.0	**8.341(413)**		
Tiger	2022-05-25	2	91.0	11.180(40)	140	154.0	53.566(379)		
Pristine	2022-06-07	2	91.0	12.781(18)	140	154.0	44.156(328)		
Hunter	2022-07-08	2	153.9	18.098(40)	80	153.9	48.275(272)	46.315	2, 3
Walter	2022-08-15	2	154.0	10.876(29)	155	154.0	42.140(30)		
Windmill	2022-09-15	2	91.0	30.426(15)	140	91.0	47.521(131)	49.803	3
Fringe	2022-10-20	2	91.0	28.343(24)	140	91.0	44.672(285)	55.926	4
Chicago	2022-11-09	2	91.0	8.752(12)	140	91.0	35.649(47)		
Mekong	2022-11-26	2	91.0	10.367(41)	140	91.0	44.325(89)		
Ginger	2022-12-29	2	154.0	3.857(11)	140	154.0	17.708(108)		
Christin	2023-04-21	2	91.0	26.079(59)	150	91.0	53.098(104)	48.831	4
Donya	2023-07-26	3	91.0	24.681(33)	135	91.0	47.269(419)	44.485	4
Barbie	2023-08-28	2	91.0	14.140(67)	100	91.0	37.817(3.338)		
Juna	2023-11-08	2	91.0	20.999(46)	70	92.0	45.497(29)		

Table 4.5: Polarimetry results for G_E^n targets as measured in the pumping chamber (PC). JLab results are preliminary as analysis is still ongoing. The rate and RF frequency listed in columns 3 and 4 were the settings which yielded the maximum lifetime in column 5. Similarly, the laser power and RF frequency listed in columns 6 and 7 were the settings which yielded the maximum polarization in column 8.

"Adj. Lifetime" is the mean lifetime of the target polarization (inverse of the relaxation rate) when adjusted to eliminate polarization losses due to AFP sweeps. This was calculated by making a three-point plot utilizing data from *at least* three spindowns with good mixing and no known technical issues. The reported adjusted lifetime was treated as the intrinsic lifetime of the target. "Max. Lifetime" refers to the longest measured mean lifetime during a single spin-down. It was not adjusted for AFP losses and is included in table 4.4 simply because, in some cases, the adjusted lifetime was smaller than what we measured on a single spin-down. As mentioned before, we discontinued three-point plots during the characterization of G_E^n-II targets, hence the only lifetimes reported in table 4.5 are maximum lifetime, not adjusted.

As to why the adjusted lifetime could be smaller than the lifetime that *included* relaxation due to AFP sweeps, there are several reasons. First, if there was poor mixing between the two chambers, we see an artificially high polarization in the pumping chamber. These lifetimes, though accurate for the pumping chamber, were not used when calculating the adjusted lifetime as our concern was adjusted lifetime of the entire target, which we can infer was the adjusted lifetime of the pumping chamber only if there was fast mixing between the chambers. Second, if tests were completed with different RF field settings, we see different losses due to each AFP sweep. A slower sweep may cause additional relaxation as could a stronger magnitude field and the opposite is true of both of those factors.

The final three columns in table 4.4 are the maximum polarization measured from a single spin-up, the saturation polarization found when simulating relaxation due to the electron-beam, and the experiment the target-cell was used in (if the target-cell was ever used in-beam). Results of our simulated beam tests (SBTs) closely matched NMR measurements taken at JLab while the targets were subjected to the electron-beam.

As you can see, some of these columns are missing from table 4.5 and results are also split between tests done with a high RF frequency (154 kHz) and a low RF frequency (91 kHz). Due to initially short lifetimes and ongoing issues related to the orientation dependence of our results (section 4.4.3), we abandoned three-point plots as they work best with longer spin-downs and taking multiple spin-downs in multiple orientations was too time consuming given the experiment schedule. A typical three-point plot during A_1^n/d_2^n involved taking three separate spin-downs at, say, 12-hour, 8-hour, and 4-hour measurement intervals and plotting the relaxation rate for each of those three spin-downs on an aptly named "three-point plot". At a minimum, a spin-down needs three data points to show a reliable measurement of the target's lifetime. For a 12-hour spin-down, that would take 24 hours (counting the first data point, then the subsequent other two). And ideally, we'd have *many* more data points than three. The spin-down in figure 4.11b was over a period of 48 hours. By the time we had reverted to an older method of determining losses per scan, I was no longer working in the lab. I mean, I have to graduate sometime, right?

4.4.2 Influence of Variations in Production on Characterization Results

Ever since I joined this group, I've heard anecdotal evidence about what dark rituals or pleas to the heavens one must perform in order to make a high quality cell. Here are just a few things I've heard over the years that I've been *assured* will affect target quality:

- Bake the target longer at a lower temperature.
- Bake the target shorter at a higher temperature.
- Mount the target on the gas handling system the *moment* you receive the target.
- Sacrifice a single graduate student to an eldritch god prior to mounting the target.
- Clean the gas *thoroughly* before it enters the target.
- *Do not* under *any* circumstances clean the gas handling system.
- Profanity. Use lots of profanity. Swear like a sailor freshly on shore leave.[26]
- If your glass blower smokes cigarettes, you get better targets!
- Remove *any* contaminants from your target before filling.
- Do not let your advisor, one Gordon D. Cates, into the lab for any reason.

My dear reader, only two of those were made up for comedic effect. I'll leave you to guess which ones[27].

These anecdotes have always always driven me a little crazy. We're *scientists!* Can we not *quantify* some of these effects?[28] I swore if I ever had time I would go back and see if any of the theories held any water. To that end, I scoured our gas handling system logs and present what information I could glean in figures 4.19, 4.20, and 4.21.

In each image, the y-axis is the maximum polarization for a target. Why maximum polarization rather than longest lifetime? Great question, dear reader! I could have just as easily used the lifetime of the target as a metric for "target quality" in these plots, but lifetime has become increasingly unimportant as we've moved away from diffusion targets; maintaining polarization for a significantly long period was less important when you can both polarize the gas more quickly with AHSEOP *and* move the polarized gas quickly from the pumping chamber where it's polarized to the target chamber where the interesting physics was going to happen. Thus, maximum polarization seemed a better metric for target quality in the post-diffusion era of ^{3}He target production. The x-axis relates to whatever production variable I was examining. I regret to inform you, dear reader, that I did not examine all the factors I mentioned above. These were the production variables that were most frequently mentioned by my colleagues. To be fair, I suppose that frequency is, ironically, also anecdotal.

Nevertheless, as you can see from figures 4.19, 4.20, and 4.21, there was no strong evidence to show that *any* of these once lauded variations in production could account for changes in

[26] As a former submariner, I can assure you that profanity was an intrinsic part of communication during an underway. It was my mother who had to remind me when I was freshly in port that most people don't use the f-word in place of filler words such as "um", "well", or "like".

[27] I'm sure one of them is pretty obvious unless, I don't know, the future has taken a *drastically* dark turn...

[28] The biggest hurdle in quantifying these effects is, from what Gordon once told me, due to what our group's primary goal is: providing high quality targets for experiments at JLab. That means we run on JLab's schedule and diving down interesting rabbit holes must necessarily take a back seat sometimes if we're going to do our part in these larger experiments. I am beyond ecstatic I had enough time to make this section and I truly hope it helps make *even better targets*!

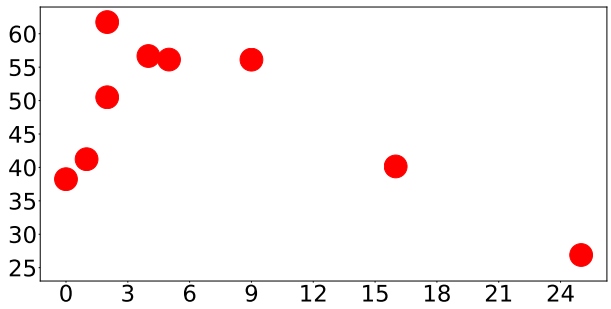

(a) Time from target receipt to assembly on the gas system (days)

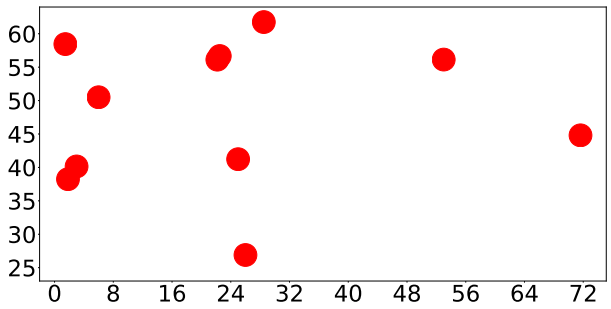

(b) Time from assembly on the gas system to beginning of the bake (hrs)

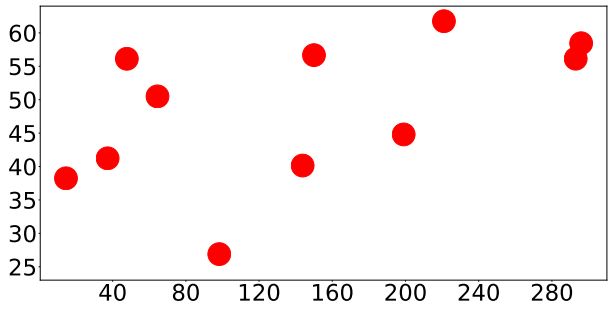

(c) Total bake time (hrs)

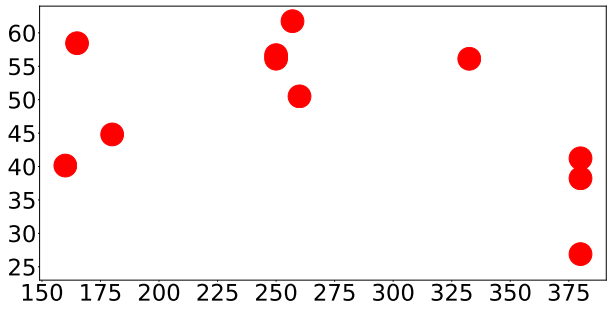

(d) Temperature of bake (°C)

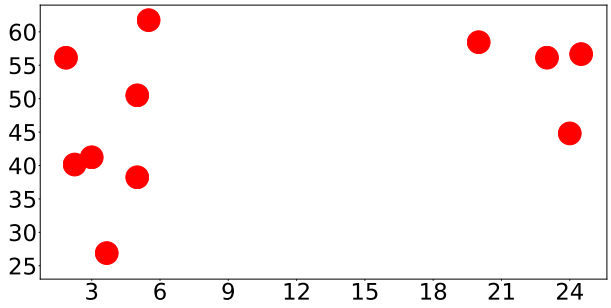

(e) Time from alkali chase to filling target (hrs)

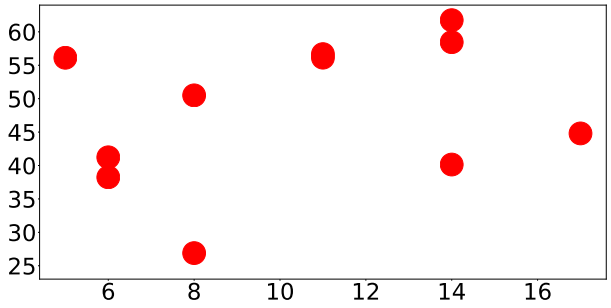

(f) Number of flame bakes

Figure 4.19: Variables in target production (x-axis) vs. max. percent target pol. (y-axis) for A_1^n/d_2^n

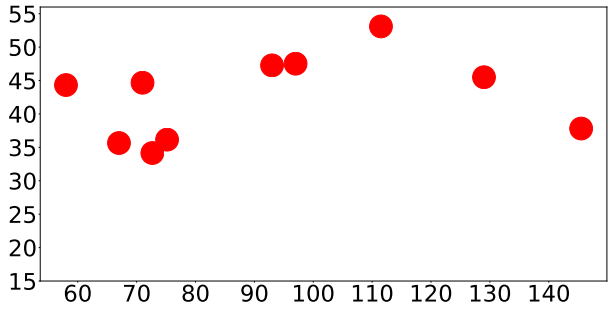

(a) Average total bake time (hrs)

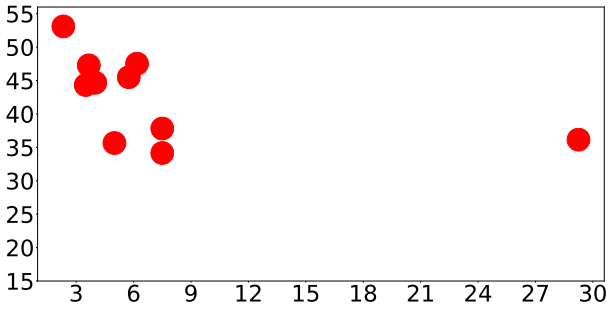

(b) Time from alkali chase to filling target (hrs)

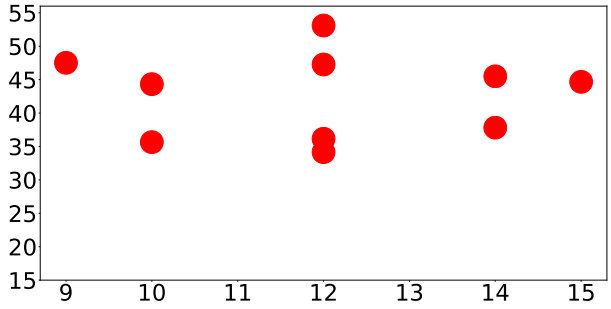

(c) Number of flame bakes

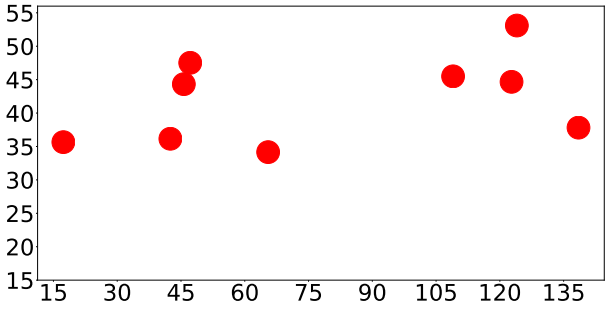

(d) Time from assembly on the gas system to beginning of the bake (hrs)

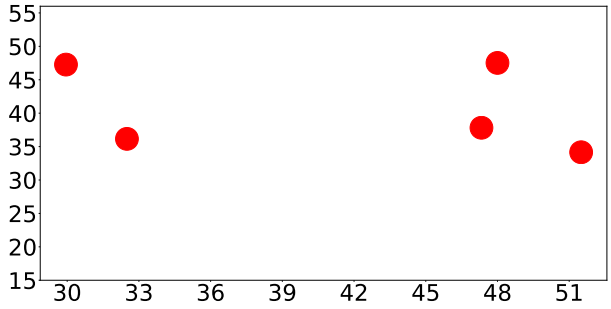

(e) Average O_2 bake time.

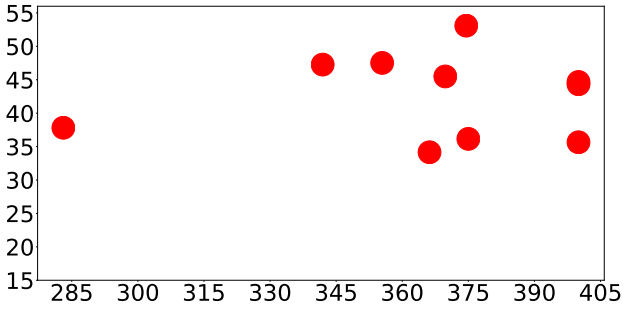

(f) Top temperature of bake (°C)

Figure 4.20: Variables in target production (x-axis) vs. max. percent target pol. (y-axis) for G_E^n at 91 kHz

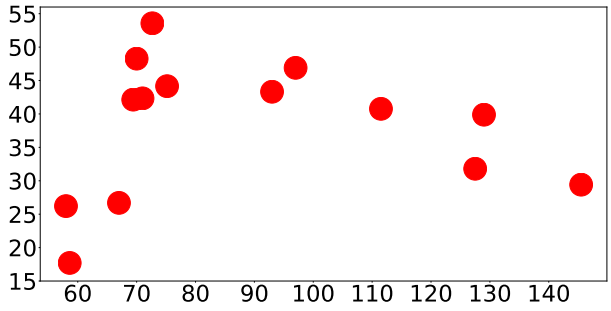

(a) Average total bake time (hrs)

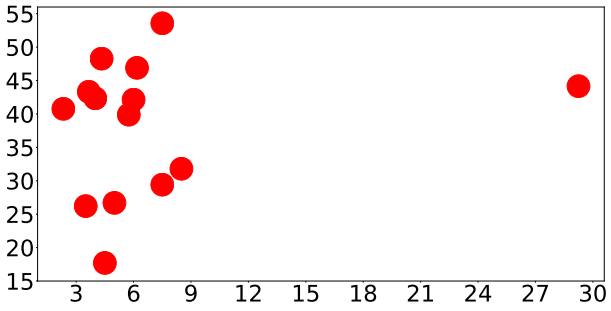

(b) Time from alkali chase to filling target (hrs)

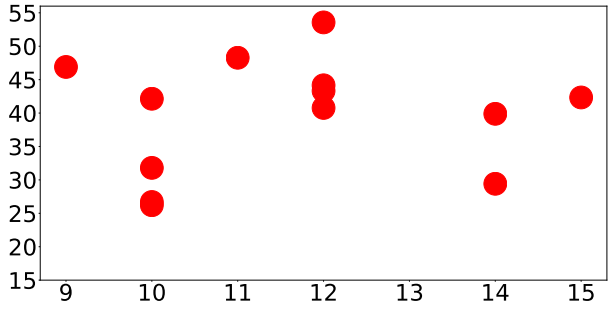

(c) Number of flame bakes

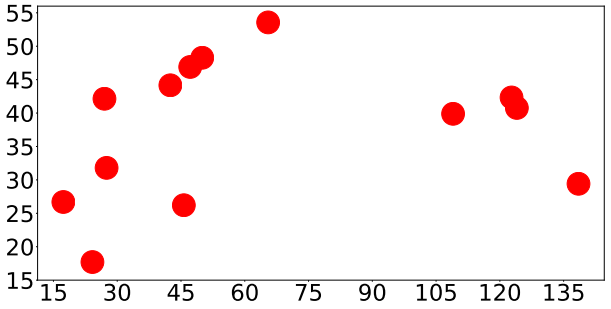

(d) Time from assembly on the gas system to beginning of the bake (hrs)

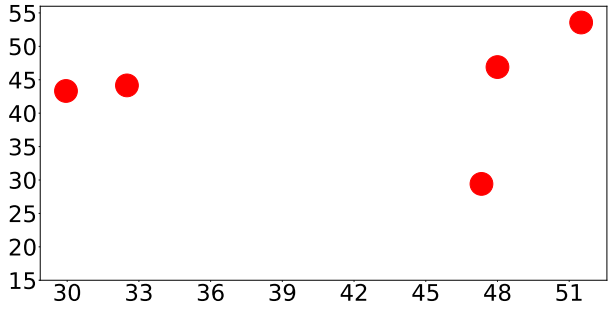

(e) Average O_2 bake time.

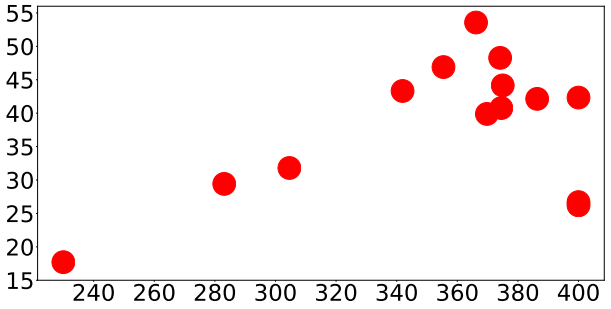

(f) Top temperature of bake (°C)

Figure 4.21: Variables in target production (x-axis) vs. max. percent target pol. (y-axis) for G_E^n at 154 kHz

maximum polarization. I've included the tables that make up this data in appendix A as tables A.2, A.4, and A.3, respectively. I have my reservations with fully trusting such a small data set, but I'll discuss that further in section 4.5

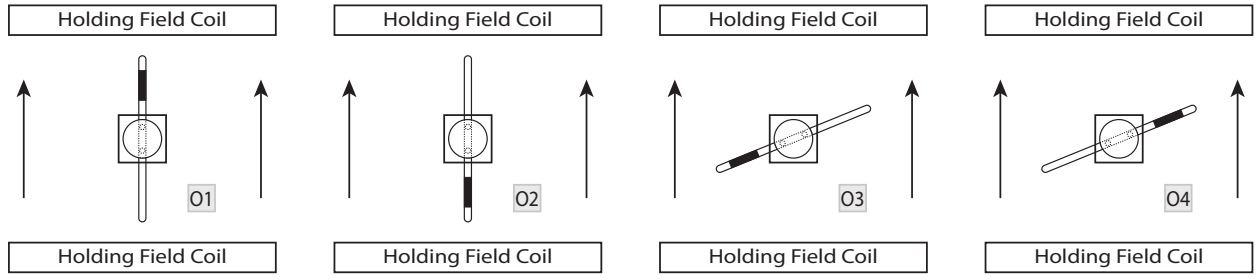

Figure 4.22: An explanation of orientations used in testing G_E^n-II targets at UVa (not to scale). The JLab system is similar to this, but not exactly the same. The arrow defines the direction of the holding field. The black box on the target chamber is an arbitrary indicator meant to break the symmetrical look of the targets in the diagram. Usually, a small paper name tag was affixed externally to the target, off-center, along the length of the target chamber. This was used to define final orientation O2(O4) from initial orientation O1(O3). The box around the pumping chamber is the oven, of course.

4.4.3 Directional Dependence of Maximum Polarization and Lifetime

During the A_1^n/d_2^n era, targets were mounted in the NMR/EPR system such that the target chamber was parallel to the holding-field. Although there was anecdotal evidence within our group to suggest that turning the target 180° would affect the polarization and/or the lifetime, not much care was taken to ensure the targets were always installed the same way. With the larger G_E^n targets, we began to see very prominent polarization and lifetime differences when installing the target for a second round of testing and we experimented with orientation of the target with respect to it's initial and secondary tests. We observed that after an initial round of tests, if we installed the target again rotated 180° from it's initial position, the lifetime was always longer (polarization was often higher, but many other factors can affect polarization, including fluctuating laser power, which was an issue).

Let's call the positions where the target was parallel or anti-parallel to the field the O1 and O2 orientations (see figures 4.22a and 4.22b). O1 and O2 are always defined such that O1 was the initial position where the target was parallel to the field and O2 was the position 180° from that initial position, anti-parallel to the field. We could also call O2 the "final" position and indeed I will in a few paragraphs. Realizing this effect was quite pronounced, differences between our system and JLab's system became much more important than during the A_1^n era and prior. So, I'll discuss those differences now.

The first difference was the target orientation with respect to the holding-field. While our targets were situated so the target chamber was parallel to the holding-field, G_E^n-II targets were mounted at JLab such that the target chamber was offset from that position by 67.8°. After retrofitting the base of our oven, our targets were now mounted with respect to the holding-field at the same angle as at JLab. These orientations will be further referred to as 03 and 04 for the initial and secondary (or final) positions at this offset (see figures 4.22c and 4.22d).

The second difference was the RF frequency and holding field strength we were using during

AFP measurements. Our field had a relatively high RF frequency at ∼154 kHz which corresponded to a holding field strength of 47.478 G (the field was swept from 38 G to 58 G). On the other hand, JLab was using a lower frequency RF field. Their field was set to ∼91 kHz which corresponded to a holding field strength of 28.055 G (the field was swept from 23 G to 33 G). We tested G_E^n-II targets using both a high RF field frequency and a low RF field frequency as reported in table 4.5. Even in the new configurations, there were still differences in maximum polarization between the initial and final positions.

One theory explaining the differences in polarization between the targets initial position (O1 or O3) and the 180° offset, final position (O2 or O4) was that we were creating permanent magnetization in ferromagnetic particles inside the glass itself. This could be due to microfissures in the glass which would allow ferromagnetic particles to get closer to the polarized gas. While we are not certain *precisely* what is going on, what we are certain of is that we consistently observe a hysteresis effect when running tests in the initial position, rotating the target, and running tests in the new position. The second (or final) position always shows better results. The RF frequency in the final position doesn't appear to be a factor either, as you can see in figure 4.23, which shows relaxation rates in the initial and final positions for the pumping chamber and target chamber. Additionally, rotating the target *again*, back to the original position, and running more tests does not seem to affect the results: we still see longer lifetimes in the final position rather than the initial.

These observations were not entirely without precedent. Jacob *et al.* [55] measured relatively small cells in two ways. One set of cells were tested immediately after being filled. The other set were filled, then exposed to a high field (greater than 1000 G), and finally degaussed. In each case, they then polarized the targets with SEOP and tested them in a 30 G field. Nearly all of their cells showed some degree of orientation dependence of spin relaxation. It's important to note here some key differences between the cells in reference [55] and ours. First, all of our targets are significantly larger. Jacob's cells were ≈50 mL whereas our cells are 9-12 times larger as you can see in table 4.1 and 4.2. Additionally, their targets were all made of Corning 7740 (Pyrex) whereas the majority of our targets were fabricated with GE-180 or Corning 1720, both of which are aluminosilicate glass.

Another set of cells reported on in reference [55] were made of GE-180 just as ours were, but were still much smaller than ours (their largest cell was "BamBam" at 327 mL) and much lower pressure (≈0.9 bar) per reference [56]. Ultimately, Jacob *et al.* concluded some portion of the permanent magnetization could be due to impurities in the glass or the Rb, due to the Rb itself, or due to a combination of these (and other) factors.

Work done by Ernst Otten and his group at Mainz confirmed the orientation dependence of a cell's relaxation rate (reference [57]) as well as showing the primary cause of relaxation was likely not the Rb in the targets nor the amount of Fe^{3+}-ions in the glass (reference [58]). More likely, they concluded ferromagnetic contaminants on or near the inner glass surface could be the cause of the hysteresis effect. While Otten *et al.* tested a variety of glass ranging from GE-180 and iron-free Corning 1720 to ordinary soda lime glass[29], their cells were, again, low pressure at approximately 1 bar. However, they did show as they increased pressure to 3 bars, there was an increased rate of relaxation (figure 3 of reference [57]).

[29]I loved this. They used *champagne* bottles. They took two green and two white glass champagne bottles, retrofitted their openings with a valve, cleaned the crap out of them, and turned them into ^{3}He containment vessels.

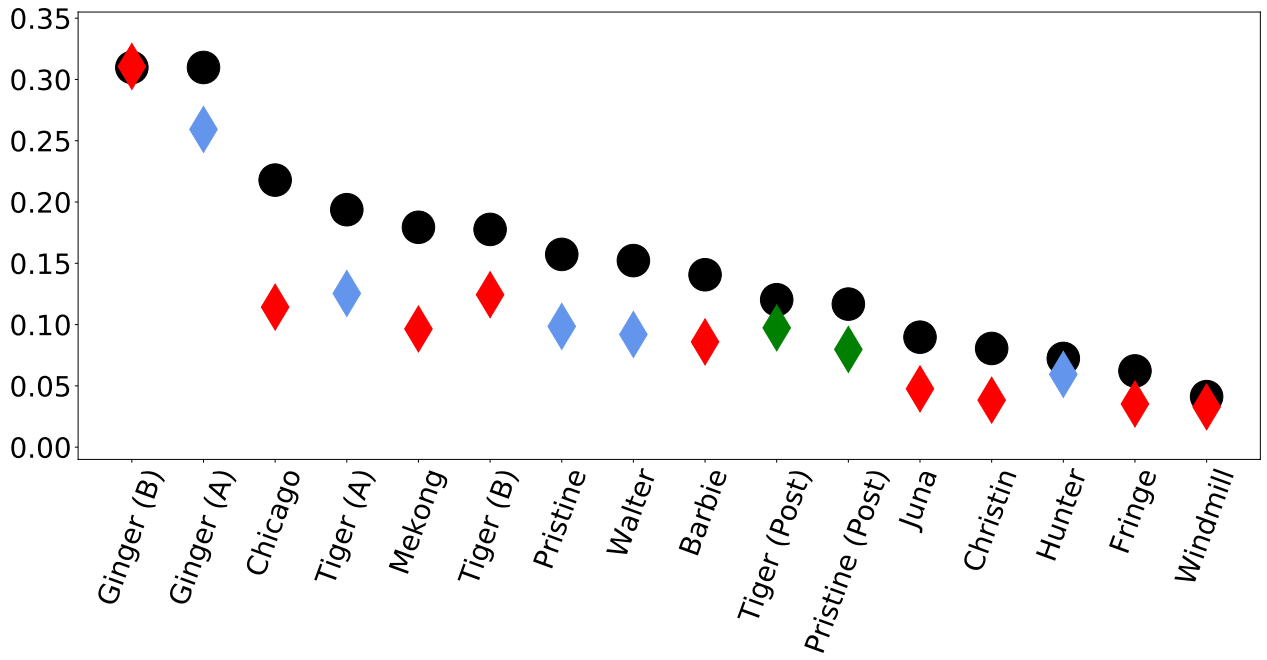

Figure 4.23: Relaxation rates, Γ, for the pumping chamber (above) and target chamber (below) in hr^{-1} for the initial (black circle) and final (diamond) positions. All spin-downs at initial positions were performed with RF ≈ 154kHz. For final positions, red diamonds indicate RF ≈ 154 kHz, blue diamonds indicate RF ≈ 91 kHz, and green diamonds indicate RF ≈ 91 kHz, though these green final measurements (and their corresponding initial measurement) were taken after the target was degaussed. Data used in making this figure can be found in table 4.6.

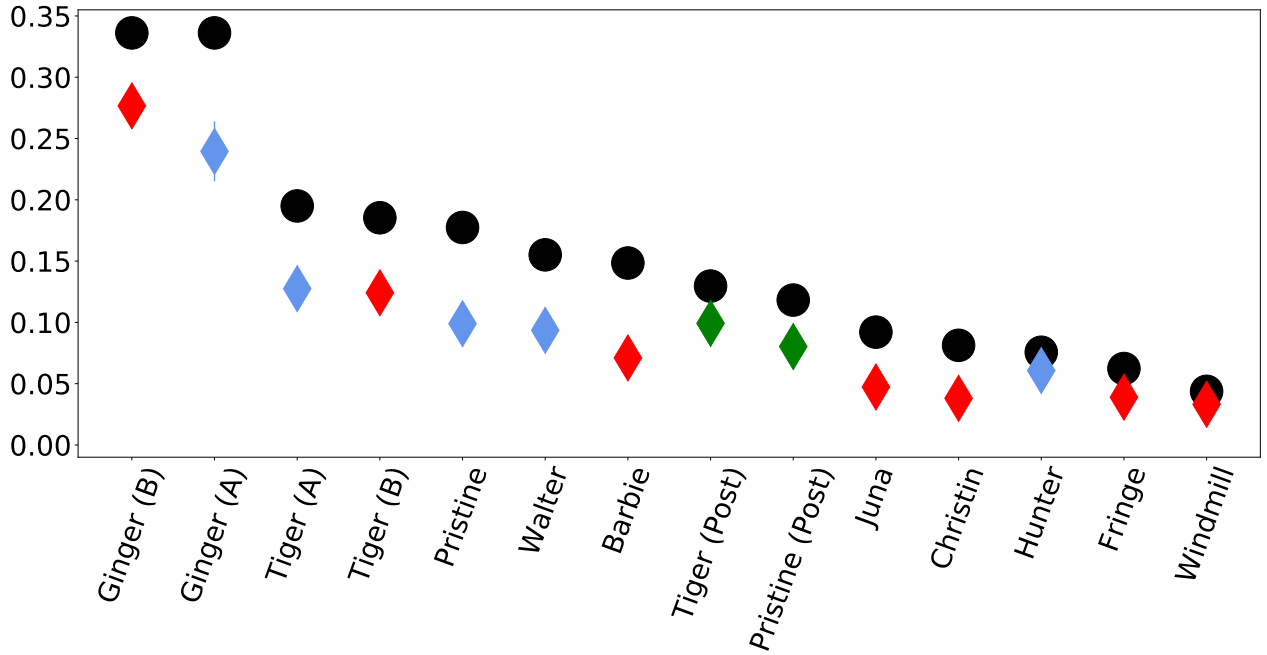

	PC		TC	
	Both positions RF = 154 kHz			
Target	Initial	Final	Initial	Final
Tiger (A)	0.19374(47)	0.12541(58)	0.19499(732)	0.12750(520)
[1]Pristine	0.15727(433)	0.09854(20)	0.17744(98)	0.09893(30)
[2]Hunter	0.07240(172)	0.05939(41)	0.07564(76)	0.06069(130)
Walter	0.15221(38)	0.09195(25)	0.15510(83)	0.09355(28)
Ginger (A)	0.30977(77)	0.25927(74)	0.33618(868)	0.23949(2406)
	Initial RF = 154 kHz, Final RF = 91 kHz			
[3]Tiger (B)	0.17765(20)	0.12439(88)	0.18536(735)	0.12413(500)
Tiger (Post)	0.12029(20)	0.09733(26)	0.12963(197)	0.09919(63)
Pristine (Post)	0.11672(30)	0.07976(29)	0.11820(62)	0.08029(66)
Windmill	0.04123(54)	0.03287(2)	0.04375(94)	0.03315(6)
Fringe	0.06220(29)	0.03528(3)	0.06235(31)	0.03894(44)
Chicago	0.21788(44)	0.11426(16)		
Mekong	0.17938(112)	0.09646(38)		
[4]Ginger (B)	0.30977(77)	0.31062(213)	0.33618(868)	0.27665(948)
Christin	0.08052(8)	0.03835(9)	0.08129(75)	0.03805(42)
Barbie	0.14067(356)	0.08589(223)	0.14844(479)	0.07099(1643)
Juna	0.08972(60)	0.04762(11)	0.09205(105)	0.04730(23)

Table 4.6: Relaxation rates in units of hr^{-1} for G_E^n-II targets in their initial orientation (Initial) and rotated 180° in their final position (Final). Error from multiple spin down measurements added in quadrature. (Post) indicates measurements taken post-degaussing. All data are from spin downs with convection on, taken consecutively, and with measurements at 2 hour intervals with the following exceptions: (1) Pristine's Initial is an average of 2 and 4 hour intervals, (2) Hunter's Final is an average of 1 and 2 hour intervals, (3) Tiger (B) Final is an average of 2, 4, and 8 hour intervals, and (4) Ginger (B) measurements were not taken consecutively. Ginger was measured in O3 at 154 kHz then O4 at 154 kHz, resulting in Ginger (A). RF was then lowered to 91 kHz, resulting in the Ginger (B) final measurement; both Ginger (A) and (B) share the same initial measurement.

Understanding the hysteresis effect was key to maximizing each target's potential. As we can see by examining the results in table 4.6, polarization was consistently higher once we switched the target orientation and the result was *not* due to the lowered magnetic field. The effect was also seen in both the pumping and target chambers, as we can see in figure 4.23. This was even true in targets like Pristine and Tiger which were exposed to all 4 orientations described in figure 4.22.

Recovering the Original Relaxation Rate Through the Magic of Television!

One final lesson learned from Otten *et al.* was a procedure to "reset" the target. In reference [58], it was shown the original relaxation rate of a target exposed to high magnetic field could consistently be recovered through a rigorous degaussing procedure, similar to how permanent magnetization was removed from cathode-ray tube screens in older televisions. In fact, Otten *et al.* began the process of recovery by purchasing and utilizing a commercial demagnetizer normally used for magnetic tapes (eventually upgrading to a larger, home-made demagnetizer). We adopted such a technique moving forward and attempted degaussing both Pristine and Tiger.

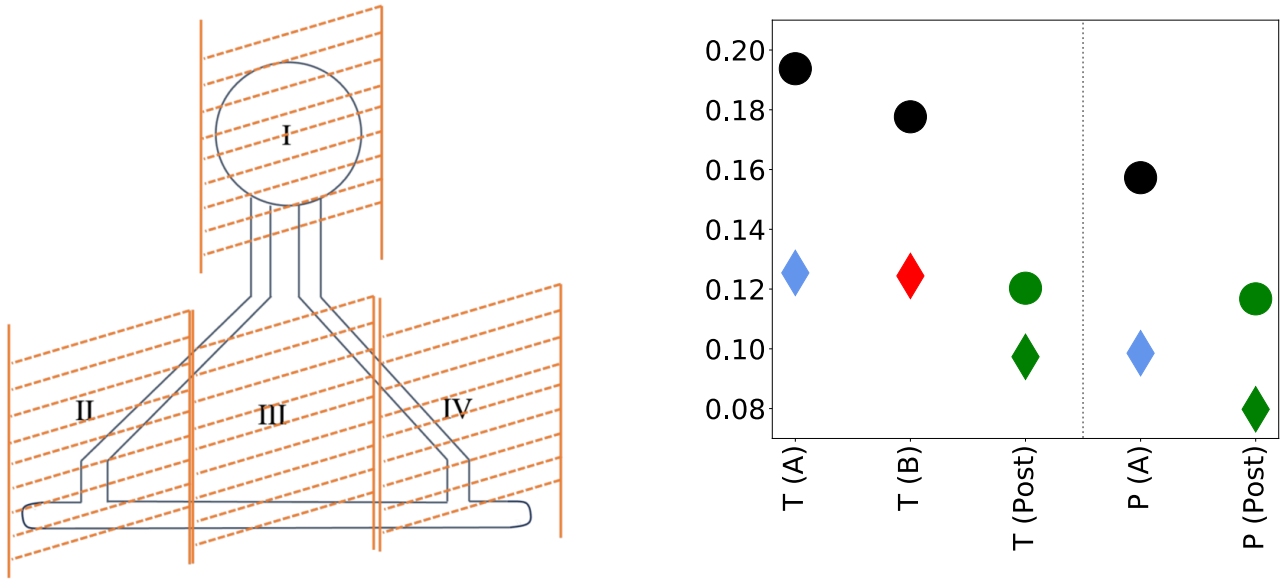

Figure 4.25: On the left, a description of the regions assigned during degaussing (image credit: Jacob Koenemann). On the right, Pristine (P) and Tiger (T) relaxation rates summarized from table 4.6. Circles are measurements in the initial position with RF $\approx$ 154 kHz. Diamonds are measurements in the final position. Red diamonds indicate RF $\approx$ 154 kHz, blue diamonds indicate RF $\approx$ 91 kHz, and green diamonds indicate RF $\approx$ 91 kHz. Green final measurements (and their corresponding initial measurement) were taken after the target was degaussed. Initial measurements for the post-degaussing data are colored green strictly for emphasis; these measurements were taken at RF $\approx$ 154 kHz as with all initial measurements described in this and the previous section.

After trying several different procedures, we settled on a protocol in which the targets were first degaussed using a Harvey-Wells electromagnet powered by a Walker Scientific, DC power source which could reach a maximum field of approximately 2500 G. The magnetic field was

small and could only accommodate a portion of the target at a time, so each of the regions described in figure 4.25 was treated in turn.

First, the region was placed in between the magnet's poles such that the center of the region was at the center of the magnetic field and the target chamber was aligned perpendicular to the field. Next, the magnet was powered up to a maximum field (≈2500 G) and held at that strength for 30 seconds. The magnet power was then reduced to zero over the course of 15 seconds by decreasing the current controlling the field by 0.2 A/s. Finally, the cell was removed and rotated 180° and the same region was again centered in the field. The field was brought to a field strength of ≈50 G less than the previous setting, increasing the field from zero to the new field strength at the same rate of 0.2 A/s. Again, the field was reduced to zero and the cell was reversed again, back to it's original orientation. This procedure of raising the field to ≈50 G less than the previous setting, lowering the field, and reversing the cell was repeated approximately 42 times at which point the last field the target was exposed to was $B < 0.1$ G. This was then repeated for the other three regions described in figure 4.25.

The target was then degaussed a second time utilizing a pair of Helmholtz coils in an apparatus built by Jacob Koenemann and Eranga Gunasekara, both of whom also developed the procedure for the Harvey-Wells magnet as well as this apparatus. This system could not reach as high a field as the Harvey-Wells Magnet, but unlike that system, this one operated at 60 Hz as it was powered by the AC power of the building. A similar but shorter procedure was followed as with the Harvey-Wells magnet. After the region was placed between the coils such that the TC was perpendicular to the field, the magnetic field strength was increased to it's maximum strength (541.4 G) over the course of ≈1s. The field was then held for ≈0.5s and then decreased to zero over the course of ≈1.5s. This procedure was then repeated for the remaining three regions.

As you can see from figure 4.25, degaussing both pristine and tiger decreased the relaxation rate for both the initial and final positions.

4.4.4 Metal End-Windows

Another thing we thought was going to be an issue for the targets of the G_E^n measurement was the integrity of the target-window under higher beam current. It was thought that just the sheer number of high-energy electrons being thrown at the paper thin, glass windows would cause the windows to overheat and eventually shatter. A reasonable concern, but one that was somewhat overcome[30] with a deeper study of the air flow across the windows and a *lot* of computational fluid dynamics calculations to maximize cooling with the same air system we used in previous experiments. However, I want to briefly detail here the work that was done in the development of metal end-windows in the interest of future target design and a possible solution to yet higher beam currents.

There were immediately two primary concerns with introducing metal to the targets. First, the oscillating RF field could produce eddy currents in any metallic, flat surfaces perpendicular to the field. Second, the metal windows themselves could induce relaxation through paramagnetic sites in the metal, contamination in the form of ferromagnetic material, or "Korringa

[30]What I mean by "somewhat overcome" is that, yes, we we able to get lots of good, usable data, but also most of our targets eventually exploded. Still, we got excellent data, so...success?

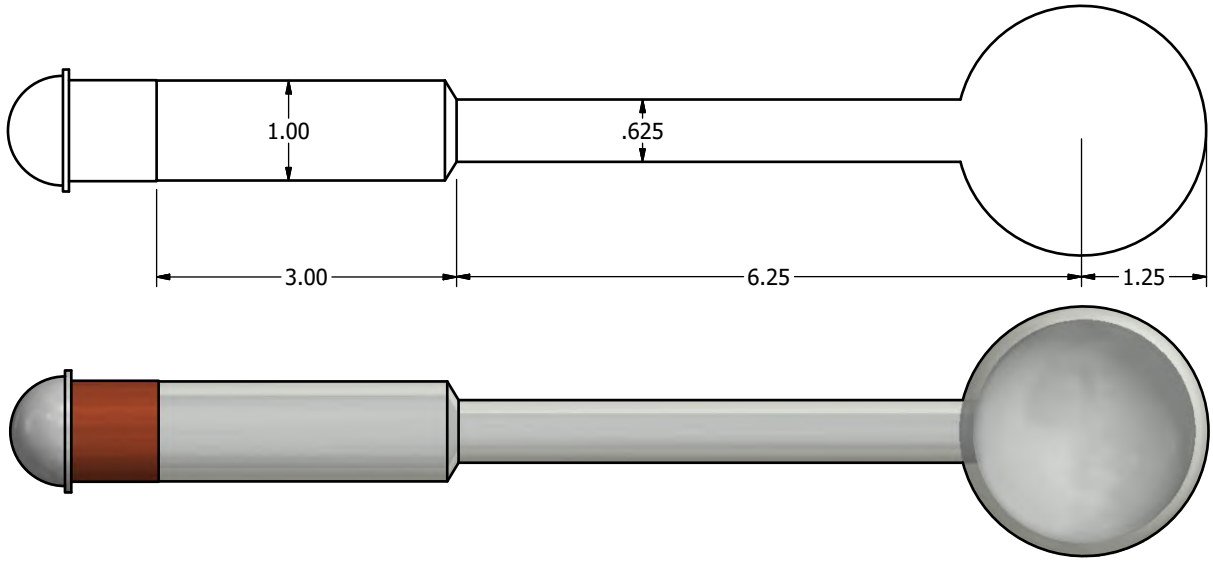

Figure 4.26: Design of a test cell (Lazarus) for the prototype metal end-windows.

scattering", where an electron in the conduction band undergoes a spin-flip[59] through a hyperfine interaction with the nucleus of a lattice atom. As it concerns our work, noble gases that are adsorbed onto the surface of the metal, even temporarily, could have a hyperfine interaction with the conduction band electron in the exact same way, depolarizing the atom. Prior work was done by Matyas *et al.* (reference [60]) studying the spin relaxation of ^{3}He due to gold, copper, titanium, and uranium glass (aka "Canary Glass"). They necessarily studied the interaction of these materials with both the ^{3}He as well as the alkali-metal vapor in the target. In addition to *that*, they also studied both Pyrex and the aluminosilicate-glass, GE-180, the glass used to fabricate the majority of our target-cells.

My time working on this project entailed expanding on the previous metal end-window design by Matyas *et al.* and the manufacture of two prototype targets: Lazarus[31] and Loretta[32]. They were tested using a pNMR coil wrapped around the transfer tube.

The target design was simple, as you can see in figure 4.26. The pumping chamber (PC) was spherical and approximately the same size as the A_1^n targets and the transfer tube simply positioned the metal window outside the oven. The glass-to-metal seals were commercially available "Houskeeper Seals"[33] made of copper and Pyrex (seen in figure 4.27c). The end-window was made of aluminum by William Fariss in our machine shop. The windows themselves were 0.005" (127 μm) thick (as you can see from the MK-I and MK-II designs in figures 4.27a and 4.27b, respectively). This was approximately the same thickness as the glass windows used in A_1^n/d_2^n targets, though it should be noted that the density was certainly different. Fariss attempted to create even thinner windows, but the process of making the windows so thin warped the 0.004" windows and punched a hole in the window when he attempted to size the

[31] Named after the biblical "Lazarus of Bethany" who rose from the dead, just as this target seemed to.

[32] Named after my grandmother, who would've been tickled by me getting a PhD, even if she didn't really track on what I was doing.

[33] Note: *Houskeeper* not *Housekeeper*. These were named for William Houskeeper, who invented them.

windows to 0.003". Fariss also trimmed the length of the copper tube to limit the total amount of metal in each target.

In the next step, we attached the two pieces. We couldn't heat the Houskeeper seal enough to simply weld the two pieces without destroying the seal, so we decided to connect the two pieces by electroplating them together.

The window and the copper piece with the Houskeeper seal were first sent to be electropolished to provide an extremely smooth surface to plate. This is a process in which the material is smoothed of all microimperfections to a tolerance below 1 mil (0.001") and often "an order of magnitude smaller" according to the Able Electropolishing website, the company that performed the electropolishing. The piece was submerged in an electrolyte, hooked to a positive DC source, and acted as an anode. A cathode was submerged as well and attracted the cations from the surface of the submerged piece. The window and copper-to-pyrex pieces were then sent to be electroplated.

Electroplating essentially works the same as electropolishing. The piece is again submerged in an electrolyte bath, this time filled with loose cations of the material that will comprise the plating. Copper can easily be plated with gold in this way, but aluminum is a bit more complicated. First, gold doesn't adhere well to aluminum. Second, the gold attacks the aluminum substrate creating a "galvanic reaction". The aluminum corrodes immediately. Adding a material between the gold and aluminum resolves both of these issues, creating an adhesion layer for the gold and protecting the aluminum from corrosion. The layer is usually comprised of nickel, which presents a problem for us as it is ferromagnetic. When a nickel plating cannot be used, a chemical film is applied to protect the aluminum during the gold plating process.[61]

The nickel used in the plating process was minimized, though I'm not sure if that means a chemical layer was added to the aluminum or just a very thin nickel layer. In either case, once the copper tube and aluminum window were plated in gold, the two pieces were connected by plating copper over the seam (see figure 4.28).

The initial design for the windows shown in figure 4.27a was meant simply as an end cap; the copper piece was unaltered save for electropolishing. A wide rim was added around the cap so it could be snugly fit onto the copper without needing to put pressure near the window itself. This was the design that was used in the production of Lazarus. Unfortunately, Lazarus leaked. We identified two possible sources of the leakage. The first possible source of leakage was the Houskeeper seal itself.

A likely culprit could have been the *fire*. I'm sure you're thinking, "Chris, why wouldn't you mention a *fire* before ***now***!?! Fires are generally bad when there's not *supposed* to be a fire!!!" Well, mostly for comedic effect, dear reader. Mostly for comedic effect. Here's what actually happened...

As discussed in section 4.2.2, the retort is removed during the filling process just after distilling the alkali (pure rubidium in the case of Lazarus and Loretta) into the reservoir (figure 4.3). The retort needs to be pulled away slowly in order to allow the glass to seal itself, to allow the constriction to, well, further constrict. If the retort is pulled away too quickly, a hole forms in the glass and atmosphere rushes in to fill the vacuum. That is what happened with Lazarus. There was an explosive re-compression of the target, allowing air and, more importantly, water vapor *in* the air to rush into the manifold and target. Distilling the alkali into the reservoir is

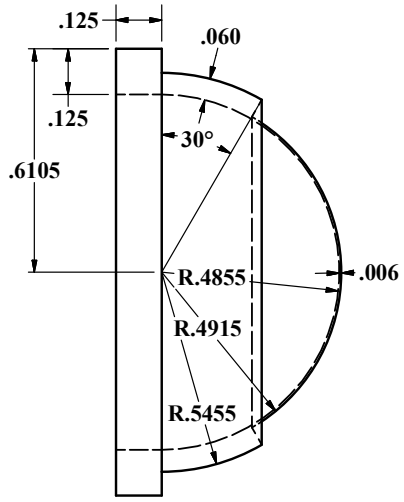

(a) The design for the "MK-I" end-window used when fabricating Lazarus.

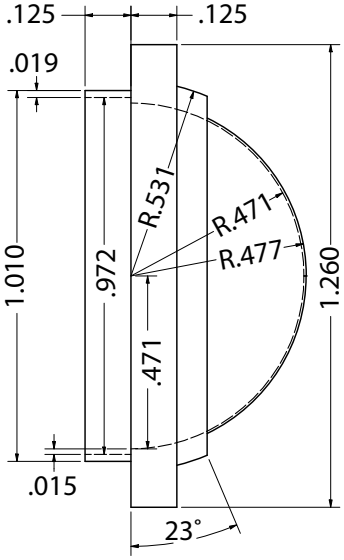

(b) The design for the "MK-II" end-window used when fabricating Loretta.

(c) Prototype MK-I (left) and MK-II (right) windows set loosely atop their copper tubes with a glass-to-metal seal. These units have been electropolished, hence their shine.

not exact and rubidium would have already made it as far as the pumping chamber. Not a lot of rubidium would be present in the pumping chamber, but what was about to happen does not take a lot of pure rubidium.

When the water vapor in the air reacted with the pure rubidium, the magic of chemistry transformed the water and alkali into hydrogen gas and an alkali hydroxide. The heat from the reaction ignited the hydrogen gas and flames spread through the entire target, through the manifold, and out the small hole in the glass, coating the entire interior of the cell and manifold in residue. This all happened in the briefest of moments and, honestly, it was quite something to see. Obviously, nobody was seriously hurt or I wouldn't feel I could make jokes about it. The only injury was to David Keder's pride as this was the first (and, to my knowledge, only) time he pulled the retort too quickly during the filling process. The target was cleaned, flushed with DI-water, dried, and given the name "Lazarus" before being re-attached to the gas handling system where it was successfully filled. The fire and rapid re-compression and resulting fire could have damaged the Houskeeper seal or the window.

The second possible source of leakage was from near the end-window itself. The electroplating may not have sealed the two pieces together properly or the polishing may not have removed all it needed to. Either process relied on a voltage gradient where the piece being worked on was either the anode or the cathode and as we know from freshman E&M, charges have a harder time gathering on the surface when there's an acute angle as the similar charges will repel one another. There were several 90° angles on the Mark-I end-window and the copper part of the glass to metal seal. Additionally, as you can see in figure 4.27c, the point where the

aluminum window and the copper piece were to attach was also a 90° angle.

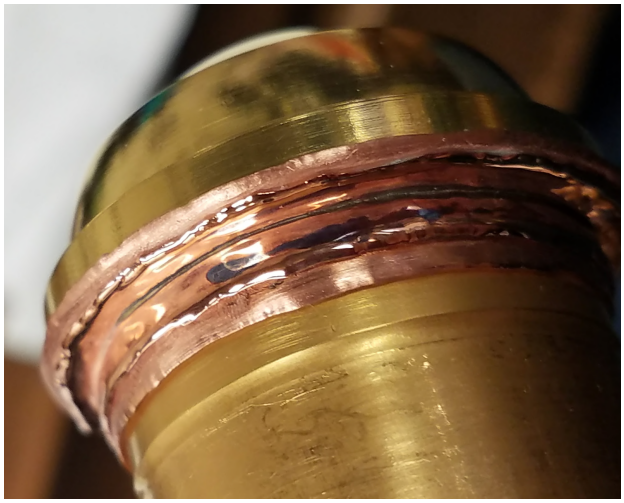

(a) The copper covering the joint between the plated copper and plated aluminum on the MK-I design (Lazarus). Visible is a small gap or stain near the center of the image).

(b) The copper covering the joint between the plated copper and plated aluminum on the MK-II design (Loretta).

Figure 4.28: Prototype MK-I and MK-II windows after being electropolished.

We attempted to fix the second issue with the next end-window design which incorporated a sleeve so the electroplated seal would be, ideally, across two pieces that were not at an acute angle from one another. The end-window for Loretta, a Mark-II design, was prepared in the same way as that of Lazarus other than the rapid re-compression and subsequent fire (because, as we know, fire bad). Again, there was leakage near either the copper seal, perhaps the Housmaker seal, or even the window itself. It was unclear. With both Lazarus and Loretta, generous amounts of epoxy were applied to the joint between the plated-aluminum window and the plated-copper end of the piece with the seal. Whether the leaks persisted or whether there was even still gas inside Lazarus or Loretta by the time they were tested was unknown. Gas exchange through the leak would have been slow and water vapor may have taken too long to reach the alkali metal for it's color to be an indicator; seeing the dull reflection of a hydroxide instead of the shiny reflection from a pure alkali would be an easy indicator that there was a leak.

4.5 Conclusions

By the most important metric, effective luminosity, target production during the 2020 A_1^n/d_2^n and 2023 G_E^n experiments was an extraordinary success. We provided unerring support for all three experiments and simultaneously shattered records regarding the luminosity FOM as you can see from figure 4.29. The technical achievements from these three experiments were challenging and represent huge leaps forward in the development of ^{3}He target-cells. The A_1^n and d_2^n experiments were the first to use convection targets and proved, without a doubt, the advantage of such a design. The target work done during G_E^n was pivotal not only in the success of the experiment, but in it's being able to continue! I wouldn't say we swooped in just in the nick of time to save everyone, because I'm *very* humble, but I will say we tried our best, we acted expeditiously, and we ably delivered quality targets in a timely manner[34].

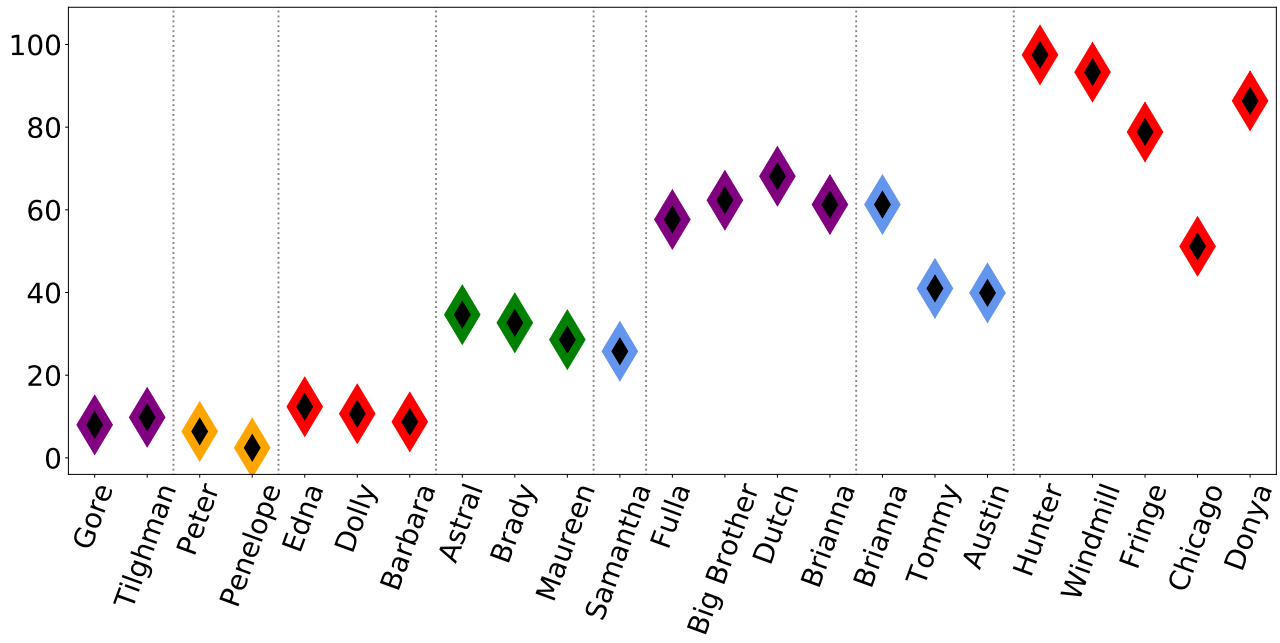

Figure 4.29: Luminosity in units of $10^{34} \cdot \text{cm}^{-2} \cdot \text{s}^{-1}$ from eight different experiments. Data (and sources) are summarized at the top of appendix A and in table A.1, but are taken from references [29], [45], [53], [62], [63], and [64]. Experiments here are color-coded: saGDH (orange), G_E^n-I and G_E^n-II (red), d_2^n-I and d_2^n-II (blue), A_1^n-I and A_1^n-II (purple), and Transversity (green). Note that the saGDH (orange) targets are Rb-only rather than a hybrid K-Rb mixture. Targets from Fulla (purple) and to the right of Fulla represent the experiments presented in this thesis. Targets to the left of Fulla are diffusion targets. All targets were used in beam and polarization results are from papers pertaining to their respective experiments.

4.5.1 Production Variables

I did not see any obvious correlation between any of the production variables discussed in section 4.4.2 and the maximum polarization of each target-cell. That said, if one were to

[34]...by swooping in and saving everyone and everything....because we're awesome.

suspend disbelief, they could imagine some of the plots in figures 4.19, 4.20, and 4.21 contained a pattern, particularly "Time from target receipt to assembly on the gas system" in figure 4.19, "Top temperature of bake" in figure 4.21, and "Average total bake time" in figures 4.20 and 4.21. Obviously, more data would be preferable and I hope one of my successors examines the production process closely in the future. There may yet be some magic method that does ensure a target turns out well...and hopefully without the need to sacrifice a graduate student to an eldritch god.[35]

4.5.2 Hysteresis Effects and the Merits of Degaussing

Having a deeper understanding of the hysteresis effect occurring in the G_E^n-II targets was crucial in delivering high-quality targets in time for the experiment, as I alluded to at the top of this section. Additionally, the work we began by degaussing both Tiger and Pristine shows strong evidence of the benefit of degaussing our targets. Indeed, both targets showed a significant decrease in relaxation rate (figures 4.23 and 4.25). I have no doubt that my successors will further explore the benefits of degaussing.

4.5.3 Metal End Windows

We were never able to successfully test a metal target-window. Additionally, leak checks for both test-cells were inconclusive. Although we were able to get a signal on Lazarus, we were never able to perform a spin-down. We couldn't even get a signal on Loretta. Tragically, all we are left with are speculations on what may have been the issues with these prototype windows.

There are myriad reasons one could use to explain why the metal end window test-cells leaked. Unfortunately, we do not know definitively where the design failed. I suspected intermetallic compounds, namely $AuAl_2$ or Au_5Al_2[36]. These compounds are brittle and less resistant to corrosion. They can even become porous (an effect known as "Kirkendall voiding")[65]. However, I don't believe the pieces reached a high enough temperature to create an amalgam. The lowest temperature at which an amalgam of these two metals forms is 575°C ($AuAl_2$) and I'm not sure when the pieces would have seen that temperature.

Another issue could be the amount of nickel (or chemical coating) used between the aluminum window and the gold plating. If the layer were too thin, perhaps there could be interactions between the two metals. Unfortunately, both of these theories also rely on an oversight by the good people at Epner Technologies and I have a hard time convincing myself the people that gold plate the Oscars[37] would make such an error.

A more likely culprit would be the Houskeeper seals, which are rated to 450°C. Again, nothing conclusive as the first window design had issues already addressed in section 4.4.4.

[35] ...I mean, unless that works. Should we *test* that? No, Chris. Just no. No morally dubious experimental techniques....never again...

[36] When looking into these compounds, I found the two most destructive compounds had fun names: "Purple plague" ($AuAl_2$) and "white plague" (Au_5Al_2) based on the colors they turn. Purple plague is used in jewelry making, apparently. Neat stuff!

[37] The Academy Awards of Merit, otherwise known as the "Oscars", are an award commemorating excellence in cinema. They are presented by the Academy of Motion Picture Arts and Sciences in the United States of America.

Chapter 5

Interferometry and Spectroscopy Measurements

I originally joined the Spin Physics Group with a singular goal: design and build a system to use laser interferometry and laser spectroscopy to characterize targets (the how and why of which comprise the contents of this chapter). Among other things, this system could be used to confirm the alkali density ratios inside the sealed targets as detailed in the latter half of this chapter, starting at section 5.5. This was a critical path item as the laser the group previously used for this work, a Ti:Sapphire laser, was no longer functioning. A new system needed to be built using new equipment...which was still in the box when I joined the group.

It's been seven years. I'm excited to finally present this work. Let's dive in.[1]

5.1 Interferometry: An introduction to window/wall measurements

In an ideal world, the electrons would smack the neutrons with nothing to get in their way. Polarize an electron. Polarize a neutron. Smash together. Reap rewards (well, data). Unfortunately, we don't have an isolated neutron. We also have several obstacles between our electrons and our neutrons and one of those obstacles is the windows into the target.

The glass windows of the target chamber were nearly paper thin (about 2-3 sheets of paper, to be specific). This was for two reasons. First and foremost, every collision adds heat. Thicker glass means more collisions and thus more heat. Eventually this results in windows shattering as discussed in section 4.4.4. They are also a parameter that needs to be accounted for in radiative corrections, though a minor one.

Our glass blower, Mike Souza, measured the thickness of the glass windows mechanically, JLab measured the target chamber walls using ultrasonic interferometry, and we measured them at UVa using laser interferometry. The minimally thin window could only be measured mechanically or using laser interferometry as ultrasonics would shatter them. Why use laser

[1] Is any of that important to you, the reader, who I suspect is reading this for the science rather than the commentary? Probably not for the sake of science, but *certainly* for the sake of a cohesive plot-line. Come on, I have to keep it a *little* entertaining.

interferometry when we're already measuring the windows mechanically? In a word: precision. In two words: crosscheck results. In three words: lasers are *cool*.[2]

5.2 Interferometry: Experimental Setup

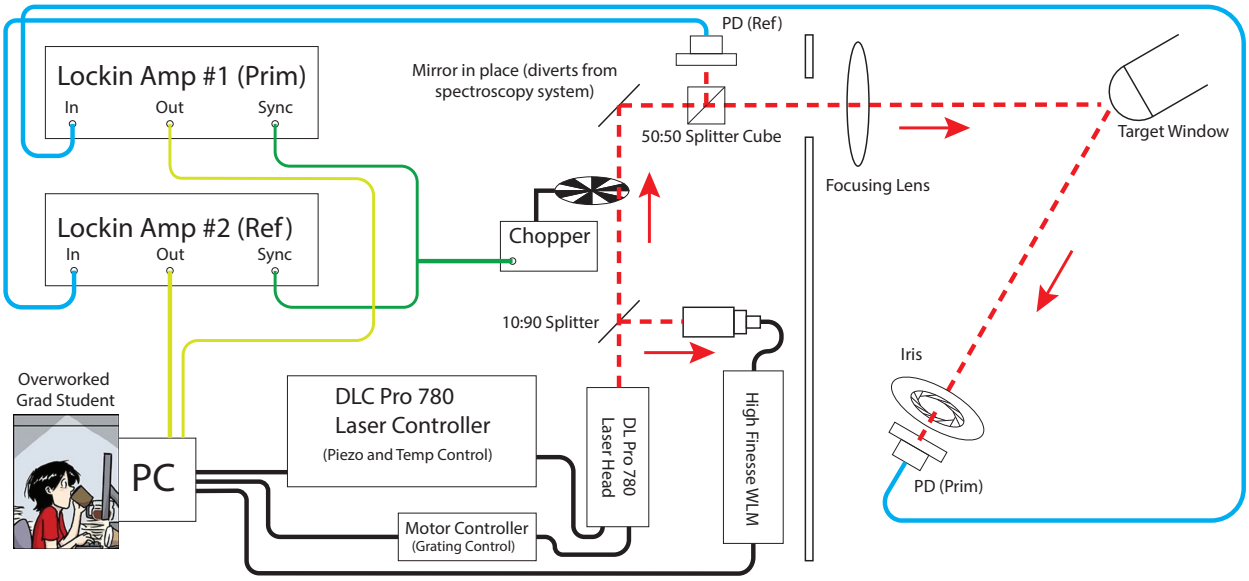

Figure 5.1: Experimental setup for measuring wall/window thickness. Grad Student Illustrated by Dr. Jorge Cham, Illustrator, PhD Comics (jorge@phdcomics.com)

Figure 5.1 is a diagram of the interferometry setup, but allow me to walk you through the path of the laser. Let's start with the diode laser head[3] or "DL". Connected to the head were the two components that controlled it. First, the motor controller[4] could make both coarse and fine adjustments[5] to the frequency by changing the angle of the grating inside the laser's resonance chamber. Second, ultra-fine adjustments to the frequency were made by adjusting the piezo voltage, the current (which adjusted somewhat automatically as the voltage changed), and temperature of the diode, all of which amounts to adjusting the length of the resonant cavity (essentially the distance between the diode and the grating). All of the ultra-fine frequency adjustments were controlled by the (conveniently named) diode laser controller[6] or "DLC". As temperature takes a long time to settle when adjusted even slightly, the temperature was kept constant so the frequency could be adjusted very quickly. The motor controller as well as the diode laser controller were both controlled via LabVIEW.

Coming out of the head, the beam was split by a 90:10 beam splitter[7] which picked off 1/10

[2]Is cool still being used as slang for "good"? If not, insert whatever new vernacular is appropriate.
[3]Toptica DL Pro 780, TOPTICA Photonics Inc., Farmington, NY
[4]Toptica DL MOT, TOPTICA Photonics Inc., Farmington, NY
[5]I understand one would normally call these all "course" adjustments, but the controller did have *two knobs* and these *were* the labels on said knobs, so this feels more accurate to say.
[6]Toptica DLC Pro, TOPTICA Photonics Inc., Farmington, NY
[7]1" Radius UVFS Beamsplitter 10:90 (R:T), Coating: 700-1100nm, p/n BSN11, ThorLabs Inc., Newton, NJ

of the beam power and diverted it to a focusing module[8]. The module sent the beam through a single mode, optical fiber cable and to the wavelength meter[9]. The other 9/10 of beam power continued on to an optical chopper[10], which blocked the beam in a periodic manner to provide a frequency for the lock-in amplifiers to focus on (I'll come back to the lock-in amplifiers in a moment). The chopper was set to a frequency of 347 Hz. This was done to avoid harmonics of the "mains hum" at 50/60 Hz as well as any other harmonics from a frequency below the 347 Hz threshold (347 is a prime number).

Next, a pair of mirrors[11] diverted the beam vertically and 90° from it's original path. This was done for two reasons. First, the targets were very tall. It made more sense to hang them upside down (as in figure 5.3) than to try and suspend them via the pumping chamber to take the measurement. The second reason was that this laser was also used for spectroscopy which will be discussed further in the latter half of this chapter (beginning at section 5.5). The first mirror that diverted the beam was also mounted[12] such that it could flip into and out of alignment with reliable accuracy (read: the beam wasn't diverted wildly each time the mirror was flipped into place). Given the option of using the mirror to divert the beam to either the interferometry or the spectroscopy setup, I opted to divert to the interferometry setup because the target would never be in the exact same place anyway; any small shifts to the diverting mirror wouldn't ruin a measurement.

Following the two mirrors, the beam reached a 50:50 beam splitter[13]. Half of the beam was diverted to a photodiode[14], which I'll refer to as the "reference signal". It's purpose will be discussed further in section 5.3. The signal from this photodiode was fed into one of the aforementioned lock-in amplifiers[15] and, from there, into the computer via a multifunction, I/O device that converted the analog signal from the lock-in to a digital signal.[16][17]

The half of the beam that was not diverted passed through a section of high grade, protective shielding. This shielding was made from found material consisting of a pressed pulp composite. This is a common reflection detection material which also acts as a buffer for stray beams. A hole was bore through the composite to create a laser throughput channel of approximately 4 in^2. The entire shielding unit was lightweight making the unit highly adjustable, though prone to unintended movement.

To be clear, the "shielding" was a used piece of cardboard I found sitting around the lab....just so we're all on the same page.

[8]Provided by Toptica

[9]WS-7, High Finesse, Tübingen, Germany

[10]Optical Chopper System with MC1F10HP 10/100 Slot Chopper Blade, ThorLabs Inc., Newton, NJ

[11]1" Broadband Dielectric Mirror, 750-1100 nm, p/n BB1-E03, ThorLabs Inc., Newton, NJ

[12]Kinematic Mirror Mount, p/n KM100, and Flip Mount Adapter, p/n FM90, ThorLabs Inc., Newton, NJ

[13]Frankly, I'm not sure if this was a non-polarizing beam splitter or a polarizing beam splitter. It was in the lab and unlabelled and *easily available* when I attempted window measurements for the first time and, might I add, on a *very* short deadline. I didn't realize my lapse until trying to describe this system in this thesis. However, I want to be as accurate here as possible, so I leave this footnote. This note continues in note 21.

[14]UDT PIN 10D, Photodiode, OSI Optoelectronics, Hawthorne CA

[15]SR510 Single Phase Lock-In Amplifier, Stanford Research Systems, Sunnyvale CA

[16]USB-6363 X-Series Data Acquisition (DAQ), National Instruments, Austin, TX

[17]Some would call this an ADC, but I'm going with what National Instruments calls it because it sounds *fancier*.

Immediately following the shielding, the beam reached a focusing lens. This lens had a focal length of 19.5", which determined the distance the window would be placed from the lens (or as close to that distance as possible). The beam was reflected off of the window at a very small angle, the reason for which will be discussed in section 5.3. In short, it simplified analysis.

The last stop for the beam was through a small iris and onto a photodiode which was identical to the reference photodiode. This photodiode was fed into a second lock-in amplifier[18] and, from there, fed into the computer via the same DAQ. I'll refer to this second photodiode as the "primary signal".

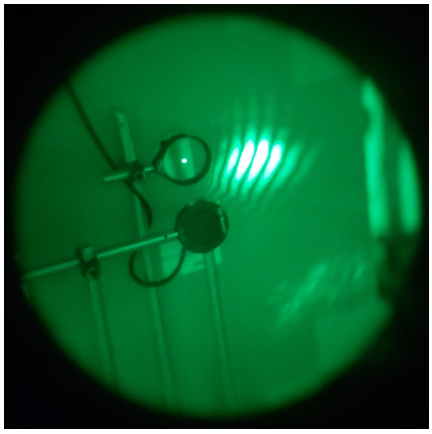

(a) An interference pattern on the high-grade-pressed-pulp-composite-reflection-detection shielding (the aforementioned used piece of used cardboard) as seen through an IR viewer.

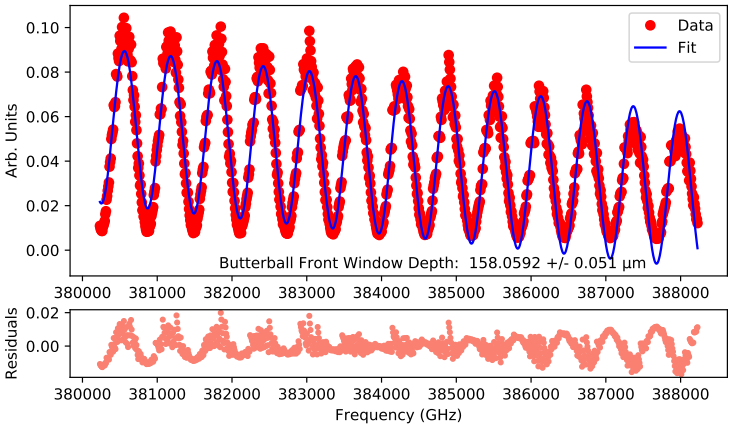

(b) Data from a window measurement of the target cell Butterball

Figure 5.2: Analyzing the constructive interference pattern of the reflected beam

"But Chris," you say, "What about the iris?" Ah, I can't sneak anything past you, dear reader! As this is interferometry, what we were looking at is an interference pattern (see figure 5.2a). More specifically, a *moving* interference pattern. The envelope, which is the roughly ovoid shaped pattern in figure 5.2a), stayed stationary. The pattern *within* the envelope appeared to move as the frequency changed, due to the varying amplitude of the interference fringes (which you'll see mathematically in equations 5.1 and 5.2). Essentially, if the frequency were changing, it would appear as though one were looking through a small porthole watching a line of fence posts go by.[19]

If the photodiode saw the reflected signal with both constructive and deconstructive interference lines, all we saw was noise. However, by using the iris, we could select a small pinhole of light from the constructive interference and watch the amplitude of that single interference fringe vary with frequency.

[18] SR530 Dual Phase Lock-In Amplifier, Stanford Research Systems, Sunnyvale CA

[19] Not an exact metaphor, but I think it gets the basic idea across.

5.2.1 Taking a Window Thickness Measurement

For A_1^n-II and d_2^n-II, targets were hung upside down to take a measurement (figure 5.3b) which consisted of a single scan for each window. This was later expanded to three data points along the horizontal plane: one center and one each about 5 mm away on opposite sides of the center. For G_E^n-II, windows were measured after being pressure tested, but before being integrated into a target-cell. This allowed for more robust window thickness measurements via laser interferometry. We scanned a central data point as well as eight additional points within a 5 mm radius of the central point (as seen in figures 5.3a and 5.3c). For the first coathanger design target-cells, the more robust measurements were important because we did not yet have a method for making uniformly shaped windows. Once we did, window thickness was measured mechanically only (read: not by me).

As you can see in figure 5.3c, the measurement positions were defined using cardinal directions as well as "center". Intermediate positions (between center and one of the cardinal directions) were defined as "center-direction". For example, the position directly above center is center-north. They were aligned to a handmade ruler, taped to an optics stand that was firmly secured[20] to the table and positioned such that beam aligned with the center mark (seen in figure 5.3a) for each axis. Measurements were taken by pointing the window towards either the center, the 2.5 mm mark or the 5 mm mark on the scale of the changing axis. The other axis would be kept at center for these measurements (i.e. if taking a center-north measurement, the horizontal angle of the window was pointing towards the center of the horizontal axis). The only other consideration in a window measurement was adjusting the position of the target such that the beam as reflected towards the iris.

5.3 Interferometry: Data Analysis

The first order of business in analysis actually happens during experimental setup: limiting noise. Of specific concern was the noise inherent in the beam. This was accounted for by splitting the beam into a reference and a primary signal. The paths of the two beams differed minimally. As you can see in figure 5.1, the beam split only after the WLM, chopper, and mirrors redirecting the beam. After the beam splitter[21], the reference signal went directly to a photodiode. The primary signal had a longer path. First, it travelled through a focusing lens, then reflected from the glass window before, finally, it reached the photodiode. By dividing the primary signal by the reference signal, we eliminated most of the noise inherent in the beam. There was still some noise because the two beams had traveled through different things. By minimizing the differences in the beam paths, we minimized those effects.

After that, analysis was shockingly simple. As discussed in section 5.2, we monitored the

[20] I often say it was "rigged for Sea-State 5", a relic from my time in the US submarine fleet. If I remember correctly, we rigged for Sea-State 5 when we passed under a hurricane, something I was "lucky" enough to sail under once. Bear in mind, we rigged for Sea-State 5 at greater than 600 feet (which isn't classified, so I can quote that number). Even that deep, we were rolling around quite a bit.

[21] Continuing on from note 13 of this chapter, the only effect in using a non-polarizing beam splitter versus a polarizing beam splitter would be the amount of noise left over after taking the ratio of the signals as described here. Fortunately, the signal-to-noise ratio was never an issue. Unfortunately, this meant my omission went unnoticed until now.

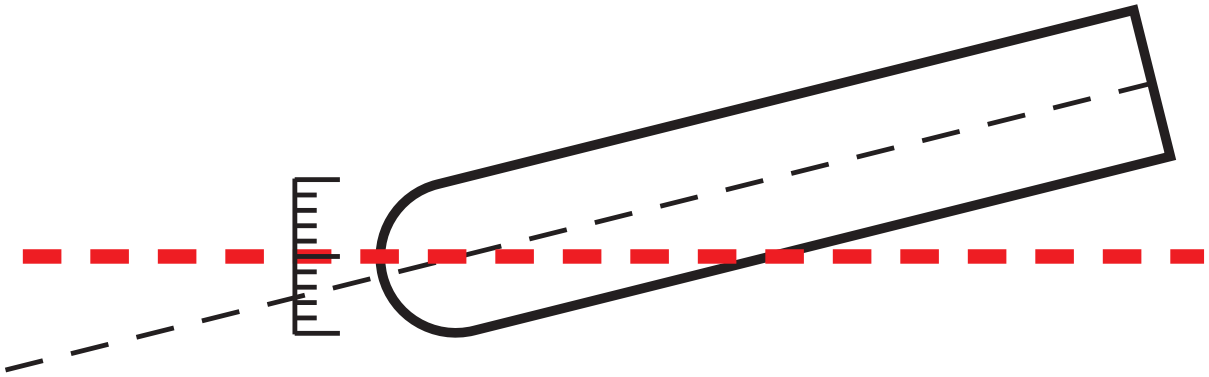

(a) Aligning a window for measurement (G_E^n-II target-cells). The scale was in mm and affixed (via tape) to a metal post usually used to hold optics. There was both a vertical and horizontal scale. This measurement is for an intermediate position between center (center-north, center-south, center-east, or center-west) with the front of the window pointing to the 2.5 mm mark. The horizontal axis would be positioned at zero for vertical measurements and vice-versa.

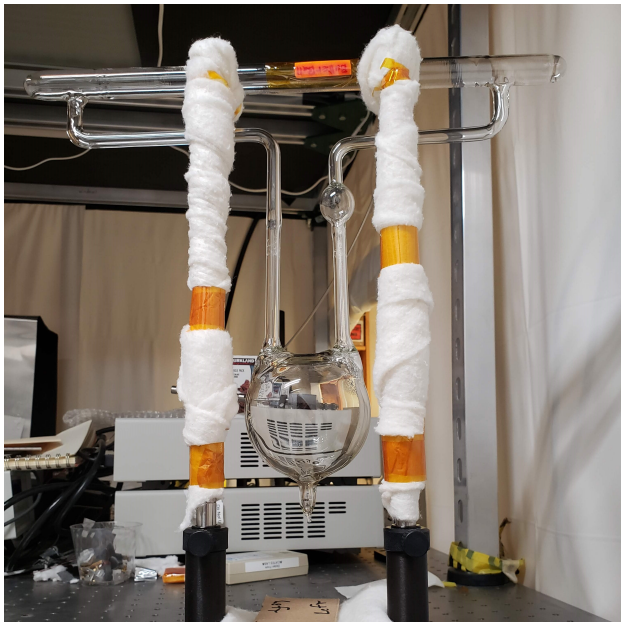

(b) Butterball, a Bastille Day design target-cell (A_1^n-II and d_2^n-II) hanging upside down for a window measurement. Window thickness was typically only measured in one position for these targets.

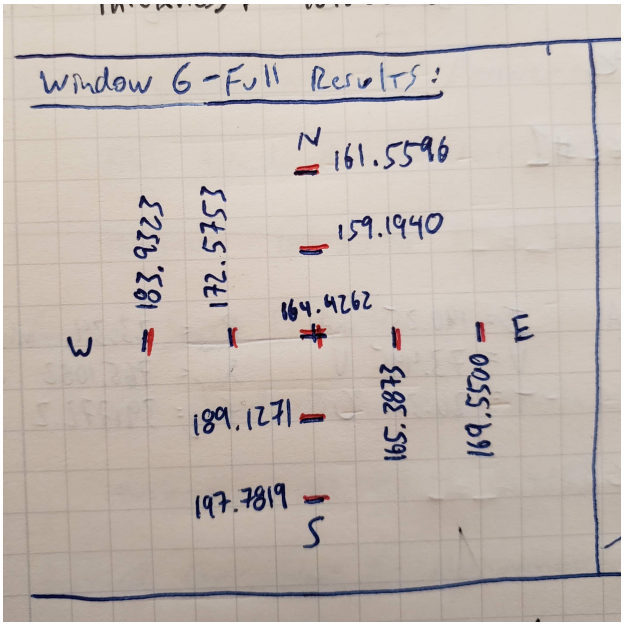

(c) A 9pt thickness map (in μm). This was a typical, early measurement of G_E^n-II windows, measured before they were integrated into a target.

Figure 5.3: Positioning a target for window measurements.

intensity of a singular interference fringe of reflected light. How that intensity varies with frequency is modelled in the following way according to page 282 of reference [66]:

$$R = \frac{F \sin^2(\phi/2)}{1 + F \sin^2(\phi/2)} \tag{5.1}$$

where F is the finesse and ϕ is

$$\phi = \frac{4\pi f}{c} d \sqrt{n_g^2 - n_a^2 \sin^2(\theta)} + \Delta\phi \tag{5.2}$$

where c is the speed of light in a vacuum, f is the frequency, n_a is the index of refraction of air ($n_a \approx 1$), n_g is the index of refraction of the glass, d is the thickness of the glass, and θ is the angle of reflection.

As I said previously, a small angle of reflection simplified the analysis and equation 5.2 shows us how. The second term under the square root goes to zero as the angle of reflection, θ, goes to zero. The center of the primary photodiode was 2.5" below the center of the focusing lens with the target at a distance of 19.5" from the focusing lens. This made the angle, θ, about 3.65°. It's a very minor contribution, but it's included in my analysis because computers are "fast but dumb", as my first CS instructor would often say; it doesn't take the computer long to factor in that $\sin^2(\theta)$ term.

According to reference [67], the index of refraction of GE-180 glass for 780 nm light is known to be 1.528, so measurements were taken over a frequency range centered around 384349 GHz (approximately 780 nm). For wall measurements, the scan range was traversed in 1 GHz steps and thickness was on the order of 1 mm. For window measurements, I used 8 GHz steps and thickness was on the order of 0.1 mm. The resulting data, plotted amplitude against frequency, varies sinusoidally (figure 5.2b). Scans were initially performed over a frequency range large enough to capture ten periods (approximately 1000 data points for each measurement), but this was extremely time consuming. The frequency range was reduced to capture only two periods and standard deviation for glass thickness remained under 1%: a massive reduction in time with minimal cost to accuracy.

5.4 Interferometry: Results

As I alluded to at the beginning of section 5.1, the thickness of the target chamber walls were generally measured in two different ways: JLab measured using ultrasonic interferometry and UVa measured using optical interferometry. Ultrasonic interferometry was sufficient for wall measurements, but would likely break windows. Additionally, errors due to electrons interacting with the windows could contribute errors to results for A_1^n-II and d_2^n-II as happened before in previous iterations of both these experiments, so higher precision was necessary for window measurements. Therefore, window measurements for A_1^n-II and d_2^n-II were made with the optical interferometry system at UVa, although some wall measurements were made at UVa as a backup to the JLab measurements (and to test the laser interferometry system out, as I had only recently finished building it).

During A_1^n and d_2^n, positions for window and wall measurements were defined differently for JLab and UVa. While I defined windows as "front" and "back", for instance, my counterpart

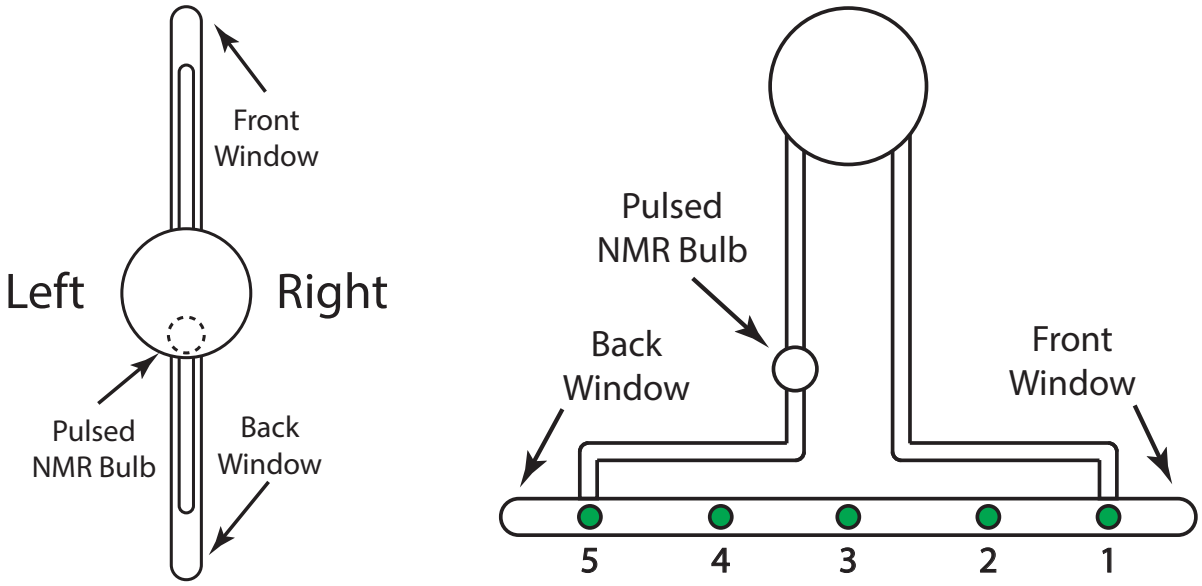

(a) Bastille Day - Top View **(b)** Bastille Day - Side View

Figure 5.4: Definitions of wall and window designations seen in A_1^n-II and d_2^n-II targets in this chapter. Positions along walls were designated by a side and a number position, i.e. L2 indicates the second position on the left side. Front, back, left, and right are assigned relative to the pNMR bulb.

Target Cell	Experiment	Window	Thickness (μm)
Fulla	A1n	Front	132.480(42)
		Back	139.191(66)
Brianna	A1n	Front	130.892(647)
		Back	127.969(243)
Dutch	A1n	Front	134.134(64)
		Back	143.469(69)
Tommy	d2n	Front	136.946(38)
		Back	145.100(53)
Big Brother	A1n	Front	138.188(59)
		Back	100.869(70)
Austin	d2n	Front	137.413(67)
		Back	156.192(130)
Butterball	d2n	Front	157.855(51)
		Back	145.133(45)

Table 5.1: Window thickness (μm) for A_1^n and d_2^n target-cells as measured using laser interferometry.

		L1		L2		L3		L4		L5	
Target	Exp.	Las.	U.So.	Las.	U.So.	Las.	U.So.	Las.	U.So.	Las.	U.So.
Fulla	A_1^n-II	1.42		1.37							
Brianna	A_1^n-II		1.42		1.45		1.51		1.50		1.50
Dutch	A_1^n-II	1.27	1.27		1.29	1.25	1.28		1.30	1.53	1.32
Tommy	d_2^n-II		1.45		1.48		1.51		1.48		1.56
Big Brother	A_1^n-II	1.55	1.53	1.50	1.52	1.49	1.53	1.48	1.53	1.34	1.51
Austin	d_2^n-II	1.43		1.29		1.33		1.32		1.43	
Butterball	d_2^n-II		1.63		1.53	1.53	1.55		1.56		1.59

Table 5.2: Target wall thickness (mm) for A_1^n-II and d_2^n-II target-cells measured with laser (Las.) ultrasonic (U.So.) interferometry. Laser interferometry measurements were performed at UVa. Uncertainty for laser interferometry measurements were on the order of 10^{-4}mm. Ultrasonic interferometry measurements were performed at JLab. Uncertainty for ultrasonic interferometry measurements are $\pm$0.05mm.

		R1		R2		R3		R4		R5	
Target	Exp.	Las.	U.So.	Las.	U.So.	Las.	U.So.	Las.	U.So.	Las.	U.So.
Fulla	A_1^n-II	1.38		1.49		1.48		1.43		1.35	
Brianna	A_1^n-II		1.30		1.35		1.33		1.33		1.35
Dutch	A_1^n-II	1.30	1.36		1.34	1.30	1.33		1.34	1.35	1.34
Tommy	d_2^n-II		1.38		1.27		1.27		1.26		1.34
Big Brother	A_1^n-II	1.39	1.41	1.38	1.41	1.36	1.41	1.41	1.44	1.37	1.42
Austin	d_2^n-II	1.39		1.32		1.33		1.32		1.52	
Butterball	d_2^n-II		1.54		1.32		1.43		1.41		1.52

at JLab defined those as "downstream" and "upstream", respectively. The wall positions were even more complex as JLab simply numbered them starting from the *upstream* end. Thus a UVa "L2" was a JLab "4" and a UVa "R1" was a JLab "10". For ease of comparison (and to save my own sanity), I've translated any JLab measurements discussed herein into the naming system I used at UVa. These positions are defined in figure 5.4.[22]

Table 5.2 shows a comparison between the ultrasonic wall measurements performed at JLab and the optical wall measurements performed at UVa. Measurement positions were aligned by hand in both optical and ultrasonic measurements and a reasonable error in position alignment for either would be up to 10 mm along the length of the wall. Considering this, results between the two methods agree reasonably well.

[22]For future reference, JLab's wall positions relate to UVa's wall positions in exactly the following way: JLab 1-10 is equivalent to L5, L4, L3, L2, L1, R5, R4, R3, R2, R1. Windows for JLab/UVa are upstream/back and downstream/front as defined in the text.

Target	Kin. Pt.	Label	Mech.	3-Pt	9-pt
Triveline		2-3	150.00	164.54(11.18)	166.05(3.46)
		2-6	149.90	174.33(13.54)	173.58(4.18)
A'bunadh		4-N	129.54	124.01(12.20)	126.76(3.86)
		5-J	143.51	150.24(4.65)	151.63(2.99)
Autobahn		6-X		126.45(5.22)	127.35(2.99)
Tiger		3-B	146.10	164.58(13.51)	161.25(3.78)
		3-D	139.70	142.37(13.42)	144.97(4.01)
Pristine		6-I	138.43	142.11(3.69)	139.50(2.25)
		6-VX	137.16	130.11(3.71)	129.67(2.17)
Walter					
		8-C		146.70(8.56)	148.56(4.45)
Windmill	3	10-I	160.02		
		10-B	147.32		
Fringe	4	10-A	139.70		
		10-L	132.08		
Chicago	4	12-9	133.35		
		12-5	134.62		
Mekong		13-III	133.35		
		13-IX	147.32		
Ginger		13-I	148.59		
		13-VIII	149.86		
"Vineland"		10-G	147.32	159.01(10.05)	160.67(4.75)
		10-H	154.94	148.83(57)	157.33(5.37)

Table 5.3: Window thickness (μm) for G_E^n target-cells as measured using laser interferometry. Mechanical measurements (Mech.) were performed by Mike Souza. The 3-Pt and 9-Pt measurements are the 3-point and 9-point measurements described in section 5.2.1.

For G_E^n-II targets, window measurements were measured mechanically by Mike Souza and, initially, we made laser interferometry measurements at UVa. The first G_E^n-II windows sometimes had varying thickness across the surface of the window, specifically the thinnest section which is where the electron beam would pass through, so these laser interferometry measurements allowed us to test the uniformity of the windows. As Mike Souza refined his process for making larger windows and the uniformity improved, the laser interferometry was discontinued as it was very time consuming.[23]

[23] I believe "Vineland" was renamed, though I could not find any record of what it was renamed as. It's entirely possible something catastrophic happened to Vineland as the target was filled after I left the group to focus on my thesis and I have no other data regarding that target.

5.5 Spectroscopy: Introduction to pressure broadening

There were many reasons we needed to know the exact amount of helium in a target because there were many reasons we needed to know the exact level of *polarization* in a target. As mentioned in chapter 4, we used absolute polarization to find a ratio of percent polarization to mV of signal when doing a spin up. Knowledge of the polarization of our targets was also critical for interpreting the data acquired during A_1^n-II, d_2^n-II, and G_E^n-II. In fact, during the 2001 run of A_1^n (A_1^n-I), the systematic errors due to target and beam polarization were the second largest contributor to total uncertainties in both $A_\parallel$ and $A_\perp$, clocking in at approximately 4.5%[14].

During the target filling process, we recorded a fairly accurate number for the ^{3}He density from the gas handling system, but a more precise way to measure the ^{3}He density (and one of the few avenues available to us once the target is sealed) was through laser spectroscopy. By observing absorption lines of rubidium (Rb) and potassium (K) in the target, we could find the density of the ^{3}He based on the width of the alkali absorption lines.

Measuring these absorption lines also served another purpose. We could find a relatively accurate ratio of the density of the two alkali metals in the target, as mentioned at the top of this chapter. While this was not important to the systematic errors in measurements of A_1^n, d_2^n, and G_E^n, we used this information to verify we had the best ratio of alkali metals in a target-cell to optimize AHSEOP.

5.5.1 Natural Linewidth and Doppler Broadening

Naively, one might expect spectral lines to be monochromatic owing to the discretized nature of atomic energy levels. In reality, absorption (or emission) lines are never strictly monochromatic. The simplest explanation for this comes from the Heisenberg uncertainty principle, $\sigma_E \sigma_t \geq \frac{\hbar}{2}$. The energy level and the lifetime of an excited electron cannot be known exactly. This uncertainty leads to a variety of different photon energies and thus different frequencies/wavelengths.

In the inertial reference frame where the atom is at rest, we observe a spectral intensity distribution for each line, $I(\nu)$, centered around a central frequency, ν_0. This distribution is called a line profile (figure 5.5) and follows a Lorentzian shape *in this frame*. We call the width we could observe in the frame where the atom is at rest the "natural linewidth". Outside of this reference frame (you know, where *we* live), the line profile is further broadened due to a number of mechanisms.

In the lab frame, the atoms are constantly in motion. As the atoms absorbing the light move toward or away from the light source, the atoms experience the Doppler Effect; the frequency is shifted in the rest frame of the atom, giving a broader range of frequencies in our line profile. The full width at half maximum (FWHM) of this broadening, called "Doppler broadening" is temperature dependent, as is expressed in the following equation from page 85 of reference [68]:

D-Line	Natural Line Width	Doppler Width
Rb D1	0.005750	0.564
Rb D2	0.006067	0.575
K D1	0.005956	0.861
K D2	0.006035	0.865

Table 5.4: Natural line width and Doppler width (in GHz) for applicable rubidium (Rb) and potassium (K) D-Lines. Doppler width calculated for $T = 373K$

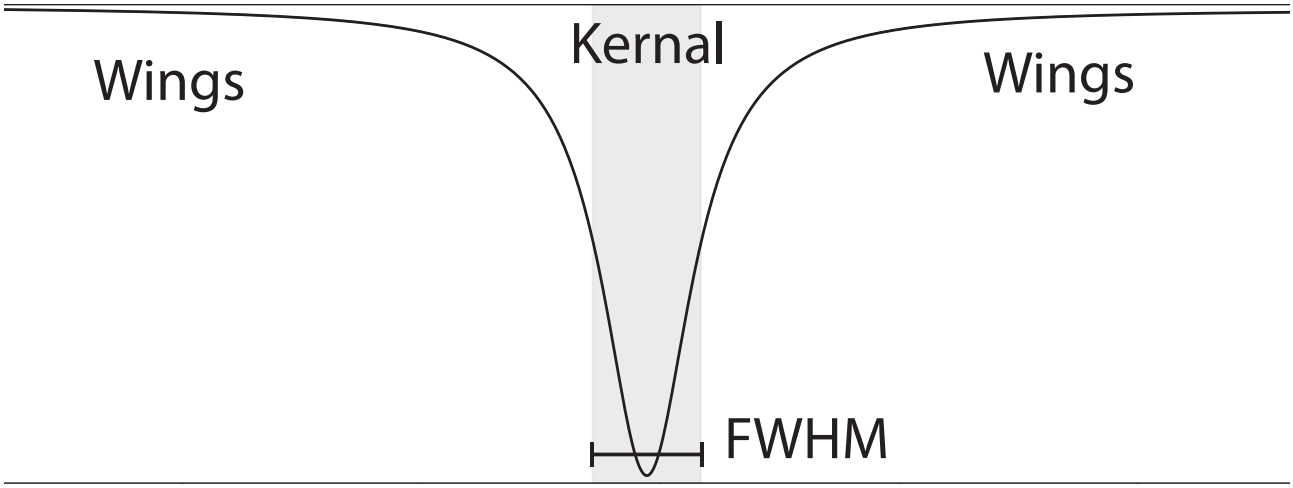

Figure 5.5: A pressure broadened line profile. The shaded area is the kernal. It is the width of the FWHM and centered on the central frequency, ν_0. The remaining portions of the line are the wings.

$$\gamma_D = \nu_0 \sqrt{8kT \ln 2/mc^2} \text{ [Hz]} \tag{5.3}$$

where ν_0 is the central frequency of the absorption line, k is the Boltzmann constant, T is the temperature in Kelvin, m is the mass of one atom of the element, and c is the speed of light in a vacuum.

To complicate matters, the intensity profile for Doppler broadening follows a Gaussian shape. As the Doppler width is several orders of magnitude larger than the natural line width (see table 5.4), the contribution from the natural line width is obscured. To account for both natural line width and the Doppler width, we can use a convolution of a Gaussian and a Lorentzian lines to describe the shape of the line profile. Information about the Doppler width can be extracted from the Kernal, where the Gaussian is dominant, and information about the natural width can be gleaned from the wings, where the Lorentzian dominates. This convolution is called a Voigt profile.

In reality, both the natural line width and the Doppler width are so small (compared to the broadening mechanism of interest) that we can generally ignore them. The FWHM for our broadened absorption spectra are on the order of approximately 80-120 GHz. As you can see from table 5.4, the natural line width is insignificant at this scale and even the Doppler width is much smaller than our FWHM.

5.5.2 Pressure / Collisional Broadening

The broadening mechanism of greatest interest to us is pressure broadening a.k.a. collisional broadening. The pressure for most of our production targets was about seven or eight atmospheres before we heated them and even greater after they were heated (due to the ideal gas law, $PV = Nk_BT$). During pressure broadening, the atoms are colliding with one other. Elastic collisions shorten the lifetime of the excited state (causing broadening) and inelastic collisions cause a shift in the excited and ground state energy levels proportional to the distance between

the two atoms colliding [68] (causing a shift in the center of the line profile). The line profile is still relatively Lorentzian, but an asymmetry is introduced because the transition probability now depends on the internuclear distance. Want to hear more about this asymmetry? Would you like an equation ridden discussion of collisional broadening? All that and more awaits you in section 5.7.

5.5.3 Additional broadening mechanisms

There are a number of other broadening and narrowing mechanisms that I could mention here, but I would simply be regurgitating reference [68]. Something more than the broadening and narrowing mechanisms I've already mentioned here is definitely at play, as you'll see in section 5.8. Truth be told, I didn't learn about most of these additional broadening/narrowing mechanisms until I was trying to find the source of an unexpected trend that permeates all of my results and that appears both internally consistent and consistent with previous pressure broadening measurements from our group *and* the group at William & Mary.

Foreshadowing, right? I *know*! Very annoying. If you'd *really* like to skip the suspense, jump to section 5.8. But look: there's a whole lot of good stuff between here and there and (with all due respect, dear reader) if I could wait these many years to tell this tale, I believe you can wait a mere two sections. I believe in you. Let us "Be Calm and Carry On".[24]

5.6 Spectroscopy: Experimental Setup

Before I walk you through the illustration of the spectroscopy setup (figure 5.7), let me first point out this system used the same laser[25] as the interferometry system. As mentioned in section 5.2, there was a mirror that was flipped into position to divert the beam in order to take a window or wall measurement. So, the path of the beam before that mirror was identical: 10% of the beam was picked off and diverted to a wavelength meter[26] while the remaining 90% traveled through an optical chopper[27] before it passed the space where it could encounter the flippable mirror. The laser was also controlled in the exact same way. The motor controller[28] adjusted the angle of the grating while the DLC[29] controlled the piezo voltage, the current, and the temperature of the diode cavity to adjust the cavity length. Further details can be found in section 5.2. To take a spectroscopy measurement, the flippable mirror was removed from the beamline and the beam continued on.

I wanted to avoid using mirrors in this system and attempted to align the beam directly to the window of the spectroscopy oven. By avoiding mirrors, I could better predict the amount of power remaining in the beam by the time it reached the oven as well as the polarization of the beam. I wanted to both limit beam noise and avoid circularly polarizing my beam and thus pumping into a specific ground state. These weren't a concern with interferometry since

[24] A phrase popularized in propaganda posters issued by the British government during WWII, urging citizens be calm in the face of Germans dropping bombs on them during the London Blitz.
[25] Toptica DL Pro 780, TOPTICA Photonics Inc., Farmington, NY
[26] WS-7, High Finesse, Tübingen, Germany
[27] Optical Chopper System with MC1F10HP 10/100 Slot Chopper Blade, ThorLabs Inc., Newton, NJ
[28] Toptica DL MOT, TOPTICA Photonics Inc., Farmington, NY
[29] Toptica DLC Pro, TOPTICA Photonics Inc., Farmington, NY

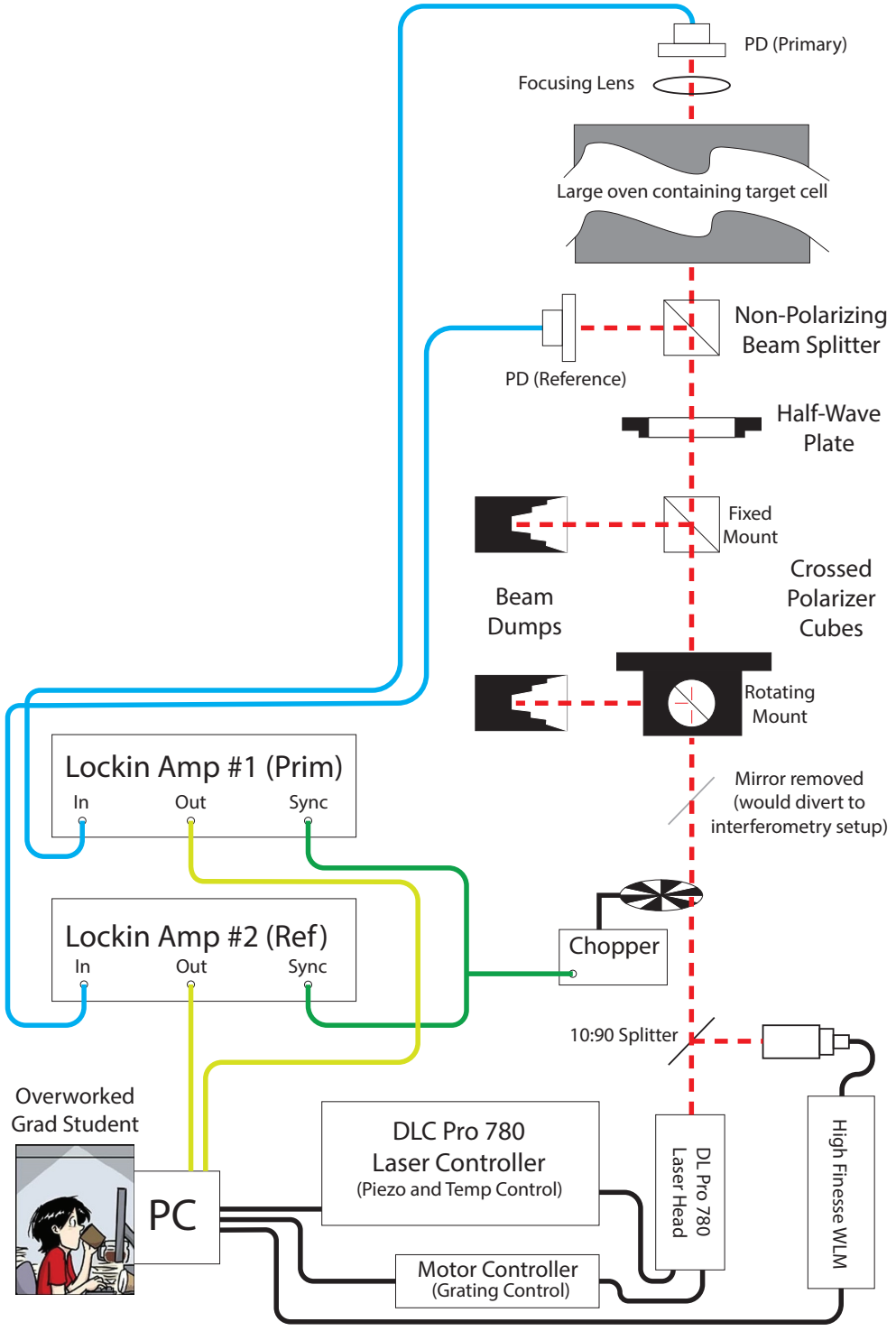

Figure 5.7: Experimental setup for measuring pressure broadened absorption lines. Grad Student Illustrated by Dr. Jorge Cham, Illustrator, PhD Comics (jorge@phdcomics.com)

reflection and power variation is the name of the game (see section 5.1 for further details and pretty pictures).

After the optical chopper, the beam reached a pair of crossed linear polarizer cubes which were used to adjust the power of the beam that reached the oven. According to previous research by Romalis *et al.*[69], the optimal amount of power going through the target cell for a spectroscopy measurement is "a few mW/cm^2", which I interpreted as 1-3 mW/cm^2. The first cube could be rotated so that the linear beam that finally emerged from the second cube was within that range. For my beam's very small spot size, this range was on the order of 10-30 μW. This also had the added benefit of making the beam polarization completely linear; the beam emitted from the head was not quite linearly polarized. The non-polarizing beam splitter (NPBS), which I will discuss more in a moment, also benefited from linear beam polarization.

The next piece of optics the beam encountered was a half wave plate (HWP) so that the angle of the polarization could be adjusted. Following that was the aforementioned NPBS[30]. Unfortunately, the beam splitter did not maintain an exact ratio of split power for the entire frequency range we worked with as you can see in figure 5.8. If we think of an angled, linearly polarized beam as a mix of p- and s-polarizations[31] leading into the non-polarizing beam splitter, we could effectively adjust the angle of the linear polarization to adjust the mix of s- & p-polarizations. This minor adjustment kept the ratio of reflected and transmitted beams from the NPBS relatively the same across the entire frequency range.

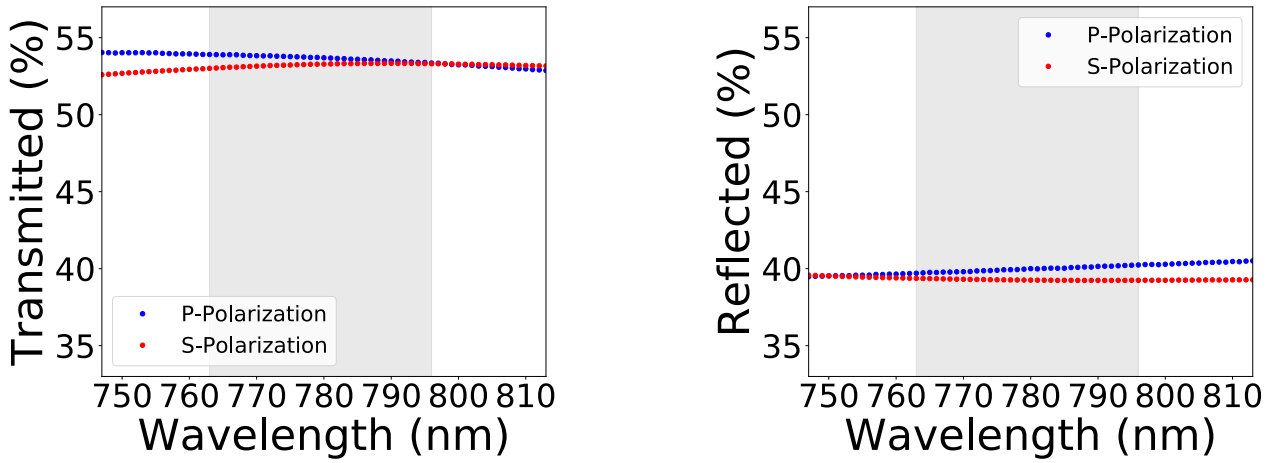

(a) Transmitted Beam (%) Versus Wavelength (nm)

(b) Reflected Beam (%) Versus Wavelength (nm)

Figure 5.8: Variance in reflected and transmitted beam intensity through the Thorlabs Non-Polarizing Beamsplitter Cube. Shaded gray area represents range of operation for the laser used in this measurement. Data for these plots can be found on the Thorlabs website. The part number for the NPBS is listed in the footnotes.

The NPBS is a nominal 50:50 splitter, which sent the reflected half of the beam directly into

[30]Thorlabs p/n BS014 - "50:50 Non-Polarizing Beamsplitter Cube, 700 - 1100 nm, 1 in."

[31]s-polarization stands for "senkreht", which is German for perpendicular. p-polarization stands for "parallel", which is German for, well, parallel.

a photodiode. This is our "reference" signal exactly as was done during interferometry. The photodiode was surrounded by a tube comprised of the same shielding material from section 5.2 (cardboard) to limit outside light reaching the photodiode. The photodiode was tipped at a 45° angle to limit etalon effects.

The portion of the beam that went directly through the cube entered the oven through a small window with a diameter of about one quarter-inch. Inside, the target was suspended such that the beam could travel in through one window of the oven, through the pumping chamber of the target, and out through an identical window at the far end of the oven. As the shape of the glass was not perfectly flat *anywhere*, there was refraction. The beam primarily spread vertically by the time it reached the far window. The target was positioned such that the majority of the light made it through the far window, but there was certainly clipping of the beam.

Once outside the oven, the refracted beam reached a focusing lens with a very short focal length and finally reached another photodiode identical to the reference photodiode placed at the focal length of the lens. This was our "primary" photodiode and was also tipped at a 45° angle and surrounded by a cardboard[32] tube just as the reference signal PD was. Each photodiode was routed to a lock-in amplifier[33] and then to the multifunction I/O unit[34] just as was done for the interferometry measurements in section 5.2. In fact, I used the same lock-ins and the same I/O device, as you can see from the footnotes.

The oven itself was heated by forced air convection just as was the oven for polarimetry from chapter 4. However, the polarimetry oven had two heaters while this oven only had one. Great care was taken to ensure this oven could reach sufficiently high temperatures. To that end, leaks were sealed[35]. The oven was insulated first with the same fibrous, flexible mat of polycrystalline alumina fiber[36] used on the NMR/EPR oven discussed in section 4.3.2. It was then wrapped in aluminum foil.[37] Even then, the maximum temperature this oven could reliably reach was only about 165°C. Technically, the temperature could have gone higher, but only with the heater running constantly, risking wild temperature fluctuations should it cycle off momentarily. Fortunately, testing never required temperatures as hot as the polarimetry oven.

A single scan was taken for each of the rubidium lines because they were sufficiently far apart. However, the potassium lines were scanned together as they are very close to one another and the width of one could affect the width of the other. In the case of all three scans, the scanner range was sufficiently large as to show the wings (or outer wings in the case of the K-lines) displayed asymptotic behaviour far from the kernal. This allowed a good, clean fit for the data. The expected central frequency for each of these absorption lines as well as the scan ranges are listed in table 5.5.

These scans were taken consecutively. That is to say I would set the system and let the

[32] I could make the same "composite material" shielding joke again, but I think I may have beaten that into the ground at this point.

[33] These were the same lock-in amplifiers as with the interferometry setup, section 5.2

[34] USB-6363 X-Series Data Acquisition (DAQ), National Instruments, Austin, TX

[35] Oven sealed with "Permatex Silicone Sealant", p/n 7479A34, McMaster-Carr, Robbinsville, NJ

[36] p/n D9201, Alumina Mat, Zircar Ceramics, Florida, NY

[37] To be a little more accurate, I loosely wrapped the oven with aluminum foil and sort of stuffed it with the insulation, creating a baffles which I thought might help keep more heat in.

D-Line	Approx. Center (GHz)	Scan Range (GHz)	Total Range (GHz)
Rb D1	377107	376552 - 377808	1256
Rb D2	384230	383219 - 385243	2024
K D1	389273	388332 - 392034	3702
K D2	391124		

Table 5.5: Scan Ranges for applicable rubidium (Rb) and potassium (K) D-Lines

computer run each of the scans in sequence: Rb D1, then Rb D2, and finally the K lines. To set the power level, I tuned the laser to the end of its scan across the K lines (392034 GHz) and adjusted the cross polarizers such that the beam power entering the NPBS would be roughly 50 μW. This frequency corresponds to the point where the laser emits the lowest power in the scan. The power for the laser maximized at around 300 μW between the Rb D1 and Rb D2 scans (382437 GHz to be more exact).

Factoring in the NPBS, the beam power the target was exposed to remained between 25-150 μW over the range of the scan. This exceeds the range dictated by Romalis *et al*. by a factor of 5 if my assumption that "a few" meant 1-3 mW/cm^2 held true. Additional scans were taken such that the power level the target was exposed to over the entire scan remained between 2.5-15 μW (10% of my normal operating power). FWHM was consistently the same at both power levels over a range of temperatures; the "excessive" power did not distort the results.

Concerns regarding total beam power, saturation, and power variation over the course of the entire scan will be discussed further in sections 5.8 and 5.9. Yes, this is more foreshadowing. No, I'm probably not going to stop doing it. I find it makes the writing more enjoyable to read end-to-end. I have to read this thing several times for tone and grammar (to make sure I do words good). You have the luxury of skipping ahead (but please don't skip ahead). My point is, I'm having fun and I hope you are to! Moving on...

Finally, each series of scans was separated into what I called "runs". A run began when the target was installed in the oven and ended when the target was adjusted, removed, or when the optics of the system were changed. As you've read, much of the adjustments were done by hand. Adjusting the beam direction after it refracts through the target was even more imprecise. The target was suspended in the oven on shelves mounted to the interior walls of the oven, which could be bent by hand if one weren't careful. The height of the target was adjusted by adding shims between the shelf and the base on which the target was mounted (usually a base from the NMR system and not necessarily the same one every time). The shims weren't exactly standard sizes as they were discarded pieces of aluminosilicate ceramic (read: parts of old ovens), metal washers, or small pieces of wood. Basically, anything sitting around the lab that was the right size and could withstand the temperature. Once height was adjusted, the target was adjusted horizontally (in the plane normal to the beam) until the beam leaving the pumping chamber aligned with the window on the back of the oven. Then these two steps were repeated (with much grumbling on my part) until the refracted light was centered on the window leading out of the oven. The target base was then taped securely to the shelves on which the base rested and, at all times, the oven was secured firmly to the optics table.[38] There is no guarantee the target was put in the same exact place once it was removed and reinstalled.

[38] As I said in section 5.2.1, rigged for a Sea-State 5.

Temperature also affected the photodiodes, so I limited the duration of a run to avoid temperature fluctuations due to changing seasons. The average length of a run was 16-17 days, though some were as short as a day and others were as long as 8 weeks. The photodiodes were also sensitive to room light and the intense light of the NMR/EPR lasers.[39] So room lights were left on and the Death Star power was not changed for the length of a scan.

By separating data sets by runs, I avoided confusion when comparing data. And while the power leading into the oven was still manually adjusted, power was always read with the same power meter at the same position in the beam path (just before the NPBS).

5.7 Spectroscopy: Data Analysis

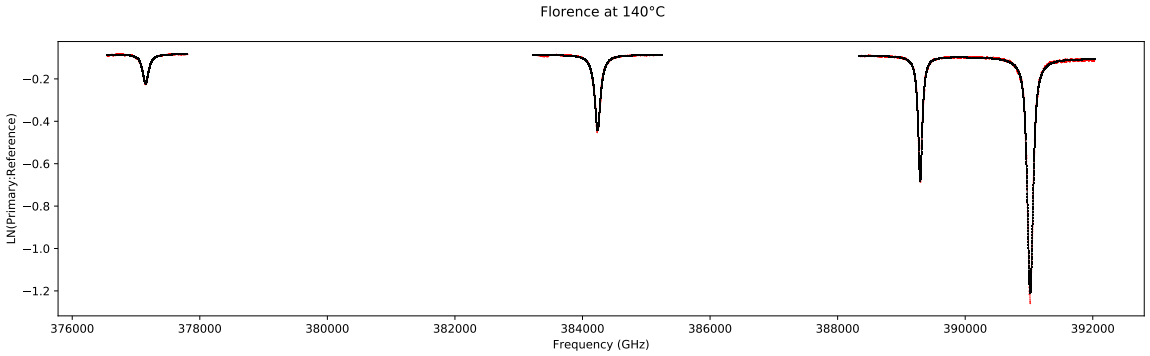

Figure 5.9: A typical example of spectroscopy data (in red) and a typical fit (in black).

Let's go back to 1984. The year, of course, not the dystopian novel[40]. Per references 1-4 of Walkup *et al.* [70], if we consider a dilute gas of absorber and radiator atoms mixed homogeneously with a gas of perturbers, we can describe the line shape for an isolated optical transition in a dilute gas using a generalized Lorentzian with a *detuning dependent* collision broadening rate, $\gamma_c(\Delta)$, which accounts for shifts from the line's center:

$$A = \frac{1}{2\pi} \frac{\gamma_N + \gamma_c(\Delta)}{(\Delta - \delta_c)^2 + [\gamma_N + \gamma_c(0)]^2/4} \tag{5.4}$$

where γ_N is the absorption line's natural rate of radiative decay, $\gamma_c(0)$ is the collisional broadening rate with zero detuning, $\Delta = \omega - \omega_0$ is the detuning from resonance, and δ_c is the collision induced line shift.

Assuming straight, classical trajectories, Walkup goes on to define the broadening rate, γ_c, for an attractive van der Waals potential, limited to the binary collision regime, in the following way:

$$\gamma_c = n_p \left(v_{th}\right) \left[8\pi R_{th}^2\right] I(T_d \Delta) \tag{5.5}$$

[39]The Death Star lasers could each provide up to 50W of power for a total possible output of 200W. This is the power equivalent of 40,000 store-bought laser pointers. Compare that to the Toptica DL Pro, whose power topped out at 125 mW or about 25 store-bought laser pointers.

[40]Orwell, G. (2021). *Nineteen eighty-four*. Penguin Classics. (Original work published 1949)

where n_p is the density of the perturber gas, v_{th} is the most probable relative velocity, R_{th} is an effective collision radius, T_d is the characteristic collision duration, Δ is again the detuning from resonance, and all detuning information is contained in the dimensionless parameter, $I(T_d\Delta)$. The bracketed term, $8\pi R_{th}^2$, is the scattering cross section for pressure broadened absorption lines.

Walkup expands v_{th}, R_{th}, and T_d to show their explicit temperature dependence in the following way:

$$\begin{aligned} v_{th} &= \left(\frac{2k_BT}{\mu}\right)^{1/2} \\ R_{th} &= \left(\frac{|C_6|}{v_{th}}\right)^{1/5} = |C_6|^{1/5}\left(\frac{\mu}{2k_BT}\right)^{1/10} \\ T_d &= \frac{R_{th}}{v_{th}} = \left(\frac{|C_6|}{v_{th}}\right)^{1/5} v_{th}^{-1} = |C_6|^{1/5} v_{th}^{-6/5} = |C_6|^{1/5}\left(\frac{\mu}{2k_BT}\right)^{3/5} \end{aligned} \tag{5.6}$$

where k_B is the Boltzmann constant, T is the temperature in Kelvin, μ is the reduced mass of the two collision participants, and C_6 is a constant that depends on the depth of the energy well and the equilibrium separation of the nuclei and is usually found by experiment.

Walkup further numerically approximates I for three regions: $T_d\Delta < -2$, $T_d\Delta > 2$, and $-1.5 < T_d\Delta < 0.5$ which accounts for much of the transition between the impact region, $|T_d\Delta| \ll 1$, and the far line wings, $|T_d\Delta| \gg 1$. The region $-1.5 < T_d\Delta < 0.5$ is the region near resonance. Using equation 5.6 to rewrite terms such that their dependence on v_{th} (and thus temperature) is more explicit, Walkup approximates $I(T_d\Delta)$ as:

$$
\begin{aligned}
T_d\Delta < -2: \qquad I(T_d\Delta) &= \frac{\pi}{6}\sqrt{T_d\Delta} \\
&= \frac{\pi}{6}\sqrt{\frac{R_{th}\Delta}{v_{th}}} \\
-1.5 < T_d\Delta < 0.5: \qquad I(T_d\Delta) &= 0.3380 - 0.2245 T_d\Delta \\
&= 0.3380 - 0.2245\frac{R_{th}\Delta}{v_{th}} \\
T_d\Delta > 2: \qquad I(T_d\Delta) &= 0.8464\sqrt{T_d\Delta}\exp\left[-2.1341(T_d\Delta)^{5/9}\right] \\
&= 0.8464\sqrt{\frac{R_{th}\Delta}{v_{th}}}\exp\left[-2.1341\left(\frac{R_{th}\Delta}{v_{th}}\right)^{5/9}\right]
\end{aligned}
\tag{5.7}
$$

Because we're working near resonance, Walkup suggests the broadening rate, $\gamma_c(\Delta)$, can instead be written in the "intuitively appealing" form $\gamma_c(0)(1 + a_1' T_d\Delta')$ with $a_1' = -0.2245/0.3380 = -0.664$.

According to the Beer-Lambert Law[68], we can relate intensity variation through an absorbing medium made of two species of atom through a distance of length L in the following way:

$$
\begin{aligned}
\tilde{I}(\nu) &= \tilde{I}_0 \exp\left(-\sum_i \tau_i\right) = \tilde{I}_0 \exp\left(-\sum_i \int_0^L \alpha_i(z)dz\right) \\
&= \tilde{I}_0 \exp\left(-\sum_i \alpha_i L\right) = \tilde{I}_0 \exp\left(-\sum_i \sigma_i(\nu)[\rho]_i L\right) \\
&= \tilde{I}_0 \exp\left[-(\sigma_{Rb}(\nu)[\mathrm{Rb}]L + \sigma_K(\nu)[\mathrm{K}]L)\right] \\
&= \tilde{I}_0 \exp\left[-(\sigma_{Rb}(\nu)[\mathrm{Rb}] + \sigma_K(\nu)[\mathrm{K}]) \cdot L\right]
\end{aligned}
\tag{5.8}
$$

where for species i, τ_i is the "optical depth" or relative intensity decrease along the absorption path. $\alpha_i(z)$ is the attenuation coefficient and $\tau_i = \alpha_i L$ in the second line of this equation is true for uniform density along the path. σ_i is the attenuation or absorption cross section, and

$[\rho]_i$ is the density of the ith atomic species. $\tilde{I} = I_t G_t$ is the transmitted intensity including the raw beam intensity transmitted, I_t, and the gain on that circuit, G_t. $\tilde{I}_0 = I_0 G_0$ is the initial intensity including the raw beam intensity initially, I_0, and the gain on *that* circuit, G_0. $\nu = \omega/2\pi$ is the frequency.

First, a quick note about the gain term in the previous equation. I am using the word "gain" here *loosely*. Normally, gain is defined as the proportional increase of intensity. So, a signal with a gain of two would be twice as large as the raw signal, noise and all. That is the *largest* portion of this term, for sure. However, that term is also encapsulating the noise in the system, which will become more important in sections 5.7.4 and 5.7.6.

We can now directly relate the primary (transmitted) and reference (initial) intensities described in section 5.6 to a line profile because these cross sections, σ_{Rb} and σ_K, are constant with density:

$$\begin{aligned} S(\nu) &= \ln\left[\frac{\tilde{I}_t}{\tilde{I}_0}\right] = \ln\left[\frac{I_t G_t}{I_0 G_0}\right] = \ln\left[\frac{I_t}{I_0}\right] + \ln\left[\frac{G_t}{G_0}\right] \\ &= -(\sigma_{Rb}(\nu)[\mathrm{Rb}] + \sigma_K(\nu)[\mathrm{K}])L + \ln\left[\frac{G_t}{G_0}\right] \end{aligned} \tag{5.9}$$

where here I've defined $S(\nu) = \ln[\tilde{I}_t/\tilde{I}_0]$ just as Romalis *et al.*[69]

We know that $[\rho]_i$ will be constant so long as we keep the temperature constant while scanning across the line profile (thank you Ideal Gas Law). L will be constant so long as the glass doesn't melt or shatter. Therefore, this relation can further be simplified if two additional things are true. First, the gain term in each circuit should be equal so the $\ln[G_t/G_0]$ term goes to zero. Second, we need to choose a line profile for each alkali species that goes to zero well before reaching the line profile for the *other* species. If those conditions are met, equation 5.9 simplifies to $S(\nu) = \ln I_t/I_0 \propto \sigma(\nu)_i$ for the ith alkali species. Now, we just have to find the right fit...

5.7.1 My Forebears: The Lorentzian Fit

Let's go back to equation 5.4, where my forebears, Romalis and Singh started (references [69] and [45], respectively). Using the approximation of $I(T_d\Delta)$ near resonance and referencing Walkup, Romalis rewrote equation 5.4 to model the dispersion-like asymmetry. Both Romalis and Singh noted that to properly model the absorption line, one would need a summation of Lorentzians to account for all hyperfine states and dominant isotopes, not simply the modified Lorentzian proscribed by Walkup. In Romalis *et al.* ([69]), Walkup's Lorentzian is described in the following way:

$$S(\nu) = \frac{C_0[1 + 0.664 * 2\pi T_d(\nu - \nu_0)}{(\nu - \nu_0)^2 + (\gamma/2)^2} + \Phi \tag{5.10}$$

The sum of four functions proscribed by Romalis and later Singh (in the case of rubidium) to account for the hyperfine splitting and the two prevalent isotopes is written in the following way:

$$S(\nu) = \sum_i A_i C_0 \left[E_i\right] \left(\frac{1 + 0.664 \times 2\pi T_d(\nu - \nu_0 + \delta\nu_i)}{(\nu - \nu_0 + \delta\nu_i)^2 + (\gamma/2)^2} \right) + \Phi \tag{5.11}$$

where variables C_0, T_d, ν_0, and γ are allowed to vary to provide the best fit. Roughly translated (via the same reference, [69]) these variables are T_d, the interaction time between the alkali atoms and the gas atoms, ν_0, the central frequency of the absorption line, and γ, FWHM of the line. E_i is the transition strength of each hyperfine ground state and A_i is the natural abundance of each isotope. $\delta\nu_i$ is the natural deviation from ν_0 for each hyperfine state of each isotope. ν is the frequency. C_0 is an amplitude which, when divided by some normalization factor, N, will be equal to the normalization factor in equation 5.4, $\gamma/2\pi$. This will come into play in section 5.7.6. For now, C_0 is varied to ensure a good fit and it is sufficient to say $NC_0 = \gamma/2\pi$.

$\Phi = m\nu + b + \ln[G_t/G_0]$ is a unitless, linear equation meant to account for the behavior as these functions go to infinity. The transmitted beam, I_T, will always have additional attenuation even in the absence of the gas-alkali mixture; the transmitted beam travels through the glass walls of the target, the windows on the oven, and the focusing lens between the oven and the photodiode. This is assuming we could even ensure an exact 50:50 split from the NPBS that separates the primary/transmitted (I_T) and reference/incident (I_0) signals, which you can see couldn't happen based on figure 5.8. Therefore, it's highly unlikely one could get the ratio of those signals to equal unity and thus their log to equal zero, which is what these distributions asymptotically approach as we move to infinity in either direction. Hence, the line dictated by this linear equation becomes the new zero; the line defined by the slope, m, and y-intercept, b, define the "zero" $S(\nu)$ goes to in the limit where $\nu \to \pm\infty$.

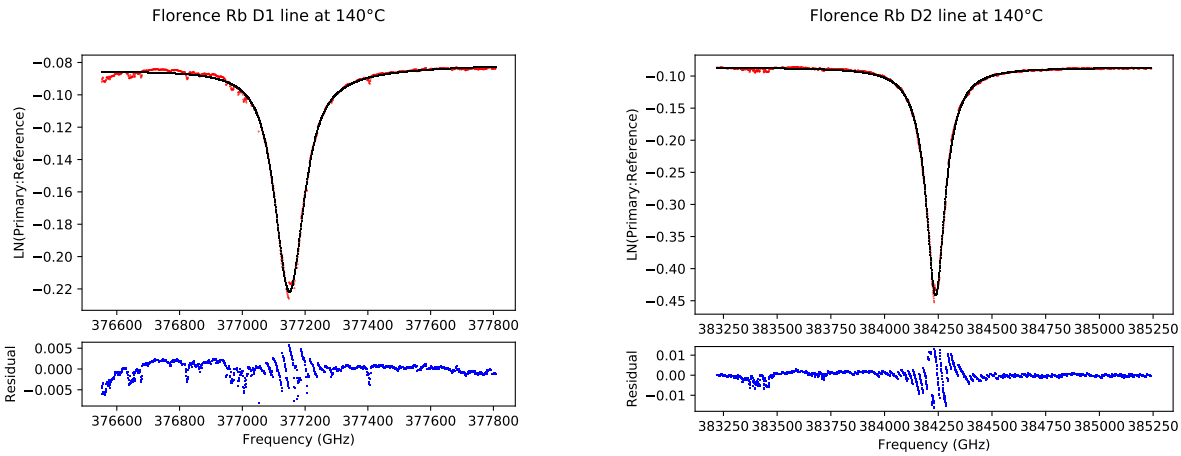

(a) Rb D1 line **(b)** Rb D2 line

Figure 5.10: Examples of rubidium data (in red) and a typical fit (in black). Differences between the fit and the data (residuals) are shown in blue in the lower figure of each image.

When considering all of this, the full Lorentzian used for fitting either the D1 or D2 line of Rb (in all of it's horror) was helpfully recorded in reference [45] and is as follows:

$$\begin{aligned} S(\nu) = 0.7217 C_{Rb} \left[\frac{7}{12}\right] \left(\frac{1 + 0.664 \times 2\pi T_d(\nu - \nu_0 + 1.264887)}{(\nu - \nu_0 + 1.264887))^2 + (\gamma/2)^2}\right) \\ + 0.7217 C_{Rb} \left[\frac{5}{12}\right] \left(\frac{1 + 0.664 \times 2\pi T_d(\nu - \nu_0 - 1.770844)}{(\nu - \nu_0 - 1.770844))^2 + (\gamma/2)^2}\right) \\ + 0.2783 C_{Rb} \left[\frac{5}{8}\right] \left(\frac{1 + 0.664 \times 2\pi T_d(\nu - \nu_0 + 2.563005)}{(\nu - \nu_0 + 2.563005))^2 + (\gamma/2)^2}\right) \\ + 0.2783 C_{Rb} \left[\frac{3}{8}\right] \left(\frac{1 + 0.664 \times 2\pi T_d(\nu - \nu_0 - 4.271676)}{(\nu - \nu_0 - 4.271676))^2 + (\gamma/2)^2}\right) \end{aligned} \tag{5.12}$$

where C_{Rb}, T_d, ν_0, and γ are as explained in equation 5.11. Transition strengths, E_i, are here calculated as $(2F + 1)/\sum_i (2F_i + 1)$ for ground state F and a summation over all possible ground states for the isotope in question. The first and second Lorentzians describe the $F = 3$ and $F = 2$ ground states of ^{85}Rb, respectively. The third and fourth Lorentzians describe the $F = 2$ and $F = 1$ ground states of ^{87}Rb, respectively.

As mentioned when describing equation 5.11, both 5.11 and 5.12 will become constant as the frequency, ν, moves far away from the line center and the term $(\nu - \nu_0 + \delta\nu_i)$ grows very large. So, if we're examining a Rb line, any absorption lines sufficiently far away can be ignored when fitting the data; we can consider the Rb D1 and Rb D2 lines separately. The same can't be said for the potassium lines, which are too close together to be fit individually. There is, however, some good news. While there are two abundant, stable, natural isotopes of Rb, the most abundant, stable, naturally occurring isotope of K, ^{39}K, accounts for about 93% of the K atoms we find in nature. Additionally, the hyperfine-split ground state energy levels only differ by about 1 GHz. Therefore, we *should* (see section 5.7.3) be able to ignore all of that and fit the potassium data with only two Lorentzians (one for each transition line). This was, yet again, helpfully recorded in reference [45]:

$$\begin{aligned} S(\nu) = C_{KD1} \left(\frac{1 + 0.664 \times 2\pi T_1(\nu - \nu_1)}{(\nu - \nu_1))^2 + (\gamma_1/2)^2}\right) \\ + C_{KD2} \left(\frac{1 + 0.664 \times 2\pi T_2(\nu - \nu_2)}{(\nu - \nu_2))^2 + (\gamma_2/2)^2}\right) \end{aligned} \tag{5.13}$$

where each line has it's own set of fitting parameters. $C_{KD1}(C_{KD2})$ are analogous to C_0 in 5.11,

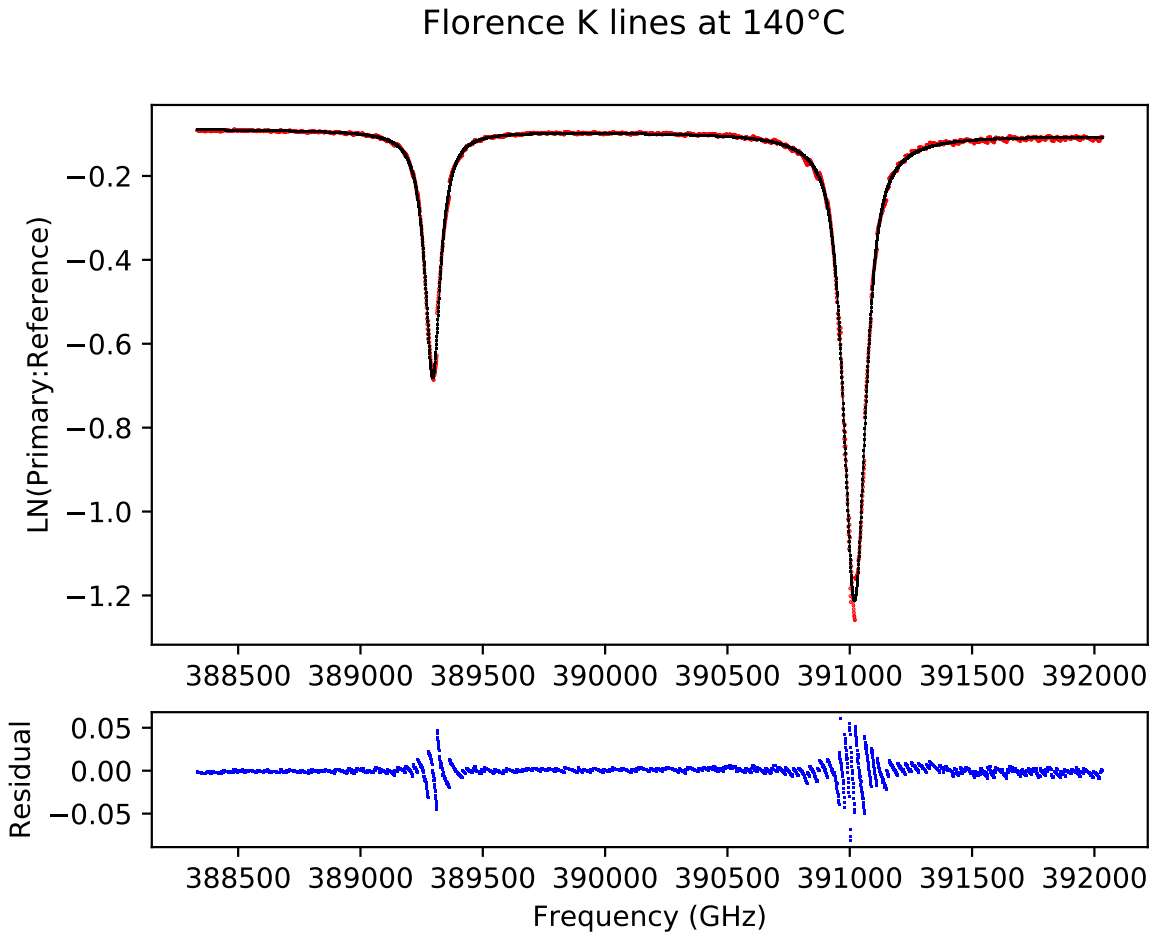

Figure 5.11: Example of potassium data (in red) and a typical fit (in black) for target-cell Florence. Differences between the fit and the data (residuals) are shown in blue in the lower figure of each image.

$T_1(T_2)$ are analogous to T_d, $\nu_1(\nu_2)$ are analogous to ν_0, and $\gamma_1(\gamma_2)$ are analogous to γ for the potassium D1(D2) line.

5.7.2 Reinventing the Wheel: The pseudo-Voigt Profile

As I've alluded to in section 5.5.3, the results of my spectroscopy measurements did not adhere to what I expected. Ultimately, I thought a better fitting equation may be the solution. I opted to use a Voigt profile that incorporated the isotope and hyperfine state considerations of equations 5.12 and 5.13 but might additionally capture whatever information I was missing, possibly from the Doppler and natural widths.

As mentioned in section 5.5.1 (and explained well in reference [68]), a Voigt Profile is a convolution of a Gaussian and a Lorentzian. Unfortunately, this is difficult to implement because it involves an integral of the two constituent functions. However, a common workaround is to fit a "pseudo-Voigt" profile. This is simply the summation of the Lorentzian and Gaussian with an appropriate weight given to each function. Using the same summation form of equation 5.11, the pseudo-Voigt profile is as follows:

$$S(\nu) = \sum_i A_i \left[E_i\right] \left[(\eta) L_i(\nu) + (1-\eta) G_i(\nu)\right] + \Phi \tag{5.14}$$

where A_i is the natural abundance of the isotope in question (as before), E_i is again the transition strength for each hyperfine state, η is a weighting function such that $0 \leq \eta \leq 1$, $L_i(\nu)$ is a Lorentzian function defined in 5.10, and $G_i(\nu)$ is a Gaussian function. As before, $\Phi = m\nu + b + \ln[G_t/G_0]$ is a unitless, linear equation simply there to aid in fitting the data and to absorb the $\ln[G_t/G_0]$ term.

It behooves us, as we'll see in section 5.7.6, to find a way to normalize the entire pseudo-Voigt function. The Lorentzian in equation 5.10 has a fitting parameter, C_0, that is already related to an as yet unknown normalization factor, N. We can redefine our Lorentzian and Gaussian in equation 5.14 such that both functions share a normalization factor via C_0 in the following way:

$$L_i = C_0 \tilde{L}_i \qquad\qquad G_i = C_0 \tilde{G}_i \tag{5.15}$$

By incorporating an asymmetry similar to equation 5.4, we can define G_i in the following way:

$$\begin{aligned}\tilde{G}_i(\nu) = G_i(\nu)/C_0 &= \frac{1}{\sqrt{2\pi}C_0}\frac{1}{\sigma(0)}\exp\left[\frac{-(\Delta)^2}{\sigma(\Delta)^2}\right] \\ &= \frac{2\pi}{\sqrt{2\pi}\gamma(0)}\frac{2\ln 2}{\gamma(0)}\exp\left[\frac{-(2\ln 2)^2(\Delta)^2}{\gamma\Delta^2}\right] \\ &= \frac{\sqrt{8\pi}\ln 2}{\gamma^2}\exp\left[\frac{-(2\ln 2)^2(\nu-\nu_0+\delta\nu_i)^2}{\gamma^2(1+0.664\times 2\pi T_d(\nu-\nu_0+\delta\nu_i))^2}\right]\end{aligned} \tag{5.16}$$

where σ from the usual Gaussian distribution has been replaced with $\sigma = \gamma/(2\ln 2)$, γ is the FWHM of the Lorentzian, T_d is the interaction time between the alkali and the gas atoms, ν_0 is the central frequency of the absorption line, $\delta\nu_i$ is the natural deviation from ν_0 for each hyperfine state of each isotope, ν is the frequency, and T_d, ν_0, and γ are again allowed to vary to provide the best fit.

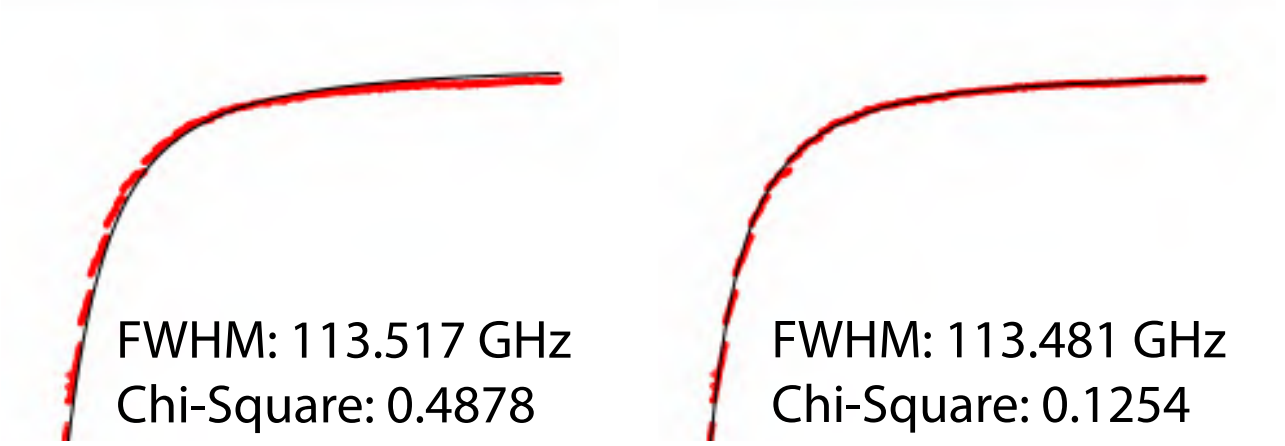

Figure 5.12: A comparison of the Lorentzian (left) and pseudo-Voigt fits for a RbD2 line measured at 155°C

As you can see from figure 5.12, while the pseudo-Voigt fit does provide a tighter fit to the data, the effect on the FWHM is minimal, being less than 0.1% difference even for data with a very high signal to noise as in the example shown. This was typical for every data to set.

5.7.3 The Rabbit Hole: Misadventures when considering all isotopes and hyperfine levels

"There are many things of which a wise man might wish to be ignorant, and these are such. Shun them as you would the secrets of the undertaker and the butcher."

– *Attributed to Ralph Waldo Emerson (unverified)*

Here, I add one last addendum to the previous fits. I want to include this addendum to save future grad students time, energy, and frustration. In trying to understand the summation of Lorentzians described in section 5.7.1, I took a hard look at the source of the number used for "transition strength". These specific fractions didn't appear in references [71] or [72] and it wasn't immediately clear to me why they were being used. Once I realized equation 5.12 only took into account the ground state energy shifts using a simple formula (described in section 5.7.1), I had what I considered at the time to be an utterly amazing idea: why not account for every possible hyperfine transition? Fortunately, my forebears had already accounted for the two stable isotopes of rubidium and it was left to me to find accurate transition strengths and energy shifts for each allowed transition.

From references [71] or [72], the transition strength (strength of the interaction between two hyperfine levels) for particular transition in rubidium can be calculated in the following way:

$$S_{FF'} = (2F'+1)(2J+1)\begin{Bmatrix} J & J' & 1 \\ F' & F & I \end{Bmatrix}^2 \tag{5.17}$$

where I is the nuclear spin of the isotope in question, $F(F')$, is the hyperfine energy level of the ground(excited) state, and $J(J')$ is the total angular momentum state for the ground(excited) state. The curly brackets here indicate a Wigner 6-j symbol.

Because selection rules dictate that allowed hyperfine transitions remain restricted to the $\Delta F = 0, \pm 1$ (with the caveat that $F' = 0 \longleftrightarrow F = 0$ is forbidden), there were only 4 transitions between the $5^2S_{1/2}$ and $5^2P_{1/2}$ states to consider and 6 transitions between the $5^2S_{1/2}$ and $5^2P_{3/2}$ states.

	Rb-85	Rb-87	K-39	K-40	K-41
Abundance	0.7217	0.2783	0.9326	0.0001	0.0673
W. Mean D1 (GHz)	377107.41		389286.07		
Shift from D1 Mean (MHz)	-0.0216	0.0561	-0.0159	0.1098	0.2196
W. Mean D2 (GHz)	384230.43		391016.19		
Shift from D2 Mean (MHz)	-0.0217	0.0564	-0.0159	0.1101	0.2203

Table 5.6: Shift from the mean freq. of the D1 and D2 lines for all stable isotopes of Rb and K

For shifts in energy transitions, I started by calculating the mean frequency for the transition between each excited energy level ($5^2P_{1/2}$ and $5^2P_{3/2}$) and the ground state ($5^2S_{1/2}$), weighted by the abundance of each isotope (see table 5.6 for all energy shifts and mean values for each level). I calculated total frequency shift from the mean frequency for each hyperfine transition in the following way:

$$\Delta f = i_e + s_g + s_e \tag{5.18}$$

where i_e is the shift in the frequency of the overall transition between the ground and excited state inherent in each isotope and $s_g(s_e)$ in the additional shift away from the frequency attributed to each of the ground(excited) states, $F(F')$, due to hyperfine splitting.

For example, while any decay from an excited state in ^{85}Rb to it's ground state, $F = 2$, would be ascribed a frequency shift of -1.770844 GHz (see equation 5.12), I would calculate

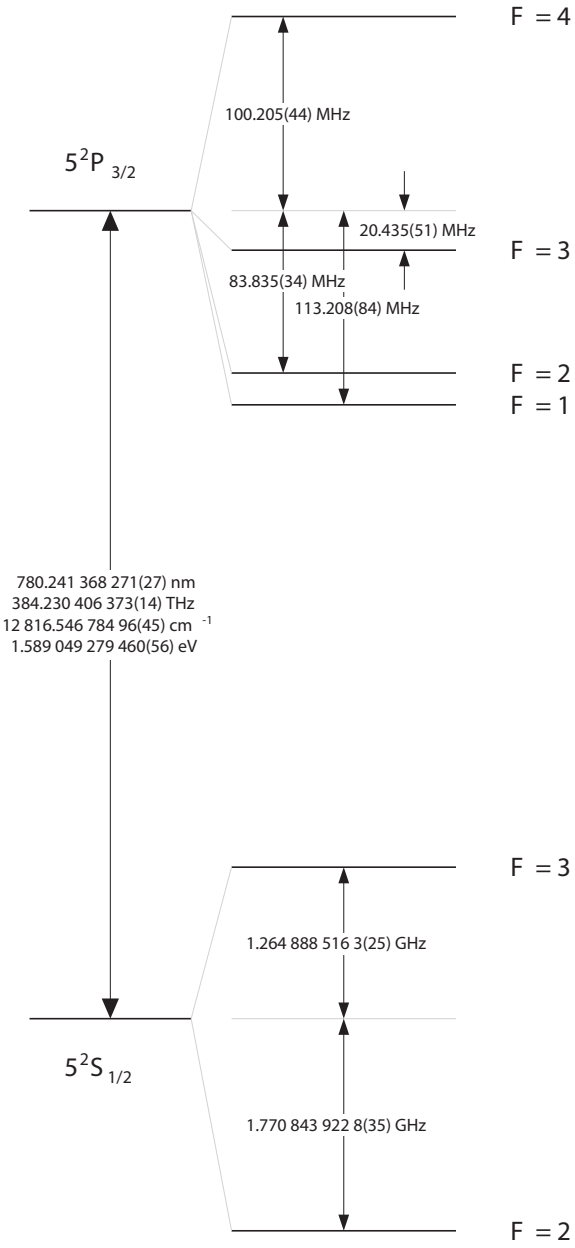

(a) Hyperfine splitting for the D2 line in ^{85}Rb, adapted from reference [71].

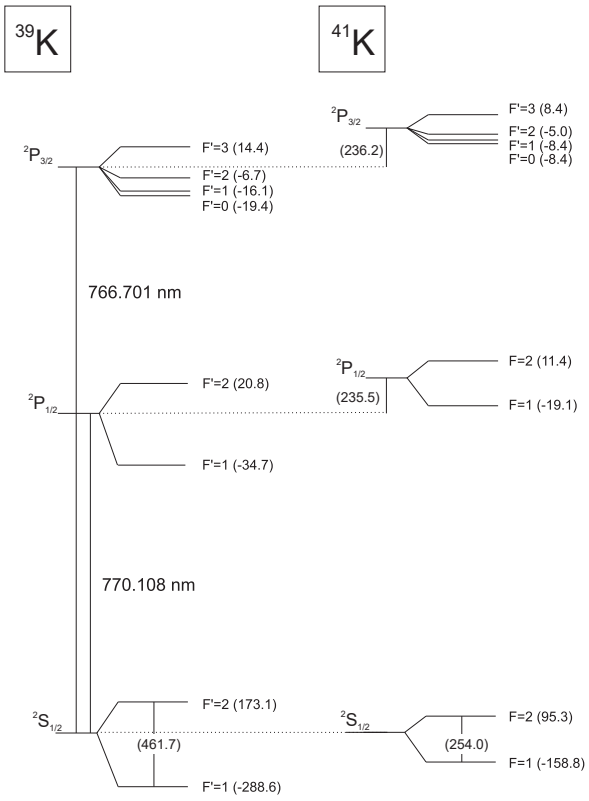

(b) Hyperfine splitting for the D1 and D2 lines in ^{39}K and ^{41}K, adapted from reference [73].

a shift from, say, the $F' = 4$ excited state in $5^2P_{3/2}$ to the $F = 2$ ground state as $\Delta f = -0.0217 + 0.1002 - 1.7708 = -1.6923$.

With an energy shift and a transition strength, it was now possible to incorporate a Lorentzian for every possible transition in rubidium amounting to a total of 20 Lorentzians (10 allowed transitions and 2 isotopes). But what of potassium? In addition to hyperfine transitions that were unaccounted for, there were also two isotopes excluded in equation 5.13: ^{41}K with an abundance of about 6.7302% and ^{40}K with an abundance of a mere 0.0117% (reference[73]). Also via reference [73], transition strength for any of these hyperfine transitions in potassium can be calculated in the following way:

$$S_{FF'} = \left[\sqrt{(2J+1)(2J'+1)(2F+1)(2F'+1)} \begin{Bmatrix} L & J' & S \\ J & L & 1 \end{Bmatrix} \begin{Bmatrix} J' & F' & I \\ F & J & I \end{Bmatrix} \begin{pmatrix} F & 1 & F' \\ m_F & q & -m'_F \end{pmatrix}\right]^2 \tag{5.19}$$

where I is the nuclear spin of the isotope in question and the following variables refer to the ground(excited) state: $F(F')$ is the hyperfine energy level, $J(J')$ is the total angular momentum, $L(L')$ is the orbital angular momentum, and $m_F(m'_F)$ is the projection of $F(F')$. The curly brackets here indicate a Wigner 6-j symbol and the parenthesis indicate a Wigner 3-j symbol.

This formula is clearly more complex as it not only incorporates energy levels, F and F', but also their projection. Still, so long as the selection rules were obeyed, transition strengths could be calculated. The same selection rules as before applied: $\Delta F = 0, \pm 1$ (with the caveat that $F'_0 \longleftrightarrow F_0$ is forbidden). *In addition* to these rules, one needs to consider the following rules as well: $\Delta m_F = 0, \pm 1$ (with the caveat that $m_{F'} = 0 \longleftrightarrow m_F = 0$ is forbidden when $\Delta F = 0$). Energy shifts were calculated similar to equation 5.18.

Target	Butterball		Kappa3	
Line	D1	D2	D1	D2
Single	126.129	117.604	15.147	13.826
Small Sum	125.959	117.427	13.947	12.519
Full Sum	125.960	117.399	13.940	12.291

Table 5.7: FWHM (in GHz) for Rb lines of two targets using three different Lorentzian fits: a single Lorentzian (eq. 5.10), a sum of 4 Lorentzians (eq. 5.12), or a sum of 20 Lorentzians (described in this section).

Dear reader, I would love to tell you that this Herculean effort resulted in a deeper understanding of my data or the nuances of spectroscopic analysis or of physics in general. But it did not, as you can see from figure 5.14. The result of plodding through this veritable ocean of new transitions to consider were results strikingly similar to analysis done using equations 5.12 and 5.13 (see table 5.7 for a few characteristic examples). The only results worth noting for this (technically) more accurate method of fitting spectroscopy lines was an exponential increase in computing time coupled with a proportional rise in frustration. In my opinion, this granular analysis is not worth the time even if one were so masochistically inclined. Let this be a warning to future generations.

5.7.4 An Act of Desperation: The Integral Fit

And yet, for all my fussing over fitting equations, trends in my results still differed from what was expected! Furthermore, I had little reason to doubt the validity of my fitting equations...and

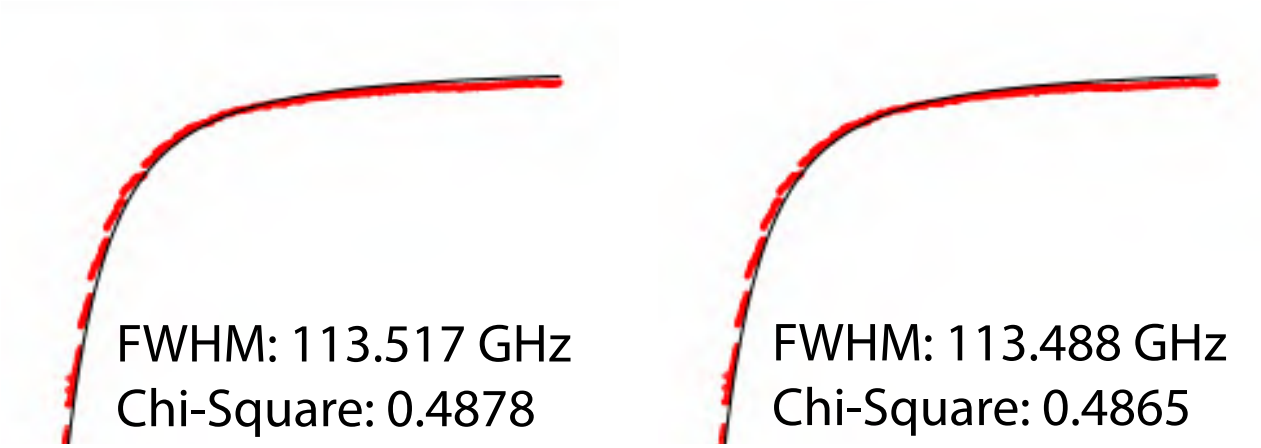

Figure 5.14: A comparison of the Lorentzian fit (left) and a full Lorentzian fit accounting for all possible hyperfine transitions for a RbD2 line measured at 155°C

yet I did. The easiest explanation for a deviation from the *expected* results *surely* had to be through some fault of my own.[41] And so, where most people would have likely considered something other than their own incompetence, I needed yet another way to fit my absorption lines in the hopes that, perhaps, the calculation of the fit was the problem.

From analyzing a fit, I really only needed two numbers to calculate the ^{3}He density and the ratio of alkali densities. In fact, the ^{3}He desity was even simpler: I just needed the FWHM at a given temperature. Alkali density is a bit more complicated, but I'll get to that in section 5.7.6. So, if all I needed was the width, I thought, "Why not just count?"

The FWHM is literally defined as the full width of the peak at half of the peak's maximum. I mean, it's right there in the name. It's easy enough to find the maximum attenuation and count all the data points within the Kernal; a simple count of all data points in the Kernal would give me the full width at half the maximum (or a reasonably close estimate). To make matters simpler, my scans took measurements of the absorption lines at intervals of $\delta f = 1$ GHz; I took data in 1 GHz steps. Therefore, it really was a simple count to find the FWHM in GHz so long as I could reliably find the maximum attenuation. This method of finding the FWHM usually agreed with both the Lorentzian and pseudo-Voigt fits for data sets with a high signal-to-noise ratio.

Looking back at all of the equations in sections 5.7.2 and 5.7.1, every fit has the term $\Phi = m(\nu) + b$, a linear equation meant to account for the behavior as these functions go to infinity. Without this term, the point of maximum attenuation could likely still be found, but it's value would be artificially inflated. Finding m and b using one of the previous equations was a task left for the computer. For this method, I calculated m and b the old fashioned way.

Call the average y-value of the first 10% of the data y_2 and the average y-value of the last 10% of the data y_1. As you may have guessed, we next call the average x-value of the first 10% of the data x_2 and the average x-value of the last 10% of the data x_1. Slope is simply $\Delta y/\Delta x$. Once we've established slope, we can find the y-intercept as long as we have a value for x and

[41] And there's the rub. When I tell you I have pretty severe depression, this lack of confidence is a primary effect of it. And yet, it *did* keep me going, asking more questions. So, there's sort of a silver lining there in not being satisfied with the initial result when it doesn't match expectations.

y. I chose to average the two y-values, y_1 and y_2, and average the two x-values, x_2 and x_1, and use those values to find b. Finally, I defined my maximum value by finding the peak y-value (and it's x-counterpart) and subtracting the value of the linear fit at that point from the peak y-value.

Summing everything up, here are my definitions for my linear fit:

$$m = (y_2 - y_1)/(x_2 - x_1)$$

$$b = \frac{y_2 + y_1}{2} - m\frac{x_2 + x_1}{2} \tag{5.20}$$

$$y_{max} = y_{peak} - (m * x_{peak} + b)$$

where y_2 and x_2 are the first 10% of the y- and x-data, respectively, and y_1 and x_1 are the last 10% of the y- and x-data, respectively. y_{peak} is the value of maximum attenuation and x_{peak} is the x-value where maximum attenuation occurs.

Then, I just counted. Well, I made a computer do it. For data with a high signal to noise ratio, this method is surprisingly accurate for finding the FWHM, the maximum attenuation, and any other information I would need to find the ^{3}He density and ratio of the alkali densities. It also allowed me to rule out "poor choice of fitting functions" as the reason I was seeing certain unexpected behaviors in my analysis.

You're being *very* patient, by the way. Thank you for not skipping ahead.

5.7.5 Finding ^{3}He Density from Spectroscopic Data

If we go all the way back to equation 5.5, we already have an equation that relates one of our fitting parameters, FWHM, to the ^{3}He density. For the three regions of $I(T_d\Delta)$ in equation 5.7, γ_c can be rewritten in the following way:

$$
\begin{aligned}
T_d\Delta < -2: \qquad \gamma_c &= n_p(v_{th})[8\pi R_{th}^2]\frac{\pi}{6}\sqrt{T_d\Delta} \\
&= n_p\left[\frac{8}{6}\sqrt{\Delta}\pi^2 R_{th}^{5/2}\right](v_{th})^{1/2} \\
-1.5 < T_d\Delta < 0.5: \qquad \gamma_c &= n_p(v_{th})[8\pi R_{th}^2][0.3380 - 0.2245 T_d\Delta] \\
&= n_p\left[0.3380 * 8\pi R_{th}^2\right][v_{th} - 0.664 R_{th}\Delta] \\
T_d\Delta > 2: \qquad \gamma_c &= n_p(v_{th})[8\pi R_{th}^2]0.8464\sqrt{T_d\Delta}\exp\left[-2.1341(T_d\Delta)^{5/9}\right] \\
&= n_p\left[0.8464 * 8\sqrt{\Delta}\pi R_{th}^{5/2}\right](v_{th})^{1/2}\exp\left[-2.1341\left(\frac{R_{th}\Delta}{v_{th}}\right)^{5/9}\right] \\
&= n_p\left[0.8464 * 8\sqrt{\Delta}\pi R_{th}^{5/2}\right]\left[\sum_{n=0}^{\infty}\frac{(-2.1341 R_{th}\Delta)^{5n/9}}{n!}(v_{th})^{(9-10n)/18}\right]
\end{aligned}
\tag{5.21}
$$

where the final form of the $T_d\Delta > 2.4$ equation incorporates the Taylor expansion for e^x to show as explicitly as possible the dependence on v_{th} and thus on temperature.

None of these agree with experiment, by the way. However, they do give the general form of an equation relating FWHM to density of the perturber gases, namely:

$$\gamma = \sum_i A_i\left(\frac{T}{T_0}\right)^{n_i}[\rho] + B_i \tag{5.22}$$

where γ is the FWHM at the temperature of the measurement, $[\rho]$ is the density of the perturber gas, $T_0 = 353$K is a scaling or benchmark temperature (discussed more at the end of section 5.8), T is the temperature of the measurement (also in Kelvin), and A_i, n_i, and B_i are a coefficient, power, and constant (respectively) specific to the perturber gas and alkali metal that are interacting.

The summation is done over all perturber gases, which were only N_2 and ^{3}He for all of our targets. The form of the equation in references [45] and [69] lacks the B_i term, but was added by Kluttz *et al.* (reference[74]), so I've incorporated it here for the sake of completeness. Specific values for A_i, n_i, and B_i can be found in those references. If we take the N_2 density from what is recorded in the gas system logs during the filling process, all we need to find the ^{3}He density inside the target is 1) the FWHM of the absorption line in question and 2) the

temperature at which we measured the FWHM. I mean, as you can see from equation 5.21 and the generalized form in equation 5.22, FWHM *clearly* increases with temperature if everything else is constant. Clearly. So, by taking spectroscopy data at multiple temperatures and across multiple absorption lines, one would (in theory) yield several values for ^{3}He density, ideally similar to one another, which could then be averaged! *What could be easier?*[42]

You may have figured out the phenomenon in the results I've been alluding to. The next few pages are *very* exciting, though. You don't want to skip ahead. Trust me.

5.7.6 Finding the Ratio of Alkali Densities from Spectroscopy Data

To use our fit to find the density of each alkali, we begin by taking an integral of our lineshape across a frequency range near the center of our absorption line. Assume for a moment that we want to find the Rb density. Call $\nu-$ and $\nu+$ some frequency below and above the center frequency of our absorption line, respectively. We start from equation 5.9 and integrate over both sides of that equation in the following way:

$$\int_{\nu-}^{\nu+} S(\nu)d\nu = \int_{\nu-}^{\nu+} \ln\left[\frac{\tilde{I}}{\tilde{I}_0}\right] d\nu = -\int_{\nu-}^{\nu+} \left(\sigma_{Rb}(\nu)[\mathrm{Rb}]L - \sigma_K(\nu)[\mathrm{K}]L\right) d\nu$$

$$N = -\int_{\nu-}^{\nu+} \sigma_{Rb}(\nu)[\mathrm{Rb}]L\, d\nu - \int_{\nu-}^{\nu+} \sigma_K(\nu)[\mathrm{K}]L\, d\nu$$

$$\frac{2\pi C_0}{\gamma} = -\int_{\nu-}^{\nu+} \sigma_{Rb}(\nu)[\mathrm{Rb}]L\, d\nu - \cancel{\int_{\nu-}^{\nu+} \sigma_K(\nu)[\mathrm{K}]L\, d\nu} \tag{5.23}$$

$$\frac{2\pi C_0}{\gamma} = -\int_{\nu-}^{\nu+} \sigma_{Rb}(\nu)[\mathrm{Rb}]L\, d\nu$$

$$\frac{2\pi C_0}{\gamma} = -[\mathrm{Rb}]L\int_{\nu-}^{\nu+} \sigma_{Rb}(\nu)\, d\nu$$

$$[\mathrm{Rb}] = -\frac{2\pi C_0}{\gamma L}\left[\int_{\nu-}^{\nu+} \sigma_{Rb}(\nu)\, d\nu\right]^{-1}$$

where [Rb] is the density of the Rb, $\tilde{I}$ and $\tilde{I}_0$ are the transmitted and incident beam intensity, respectively, σ_{Rb} is the attenuation cross section for Rb, L is the length of the pumping chamber, γ is the FWHM of the line we're examining, and N is the normalization factor which will be discussed in the next succeeding paragraphs.

For either Rb line, the integral over $S(\nu)$ from $\nu-$ to $\nu+$ is sufficiently far from the K-lines and the other Rb-line that those other lines can safely be ignored, hence the cancellation in line

[42]...Chris typed, sarcastically.

three of equation 5.23. In section 5.7.1, I said both the KD1 and KD2 lines must be fit together and this is why. While the Rb-lines are separated from one another by over 7000 GHz and from the K-lines by over 5000 GHz (minimum), the center frequencies of the two potassium lines are separated by less than 2000 GHz. The FWHM of a pressure broadened line in our targets have a width of roughly 100 GHz, making the width a significant portion of the distance between the two potassium lines.

And because $S(\nu)$ is not normalized, the solution to the integral is the normalization factor. Recall the Lorentzian from Walkup *et al.* [70] *was* normalized by a factor of $\gamma/2\pi$. We also defined the amplitude C_0 in the asymmetric Lorentzian (eqn. 5.10) as proportional to the $\gamma/2\pi$ normalization factor *and* we took care in defining the pseudo-Voigt profile (eqn. 5.14) such that the amplitude C_0 could be applied to the entire pseudo-Voigt profile.

Using two formula from table 2.2 of [68], we can relate the integral of the normalized attenuation cross-section, σ_{Rb}, to the Einstein coefficient, B_{ik}, which will be related to some very useful constants as follows:

$$\begin{aligned}\int_{\nu-}^{\nu+} \sigma_{Rb}(\nu)\,d\nu = \frac{h\nu_0}{c}B_{ik} &= \frac{h\nu_0}{c}\left[\frac{e^2 f_{ik}}{4m_e\varepsilon_0 h\nu_0}\right] \\ &= \frac{\cancel{h\nu_0}}{c}\left[\frac{e^2 f_{ik}}{4m_e\varepsilon_0\cancel{h\nu_0}}\right] = \frac{c\pi}{c\pi}\frac{1}{c}\left[\frac{e^2}{4m_e\varepsilon_0}\right] f_{ik} \\ &= c\pi\left[\frac{1}{4\pi\varepsilon_0}\frac{e^2}{m_e c^2}\right] f_{ik} = c\pi r_e f_{ik}\end{aligned} \tag{5.24}$$

where B_{ik} is the Einstein coefficient for stimulated emission between the i and k energy levels, h is Planck's constant, c is the speed of light, $r_e = e^2/4\pi\varepsilon_0 m_e c^2$ is the classical electron radius, and f_{ik} is the oscillator strength that defines the transition (and are listed in table 5.8).

Finally, we replace the integral in the last line of equation 5.23 with the equivalent integral in equation 5.24 to find the alkali density in terms of fitting parameters and known constants:

$$\begin{aligned}[\mathrm{Rb}] &= -\frac{2\pi C_0}{\gamma L}\left[\int_{\nu-}^{\nu+}\sigma_{Rb}(\nu)\,d\nu\right]^{-1} \\ [\mathrm{Rb}] &= -\frac{2\pi C_0}{\gamma L}\frac{1}{c\pi r_e f_{ik}} = -\frac{2\cancel{\pi}C_0}{\gamma L}\frac{1}{c\cancel{\pi} r_e f_{ik}} \\ [\mathrm{Rb}] &= -\frac{2C_0}{\gamma L r_e c f_{ik}}\end{aligned} \tag{5.25}$$

Line	f
Rb D1	0.34231
Rb D2	0.69577
K D1	0.334
K D2	0.672

Table 5.8: Oscillator strengths for Rb lines (ref [71] and [72]) and K lines (ref [75])

where our final equation for alkali density is composed of C_0 and γ, the amplitude and FWHM found from the fit, L the length the beam travels through the pumping chamber, r_e, the classical electron radius, c, the speed of light, and f the oscillator strength for the transition under examination.

While I've used Rb as an example here, the equation is valid for any of the four D-lines of concern in this chapter: RbD1, RbD2, KD1, and KD2.

The Integral Fit Redux

Computing an integral gives us yet another way to find the alkali density so long as we have a high signal to noise ratio. Let's take another look at equation 5.23, incorporating what we found in equation 5.24. Using Rb again as an example, we find the following correlation:

$$
\begin{aligned}
-[\mathrm{Rb}]L\left[\int_{\nu-}^{\nu+}\sigma_{Rb}(\nu)\,d\nu\right] &= \int_{\nu-}^{\nu+}S(\nu)d\nu = \int_{\nu-}^{\nu+}\ln\left[\frac{\tilde{I}}{\tilde{I}_0}\right]d\nu \\
-[\mathrm{Rb}]L[c\pi r_e f_{ik}] &= \int_{\nu-}^{\nu+}\ln\left[\frac{IG}{I_0G_0}\right]d\nu \\
-[\mathrm{Rb}]Lr_e c\pi f_{ik} &= \int_{\nu-}^{\nu+}\ln\left[\frac{I}{I_0}\right]d\nu + \int_{\nu-}^{\nu+}\ln\left[\frac{G}{G_0}\right]d\nu
\end{aligned}
\tag{5.26}
$$

where I've once again introduced the gain terms from equation 5.9. Rearranging one final time, we find the density from the integral over our data in the following way:

$$
[\mathrm{Rb}] = \frac{-1}{Lr_e c\pi f_{ik}}\left(\int_{\nu-}^{\nu+}\ln\left[\frac{I}{I_0}\right]d\nu + \int_{\nu-}^{\nu+}\ln\left[\frac{G}{G_0}\right]d\nu\right) \tag{5.27}
$$

Because the $\ln[G/G_0]$ term is integrated over all frequencies, this method only works when gain (as well as noise) can be cancelled out so that the second log term goes to zero. While fitting using a Lorentzian or a pseudo-Voigt profile is much more reliable, this method of finding alkali density was surprisingly accurate for some of my cleanest data as you can see in the results tables of appendix B. No peeking ahead, though. You're almost to the big reveal. Only one more section to go!

5.7.7 Extrapolating Alkali Density to High Temperatures with Vapor Pressure Curves

As stated in chapter 4, a number density ratio of 6 ± 1 for K vapor to Rb vapor was found to be optimal according to references [41] and [42]. This alkali density ratio maximizes the

effectiveness of AHSEOP. However, while the typical operating temperature for the pumping chamber during any of the experiments discussed in chapter 3 was between 230-245°C, the temperature of the spectroscopy oven could not maintain temperatures above 165°C due to the oven being significantly larger than the NMR/EPR oven as the spectroscopy oven must contain the entire target rather than just the pumping chamber. Therefore, it's necessary to estimate the alkali density at the operating temperature if we want to assess the target's ability to reach higher saturation polarization. We can make that estimation starting with the Clausius-Clapeyron relation, which can be found in most graduate and undergraduate thermodynamics textbooks, statistical mechanics textbooks, seemingly every single thesis from this group for the last 20 years, or in the following equation (which I adapted from references [45] and [76]):

$$\left(\frac{\partial P_{\text{vp}}}{\partial T}\right)_V = \frac{\Delta H(T)}{T\Delta\nu(P)} \tag{5.28}$$

where P_{vp} is the vapor pressure, T is temperature, $\Delta H(T)$ is the change in enthalpy as a function of temperature, and $\Delta\nu(P) = \nu_v(P) - \nu_l(P)$ is the change in specific volume from liquid (l) state to the gaseous vapor (v) state as a function of internal pressure, P. The partial derivative, $\partial P_{\text{vp}}/\partial T$, is performed over constant total volume, V, but remains a partial derivative as we're finding a relationship such that pressure and temperature may change.

Two changes can be made to this equation to more explicitly reflect the temperature and pressure dependencies of $\Delta H(T)$ and $\Delta\nu(P)$. First, consider the change in specific volume. The specific volume of the gaseous alkali is much larger than that of the liquid and so $\Delta\nu(P) = \nu_v(P) - \nu_l(P) = \nu_v(P)\,(1 - \nu_l/\nu_v) \approx \nu_v = V_v/N_v = k_BT/P_{\text{vp}}$, where the last step was made using the ideal gas law. This is justified because the vapor is low density. Second, change in enthalpy, ΔH, depends on internal energy which, in turn depends on temperature. Rather than define a specific form for internal energy (as it is usually a summation of energies used to create the system), we can expand $\Delta H(T)$ in a power series. Equation 5.28 now takes the following form:

$$\begin{aligned}\left(\frac{\partial P_{\text{vp}}}{\partial T}\right)_V &= \frac{\Delta H(T)}{T\Delta\nu(P)} = \frac{1}{T\Delta\nu(P)}\Delta H(T) \\ &= \left(\frac{P_{\text{vp}}}{k_BT^2}\right)\left(H_0 + H_1T + H_2T^2 + H_3T^3 + ...\right) \\ &= \frac{P_{\text{vp}}}{k_B}\left(\frac{H_0}{T^2} + \frac{H_1}{T} + H_2 + H_3T + ...\right)\end{aligned} \tag{5.29}$$

where H_i are constants.

Finally, we'll rearrange equation 5.29 and integrate both sides:

$$\left(\frac{\partial P_{\text{vp}}}{P_{\text{vp}}}\right)_V = \frac{1}{k_B}\left(\frac{H_0}{T^2} + \frac{H_1}{T} + H_2 + H_3 T + ...\right)\partial T$$
$$\log P_{\text{vp}} = \frac{1}{k_B}\left(H_{int} + \frac{H_0}{T} + H_1 \log T + H_2 T + H_3 T^2 + ...\right) \tag{5.30}$$

where the new term, H_{int}, is simply the constant of integration.

This is the general form of equations describing vapor pressure curves. Each of the following equations is equal to $\log(P_{\text{vp}})$ or $\ln(P_{\text{vp}})$, which can be used interchangeably without loss of accuracy:

$$\text{Antoine Eqn.[76]} = A - \frac{B}{C+T} \text{ or } A - \frac{B}{T}$$
$$\text{Wagner Eqn.[77]} = \frac{A\tau + B\tau^{1.5} + C\tau^{2.5} + D\tau^5}{T_r}$$
$$\text{Nesmeyanov formula[45]} = A - \frac{B}{T} + CT + D\ln(T) \tag{5.31}$$
$$\text{Riedel Eqn.[76]} = A + \frac{B}{T} + C\ln(T) + DT^6$$

where A, B, C, D are constants found through experimentation, $T_r = T/T_C$ is the reduced temperature, T_C is the critical temperature, and $\tau = 1 - T/T_C$ in the Wagner equation. Although, my favorite so far is the Ambrose-Walton formula [77] which looks like this:

$$\ln(P_v) = f_0(T_r) + \omega f_{(1)} + \omega^2 f_{(2)}$$
$$f^i = \frac{a_i\tau + b_i\tau^{1.5} + c_i\tau^{2.5} + d_i\tau^5}{T_r} \tag{5.32}$$
$$\omega = -\frac{\ln(P_C/1.01325) + f_{(0)}(T_{Br})}{f_{(1)}(T_r)}$$

where $\tau = 1 - T_{Br}$, $T_{Br} = T_B/T_C$ is the reduced boiling point, $T_r = T/T_C$ is the reduced temperature, and $T_C(P_C)$ is the critical temperature (pressure).

And now the big question: which equation did I use to calculate alkali densities? Well, according to reference [76], the Ambrose-Walton method or the Riedel method are better than the Clausius-Clapyeron method or Antoine equation when calculating alkali densities at low temperatures. If no constants are available, the same source suggests the Wagner equation, constrained to fit Watson's recommendations. Low temperatures are defined here as $T_r < 0.5$. For $T = 240°C$, $T_r < 0.25$ for Rb and that's the alkali with the lower T_C (thus prone to larger T_r than K). Singh (reference [45]) used the Nesmeyanov formula, which is essentially a modified Wagner or Riedel, but I can't find that paper. I cannot find constants for Rb-K systems at low temperatures for these equations anyway.

As I could not find constants for the formulae I preferred in the literature, I fell back on the thesis of Peter Dolph [78] who uses the following variation on the Antoine equation in eq. 5.31 taken from his reference [2][43]:

$$P = (\alpha + 10^{5.006}) + \frac{\beta}{T}$$

$$\alpha_{Rb} = 4.312 \qquad \beta_{Rb} = -4040 \tag{5.33}$$

$$\alpha_K = 4.402 \qquad \beta_K = -4453$$

which can be rearranged using the Ideal Gas Law to find alkali density in the following way:

$$[A] = \frac{N}{V} = \frac{P}{kT} = \frac{1}{kT}\left[(\alpha + 10^{5.006}) + \frac{\beta}{T}\right] \tag{5.34}$$

This was the same formula used when creating the alkali blends that would eventually be used in a target, so it makes sense to use this equation to estimate alkali density ratios at higher temperatures. The alkali density ratios for the temperatures I measured are in the tables of appendix B.

[43] I am not citing his reference directly as I could not gain access to the paper because, for some reason, a 40-year old paper is still behind a $60 paywall.

5.8 Spectroscopy: Results

Well, you did it. You made it. You've found The Monster at the End of this Book.[44] And much like the titular monster at the end of the children's book, the trend in my results that does not match expectations isn't as bad as I feared when I started this journey.

As I've discussed in section 5.5, I expected a Lorentzian shape for a pressure broadened absorption line and indeed I did see a Lorentzian! "Mission Accomplished!", as they say[45]. With increased temperature, I expected the Lorentzian to change in two fundamental ways. First, the amount of alkali vapor increased, so I expected the lines to become deeper; I expected less light would pass through the entire target near resonance because there would be more alkali vapor to absorb the light and re-emit it in some random direction.

To illustrate this deepening of lines, the results presented are first separated into "high power" and "low power" results. I've plotted the attenuation of the beam versus temperature in several figures: 5.15 and 5.16 are runs completed at high power while 5.17 and 5.18 are runs completed at low power. Attenuation (i.e. the magnitude by which the beam intensity is reduced) is defined in equation 5.8.

The fact I have both high- and low-power results is serendipitous. When I began the task of building a spectroscopy system, I did not understand saturation broadening. The power of the beam entering the oven during these tests was typically between 20-125 mW. Once I better understood what I was doing, I adjusted the power as described in section 5.6. So, the "high" and "low" power labels simply separate results between those that may have experienced saturation broadening and those that did not, respectively. It's actually fortunate that I have both high- and low-power data as I now have a plethora of data that was likely experiencing saturation broadening (and the importance of that will be further discussed in section 5.9.

[44] This is a reference to one of my favorite children's books, "The Monster at the End of this Book: Starring Lovable, Furry Old Grover" (1971), written by Jon Stone and illustrated by Michael Smollin. It's delightful.

[45] In May 2003, then president George W. Bush gave a speech aboard the aircraft carrier USS Abraham Lincoln with a banner in the background touting the phrase "Mission Accomplished". Some thought Bush was announcing the end of the Iraq war which was in the beginning of it's second year. It would last at least another *eight* years and arguably much longer as we had other countries to spread "democracy" to (by force, if necessary). Forgive my dark humor here, gentle reader. I may be a little disillusioned and cynical, but I do aim to entertain with these references.

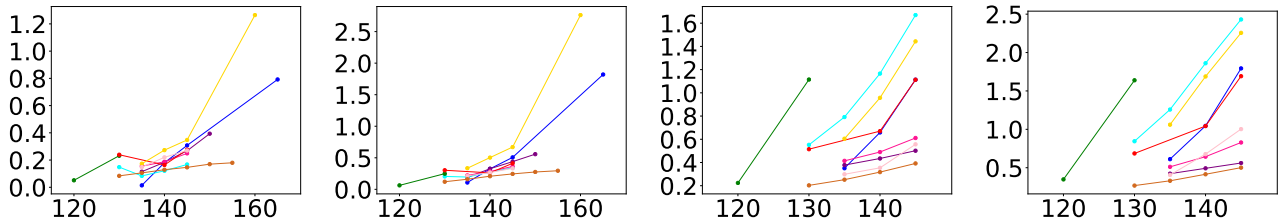

Figure 5.15: Maximum attenuation vs. temperature (in °C) of absorption lines for all target cells scanned at high power. From left to right, plots are Rb D1, Rb D2, K D1, and K D2. Colors are for the following runs: Brianna Run 1 (blue), Florence Run 2 (red), Fulla Run 1 (purple), Fulla Run 2 (green), Fulla Run 5 (cyan), Noah Run 1 (deep pink), Sandy II Run 1 (gold), Sandy II Run 2 (pink), and Wayne Run 1 (chocolate).

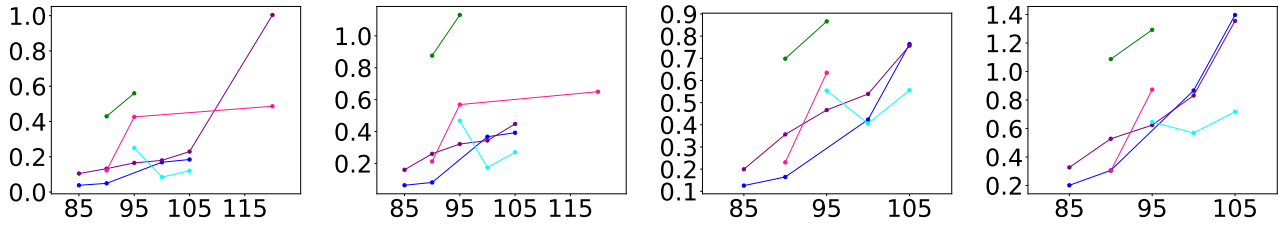

Figure 5.16: Maximum attenuation vs. temperature (in °C) of absorption lines for all Kappa cells scanned at high power. From left to right, plots are Rb D1, Rb D2, K D1, and K D2. Colors are for the following runs: Kappa 1 Run 2 (blue), Kappa 2 Run 1 (red), Kappa 3 Run 1 (purple), Kappa 4 Run 1 (green), and Kappa 4 Run 2 (cyan).

Additionally, I separated results by the pressure/shape of the cell. Target-cells are are the Bastille-Day design shown in figure 4.1 and used in the A_1^n-II and d_2^n-II experiments. Sadly, the coathanger design used in the G_E^n-II experiment was too large to fit in the spectroscopy oven. The other type of cells were "Kappa" cells. These were small, roughly spherical cells approximately the size and shape of a target-cell pumping chamber. Kappa cells were filled to just under 1 atm and were used primarily to test the gas handling system during it's retrofit. The first few Kappa cells (specifically Kappas 1-4) were also used to measure κ_0, the dimensionless parameter discussed in section 4.3.5. See Katugampola *et al.* [49] for details on those measurements.

The first thing you'll notice about these plots is they are *incredibly* busy. That is by design: you're looking at all of the spectroscopy data I've ever taken. Even through all of that noise, the trend is very clear in the low power data: the line goes up. That is to say higher temperatures do indeed relate to higher attenuation in the low power target-cell data and the low power Kappa-cell data. To a lesser extent, the trend is visible in the high power data, even through the noise of so many data sets. We're off to a great start!

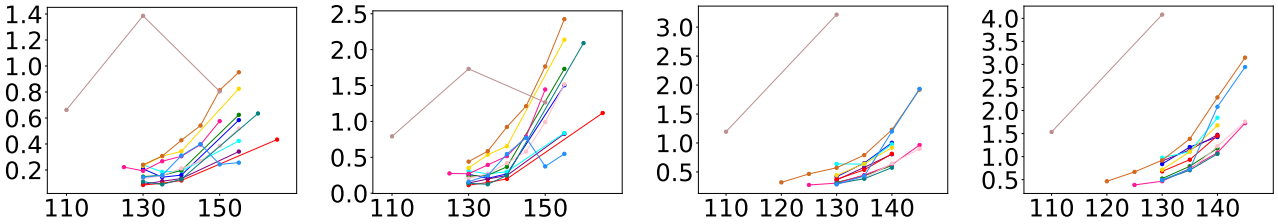

Figure 5.17: Maximum attenuation vs. temperature (in °C) of absorption lines for all target cells scanned at low power. From left to right, plots are Rb D1, Rb D2, K D1, and K D2. Colors are for the following runs: Austin Run 1 (blue), Big Brother Run 1 (red), Brianna Run 2 (purple), Butterball Run1 (green), Butterball Run 2 (cyan), Dutch (deep pink), Florence Run 3 (gold), Florence Run 4 (pink), Florence Run 5 (chocolate), Fulla Run 6 (rosy brown), Tommy Run 1 (teal), and Wayne Run 2 (Dodger blue).

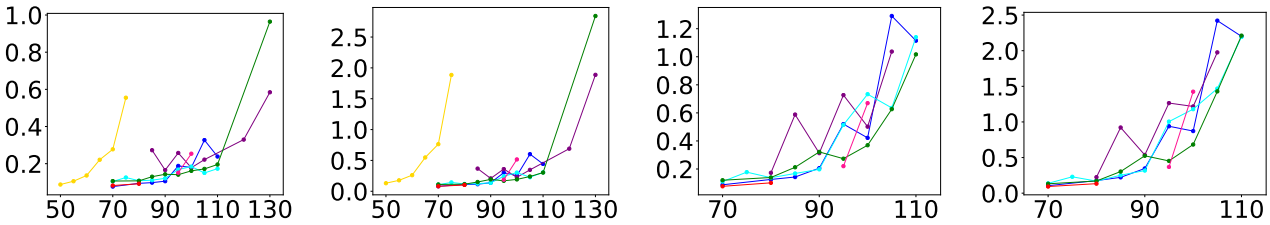

Figure 5.18: Maximum attenuation vs. temperature (in °C) of absorption lines for all Kappa cells scanned at low power. From left to right, plots are Rb D1, Rb D2, K D1, and K D2. Colors are for the following runs: Kappa 2 Run 2 (blue), Kappa 3 Run 2 (red), Kappa 3 Run 3 (purple), Kappa 3 Run 4 (green), Kappa 4 Run 3 (cyan), Kappa 4 Run 4 (deep pink) and Kappa 5 Run 1 (gold).

The second thing I expected to see was pressure broadening of the spectral lines as the atoms would collide more, de-exciting electrons faster than at lower temperatures, and leading to a wider range of lifetimes for the electrons in the excited state. Indeed, several of the broadening factors mentioned at the top of this chapter depend on temperature and increase as temperature increases. Additionally, equation 5.22 shows that if ^{3}He and N_2 density were constant, FWHM most certainly *increases* as temperature does. Naively, it is not obvious to me why I should expect a behavior any different from that shown in eq. 5.22, which would be consistent with that described by Romalis *et al.* *and* by Demtröder.

But that's just not what I observed. Behold, the fascinating trend I've alluded to this entire chapter: the line that should[46] go up...goes *down*!!!

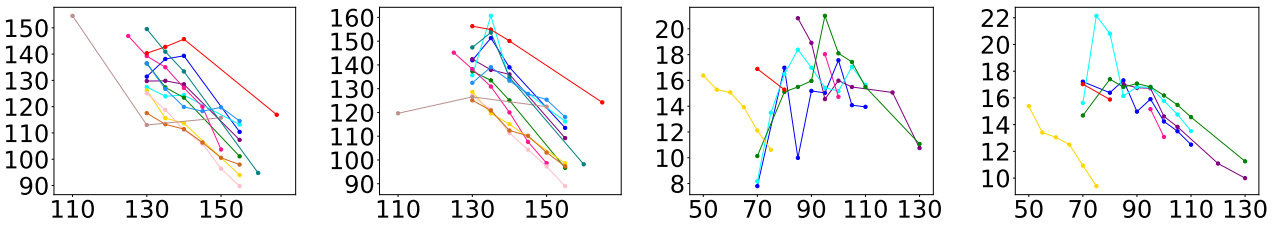

(a) Target Rb D1 **(b)** Target Rb D2 **(c)** Kappa Rb D1 **(d)** Kappa Rb D2

Figure 5.19: FWHM (GHz) vs. temperature (in °C) for TARGET and KAPPA cell Rb D-lines measured at LOW POWER.

I've plotted the FWHM versus changes in temperature for Rb D1 and D2 lines measured at low power for both target-cells and Kappa-cells (fig. 5.19). These plots are indicative of the overall trend I saw in all low power data, which is in direct opposition to what I expected based on the work of Romalis *et al.* and Kluttz *et al.* (references [69] and [74]) as well as what I understood from Demtröder (reference [68]). The high power data is more ambiguous, but this could be a result of saturation broadening. Certainly for the low power tests, where saturation broadening is *not* an issue, the trend is clear: FWHM decreases as temperature increases.

Another way to examine this trend is by taking the ratio of the FWHM and the combined density of the gases in the cells to examine how the constants described in equation 5.22 change as temperature increases. I justify combining the ^{3}He density and N_2 density because the coefficients given by Romalis *et al.* for each gas are similar and the amount of N_2 in the cells is small. The results for data taken at high power are plotted in figures 5.20 and 5.21. The data points are the average of the FWHM/Density for all target-cells or Kappa-cells, respectively. The uncertainties are the combined standard deviation from the fit of the FWHM, the assumed uncertainty in the density found from the filling process, and the standard deviation of the ratio of FWHM/density for all cells in that figure.

From figures 5.20 and 5.21, we can see the results for measurements at high power do not conclusively show this same trend as the FWHM plotted against temperature that is so clear in the low power data shown in figure 5.19. The results at low power are less ambiguous, as

[46] I say "should" based on previous work by this group and based on my expectations from literature I have been exposed to. I definitely expected the opposite trend, but I'll get into that more in section 5.9

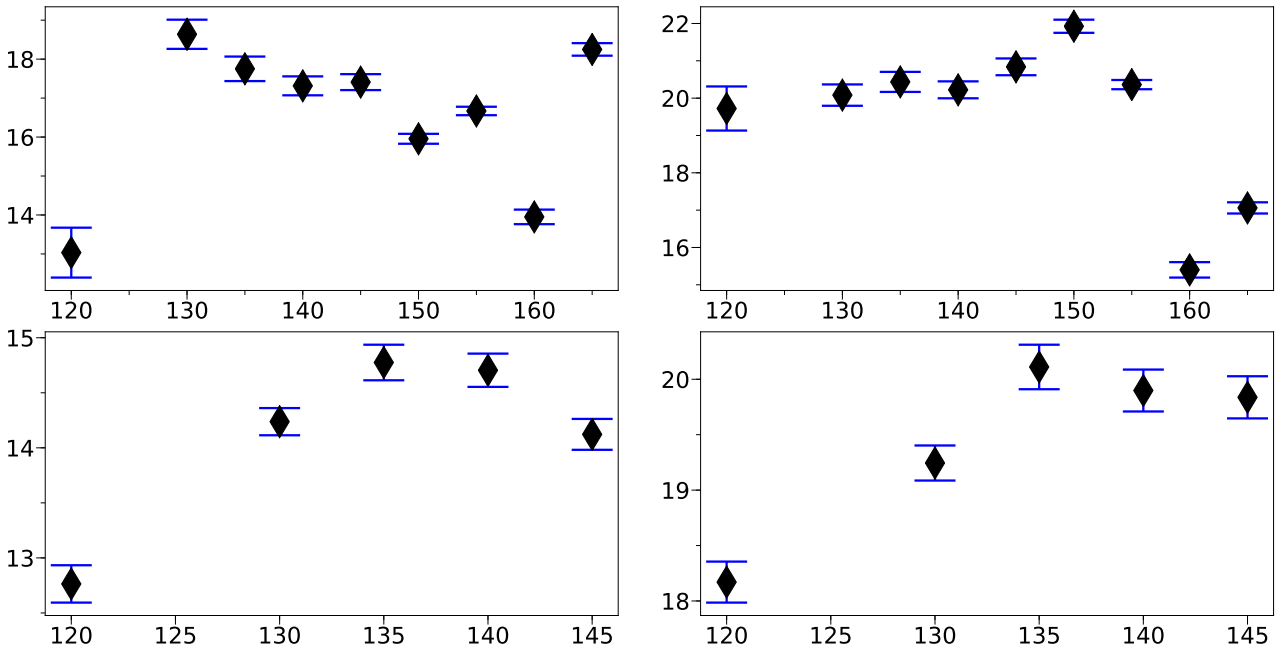

Figure 5.20: Average FWHM/Density (GHz/Amagats) vs. temperature (in °C) for TARGET cell absorption lines measured at HIGH POWER. Starting from upper left, plots are Rb D1, Rb D2, K D1, and K D2.

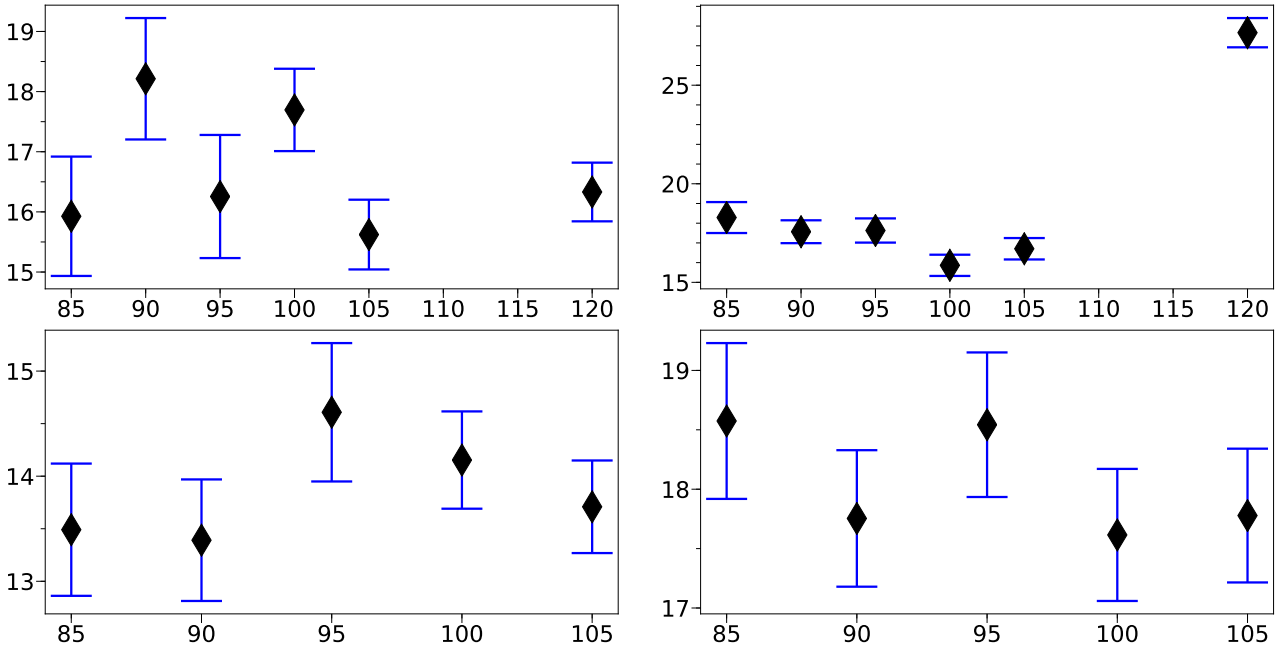

Figure 5.21: Average FWHM/Density (GHz/Amagats) vs. temperature (in °C) for KAPPA cell absorption lines measured at HIGH POWER. Starting from upper left, plots are Rb D1, Rb D2, K D1, and K D2.

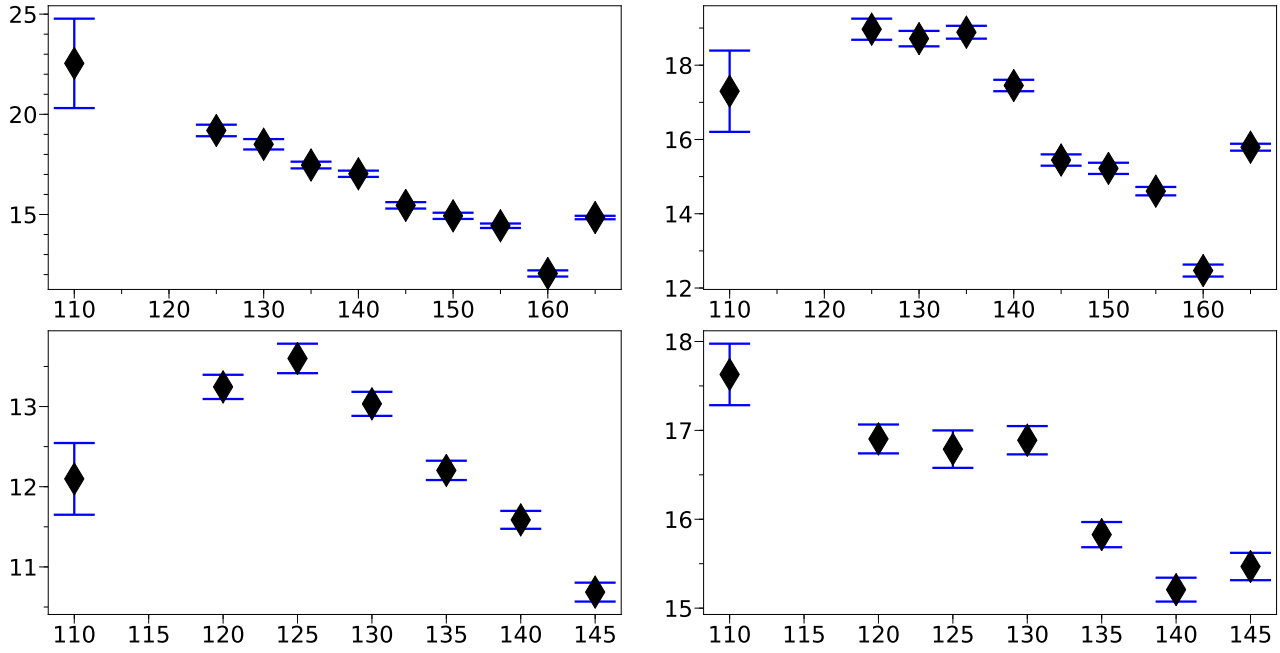

Figure 5.22: Average FWHM/Density (GHz/Amagats) vs. temperature (in °C) for TARGET cell absorption lines measured at LOW POWER. Starting from upper left, plots are Rb D1, Rb D2, K D1, and K D2.

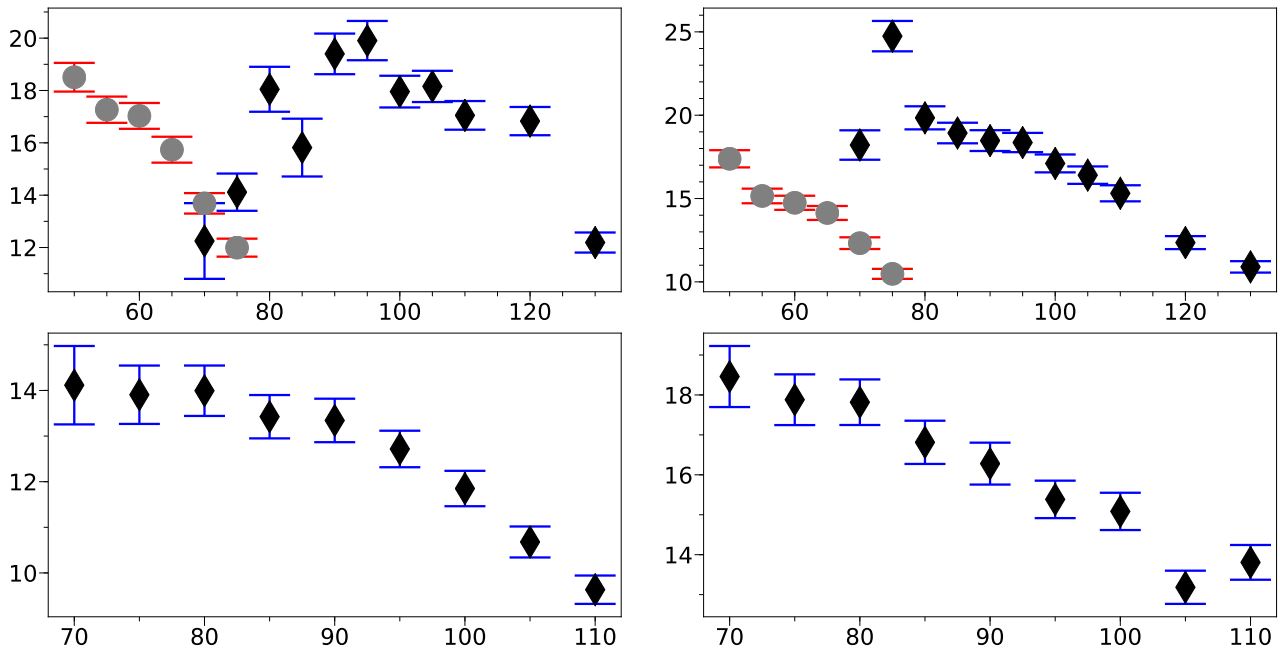

Figure 5.23: Average FWHM/Density (GHz/Amagats) vs. temperature (in °C) for KAPPA cell absorption lines measured at LOW POWER. The gray circles represent Kappa 5, the only Rb-only cell for which I gathered data. Starting from upper left, plots are Rb D1, Rb D2, K D1, and K D2.

you can see in figures 5.22 and 5.23. In all of the absorption lines for Kappa-cells and most of the absorption lines for target-cells, the same trend as before is visible: the FWHM/density appears to decrease as temperature increases, in direct opposition with the trend expected as reported by Romalis *et al.* and Kluttz *et al.* as well their predecessors.

I conferred with Todd Averett at the College of William and Mary (W&M) regarding this trend, considering his previous work on this and close association with our group at the University of Virginia (UVa)[47] (Averett is part of the "*et al.*" in "Kluttz *et al.*"). His system was recently upgraded to the same diode laser system we used, the Toptica DLC and DL Pro described in section 5.2. We loaned him Florence, one of the Bastille Day target-cells, and he performed spectroscopy measurements. The results are in table 5.9.

	Temp	Power	RbD1	RbD2	KD1	KD2
Date	K	mW	GHz			
2021-03-03	136				108	149
2021-03-12	144	0.127	135	156	112	162
		0.1			120	169
2021-03-15	146	0.2		155		
		1		155	110	153
	145	1			109	152
		0.123 to 0.246			110	156
	157	1	134		116	180
2021-03-16	162			158		
2021-03-19	162	1			120	196
		1	135	158	122	199
2021-03-23	162	1-4	135	159	121	198

Table 5.9: Results from Averett *et al.* at the College William and Mary for target-cell Florence. I do not know if power here refers to the power from the laser or the power of the laser going through the pumping chamber.

As you can see from table 5.9, the trend is not as pronounced as in my data, though it is present. Additionally, there are nuances regarding the differences in their data versus mine that will be discussed further in section 5.9. Averett and I were in the process of comparing the two systems in mid-2021 when my primary focus necessarily shifted to characterizing G_E^n-II target-cells.

There was a question of whether the system Kluttz *et al.* used was, perhaps, too different from my system to make a direct comparison (different optics, different noise reduction techniques, etc.). There was also the question of whether or not they were attenuating power and whether *my* power attenuation had an effect on the results; I wanted to investigate the effect of saturation broadening on my results. I opted to take a run mimicking the power attenuation,

[47] Here's a fun history fact about these two schools. Thomas Jefferson founded UVa, but attended the College of William and Mary. Jefferson owed W&M $17k and it caused W&M to shut down in the 1880's. He never fully paid it back. UVa gave them a statue of Jefferson 1992, but I hardly think this counts as repayment. I mean...how much could a statue cost in 1992? Certainly not $17k! Adjusting for inflation, Jefferson owes over $300k to W&M for his two years of school. Shameless.

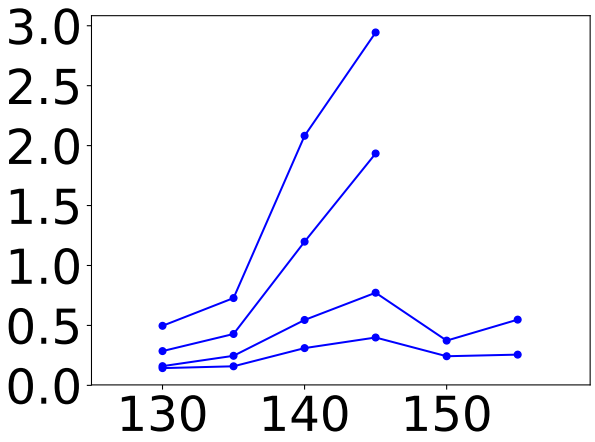

(a) Attenuation for low power

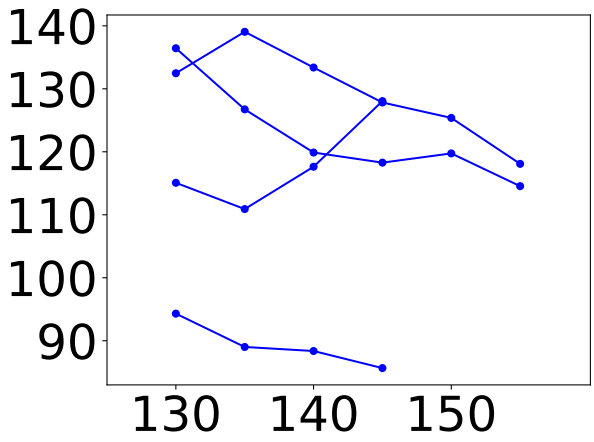

(b) FWHM for low power

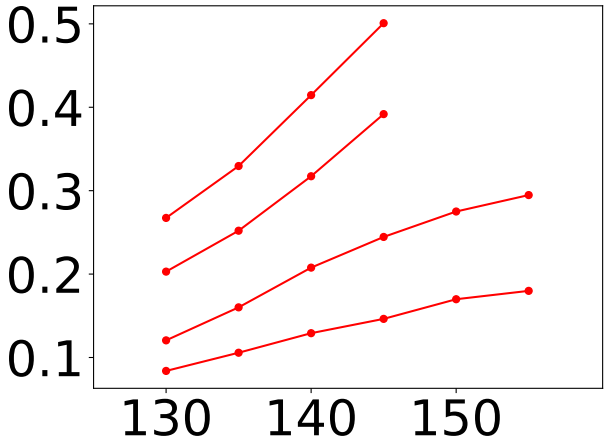

(c) Attenuation for high power

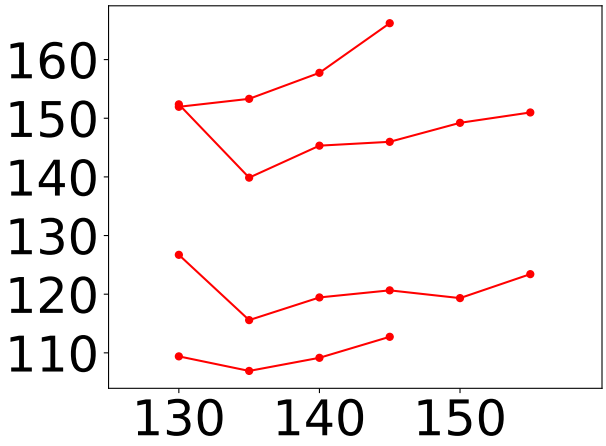

(d) FWHM for high power

Figure 5.24: Results for run 1 (high power, bottom) and run 2 (low power, top) of target-cell Wayne for each of the 4 absorption lines. of low power tests for Wayne. On the left, attenuation plotted against temperature (°C). On the right, FWHM (GHz) plotted against temperature.

gain, settings, etc of the group at W&M followed by another run on the same target but with my usual settings. This resulted in two runs for target-cell Wayne. For run 1, I removed the crossed polarizer cubes and did *not* attenuate power in any way. additionally, I bypassed the lock-in amplifiers as Averett informed me via email that they were not using them at the time. The results for these tests are in figure 5.24. FWHM trended down with increased temperature for the low power results (save for the KD2 line), but not for the high power results, either increasing or staying relatively even.

Additionally, before passing Florence along to Todd Averett at William and Mary, I collected several data sets at low power at each temperature, intending to see if the FWHM trending down survived the application of (gasp) *statistics*. This resulted in Florence run 4. I scanned the four absorption lines at four different temperatures: 130°C, 135°C, 140°C, and 145°C. As you may have noticed in the plots of this section (and certainly will notice in the tables in appendix B), these were my four standard temperatures when taking a run of data. The difference with Florence run 4 was that I took 5 data sets at each temperature. I also took one data set each at two additional temperatures (150°C and 155°C) for the Rb-lines only, though my standard operating procedure with a target was to only take data for one additional, higher temperature for the Rb-lines.

These results are on display in figure 5.25. Errors for these data were added in quadrature, as per usual. As you can see, the attenuation for each of the four absorption lines trends up, as expected. The FWHM unambiguously trends down.

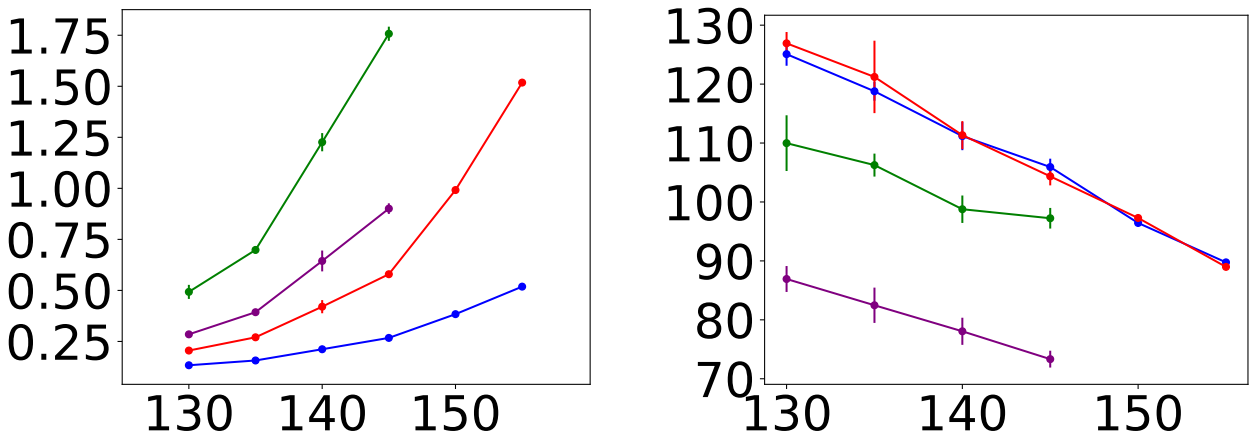

Figure 5.25: Results of low power test, Florence Run 4, with error bars reflecting combined error from all measurements at that temperature for each of the 4 absorption lines: RbD1 (blue), RbD2 (red), KD1 (purple), and KD2 (green). On the left, attenuation plotted against temperature (°C). On the right, FWHM (GHz) plotted against temperature.

One last comparison to make is between the results herein and the results of both Romalis *et al.* and Kluttz *et al.*, though there is unfortunately not much crossover in the temperature ranges studied in both of those papers and the temperature ranges studied herein. However, we all collected data at 80°C. So, in table 5.10, I show the results from those previous works

and my results here for low power measurements of Kappa-cells, the only data I have at 80°C.[48] These data exclude Kappa 5 (the only Rb-only cell) because I did not take measurements for Kappa 5 at 80°C. As you can see from table 5.10, the three sets of measurements are consistent with one another at 80°C.

	RbD1	RbD2	KD1	KD2
Romalis	18.7(3)	20.8(2)		
Kluttz	18.31(7)	20.51(8)	14.26(9)	19.59(1)
This Work	18.05(86)	19.84(69)	14.00(55)	17.82(57)

Table 5.10: A comparison of FWHM/density (GHz/amagats) for absorption lines of Kappa-cells measured at low power with FWHM/density for those same lines taken at 80°C from Romalis *et al.* and Kluttz *et al.*

Finally, while the plots in this section summarize these spectroscopy results, full results are available in the veritable cornucopia of tables residing in appendix B. I warn you: it's about 30 pages long. You're free to peruse it, of course, if you're feeling particularly masochistic.

5.9 Spectroscopy: Conclusions

While I am infinitely proud of how well the spectroscopy and interferometry systems work, I am mildly disappointed that I did not figure out why the FWHM as well as the FWHM divided by density trended down as temperature increased. I have no doubt that is what is occurring as the data are quite clear. However, I truly wish I could have found the narrowing mechanism or systematic that was causing the phenomenon. I'm *very* certain it was the former. Additionally, maybe I could have had my name on something? Unlikely. I'm sure if anyone gets their name on it, it's Enrico Fermi[49].

And why am I so sure the phenomenon is not caused by a systematic issue? Well...

5.9.1 Systematic Issues Resolved

While I initially thought the phenomenon was due to some systematic oversight on my part, I seem to have swapped out most of the components of the system for different models at one time or another. This includes the optical chopper, both the non-polarizing and polarizing beam-splitters, and the elimination of every mirror in the spectroscopy system (and even *those* were changed out before being removed completely).

I'd like to detail for you some systematic concerns that I have ruled out. First, the trend appears in the primary signal as well as the ratio of the primary and reference signal, so I know the phenomenon is actually in the data and not an artifact of that particular noise-reduction

[48] For future generations looking into this, a brief note relayed to me by Todd Averett: Tom Gentile measured the numbers in table 5.10 for K-lines, though that work remains unpublished. While not important to this thesis, this information may come in handy to the next researcher. If not, I've wasted very little ink passing the information along.

[49] Why Fermi? Because his name is on *everything*! Seriously, Fermi, save some discoveries for the *rest* of us!!!

technique (which I do not believe the William & Mary group utilizes at the time of this writing). Temperature differentials, which I initially suspected, are likely not the cause either. If this were the case, the phenomenon would not appear in data from Kappa-cells. Additionally, temperature differentials within the oven only range as high as ±5°C. Experience with the NMR/EPR system leads me to believe a significantly higher temperature differential would be required to induce the kind of convection that would spoil my spectroscopy results. And again, the trend appears in data from Kappa *and* target-cells. I have no explanation as to why the phenomenon would appear in Kappa-cells if it were due to temperature differential-induced convection.

Two components I certainly never changed were the photo diodes. The phase of the signal coming from the photo diodes appears to be temperature sensitive. While a phase difference was handled by adjusting the phase of the signal at the lock-in and only after the oven temperature settled at its set temperature, I do not know if there were other temperature dependent effects present in the photo diodes. Additionally, the photo diodes appear to be sensitive to background light such as the lights in the room and the light from the "Death Star"[50]. I attempted to shield these with cardboard tubes, but to no avail. My solution was to only began a scan when the Death Star[51] lasers were on or off and when that status would not be changing during the length of the entire scan. Also, I left the room lights on perpetually.

I can also rule out saturation broadening (in the low power results, anyway). A quick and simple test to check for line saturation is to check the ratio of the oscillator strengths of the D1 and D2 lines for a particular alkali and compare this ratio to the ratio of the maximum attenuation of the same two lines. Indeed, this is how I first discovered I was using too much power. After attenuating my laser power, the ratio of the oscillator strengths and the ratio of the D1 and D2 maximum attenuation are in good agreement for both alkali species.

I can also rule out inadvertent pumping to a specific ground state through accidental circular polarization. While there was some initial concern I was seeing the effects of circularly polarized light, the introduction of the crossed linear polarizers eliminates that concern completely.

One last systematic concern I feel I've ruled out is the scanning rate. When I collected data for a single data point, I accumulated data for 4 seconds and then averaged those data to create a single data point. If this were faster than the population mechanisms in the alkali, there would be transit-time effects[79]. However, most of these effects would be broadening and I am certain I am looking for a narrowing mechanism. Additionally, transition-time broadening has a Gaussian shape similar to Doppler broadening[68] and my absorption lines were clearly Lorentzian. Even when fitting with the pseudo-Voigt profile, the dominant contribution to the line shape was Lorentzian as you can see by the reported values of η in every table in appendix B.

[50] A reference to *Star Wars*, Directed by George Lucas, Performances by Mark Hamill, Harrison Ford, Carrie Fisher, Peter Cushing, and Alec Guiness, 20th Century Fox, 1977

[51] Seriously, I hope this franchise is still being talked about if you're reading this in a hundred years. Absolute classic.

5.9.2 Differences Between the Ti:Sapphire system and the Diode Laser System

While I am confident my results after I began attenuating power were not power-broadened, I am not confident the Ti:Sapphire laser was not experiencing saturation broadening. The Ti:Sapphire laser system can provide power up to 500-600 mW (though I believe the system was being operated between 200-300 mW). Even prior to attenuating my power, the Toptica DL Pro provides a maximum power of only 125 mW. Additionally, I do not know the size of the Ti:Sapphire laser beam when it interacted with a target (also known as the "spot-size"). If it was similarly as small as the Toptica DL Pro used in my measurements, I have no doubt the Ti:Sapphire system would experience saturation broadening. Like collisional broadening, saturation broadening has a Lorentzian shape meaning the trend seen in the Ti:Sapphire system, where FWHM trended upward with increases to temperature, could be an effect of saturation broadening and not collisional broadening.

Another key difference in the systems was the size of the targets being measured, but the only effect I can imagine this would have would involve temperature gradients. The Ti:Sapphire system would then have smaller temperature gradients. However, I have little reason to believe temperature gradients are causing this phenomenon because, as I previously stated, the Kappa-cells show the FWHM and FWHM/density decrease as temperature increases. I simply include this statement for the sake of completeness.

5.9.3 Differences Between the W&M system and the UVa System

I'm not confident the laser power in the work done by Kluttz *et al.* was attenuated. If that were the case, there may have been power broadening. Unfortunately, the paper does not mention power attenuation at all. However, this is a moot point as that work measured temperatures between 67°C and 127°C, which is well outside of the range of temperatures I have examined in the target-cell measurements. Additionally, the targets used in that work utilized a variable density and pressure as they were also investigating pressure dependence on the broadening of the absorption lines.

The new system at William & Mary (W&M) utilizes the same laser and controller system as UVa. In discussion with the Averett group at W&M, we found the differences in our current spectroscopy systems are primarily in our procedure. First, when I set the power leading into the oven, I set the power at the end of the K D2 line, which is both the end of my scan and where the power output of the laser is minimal. I then scan across the entire range of all four absorption lines. The procedure of the Averett group at W&M differs in that they set the power at the beginning of each individual line. They then scan the individual lines one at a time rather than the "set it and forget it" method I use. Still, the power variation over my entire scan range was well below the proscribed power (1-3 mW/cm^2) from Romalis *et al.* when I lowered the power to 10% of my usual operating power. I saw no unexpected difference between the results at my normal power output and results at 10% of that output.

More tests would be necessary to thoroughly compare the system at W&M and the system at UVa. I will close this section by noting that, just as I observed with my data and my numerous fitting equations, the fitting equation used by the Averett group at W&M is in good agreement with their data and so Averett trusts the widths. I look forward to seeing more

results from William & Mary and seeing them compared to our system.

5.9.4 Final Thoughts

I don't believe any systematic effect would explain the trend in which the FWHM *and* the FWHM/density appear to decrease with increasing temperature. From what I observe and what I have reported here, the phenomenon is clearly present in data where all possible systematic concerns were accounted for. However, there must be some narrowing mechanism to explain the phenomenon, a mechanism I have not yet encountered.

I do not believe the phenomenon is due to Dicke narrowing (also known as collisional narrowing) as Dicke narrowing requires lower pressures[68] than even the Kappa-cells. As temperature increases, pressure-broadening overtakes Dicke narrowing as the dominant collision-related effect.

And I'll end my speculation with one more theory based on reference [79]. As Himsworth and Freegarde say in that 2010 paper, "closed two-level systems [...] will generally have several ground and excited states into which they may be optically pumped. If these additional states are separated by frequencies greater than the laser linewidth, then once these states are populated, the atom will become transparent to the laser radiation." The laser linewidth of the Toptica DL Pro is quite small, ranging from 0.5 - 90 kHz. Himsworth and Freegarde also say this could happen even at low laser intensity and significantly affects sub-Doppler features. Maybe that's something considering the pseudo-Voigt fit conforms to the data better than the Lorentzian fit, I'm not sure. I personally feel it warrants further investigation.

I wish my successors the best of luck in determining the source of this unexpected (and perhaps novel) phenomenon!

Chapter 6

...and an ending.

Harry: "*Anyhow, so....thanks for coming.* [...] *If I had to sum it up, and I do– because, you know, it's like, the end. I would say that this* [thesis] *is about– it's about friendship.*"
Perry: "*What are you doing?*"
Harry: "*I'm trying to wrap up the* [thesis] *and leave the people with a message.*"
Perry: "*I've got a message for you: Get your feet off my* [...] *desk* [...] *and stop narrating...obviously.*"

– *Excerpt from "Kiss Kiss Bang Bang"*[1]

So, obviously, this thesis is about friendship. From Sumudu Katugampola and his predecessors to me to Jacob Koenemann and Braian Mederos and the helpful guidance of Huong Thi Nguyen, Gordon Cates Jr. and Vladimir Nelyubin. I mean, have I even mentioned the numerous people that have helped me along the way!?! Yes. Yes, I mentioned some of them. They're in the acknowledgements section. But I will say this about earning a PhD: no task I've ever aimed for in my entire life has relied so heavily on the kindness and support of others.

But you, my dear reader, are not here to hear me ramble....you are interested in the *science*. Well, here's some closing thoughts about that...

6.1 The future of A_1^n, d_2^n, and G_E^n Measurements: The Next Stage in ^{3}He Targets

Successful employment of convection targets in these three experiments at JLab mark the closing of a chapter both in my personal history as well as the overall development of polarized ^{3}He targets. Of course, challenges lie ahead for future experiments, especially as beam current continues to increase. The Bastille Day and coat hanger designs as well as the work understanding the permanent magnetization and hysteresis effects which appeared in our targets puts us on solid ground for developing even more advanced targets in the future. Maybe a metal

[1] *Kiss Kiss, Bang Bang.* Directed by Shane Black, performances by Robert Downey Jr., Val Kilmer, Michelle Monaghan, and Corbin Bernsen, Warner Bros. Pictures, 2005

end-window will make an appearance in the next generation of targets. That would be pretty neat.

6.2 The Future of Spectroscopic Measurements in Cates Group: A Tantalizing Mystery

If there's one thing that makes the writing of this thesis as well as my imminent graduation bittersweet, it's the work I leave behind. The unexpected trend in the FWHM and FWHM/Density is fascinating, right? I've been puzzling with that issue, first as a systematic error and then as an interesting physics problem, for the better part of six years. The work is in very capable hands, though, as Jacob Koenemann has hit the ground running and is already taking fresh data and trying new ideas. My time investigating this mystery is likely at an end. C'est la vie.

6.3 The End of the Line

Some would say this final chapter was a waste of time. Is there anything really left to say after so many pages? Well, I mean, *I* clearly think so. It seems silly to end with the conclusion section of a chapter without adding some final thoughts, right? And, I suppose, here they are.

Thank you.

Thank you for taking time to read this thesis, thank you for your interest regarding the topics herein, and thank you for indulging me and my humor. I leave you with the immortal words of President Abraham Lincoln: "Be excellent to each other."[2]

[2]This is actually Robert V. Barron portraying President Abraham Lincoln in the film *Bill and Ted's Excellent Adventure*. Directed by Stephen Herek. Performances by Keanu Reeves, Alex Winter, and George Carlin. Orion Pictures. 1989.

Appendix A

Data Tables of Chapter 4

The following tables represent the data used for figures in chapter 4. Much of the data from older targets in table A.1 was retrieved from the UVa Spin Physics group website which can be found at (https://galileo.phys.virginia.edu/research/groups/spinphysics) or from the "Hybrid Paper", which is reference [53]. The data in table A.1 was used to construct figure 4.29 and was gathered from the following sources:

1. 2001 A_1^n-I: Target polarization, ^{3}He density, and the names of the actual targets are taken from Zheng's thesis [80] and the experiment's corresponding paper, Zheng *et al.* [14]. All other information was taken from the Spin Physics Group website.

2. 2003 small angle GDH: Target and beam polarization estimates for saGDH targets were taken from Singh's thesis [45]. All other data was sourced from the Hybrid Paper.

3. 2006 G_E^n-I: Target polarization was retrieved from both Kelleher's thesis [62] and Singh's thesis [45]. Beam current and polarization were taken from the experiment's corresponding paper, Riordan *et al.* [40] and Singh's thesis [45]. All other data was retrieved from the group website and the Hybrid Paper.

4. 2008 Transversity: Target polarization comes from Huang's thesis [63] and matches the target polarization discussed in Katich's thesis [64]. Beam polarization is also from Katich's thesis [64]. Target volumes (save for Maureen) were taken from the group website. All other data comes from Hybrid Paper.

5. 2009 d_2^n-I: Current and target polarization are from corresponding paper, Flay *et al.* [29]. All other information is from the group website and Hybrid Paper.

6. 2020 A_1^n-II: Target polarization is the average target polarization as reported in Murchana's thesis [33].

7. 2020 d_2^n-II: Target polarization is the average target polarization as reported in Chen's thesis [32].

8. 2023 G_E^n-II: Target and beam polarization are from preliminary analysis at JLab [39].

For differential temperatures in the PC and TC, ^{3}He density can be scaled using the following formula from Zheng's thesis [80]:

$$n_{pc} = \frac{n_0}{1 + \frac{V_{tc}}{V_0}\left(\frac{T_{pc}}{T_{tc}} - 1\right)}$$
$$n_{tc} = \frac{n_0}{1 + \frac{V_{pc}}{V_0}\left(\frac{T_{tc}}{T_{pc}} - 1\right)} \tag{A.1}$$

where n_{pc} and n_{tc} are the densities in the PC and TC at operating temperature, respectively. n_0 is the fill density at room temperature. V_0, V_{pc}, and V_{tc} are the total, PC, and TC volumes, respectively. T_{pc} and T_{tc} are the temperature *inside* of the pumping chamber and target chamber, respectively.

When finding estimated ^{3}He density in the target chamber at operating temperature, internal temperature for PC and TC were estimated as the estimated external temperature plus 15°C. This was the same estimation used when taking polarimetry measurements at UVa. Therefore, when assuming the external temperatures of the PC and TC were 240°C and 50°C, respectively, internal temperatures for the PC and TC are estimated at 255°C and 65°C, respectively.

Table A.1: Comparison of Effective Luminosity in units of $10^{34} \cdot \text{cm}^{-2} \cdot \text{s}^{-1}$ from several eras of target production across 8 experiments. ^{3}He Den. is fill density at room temperature and is scaled to operating temperature using equation A.1.

	I_b	^{3}He Den.	Total Vol.	TC Len.	Max Pol.	Scaled FOM
Target	μA	(amg)	mL	cm.	%	$10^{34}\text{cm}^{-2}\text{s}^{-1}$
2001 - A_1^n-I						
Gore	12.0	9.10	171.90	25.00	36.32	7.99
Tilghman	12.0	8.28	173.50	25.00	42.17	9.81
2003 - saGDH						
Peter	6.1	8.80	208.60	39.40	38.20	6.39
Penelope	2.2	8.93	204.30	39.70	39.00	2.44
2006 - G_E^n-I						
Edna	8.0	7.40	378.30	38.70	48.50	12.37
Dolly	8.0	7.39	378.30	38.70	45.00	10.68
Barbara	8.0	7.56	386.20	38.70	40.00	8.71
2008 - Transversity						
Astral	12.0	8.18	251.40	38.40	65.00	34.64
Brady	12.0	7.88	249.90	38.40	64.00	32.68
Maureen	12.0	7.63	268.50	39.80	60.00	28.59
2009 - d_2^n-I						

Continued on next page

Table A.1 – continued from previous page

	I_b	^{3}He Den.	Total Vol.	TC Len.	Max Pol.	Scaled FOM
Target	μA	(amg)	mL	cm.	%	$10^{34}\text{cm}^{-2}\text{s}^{-1}$
Samantha	15.0	7.97	259.00	38.40	50.50	25.79
2020 - A_1^n-II						
Fulla	30.0	6.33	470.98	40.32	58.00	57.67
Big Brother	30.0	6.99	427.18	40.01	58.00	62.33
Dutch	30.0	7.76	441.54	39.69	58.00	68.13
Brianna	30.0	6.94	416.38	39.50	58.00	61.28
2020 - d_2^n-II						
Brianna	30.0	6.94	416.38	39.50	58.00	61.28
Tommy	30.0	7.76	433.61	40.00	45.00	40.99
Austin	30.0	7.54	438.97	40.40	44.99	39.91
2023 G_E^n-II						
Hunter	45.0	7.39	511.94	59.44	48.28	97.48
Windmill	45.0	6.99	665.54	60.33	47.52	93.31
Fringe	45.0	6.71	703.57	60.12	44.67	78.83
Chicago	45.0	6.89	682.04	60.34	35.65	51.17
Donya	45.0	6.88	583.45	59.78	47.27	86.37

	Max Pol.	Max Lifetime	Receipt to Assembly	Assembly to Bake
	%	Hrs	Days	Hrs
Phoenix	26.894	2.71	25	26.00
Dutch	38.239	20.43		1.83
Savior	40.145	10.887	16	3.00
Wayne	41.230	2.556	1	25.00
Florence	44.802	9.837		71.63
Chout	50.499	8.957	2	6.00
Brianna	56.122	19.889	9	22.17
Butterball	56.136	14.307	5	53.00
Austin	56.668	18.705	4	22.50
Fulla	58.452	26.537		1.47
Big Brother	61.748	23.424	2	28.50

Table A.2: Two tables showing the data displayed in 4.19 as well as the longest measured lifetime for each target.

	Bake Time	Bake Temp	Chase to Fill	Flamebakes
	Hrs	(°C)	Hrs	
Phoenix	98.25	380	3.66	8
Dutch	14.50	380	5	6
Savior	143.80	160	2.25	14
Wayne	37.25	380	3	6
Florence	199.00	180	24	17
Chout	64.50	260	5	8
Brianna	47.75	332.5	1.87	5
Butterball	293.00	250	23	11
Austin	150.00	250	24.5	11
Fulla	295.97	165	20	14
Big Brother	221.00	257	5.5	14

	Max Pol.	Max Life.	O_2 Bake	Make to Bake	Reg. Bake	Avg. Temp.	Chase to Fill	Flamebakes
	%	Hrs	Hrs	Hrs	Hrs	(°C)	Hrs	
Triveline	(**8.55**)	1.302		813.00	142.50	272.30	9.50	9
Autobahn	(**8.34**)	1.491		45.00	96.00	356.88	7.50	16
Talisker	(**4.41**)	17.097		191.00	118.50	273.12	4.50	12
Tiger	53.566	10.164	51.50	65.50	72.67	366.19	7.50	12
Hunter	48.275	18.098		50.00	70.00	374.14	4.33	11
Windmill	46.900	23.299	48.00	47.17	97.00	355.44	6.18	9
Pristine	44.156	10.148	32.50	42.50	75.17	375.00	29.25	12
Donya	43.322	14.481	29.95		93.00	341.94	3.66	12
Fringe	42.334	16.077		122.75	71.00	400.00	4.00	15
Walter	42.140	10.876		27.00	69.42	386.36	6.00	10
Christin	40.766	12.419		124.00	111.50	374.53	2.33	12
Juna	39.887	11.146		109.00	129.00	369.77	5.75	14
Ukraine	31.799	8.245		27.50	127.50	304.59	8.50	10
Barbie	29.417	9.895	47.33	138.50	145.500	283.09	7.50	14
Chicago	26.694	4.590		17.33	67.000	400.00	5.00	10
Mekong	26.211	5.575		45.67	58.000	400.00	3.50	10
Ginger	17.708	3.857		24.17	58.633	230.00	4.50	

Table A.3: The data displayed in 4.21 as well as the longest measured lifetime for each target. Triveline, Autobahn, and Talisker were excluded from the plots because they did not have EPR calibrations.

	Max Pol.	Max Life.	O_2 Bake	Make to Bake	Reg. Bake	Avg. Temp.	Chase to Fill	Flamebakes
	%	Hrs	Hrs	Hrs	Hrs	(°C)	Hrs	
Christin	53.098	26.079		124.00	111.50	374.53	2.33	12
Windmill	47.521	30.426	48.00	47.17	97.00	355.44	6.18	9
Donya	47.269	24.681	29.95		93.00	341.94	3.66	12
Juna	45.497	20.999		109.00	129.00	369.77	5.75	14
Fringe	44.672	28.343		122.75	71.00	400.00	4.00	15
Mekong	44.325	10.367		45.67	58.00	400.00	3.50	10
Barbie	37.817	14.140	47.33	138.50	145.50	283.09	7.50	14
Pristine	36.155	5.261	32.50	42.50	75.17	375.00	29.25	12
Chicago	35.649	8.752		17.33	67.00	400.00	5.00	10
Tiger	34.155	7.616	51.50	65.50	72.67	366.19	7.50	12

Table A.4: The data displayed in 4.20 as well as the longest measured lifetime for each target. Triveline, Autobahn, and Talisker were excluded from the plots because they did not have EPR calibrations.

Appendix B

Data Tables of Chapter 5

The following tables report spectroscopy results for A_1^n/d_2^n targets as well as five "Kappa" cells, which are simply a sphere. These were generally made to test modifications to the gas handling system and were also a useful benchmark in studying pressure broadened spectroscopy lines as they are only filled to 1 atmosphere (or less).

For the tables in this appendix, FWHM and line center are in GHz. Maximum attenuation and η are unitless. η is the weighting factor for the pseudo-Voigt profile such that $0 \leq \eta \leq 1$. A larger number gives more weight to the Lorentzian and smaller more weight to the Gaussian. Note, this factor was not present in the Lorentzian fit, only the pseudo-Voigt and is presented here simply as an indication of where the pseudo-Voigt fit was able to utilize the Gaussian function to better fit the lines. When multiple data sets were taken at a given temperature, their results were averaged. As the Lorentzian and pseudo-Voigt profile fits were usually in good agreement, they are presented here under the "fitted" results, also averaged. The integral "fit" results are presented separately as they did not always agree with the two other methods of fitting.

Alkali density ratio for each temperature is found by averaged the alkali density ratio found by comparing the two D1 lines or the two D2 lines (KD1:RbD1 and KD2:RbD2). These numbers were then averaged and extrapolated to higher temperatures. Alkali density ratios were, of course, omitted for scans at a particular temperature when the absorption of only one alkali species was examined. All alkali density ratio values are preliminary.

Table B.1: Austin - Low Power Spec. Results (Fitted)

			FWHM	Center	Max.Att.	η
Run 1	130°C	RbD1	131.428(2.308)	377149.75(1.29)	-0.087	0.927(0.047)
		RbD2	141.947(0.968)	384235.67(0.53)	-0.166	0.936(0.016)
		KD1	95.148(2.465)	389295.46(1.25)	-0.306	0.935(0.06)
		KD2	132.853(1.443)	391013.8(0.7)	-0.722	0.969(0.026)
Alk.Ratio (K:Rb): 3.321(3.361) → at 235°C: 5.407(4.753)						
	135°C	RbD1	138.136(0.439)	377151.76(0.24)	-0.063	1.0(0.008)
		RbD2	151.312(0.69)	384236.53(0.37)	-0.119	0.943(0.011)
		KD1	92.369(0.737)	389296.22(0.37)	-0.552	0.977(0.018)
		KD2	120.228(0.423)	391018.78(0.22)	-1.092	0.845(0.008)
Alk.Ratio (K:Rb): 6.785(6.829) → at 235°C: 10.732(9.658)						
	140°C	RbD1	139.342(0.592)	377149.11(0.33)	-0.076	1.0(0.011)
		RbD2	138.993(0.403)	384235.29(0.22)	-0.178	1.0(0.007)
		KD1	89.228(0.57)	389294.57(0.28)	-0.912	1.0(0.014)
		KD2	120.358(0.433)	391018.91(0.23)	-1.35	0.729(0.008)
Alk.Ratio (K:Rb): 7.419(7.436) → at 235°C: 11.409(10.516)						
	155°C	RbD1	110.394(0.21)	377152.08(0.11)	-0.5	0.976(0.005)
		RbD2	113.499(0.217)	384236.69(0.12)	-1.422	0.831(0.004)
→ → Avg. Estimated Alk. Ratio (K:Rb) at 235°C: 9.183(15.285) ← ←						

Table B.2: Austin - Low Power Spec. Results (Integrated)

			FWHM	Center	Max.Att.
Run 1	130°C	RbD1	128.8	377151.21	-0.089
		RbD2	137.5	384234.01	-0.173
		KD1	91.5	389293.76	-0.321
		KD2	118.333	391016.67	-0.788
Alk.Ratio (K:Rb): 3.395(3.426) → at 235°C: 5.527(4.845)					
	135°C	RbD1	133.0	377145.01	-0.063
		RbD2	141.0	384239.01	-0.125
		KD1	86.0	389301.01	-0.587
		KD2	127.0	391008.01	-1.091
Alk.Ratio (K:Rb): 6.934(6.975) → at 235°C: 10.968(9.865)					
	140°C	RbD1	132.0	377155.01	-0.075
		RbD2	128.0	384228.01	-0.187
		KD1	84.0	389302.01	-0.977
		KD2	128.0	391025.01	-1.351
Alk.Ratio (K:Rb): 8.217(8.414) → at 235°C: 12.636(11.9)					
	155°C	RbD1	107.0	377144.01	-0.498
		RbD2	118.0	384242.01	-1.435

Continued on next page

Table B.2 – continued from previous page

	FWHM	Center	Max.Att.		
→	→	Avg. Estimated Alk. Ratio (K:Rb) at 235°C: 9.71(16.48)		←	←

Table B.3: Big Brother - Low Power Spec. Results (Fitted)

			FWHM	Center	Max.Att.	η
Run 1	130°C	RbD1	129.741(1.589)	377145.38(0.87)	-0.053	1.0(0.032)
		RbD2	142.435(0.518)	384236.16(0.28)	-0.109	1.0(0.009)
		KD1	97.458(1.765)	389296.35(0.89)	-0.345	0.954(0.042)
		KD2	124.666(0.789)	391011.89(0.39)	-0.89	0.938(0.015)
Alk.Ratio (K:Rb): 6.219(6.333) → at 235°C: 10.125(8.956)						
	135°C	RbD1	129.817(1.036)	377149.79(0.56)	-0.08	1.0(0.02)
		RbD2	137.924(0.382)	384235.01(0.2)	-0.169	1.0(0.007)
		KD1	93.817(0.596)	389294.21(0.31)	-0.566	0.85(0.015)
		KD2	125.206(0.357)	391016.57(0.18)	-1.149	0.898(0.007)
Alk.Ratio (K:Rb): 5.831(5.859) → at 235°C: 9.223(8.287)						
	140°C	RbD1	128.511(0.68)	377148.76(0.37)	-0.098	1.0(0.013)
		RbD2	136.016(0.344)	384236.46(0.18)	-0.215	0.965(0.006)
		KD1	85.311(0.473)	389293.73(0.24)	-0.79	0.876(0.012)
		KD2	116.348(0.305)	391018.07(0.15)	-1.474	0.793(0.006)
Alk.Ratio (K:Rb): 5.816(5.825) → at 235°C: 8.944(8.238)						
	155°C	RbD1	107.364(0.286)	377148.62(0.15)	-0.291	0.999(0.007)
		RbD2	109.204(0.213)	384237.41(0.11)	-0.782	0.894(0.004)
→ → Avg. Estimated Alk. Ratio (K:Rb) at 235°C: 9.431(14.731) ← ←						

Table B.4: Big Brother - Low Power Spec. Results (Integrated)

			FWHM	Center	Max.Att.
Run 1	130°C	RbD1	123.0	377160.99	-0.053
		RbD2	141.0	384249.01	-0.109
		KD1	98.0	389302.0	-0.344
		KD2	120.0	390998.01	-0.928
Alk.Ratio (K:Rb): 6.225(6.314) → at 235°C: 10.136(8.929)					
	135°C	RbD1	127.0	377154.01	-0.082
		RbD2	125.0	384234.01	-0.184
		KD1	94.0	389288.01	-0.58
		KD2	119.0	391018.0	-1.19
Alk.Ratio (K:Rb): 5.448(5.49) → at 235°C: 8.617(7.763)					
	140°C	RbD1	124.0	377151.01	-0.099
		RbD2	136.0	384241.03	-0.217
		KD1	84.0	389296.01	-0.807
		KD2	116.0	391011.01	-1.505
Alk.Ratio (K:Rb): 5.802(5.803) → at 235°C: 8.922(8.206)					
	155°C	RbD1	105.0	377153.01	-0.293
		RbD2	110.0	384240.01	-0.786

Continued on next page

Table B.4 – continued from previous page

	FWHM	Center	Max.Att.		
→	→	Avg. Estimated Alk. Ratio (K:Rb) at 235°C: 9.225(14.414)		←	←

Table B.5: Brianna - High Power Spec. Results (Fitted)

			FWHM	Center	Max.Att.	η
Run 1	135°C	RbD1	123.418(1.645)	377145.95(0.92)	-0.131	0.832(0.034)
		RbD2	144.875(1.168)	384231.36(0.64)	-0.224	0.89(0.02)
		KD1	102.083(0.753)	389294.42(0.38)	-0.438	0.893(0.017)
		KD2	135.085(0.575)	391018.82(0.29)	-0.682	1.0(0.011)
Alk.Ratio (K:Rb): 2.862(2.863) → at 235°C: 4.527(4.048)						
	140°C	RbD1	126.627(0.815)	377149.64(0.4)	-0.178	0.896(0.017)
		RbD2	145.809(0.5)	384234.45(0.27)	-0.301	0.947(0.008)
		KD1	98.546(0.251)	389295.32(0.12)	-0.615	1.0(0.006)
		KD2	125.094(0.176)	391019.42(0.09)	-0.999	1.0(0.003)
Alk.Ratio (K:Rb): 2.831(2.833) → at 235°C: 4.353(4.006)						
	145°C	RbD1	129.394(0.568)	377144.77(0.31)	-0.263	0.955(0.011)
		RbD2	146.302(0.48)	384235.34(0.26)	-0.435	0.987(0.008)
		KD1	88.315(0.297)	389294.56(0.15)	-1.016	1.0(0.008)
		KD2	119.492(0.209)	391019.56(0.11)	-1.687	0.905(0.004)
Alk.Ratio (K:Rb): 2.991(3.006) → at 235°C: 4.474(4.251)						
	165°C	RbD1	120.029(0.206)	377146.31(0.11)	-0.761	1.0(0.004)
		RbD2	112.205(0.167)	384237.17(0.09)	-1.753	1.0(0.004)
→ → Avg. Estimated Alk. Ratio (K:Rb) at 235°C: 4.451(7.108) ← ←						

Table B.6: Brianna - High Power Spec. Results (Integrated)

			FWHM	Center	Max.Att.
Run 1	135°C	RbD1	120.0	377142.0	-0.127
		RbD2	127.0	384236.01	-0.228
		KD1	100.0	389294.0	-0.437
		KD2	132.0	391018.0	-0.685
Alk.Ratio (K:Rb): 3.016(3.017) → at 235°C: 4.771(4.267)					
	140°C	RbD1	120.0	377152.01	-0.174
		RbD2	141.0	384233.0	-0.305
		KD1	97.0	389296.0	-0.615
		KD2	121.0	391023.01	-1.013
Alk.Ratio (K:Rb): 3.144(3.149) → at 235°C: 4.834(4.454)					
	145°C	RbD1	121.0	377150.01	-0.264
		RbD2	147.0	384233.0	-0.432
		KD1	87.0	389296.01	-1.008
		KD2	119.0	391015.01	-1.626
Alk.Ratio (K:Rb): 3.289(3.29) → at 235°C: 4.92(4.653)					
	165°C	RbD1	116.0	377151.01	-0.766
		RbD2	110.0	384239.0	-1.737
Continued on next page					

Table B.6 – continued from previous page

	FWHM	Center	Max.Att.	
→ →	Avg. Estimated Alk. Ratio (K:Rb) at 235°C: 4.842(7.726)			← ←

Table B.7: Brianna - Low Power Spec. Results (Fitted)

			FWHM	Center	Max.Att.	η
Run 2	130°C	RbD1	127.454(0.688)	377147.47(0.38)	-0.069	0.947(0.014)
		RbD2	135.645(0.813)	384236.76(0.44)	-0.141	0.84(0.014)
		KD1	90.606(0.491)	389295.58(0.24)	-0.461	1.0(0.013)
		KD2	118.842(0.329)	391017.9(0.16)	-0.793	0.963(0.007)
Alk.Ratio (K:Rb): 4.956(4.957) → at 235°C: 8.069(7.011)						
	135°C	RbD1	123.946(0.896)	377148.23(0.49)	-0.072	0.901(0.018)
		RbD2	160.666(0.8)	384226.99(0.43)	-0.158	0.941(0.013)
		KD1	88.654(0.335)	389293.94(0.17)	-0.539	0.918(0.009)
		KD2	113.808(0.204)	391019.9(0.1)	-1.019	0.92(0.004)
Alk.Ratio (K:Rb): 4.92(4.923) → at 235°C: 7.782(6.963)						
	140°C	RbD1	124.407(0.355)	377147.2(0.19)	-0.102	1.0(0.007)
		RbD2	133.885(0.409)	384233.17(0.22)	-0.215	0.994(0.007)
		KD1	83.132(0.399)	389294.54(0.2)	-0.901	0.961(0.011)
		KD2	105.255(0.229)	391018.08(0.12)	-1.763	0.891(0.005)
Alk.Ratio (K:Rb): 6.371(6.379) → at 235°C: 9.797(9.022)						
	155°C	RbD1	113.186(0.304)	377147.57(0.16)	-0.288	0.997(0.007)
		RbD2	116.209(0.303)	384234.93(0.16)	-0.702	0.94(0.006)
→ → Avg. Estimated Alk. Ratio (K:Rb) at 235°C: 8.549(13.409) ← ←						

Table B.8: Brianna - Low Power Spec. Results (Integrated)

			FWHM	Center	Max.Att.
Run 2	130°C	RbD1	125.0	377153.01	-0.069
		RbD2	126.0	384234.01	-0.151
		KD1	83.0	389302.01	-0.465
		KD2	113.0	391011.01	-0.826
Alk.Ratio (K:Rb): 5.267(5.269) → at 235°C: 8.575(7.452)					
	135°C	RbD1	120.0	377150.01	-0.072
		RbD2	145.0	384226.01	-0.174
		KD1	92.0	389286.0	-0.53
		KD2	114.0	391021.01	-1.051
Alk.Ratio (K:Rb): 4.895(4.9) → at 235°C: 7.743(6.93)					
	140°C	RbD1	120.0	377155.04	-0.102
		RbD2	124.0	384234.01	-0.23
		KD1	80.0	389300.02	-0.928
		KD2	105.0	391017.01	-1.783
Alk.Ratio (K:Rb): 6.333(6.334) → at 235°C: 9.739(8.957)					
	155°C	RbD1	106.0	377151.0	-0.297
		RbD2	114.0	384228.01	-0.722

Continued on next page

Table B.8 – continued from previous page

	FWHM	Center	Max.Att.		
→	→	Avg. Estimated Alk. Ratio (K:Rb) at 235°C: 8.686(13.581)		←	←

Table B.9: Butterball - Low Power Spec. Results (Fitted)

			FWHM	Center	Max.Att.	η
Run 1	130°C	RbD1	136.431(0.369)	377150.0(0.2)	-0.066	1.0(0.007)
		RbD2	137.342(0.296)	384234.02(0.16)	-0.15	0.976(0.005)
		KD1	99.29(0.769)	389296.64(0.39)	-0.225	0.881(0.018)
		KD2	124.496(0.457)	391018.51(0.24)	-0.424	0.824(0.009)
Alk.Ratio (K:Rb): 2.624(2.625) → at 235°C: 4.272(3.712)						
	135°C	RbD1	127.327(0.868)	377151.46(0.47)	-0.079	1.0(0.017)
		RbD2	133.513(0.762)	384234.37(0.41)	-0.17	0.929(0.014)
		KD1	90.434(1.026)	389295.87(0.52)	-4.117	0.922(0.026)
		KD2	114.138(0.515)	391017.68(0.26)	-0.702	0.883(0.011)
Alk.Ratio (K:Rb): 3.428(3.439) → at 235°C: 5.422(4.864)						
	140°C	RbD1	123.436(0.262)	377151.88(0.14)	-0.113	1.0(0.005)
		RbD2	125.07(0.302)	384234.71(0.16)	-0.284	0.969(0.006)
		KD1	83.605(0.418)	389296.7(0.21)	-0.522	0.918(0.011)
		KD2	107.59(0.229)	391020.69(0.12)	-1.089	0.907(0.005)
Alk.Ratio (K:Rb): 3.323(3.325) → at 235°C: 5.11(4.702)						
	155°C	RbD1	101.095(0.278)	377152.15(0.15)	-0.516	0.825(0.006)
		RbD2	96.664(0.209)	384235.59(0.11)	-1.631	0.79(0.004)
→ → Avg. Estimated Alk. Ratio (K:Rb) at 235°C: 4.935(7.732) ← ←						
Run 2	125°C	RbD1	146.902(0.419)	377151.38(0.23)	-0.058	1.0(0.007)
		RbD2	145.176(0.368)	384234.29(0.2)	-0.111	1.0(0.006)
		KD1	100.793(0.833)	389294.56(0.41)	-0.111	1.0(0.019)
		KD2	126.937(0.478)	391018.26(0.24)	-0.22	1.0(0.009)
Alk.Ratio (K:Rb): 1.567(1.584) → at 235°C: 2.629(2.24)						
	130°C	RbD1	139.247(0.85)	377151.39(0.47)	-0.066	1.0(0.016)
		RbD2	138.214(0.886)	384236.37(0.47)	-0.142	0.993(0.016)
		KD1	98.749(1.489)	389295.8(0.76)	-0.177	0.895(0.035)
		KD2	125.54(0.898)	391019.66(0.46)	-0.335	0.89(0.017)
Alk.Ratio (K:Rb): 2.121(2.143) → at 235°C: 3.453(3.031)						
	135°C	RbD1	134.996(0.411)	377149.34(0.23)	-0.098	1.0(0.008)
		RbD2	130.907(0.445)	384236.32(0.24)	-0.224	0.978(0.008)
		KD1	90.628(1.045)	389297.21(0.52)	-0.274	0.943(0.027)
		KD2	114.738(0.573)	391021.14(0.29)	-0.567	0.897(0.012)
Alk.Ratio (K:Rb): 2.135(2.152) → at 235°C: 3.377(3.044)						
	140°C	RbD1	127.14(0.53)	377149.82(0.29)	-0.136	1.0(0.011)
		RbD2	120.005(0.417)	384236.63(0.22)	-0.348	0.988(0.008)
		KD1	83.176(0.851)	389296.42(0.43)	-0.458	0.96(0.023)
		KD2	106.672(0.479)	391018.8(0.25)	-0.919	0.855(0.01)
Alk.Ratio (K:Rb): 2.379(2.392) → at 235°C: 3.659(3.383)						
	145°C	RbD1	119.956(0.54)	377151.06(0.29)	-0.21	0.998(0.011)
		RbD2	107.629(0.362)	384235.78(0.19)	-0.602	0.908(0.008)

Continued on next page

Table B.9 – continued from previous page

			FWHM	Center	Max.Att.	η
		KD1	75.124(0.594)	389295.93(0.3)	-0.782	0.957(0.015)
		KD2	105.683(0.345)	391017.33(0.18)	-1.547	0.62(0.006)
Alk.Ratio (K:Rb): 2.28(2.284) → at 235°C: 3.412(3.23)						
	150°C	RbD1	103.704(0.287)	377153.41(0.15)	-0.361	1.0(0.007)
		RbD2	98.669(0.212)	384237.1(0.11)	-1.24	0.776(0.004)
→ → Avg. Estimated Alk. Ratio (K:Rb) at 235°C: 3.306(6.743) ← ←						

Table B.10: Butterball - Low Power Spec. Results (Integrated)

			FWHM	Center	Max.Att.
Run 1	130°C	RbD1	131.0	377155.0	-0.065
		RbD2	132.0	384241.0	-0.155
		KD1	97.0	389292.0	-0.232
		KD2	126.0	391007.0	-0.44
Alk.Ratio (K:Rb): 2.744(2.746) → at 235°C: 4.468(3.883)					
	135°C	RbD1	120.333	377158.01	-0.082
		RbD2	130.0	384239.01	-0.173
		KD1	87.667	389287.34	-0.355
		KD2	108.5	391022.51	-0.751
Alk.Ratio (K:Rb): 3.506(3.525) → at 235°C: 5.546(4.985)					
	140°C	RbD1	119.0	377156.0	-0.115
		RbD2	120.0	384228.0	-0.292
		KD1	76.0	389299.0	-0.54
		KD2	107.0	391028.0	-1.1
Alk.Ratio (K:Rb): 3.241(3.242) → at 235°C: 4.984(4.585)					
	155°C	RbD1	102.0	377154.0	-0.527
		RbD2	101.0	384241.0	-1.595
→ → Avg. Estimated Alk. Ratio (K:Rb) at 235°C: 4.999(7.819) ← ←					
Run 2	125°C	RbD1	140.0	377151.99	-0.058
		RbD2	136.0	384228.01	-0.115
		KD1	90.0	389298.01	-0.119
		KD2	118.0	391010.01	-0.229
Alk.Ratio (K:Rb): 1.521(1.525) → at 235°C: 2.55(2.156)					
	130°C	RbD1	133.75	377153.01	-0.066
		RbD2	131.0	384243.76	-0.149
		KD1	99.5	389294.26	-0.179
		KD2	123.25	391021.76	-0.348
Alk.Ratio (K:Rb): 2.09(2.106) → at 235°C: 3.403(2.979)					
	135°C	RbD1	129.0	377152.01	-0.1
		RbD2	126.5	384242.01	-0.227

Continued on next page

Table B.10 – continued from previous page

			FWHM	Center	Max.Att.
		KD1	88.5	389302.01	-0.272
		KD2	106.0	391035.01	-0.582
Alk.Ratio (K:Rb): 2.161(2.176) → at 235°C: 3.418(3.077)					
	140°C	RbD1	123.5	377151.51	-0.135
		RbD2	113.0	384244.03	-0.357
		KD1	84.0	389297.51	-0.46
		KD2	106.0	391009.0	-0.941
Alk.Ratio (K:Rb): 2.442(2.458) → at 235°C: 3.755(3.476)					
	145°C	RbD1	110.0	377153.52	-0.222
		RbD2	104.5	384227.51	-0.617
		KD1	76.0	389299.01	-0.782
		KD2	116.0	391026.3	-1.523
Alk.Ratio (K:Rb): 2.244(2.244) → at 235°C: 3.357(3.173)					
	150°C	RbD1	102.0	377158.01	-0.36
		RbD2	103.0	384234.01	-1.231
→ → Avg. Estimated Alk. Ratio (K:Rb) at 235°C: 3.297(6.731) ← ←					

Table B.11: Dutch - Low Power Spec. Results (Fitted)

			FWHM	Center	Max.Att.	η
Run 1	130°C	RbD1	140.332(6.188)	377146.86(5.42)	-0.037	0.972(0.202)
		RbD2	156.299(3.342)	384234.67(1.83)	-0.078	0.872(0.055)
		KD1	102.696(27.817)	389292.79(17.24)	0.391	0.847(0.883)
		KD2	138.486(27.503)	391018.61(15.45)	-0.595	0.884(0.864)
Alk.Ratio (K:Rb): 6.852(8.464) → at 235°C: 11.156(11.969)						
	135°C	RbD1	142.752(1.209)	377150.32(0.67)	-0.052	0.896(0.022)
		RbD2	154.87(0.495)	384236.96(0.27)	-0.111	0.909(0.008)
		KD1	97.233(0.401)	389294.22(0.2)	-0.513	0.976(0.01)
		KD2	130.672(0.263)	391019.71(0.13)	-0.918	0.916(0.005)
Alk.Ratio (K:Rb): 7.017(7.019) → at 235°C: 11.099(9.926)						
	140°C	RbD1	145.688(1.144)	377151.58(0.63)	-0.073	1.0(0.02)
		RbD2	150.084(0.567)	384233.89(0.3)	-0.162	1.0(0.009)
		KD1	94.902(0.717)	389295.3(0.36)	-0.793	0.96(0.017)
		KD2	129.573(0.463)	391018.64(0.24)	-1.432	0.834(0.008)
Alk.Ratio (K:Rb): 7.632(7.64) → at 235°C: 11.736(10.805)						
	165°C	RbD1	116.92(0.233)	377153.85(0.13)	-0.382	1.0(0.005)
		RbD2	124.232(0.281)	384234.83(0.15)	-1.073	0.862(0.005)
→ → Avg. Estimated Alk. Ratio (K:Rb) at 235°C: 11.33(18.938) ← ←						

Table B.12: Dutch - Low Power Spec. Results (Integrated)

			FWHM	Center	Max.Att.
Run 1	130°C	RbD1	131.8	377154.4	-0.039
		RbD2	155.2	384235.0	-0.078
		KD1	95.6	389298.4	-0.375
		KD2	133.25	391025.5	-0.691
Alk.Ratio (K:Rb): 10.588(14.426) → at 235°C: 17.239(20.402)					
	135°C	RbD1	142.0	377153.0	-0.051
		RbD2	152.0	384245.0	-0.112
		KD1	91.0	389289.0	-0.54
		KD2	119.0	391010.0	-0.936
Alk.Ratio (K:Rb): 7.709(7.715) → at 235°C: 12.193(10.911)					
	140°C	RbD1	143.0	377152.0	-0.072
		RbD2	140.0	384225.0	-0.167
		KD1	91.0	389293.0	-0.812
		KD2	125.0	391018.0	-1.45
Alk.Ratio (K:Rb): 7.287(7.296) → at 235°C: 11.205(10.318)					
	165°C	RbD1	111.0	377156.01	-0.386
		RbD2	120.0	384229.01	-1.115

Continued on next page

Table B.12 – continued from previous page

	FWHM	Center	Max.Att.	
→ →	Avg. Estimated Alk. Ratio (K:Rb) at 235°C: 13.546(25.47)			← ←

Table B.13: Florence - High Power Spec. Results (Fitted)

			FWHM	Center	Max.Att.	η
Run 1	140°C	RbD1	104.936(0.61)	377146.33(0.34)	-0.149	0.879(0.014)
		RbD2	131.128(0.342)	384236.56(0.19)	-0.313	0.858(0.006)
		KD1	95.476(1.137)	389294.91(0.57)	-0.65	0.944(0.028)
		KD2	128.298(0.85)	391018.45(0.43)	-1.022	0.95(0.016)
Alk.Ratio (K:Rb): 3.661(3.681) → at 235°C: 5.63(5.205)						
→ → Avg. Estimated Alk. Ratio (K:Rb) at 235°C: 5.63(5.205) ← ←						
Run 2	135°C	RbD1	108.401(2.844)	377149.11(1.54)	-0.044	0.969(0.064)
		RbD2	129.894(1.506)	384235.03(0.8)	-0.109	0.921(0.028)
		KD1	104.247(0.468)	389294.35(0.25)	-0.285	0.878(0.011)
		KD2	169.334(0.226)	391018.9(0.11)	-0.325	0.881(0.003)
Alk.Ratio (K:Rb): 3.908(4.006) → at 235°C: 6.181(5.665)						
	140°C	RbD1	108.881(0.644)	377148.09(0.36)	-0.106	0.827(0.014)
		RbD2	134.799(0.327)	384235.17(0.18)	-0.24	0.814(0.005)
		KD1	114.893(0.277)	389294.87(0.14)	-0.337	0.845(0.005)
		KD2	184.299(0.317)	391018.3(0.16)	-0.392	0.829(0.004)
Alk.Ratio (K:Rb): 2.861(2.915) → at 235°C: 4.4(4.123)						
	145°C	RbD1	103.636(0.476)	377148.92(0.26)	-0.189	0.866(0.011)
		RbD2	145.826(0.335)	384234.95(0.18)	-0.351	0.766(0.004)
		KD1	124.694(0.312)	389293.92(0.16)	-0.401	0.797(0.005)
		KD2	200.055(0.366)	391018.42(0.18)	-0.457	0.823(0.004)
Alk.Ratio (K:Rb): 2.226(2.26) → at 235°C: 3.331(3.196)						
	150°C	RbD1	110.571(0.394)	377148.86(0.22)	-0.317	0.716(0.007)
		RbD2	165.482(0.469)	384234.76(0.26)	-0.471	0.65(0.004)
→ → Avg. Estimated Alk. Ratio (K:Rb) at 235°C: 4.637(7.79) ← ←						

Table B.14: Florence - High Power Spec. Results (Integrated)

			FWHM	Center	Max.Att.
Run 1	140°C	RbD1	108.0	377149.0	-0.15
		RbD2	137.0	384240.01	-0.309
		KD1	96.0	389296.0	-0.643
		KD2	116.0	391444.0	-1.123
Alk.Ratio (K:Rb): 3.671(3.693) → at 235°C: 5.645(5.222)					
→ → Avg. Estimated Alk. Ratio (K:Rb) at 235°C: 5.645(5.222) ← ←					
Run 2	135°C	RbD1	90.0	377145.01	-0.048
		RbD2	128.5	384232.01	-0.114
		KD1	105.0	389294.5	-0.279
		KD2	169.0	391014.0	-0.321
Alk.Ratio (K:Rb): 3.845(3.963) → at 235°C: 6.082(5.605)					
Continued on next page					

Table B.14 – continued from previous page

			FWHM	Center	Max.Att.
	140°C	RbD1	108.0	377134.0	-0.108
		RbD2	141.0	384240.01	-0.238
		KD1	117.0	389295.98	-0.329
		KD2	187.0	391011.99	-0.384
Alk.Ratio (K:Rb): 2.832(2.904) → at 235°C: 4.355(4.107)					
	145°C	RbD1	107.0	377155.01	-0.186
		RbD2	153.0	384235.0	-0.343
		KD1	130.0	389292.01	-0.387
		KD2	202.0	391017.0	-0.451
Alk.Ratio (K:Rb): 2.156(2.195) → at 235°C: 3.226(3.104)					
	150°C	RbD1	117.0	377153.01	-0.309
		RbD2	179.0	384237.01	-0.453
→ → Avg. Estimated Alk. Ratio (K:Rb) at 235°C: 4.554(7.7) ← ←					

Table B.15: Florence - Low Power Spec. Results (Fitted)

			FWHM	Center	Max.Att.	η
Run 3	130°C	RbD1	126.18(0.574)	377146.95(0.31)	-0.109	1.0(0.011)
		RbD2	128.658(0.354)	384234.45(0.19)	-0.239	1.0(0.007)
		KD1	89.693(0.414)	389294.2(0.21)	-0.349	1.0(0.011)
		KD2	119.621(0.266)	391020.92(0.13)	-0.637	0.976(0.005)
Alk.Ratio (K:Rb): 2.444(2.447) → at 235°C: 3.979(3.46)						
	135°C	RbD1	115.622(0.313)	377146.85(0.17)	-0.186	1.0(0.007)
		RbD2	119.603(0.254)	384234.89(0.14)	-0.423	0.974(0.005)
		KD1	82.376(0.447)	389294.13(0.22)	-0.554	0.979(0.013)
		KD2	114.479(0.285)	391019.49(0.14)	-1.028	0.909(0.006)
Alk.Ratio (K:Rb): 2.296(2.299) → at 235°C: 3.631(3.251)						
	140°C	RbD1	113.703(0.301)	377148.36(0.16)	-0.223	1.0(0.007)
		RbD2	115.06(0.271)	384235.45(0.14)	-0.541	0.957(0.006)
		KD1	80.372(0.368)	389295.04(0.18)	-0.83	0.959(0.01)
		KD2	109.86(0.222)	391017.79(0.11)	-1.603	0.84(0.004)
Alk.Ratio (K:Rb): 2.822(2.825) → at 235°C: 4.339(3.995)						
	155°C	RbD1	93.984(0.194)	377148.51(0.11)	-0.715	0.925(0.005)
		RbD2	98.607(0.241)	384235.89(0.13)	-2.033	0.75(0.004)
→ → Avg. Estimated Alk. Ratio (K:Rb) at 235°C: 3.983(6.211) ← ←						
Run 4	130°C	RbD1	125.084(0.912)	377145.86(0.5)	-0.06	0.984(0.019)
		RbD2	126.92(0.678)	384234.59(0.36)	-0.128	0.988(0.013)
		KD1	86.929(1.593)	389293.57(0.81)	-0.202	0.913(0.043)
		KD2	109.981(0.913)	391019.39(0.45)	-0.406	0.978(0.019)
Alk.Ratio (K:Rb): 2.622(2.634) → at 235°C: 4.268(3.726)						
	135°C	RbD1	118.782(0.698)	377147.25(0.38)	-0.085	0.987(0.015)
		RbD2	121.221(2.282)	384234.9(0.96)	-0.194	0.926(0.043)
		KD1	82.472(1.185)	389294.7(0.6)	-0.315	0.926(0.033)
		KD2	106.257(0.69)	391018.3(0.35)	-0.616	0.891(0.015)
Alk.Ratio (K:Rb): 2.808(2.813) → at 235°C: 4.442(3.978)						
	140°C	RbD1	111.179(0.714)	377148.11(0.39)	-0.131	0.969(0.016)
		RbD2	111.341(0.598)	384236.57(0.32)	-0.335	0.941(0.013)
		KD1	78.056(1.084)	389294.54(0.55)	-0.552	0.917(0.031)
		KD2	98.769(0.589)	391019.92(0.3)	-1.13	0.828(0.013)
Alk.Ratio (K:Rb): 3.079(3.083) → at 235°C: 4.735(4.36)						
	145°C	RbD1	105.93(0.669)	377147.01(0.36)	-0.179	0.992(0.016)
		RbD2	104.347(0.539)	384235.17(0.29)	-0.487	0.859(0.011)
		KD1	73.331(1.018)	389294.88(0.52)	-0.805	0.809(0.027)
		KD2	97.238(0.57)	391018.65(0.3)	-1.66	0.727(0.012)
Alk.Ratio (K:Rb): 3.273(3.276) → at 235°C: 4.896(4.633)						
	150°C	RbD1	96.436(0.218)	377147.55(0.12)	-0.295	1.0(0.006)
		RbD2	97.285(0.177)	384235.91(0.1)	-0.897	0.836(0.003)

Continued on next page

Table B.15 – continued from previous page

			FWHM	Center	Max.Att.	η
	155°C	RbD1	89.753(0.256)	377149.26(0.14)	-0.431	0.929(0.007)
		RbD2	88.985(0.245)	384234.72(0.13)	-1.428	0.724(0.005)
→ →	Avg. Estimated Alk. Ratio (K:Rb) at 235°C: 4.585(8.381)					← ←
Run 5	130°C	RbD1	117.536(0.411)	377148.27(0.22)	-0.147	0.986(0.009)
		RbD2	125.12(0.317)	384234.45(0.17)	-0.338	0.93(0.006)
		KD1	88.711(0.537)	389294.47(0.27)	-0.452	0.992(0.014)
		KD2	117.53(0.358)	391017.12(0.18)	-0.794	1.0(0.007)
Alk.Ratio (K:Rb): 2.319(2.32) → at 235°C: 3.776(3.281)						
	135°C	RbD1	113.286(0.384)	377146.33(0.21)	-0.209	0.9(0.008)
		RbD2	120.814(0.253)	384235.48(0.13)	-0.479	0.974(0.005)
		KD1	84.961(0.637)	389294.92(0.32)	-0.671	0.972(0.018)
		KD2	108.578(0.386)	391020.16(0.19)	-1.257	0.935(0.008)
Alk.Ratio (K:Rb): 2.446(2.446) → at 235°C: 3.869(3.459)						
	140°C	RbD1	111.453(1.069)	377146.87(0.58)	-0.318	0.978(0.024)
		RbD2	112.405(0.442)	384233.69(0.23)	-0.802	0.977(0.009)
		KD1	80.283(0.638)	389294.88(0.32)	-1.101	0.91(0.018)
		KD2	103.579(0.371)	391019.4(0.19)	-2.155	0.838(0.008)
Alk.Ratio (K:Rb): 2.576(2.576) → at 235°C: 3.961(3.643)						
	145°C	RbD1	106.365(0.297)	377149.19(0.16)	-0.437	0.961(0.007)
		RbD2	110.175(0.204)	384234.13(0.11)	-1.103	0.929(0.004)
		KD1	76.367(0.465)	389295.86(0.24)	-1.799	0.835(0.011)
		KD2	118.412(0.345)	391019.5(0.18)	-3.009	0.645(0.006)
Alk.Ratio (K:Rb): 3.067(3.067) → at 235°C: 4.588(4.337)						
	150°C	RbD1	100.544(0.277)	377149.08(0.15)	-0.692	0.932(0.007)
		RbD2	103.124(0.208)	384234.82(0.11)	-1.646	0.83(0.004)
	155°C	RbD1	97.953(0.191)	377145.29(0.1)	-0.778	0.96(0.005)
		RbD2	97.333(0.23)	384236.27(0.12)	-2.257	0.821(0.005)
→ →	Avg. Estimated Alk. Ratio (K:Rb) at 235°C: 4.048(7.41)					← ←

Table B.16: Florence - Low Power Spec. Results (Integrated)

			FWHM	Center	Max.Att.
Run 3	130°C	RbD1	121.0	377151.04	-0.112
		RbD2	126.0	384239.01	-0.241
		KD1	85.0	389300.01	-0.355
		KD2	114.0	391024.01	-0.645
Alk.Ratio (K:Rb): 2.399(2.401) → at 235°C: 3.906(3.395)					
	135°C	RbD1	113.0	377153.01	-0.186
		RbD2	118.0	384237.0	-0.427
		KD1	81.0	389299.0	-0.556
Continued on next page					

Table B.16 – continued from previous page

			FWHM	Center	Max.Att.
		KD2	109.0	391018.01	-1.096
Alk.Ratio (K:Rb): 2.335(2.335) → at 235°C: 3.693(3.302)					
	140°C	RbD1	108.0	377154.01	-0.229
		RbD2	111.0	384229.01	-0.566
		KD1	79.0	389298.01	-0.837
		KD2	107.0	391016.01	-1.672
Alk.Ratio (K:Rb): 2.818(2.818) → at 235°C: 4.333(3.985)					
	155°C	RbD1	93.0	377148.01	-0.727
		RbD2	103.0	384239.01	-1.998
→ → Avg. Estimated Alk. Ratio (K:Rb) at 235°C: 3.978(6.196) ← ←					
Run 4	130°C	RbD1	123.0	377148.2	-0.06
		RbD2	122.0	384238.6	-0.13
		KD1	82.8	389292.4	-0.212
		KD2	101.4	391018.39	-0.434
Alk.Ratio (K:Rb): 2.67(2.681) → at 235°C: 4.348(3.792)					
	135°C	RbD1	115.5	377150.34	-0.085
		RbD2	100.333	384234.0	-0.174
		KD1	79.8	389293.4	-0.321
		KD2	102.6	391018.6	-0.628
Alk.Ratio (K:Rb): 2.843(2.845) → at 235°C: 4.496(4.024)					
	140°C	RbD1	109.0	377147.2	-0.133
		RbD2	108.0	384237.6	-0.341
		KD1	76.8	389293.4	-0.567
		KD2	97.6	391019.4	-1.136
Alk.Ratio (K:Rb): 3.149(3.158) → at 235°C: 4.843(4.466)					
	145°C	RbD1	103.0	377147.6	-0.182
		RbD2	103.8	384235.2	-0.495
		KD1	74.8	389297.58	-0.803
		KD2	99.4	391018.0	-1.648
Alk.Ratio (K:Rb): 3.197(3.2) → at 235°C: 4.782(4.525)					
	150°C	RbD1	94.0	377151.0	-0.296
		RbD2	95.0	384235.0	-0.911
	155°C	RbD1	88.0	377152.0	-0.442
		RbD2	90.0	384229.16	-1.428
→ → Avg. Estimated Alk. Ratio (K:Rb) at 235°C: 4.617(8.428) ← ←					
Run 5	130°C	RbD1	110.0	377153.01	-0.15
		RbD2	122.0	384228.01	-0.345
		KD1	86.0	389298.0	-0.457
		KD2	111.0	391020.0	-0.817
Alk.Ratio (K:Rb): 2.462(2.469) → at 235°C: 4.009(3.492)					

Continued on next page

Table B.16 – continued from previous page

			FWHM	Center	Max.Att.
	135°C	RbD1	111.0	377150.01	-0.212
		RbD2	119.0	384225.01	-0.481
		KD1	83.0	389300.0	-0.692
		KD2	108.0	391023.0	-1.27
Alk.Ratio (K:Rb): 2.514(2.516) → at 235°C: 3.977(3.559)					
	140°C	RbD1	105.5	377151.5	-0.334
		RbD2	112.0	384236.01	-0.809
		KD1	78.5	389290.5	-1.12
		KD2	105.5	391015.5	-2.161
Alk.Ratio (K:Rb): 2.479(2.479) → at 235°C: 3.811(3.506)					
	145°C	RbD1	106.0	377154.01	-0.444
		RbD2	104.0	384230.01	-1.123
		KD1	81.0	389298.03	-1.828
		KD2	124.0	391021.0	-2.924
Alk.Ratio (K:Rb): 2.994(2.997) → at 235°C: 4.479(4.238)					
	150°C	RbD1	103.0	377153.01	-0.698
		RbD2	106.0	384241.01	-1.64
	155°C	RbD1	98.0	377151.01	-0.792
		RbD2	104.0	384226.01	-2.194
→ → Avg. Estimated Alk. Ratio (K:Rb) at 235°C: 4.069(7.428) ← ←					

Table B.17: Fulla - High Power Spec. Results (Fitted)

			FWHM	Center	Max.Att.	η
Run 1	130°C	RbD1	136.766(5.987)	377144.4(3.25)	-0.058	1.0(0.111)
		RbD2	127.947(3.061)	384234.72(1.68)	-0.104	0.839(0.058)
		KD1	88.608(0.541)	389294.33(0.27)	-0.451	0.886(0.014)
		KD2	117.687(0.388)	391018.19(0.19)	-0.741	0.956(0.008)
Alk.Ratio (K:Rb): 5.978(6.026) → at 235°C: 9.732(8.522)						
	135°C	RbD1	117.424(8.295)	377141.27(4.45)	-0.059	0.93(0.201)
		RbD2	118.512(5.132)	384224.44(2.77)	-0.142	0.973(0.111)
		KD1	86.379(0.993)	389294.72(0.5)	-0.682	0.931(0.027)
		KD2	121.746(0.73)	391019.74(0.37)	-1.125	0.874(0.014)
Alk.Ratio (K:Rb): 8.279(8.294) → at 235°C: 13.095(11.73)						
	140°C	RbD1	114.367(4.632)	377146.48(2.47)	-0.088	1.0(0.109)
		RbD2	123.6(2.643)	384239.54(1.46)	-0.208	0.791(0.052)
		KD1	83.095(0.749)	389292.3(0.37)	-1.042	0.981(0.021)
		KD2	113.803(0.527)	391020.68(0.27)	-1.711	0.859(0.011)
Alk.Ratio (K:Rb): 8.287(8.31) → at 235°C: 12.743(11.753)						
	145°C	RbD1	95.594(2.262)	377144.1(1.23)	-0.143	1.0(0.06)
		RbD2	127.082(2.027)	384233.08(1.1)	-0.287	0.937(0.039)
		KD1	79.782(0.654)	389293.56(0.33)	-1.55	0.961(0.018)
		KD2	124.12(0.55)	391019.04(0.29)	-2.269	0.704(0.01)
Alk.Ratio (K:Rb): 8.671(8.692) → at 235°C: 12.972(12.292)						
→ → Avg. Estimated Alk. Ratio (K:Rb) at 235°C: 12.136(22.391) ← ←						
Run 2	120°C	RbD1	90.161(8.713)	377135.4(4.4)	-0.024	0.668(0.225)
		RbD2	135.227(8.094)	384217.83(4.57)	-0.048	1.0(0.163)
		KD1	87.545(1.786)	389294.5(0.88)	-0.195	0.977(0.046)
		KD2	124.577(1.374)	391013.24(0.68)	-0.307	1.0(0.028)
Alk.Ratio (K:Rb): 7.155(7.402) → at 235°C: 12.369(10.467)						
	130°C	RbD1	124.056(4.537)	377142.36(2.49)	-0.285	0.965(0.093)
		RbD2	133.394(5.858)	384232.44(3.14)	-0.433	0.829(0.101)
		KD1	97.384(0.923)	389293.62(0.46)	-1.365	0.974(0.023)
		KD2	133.976(0.749)	391017.54(0.37)	-1.908	0.963(0.014)
Alk.Ratio (K:Rb): 5.203(5.522) → at 235°C: 8.471(7.809)						
→ → Avg. Estimated Alk. Ratio (K:Rb) at 235°C: 10.42(13.204) ← ←						
Run 3	140°C	RbD1	111.734(0.516)	377145.51(0.28)	-0.077	0.9(0.011)
		RbD2	128.138(0.432)	384234.95(0.23)	-0.158	0.956(0.008)
		KD1	89.238(0.203)	389294.36(0.1)	-0.681	0.946(0.005)
		KD2	119.379(0.149)	391019.63(0.07)	-1.093	0.951(0.003)
Alk.Ratio (K:Rb): 6.927(6.933) → at 235°C: 10.652(9.805)						
→ → Avg. Estimated Alk. Ratio (K:Rb) at 235°C: 10.652(9.805) ← ←						
Run 4	135°C	RbD1	128.124(4.335)	377144.2(2.38)	-0.073	0.943(0.083)
		RbD2	152.123(0.81)	384233.53(0.44)	-0.106	1.0(0.013)

Continued on next page

Table B.17 – continued from previous page

			FWHM	Center	Max.Att.	η
		KD1	100.907(0.546)	389293.38(0.27)	-0.284	1.0(0.013)
		KD2	117.974(0.365)	391019.28(0.18)	-0.488	0.982(0.007)
Alk.Ratio (K:Rb): 3.432(3.456) → at 235°C: 5.429(4.888)						
→ → Avg. Estimated Alk. Ratio (K:Rb) at 235°C: 5.429(4.888) ← ←						
Run 5	135°C	RbD1	128.503(2.242)	377149.33(1.22)	-0.093	1.0(0.044)
		RbD2	148.645(1.517)	384235.58(0.81)	-0.146	1.0(0.025)
		KD1	112.219(0.394)	389293.9(0.2)	-0.312	0.987(0.008)
		KD2	156.581(0.377)	391018.01(0.19)	-0.398	1.0(0.006)
Alk.Ratio (K:Rb): 2.982(2.982) → at 235°C: 4.716(4.217)						
	140°C	RbD1	125.981(1.763)	377145.84(0.96)	-0.124	1.0(0.035)
		RbD2	151.942(1.178)	384234.19(0.63)	-0.207	1.0(0.019)
		KD1	115.83(0.404)	389293.93(0.2)	-0.386	0.953(0.008)
		KD2	150.091(0.348)	391018.76(0.17)	-0.528	1.0(0.006)
Alk.Ratio (K:Rb): 2.769(2.775) → at 235°C: 4.259(3.924)						
	145°C	RbD1	121.428(1.147)	377146.22(0.63)	-0.183	0.936(0.024)
		RbD2	149.861(0.786)	384235.78(0.42)	-0.283	0.983(0.013)
		KD1	114.683(0.406)	389293.82(0.2)	-0.501	1.0(0.008)
		KD2	143.143(0.327)	391018.94(0.16)	-0.707	1.0(0.005)
Alk.Ratio (K:Rb): 2.549(2.55) → at 235°C: 3.814(3.607)						
→ → Avg. Estimated Alk. Ratio (K:Rb) at 235°C: 4.263(6.806) ← ←						

Table B.18: Fulla - High Power Spec. Results (Integrated)

			FWHM	Center	Max.Att.
Run 1	130°C	RbD1	127.0	377136.01	-0.064
		RbD2	126.0	384217.97	-0.106
		KD1	87.0	389291.02	-0.457
		KD2	112.0	391014.99	-0.767
Alk.Ratio (K:Rb): 5.648(5.65) → at 235°C: 9.195(7.99)					
	135°C	RbD1	71.5	377147.03	-0.079
		RbD2	85.5	384235.54	-0.177
		KD1	75.0	389295.03	-0.784
		KD2	118.0	391021.04	-1.133
Alk.Ratio (K:Rb): 10.282(10.297) → at 235°C: 16.263(14.562)					
	140°C	RbD1	91.0	377131.05	-0.099
		RbD2	95.0	384233.0	-0.243
		KD1	75.0	389285.05	-1.077
		KD2	116.0	391008.99	-1.704
Alk.Ratio (K:Rb): 9.393(9.402) → at 235°C: 14.444(13.296)					
	145°C	RbD1	84.0	377140.0	-0.164

Continued on next page

Table B.18 – continued from previous page

			FWHM	Center	Max.Att.
		RbD2	94.0	384244.99	-0.345
		KD1	70.0	389295.05	-1.694
		KD2	126.0	391026.03	-2.186
Alk.Ratio (K:Rb): 8.9(8.905) → at 235°C: 13.315(12.593)					
→ → Avg. Estimated Alk. Ratio (K:Rb) at 235°C: 13.304(24.86) ← ←					
Run 2	120°C	RbD1	54.0	377132.51	-0.027
		RbD2	74.0	384231.01	-0.062
		KD1	82.5	389295.01	-0.195
		KD2	113.0	391022.01	-0.326
Alk.Ratio (K:Rb): 9.953(10.662) → at 235°C: 17.207(15.079)					
	130°C	RbD1	113.333	377145.67	-0.298
		RbD2	109.667	384228.01	-0.471
		KD1	96.333	389291.34	-1.371
		KD2	129.667	391022.33	-1.916
Alk.Ratio (K:Rb): 5.135(5.475) → at 235°C: 8.36(7.743)					
→ → Avg. Estimated Alk. Ratio (K:Rb) at 235°C: 12.784(17.518) ← ←					
Run 3	140°C	RbD1	106.0	377156.01	-0.078
		RbD2	125.0	384231.01	-0.164
		KD1	90.0	389296.0	-0.668
		KD2	119.0	391015.01	-1.084
Alk.Ratio (K:Rb): 7.173(7.204) → at 235°C: 11.03(10.188)					
→ → Avg. Estimated Alk. Ratio (K:Rb) at 235°C: 11.03(10.188) ← ←					
Run 4	135°C	RbD1	122.0	377361.35	-0.074
		RbD2	147.5	384235.98	-0.108
		KD1	98.5	389300.01	-0.287
		KD2	113.0	391021.51	-0.497
Alk.Ratio (K:Rb): 3.546(3.559) → at 235°C: 5.609(5.034)					
→ → Avg. Estimated Alk. Ratio (K:Rb) at 235°C: 5.609(5.034) ← ←					
Run 5	135°C	RbD1	121.0	377146.01	-0.097
		RbD2	148.0	384239.01	-0.151
		KD1	112.0	389293.0	-0.309
		KD2	152.0	391021.02	-0.401
Alk.Ratio (K:Rb): 3.074(3.078) → at 235°C: 4.862(4.353)					
	140°C	RbD1	118.0	377138.01	-0.13
		RbD2	143.0	384241.0	-0.208
		KD1	114.0	389292.01	-0.384
		KD2	139.0	391020.0	-0.541
Alk.Ratio (K:Rb): 2.858(2.861) → at 235°C: 4.395(4.046)					
	145°C	RbD1	125.0	377149.04	-0.184
		RbD2	146.0	384228.01	-0.28

Continued on next page

Table B.18 – continued from previous page

			FWHM	Center	Max.Att.
		KD1	109.0	389294.03	-0.511
		KD2	132.0	391018.0	-0.713
Alk.Ratio (K:Rb): 2.548(2.549) → at 235°C: 3.812(3.605)					
→ → Avg. Estimated Alk. Ratio (K:Rb) at 235°C: 4.356(6.964) ← ←					

Table B.19: Fulla - Low Power Spec. Results (Fitted)

			FWHM	Center	Max.Att.	η
Run 6	110°C	RbD1	153.346(31.559)	377151.02(17.25)	-0.028	0.945(0.519)
		RbD2	119.635(14.389)	384209.58(7.99)	-0.07	0.366(0.318)
		KD1	83.327(5.534)	389293.96(3.13)	-0.283	0.507(0.162)
		KD2	122.81(3.98)	391018.09(2.2)	-0.479	0.532(0.081)
Alk.Ratio (K:Rb): 7.191(10.01) $\rightarrow$ at 235°C: 13.242(14.157)						
	130°C	RbD1	113.024(3.684)	377146.36(2.0)	-0.244	1.0(0.081)
		RbD2	126.549(3.113)	384236.35(1.65)	-0.422	1.0(0.059)
		KD1	98.067(1.105)	389294.86(0.57)	-1.618	0.872(0.027)
		KD2	131.206(0.928)	391017.18(0.46)	-2.32	0.973(0.017)
Alk.Ratio (K:Rb): 5.915(5.916) $\rightarrow$ at 235°C: 9.63(8.367)						
	150°C	RbD1	115.802(1.172)	377143.29(0.64)	-0.289	0.949(0.026)
		RbD2	122.436(0.768)	384234.46(0.41)	-0.684	1.0(0.015)
$\rightarrow$ $\rightarrow$ Avg. Estimated Alk. Ratio (K:Rb) at 235°C: 11.436(16.543) $\leftarrow$ $\leftarrow$						

Table B.20: Fulla - Low Power Spec. Results (Integrated)

			FWHM	Center	Max.Att.
Run 6	110°C	RbD1	156.5	377191.51	-0.048
		RbD2	92.0	384201.01	-0.1
		KD1	76.5	389301.51	-0.316
		KD2	100.5	391012.51	-0.56
Alk.Ratio (K:Rb): 6.268(6.923) $\rightarrow$ at 235°C: 11.542(9.791)					
	130°C	RbD1	95.0	377159.01	-0.276
		RbD2	117.0	384240.0	-0.449
		KD1	99.0	389287.01	-1.636
		KD2	135.0	391025.01	-2.319
Alk.Ratio (K:Rb): 6.115(6.122) $\rightarrow$ at 235°C: 9.956(8.658)					
	150°C	RbD1	115.0	377141.01	-0.303
		RbD2	121.0	384223.01	-0.709
$\rightarrow$ $\rightarrow$ Avg. Estimated Alk. Ratio (K:Rb) at 235°C: 10.749(13.094) $\leftarrow$ $\leftarrow$					

Table B.21: Kappa 1 - High Power Spec. Results (Fitted)

			FWHM	Center	Max.Att.	η
Run 2	85°C	RbD1	10.916(0.906)	377110.24(0.44)	-0.028	0.414(0.192)
		RbD2	16.091(0.867)	384229.56(0.42)	-0.078	0.981(0.136)
		KD1	10.555(0.516)	389286.32(0.27)	-0.144	0.746(0.124)
		KD2	17.065(0.471)	391014.66(0.26)	-0.202	1.0(0.069)
Alk.Ratio (K:Rb): 3.56(3.703) → at 235°C: 7.795(5.237)						
	90°C	RbD1	15.661(1.09)	377111.53(0.52)	-0.038	1.0(0.157)
		RbD2	17.45(0.447)	384229.63(0.22)	-0.102	0.903(0.059)
		KD1	11.508(0.383)	389286.5(0.18)	-0.182	0.902(0.082)
		KD2	14.864(0.238)	391015.45(0.13)	-0.306	0.902(0.039)
Alk.Ratio (K:Rb): 2.948(2.985) → at 235°C: 6.224(4.221)						
	100°C	RbD1	11.469(0.137)	377111.08(0.07)	-0.161	1.0(0.027)
		RbD2	13.275(0.159)	384229.78(0.08)	-0.39	1.0(0.029)
		KD1	11.434(0.175)	389286.61(0.09)	-0.446	0.889(0.038)
		KD2	14.22(0.099)	391016.13(0.05)	-0.871	0.924(0.016)
Alk.Ratio (K:Rb): 2.402(2.406) → at 235°C: 4.728(3.402)						
	105°C	RbD1	12.03(0.23)	377111.07(0.11)	-0.169	0.998(0.044)
		RbD2	14.588(0.243)	384230.33(0.13)	-0.398	1.0(0.038)
		KD1	10.879(0.113)	389286.3(0.06)	-0.762	0.957(0.023)
		KD2	13.996(0.069)	391016.12(0.04)	-1.377	0.816(0.011)
Alk.Ratio (K:Rb): 3.483(3.493) → at 235°C: 6.628(4.94)						
→ → Avg. Estimated Alk. Ratio (K:Rb) at 235°C: 6.344(9.079) ← ←						

Table B.22: Kappa 1 - High Power Spec. Results (Integrated)

			FWHM	Center	Max.Att.
Run 2	85°C	RbD1	13.0	377112.01	-0.028
		RbD2	18.0	384230.01	-0.081
		KD1	11.0	389287.02	-0.14
		KD2	15.0	391016.01	-0.207
Alk.Ratio (K:Rb): 0.857(1.4) → at 235°C: 1.876(1.98)					
	90°C	RbD1	16.0	377111.0	-0.041
		RbD2	18.0	384230.01	-0.105
		KD1	11.0	389286.01	-0.181
		KD2	15.0	391016.0	-0.301
Alk.Ratio (K:Rb): 1.012(1.255) → at 235°C: 2.137(1.775)					
	100°C	RbD1	13.0	377111.01	-0.164
		RbD2	15.0	384230.01	-0.416
		KD1	12.0	389287.0	-0.439
		KD2	15.0	391016.01	-0.854
Continued on next page					

Table B.22 – continued from previous page

			FWHM	Center	Max.Att.
Alk.Ratio (K:Rb): 1.888(1.888) → at 235°C: 3.715(2.67)					
	105°C	RbD1	14.0	377111.01	-0.17
		RbD2	16.0	384231.0	-0.405
		KD1	11.0	389287.01	-0.757
		KD2	15.0	391016.01	-1.343
Alk.Ratio (K:Rb): 3.99(4.014) → at 235°C: 7.593(5.676)					
→ → Avg. Estimated Alk. Ratio (K:Rb) at 235°C: 3.83(7.185) ← ←					

Table B.23: Kappa 2 - High Power Spec. Results (Fitted)

			FWHM	Center	Max.Att.	η
Run 1	85°C	RbD1	16.486(1.079)	377108.23(0.64)	-0.028	0.349(0.15)
		RbD2	15.479(0.379)	384230.5(0.18)	-0.079	1.0(0.055)
		KD1	12.888(0.622)	389286.28(0.31)	-0.101	1.0(0.11)
		KD2	15.183(0.31)	391016.1(0.15)	-0.221	1.0(0.047)
Alk.Ratio (K:Rb): 2.658(2.661) → at 235°C: 5.819(3.764)						
	90°C	RbD1	19.883(2.726)	377109.17(1.38)	-0.046	0.922(0.28)
		RbD2	14.633(0.591)	384230.62(0.34)	-0.14	0.723(0.098)
		KD1	11.261(1.022)	389286.03(0.57)	-0.18	0.707(0.223)
		KD2	14.964(0.738)	391015.16(0.36)	-0.323	1.0(0.115)
Alk.Ratio (K:Rb): 2.339(2.41) → at 235°C: 4.938(3.408)						
	95°C	RbD1	14.38(1.335)	377110.72(0.66)	-0.076	1.0(0.225)
		RbD2	14.895(0.641)	384230.16(0.31)	-0.197	1.0(0.098)
		KD1	11.329(0.53)	389286.63(0.32)	-0.283	0.647(0.115)
		KD2	15.022(0.097)	391016.13(0.05)	-0.52	0.954(0.015)
Alk.Ratio (K:Rb): 2.778(2.779) → at 235°C: 5.66(3.93)						
	100°C	RbD1	14.831(0.302)	377110.67(0.16)	-0.102	0.741(0.045)
		RbD2	14.498(0.133)	384230.55(0.07)	-0.26	1.0(0.021)
		KD1	11.536(0.097)	389286.32(0.05)	-0.441	1.0(0.019)
		KD2	14.942(0.067)	391016.19(0.03)	-0.728	0.998(0.01)
Alk.Ratio (K:Rb): 2.953(2.96) → at 235°C: 5.812(4.186)						
	105°C	RbD1	13.085(0.2)	377111.27(0.1)	-0.152	1.0(0.034)
		RbD2	14.538(0.092)	384230.42(0.04)	-0.364	0.98(0.014)
		KD1	11.554(0.079)	389286.38(0.04)	-0.658	0.936(0.015)
		KD2	14.048(0.046)	391016.23(0.02)	-1.252	0.938(0.007)
Alk.Ratio (K:Rb): 3.384(3.389) → at 235°C: 6.439(4.793)						
	120°C	RbD1	11.033(0.145)	377111.17(0.07)	-0.899	0.955(0.03)
→ → Avg. Estimated Alk. Ratio (K:Rb) at 235°C: 5.734(9.052) ← ←						

Table B.24: Kappa 2 - High Power Spec. Results (Integrated)

			FWHM	Center	Max.Att.
Run 1	85°C	RbD1	17.0	377106.01	-0.03
		RbD2	15.0	384230.01	-0.081
		KD1	13.0	389287.0	-0.103
		KD2	16.0	391017.01	-0.216
Alk.Ratio (K:Rb): -5.337(9.663) → at 235°C: -11.687(13.666)					
	90°C	RbD1	19.0	377111.51	-0.051
		RbD2	16.5	384230.01	-0.14
		KD1	11.0	389286.5	-0.192
Continued on next page					

Table B.24 – continued from previous page

			FWHM	Center	Max.Att.
		KD2	15.5	391015.5	-0.327
Alk.Ratio (K:Rb): 5.194(8.134) → at 235°C: 10.965(11.504)					
	95°C	RbD1	15.0	377111.5	-0.08
		RbD2	16.0	384230.5	-0.197
		KD1	12.0	389286.0	-0.28
		KD2	15.0	391016.01	-0.512
Alk.Ratio (K:Rb): 2.41(2.411) → at 235°C: 4.909(3.41)					
	100°C	RbD1	17.0	377111.01	-0.105
		RbD2	15.0	384229.01	-0.26
		KD1	12.0	389287.01	-0.447
		KD2	15.0	391016.0	-0.723
Alk.Ratio (K:Rb): 3.239(3.241) → at 235°C: 6.375(4.583)					
	105°C	RbD1	14.0	377111.01	-0.153
		RbD2	16.0	384230.0	-0.363
		KD1	12.0	389287.01	-0.645
		KD2	15.0	391016.0	-1.227
Alk.Ratio (K:Rb): 3.457(3.499) → at 235°C: 6.578(4.948)					
	120°C	RbD1	13.0	377111.01	-0.914
→ → Avg. Estimated Alk. Ratio (K:Rb) at 235°C: 3.428(20.915) ← ←					

Table B.25: Kappa 2 - Low Power Spec. Results (Fitted)

			FWHM	Center	Max.Att.	η
Run 2	70°C	RbD1	7.797(2.488)	377109.55(1.7)	-0.005	0.0(0.654)
		RbD2	17.215(0.771)	384229.24(0.38)	-0.013	1.0(0.102)
		KD1	10.885(1.084)	389286.74(0.66)	-0.018	0.071(0.23)
		KD2	18.17(0.946)	391014.12(0.52)	-0.03	0.498(0.119)
Alk.Ratio (K:Rb): 3.459(8.391) → at 235°C: 8.507(11.867)						
	80°C	RbD1	16.987(0.682)	377110.16(0.34)	-0.012	1.0(0.091)
		RbD2	16.387(0.345)	384230.45(0.17)	-0.028	1.0(0.048)
		KD1	10.894(0.471)	389286.19(0.24)	-0.043	0.657(0.094)
		KD2	15.772(0.278)	391015.75(0.14)	-0.088	1.0(0.04)
Alk.Ratio (K:Rb): 2.585(2.61) → at 235°C: 5.878(3.692)						
	85°C	RbD1	9.989(1.775)	377110.56(1.19)	-0.016	0.0(0.383)
		RbD2	17.312(0.218)	384230.31(0.11)	-0.04	1.0(0.028)
		KD1	11.811(0.334)	389286.29(0.17)	-0.068	0.874(0.064)
		KD2	13.651(0.17)	391016.21(0.09)	-0.142	0.776(0.028)
Alk.Ratio (K:Rb): 3.564(4.201) → at 235°C: 7.805(5.942)						
	90°C	RbD1	15.182(0.269)	377110.95(0.13)	-0.026	1.0(0.04)
		RbD2	14.975(0.139)	384230.33(0.07)	-0.06	1.0(0.021)
		KD1	11.641(0.2)	389286.7(0.1)	-0.123	1.0(0.039)
		KD2	13.893(0.103)	391016.0(0.05)	-0.258	1.0(0.017)
Alk.Ratio (K:Rb): 3.644(3.65) → at 235°C: 7.694(5.162)						
	95°C	RbD1	15.032(0.125)	377111.06(0.06)	-0.083	1.0(0.019)
		RbD2	15.906(0.095)	384230.44(0.05)	-0.197	1.0(0.013)
		KD1	11.024(0.104)	389286.36(0.05)	-0.411	1.0(0.021)
		KD2	13.545(0.058)	391015.89(0.03)	-0.822	1.0(0.01)
Alk.Ratio (K:Rb): 3.451(3.451) → at 235°C: 7.031(4.88)						
	100°C	RbD1	17.561(0.304)	377111.07(0.15)	-0.054	1.0(0.039)
		RbD2	14.237(0.116)	384229.87(0.05)	-0.131	1.0(0.018)
		KD1	9.838(0.089)	389286.64(0.04)	-0.309	0.927(0.02)
		KD2	11.837(0.039)	391016.23(0.02)	-0.759	0.829(0.007)
Alk.Ratio (K:Rb): 3.891(3.963) → at 235°C: 7.658(5.604)						
	105°C	RbD1	14.077(0.104)	377111.27(0.05)	-0.183	1.0(0.017)
		RbD2	13.504(0.074)	384230.64(0.04)	-0.493	1.0(0.012)
		KD1	9.628(0.045)	389286.59(0.02)	-1.19	0.882(0.006)
		KD2	13.232(0.025)	391016.06(0.01)	-2.321	0.723(0.003)
Alk.Ratio (K:Rb): 4.333(4.335) → at 235°C: 8.245(6.13)						
	110°C	RbD1	13.948(0.13)	377111.14(0.06)	-0.11	1.0(0.021)
		RbD2	12.504(0.043)	384230.43(0.02)	-0.318	1.0(0.008)
		KD1	8.312(0.078)	389286.62(0.04)	-0.995	0.746(0.012)
		KD2	12.4(0.043)	391016.09(0.02)	-2.084	0.465(0.004)
Alk.Ratio (K:Rb): 5.724(5.755) → at 235°C: 10.541(8.139)						

Continued on next page

Table B.25 – continued from previous page

			FWHM	Center	Max.Att.	η
→ → Avg. Estimated Alk. Ratio (K:Rb) at 235°C: 7.92(19.416) ← ←						
Run 3	70°C	RbD1	13.865(1.983)	377111.01(1.02)	-0.009	0.676(0.327)
		RbD2	16.913(1.229)	384230.12(0.61)	-0.019	0.937(0.161)
		KD1	13.224(1.608)	389286.89(0.81)	-0.027	0.891(0.264)
		KD2	14.354(0.852)	391014.82(0.45)	-0.049	0.689(0.14)
Alk.Ratio (K:Rb): 2.31(2.409) → at 235°C: 5.681(3.407)						
→ → Avg. Estimated Alk. Ratio (K:Rb) at 235°C: 5.681(3.407) ← ←						

Table B.26: Kappa 2 - Low Power Spec. Results (Integrated)

			FWHM	Center	Max.Att.
Run 2	70°C	RbD1	8.0	377110.98	-0.003
		RbD2	17.0	384229.01	-0.014
		KD1	11.0	389286.0	-0.018
		KD2	17.0	391015.0	-0.033
Alk.Ratio (K:Rb): 2.107(2.693) → at 235°C: 5.181(3.808)					
	80°C	RbD1	16.0	377111.01	-0.013
		RbD2	18.0	384231.01	-0.028
		KD1	11.0	389285.01	-0.042
		KD2	14.0	391016.01	-0.093
Alk.Ratio (K:Rb): 0.686(1.892) → at 235°C: 1.56(2.675)					
	85°C	RbD1	11.0	377111.98	-0.011
		RbD2	18.0	384229.0	-0.041
		KD1	12.0	389285.01	-0.068
		KD2	14.0	391016.0	-0.14
Alk.Ratio (K:Rb): 1.416(2.097) → at 235°C: 3.102(2.966)					
	90°C	RbD1	17.0	377111.0	-0.027
		RbD2	16.0	384230.01	-0.061
		KD1	12.0	389287.01	-0.123
		KD2	13.0	391016.0	-0.257
Alk.Ratio (K:Rb): 4.466(4.557) → at 235°C: 9.428(6.444)					
	95°C	RbD1	17.0	377111.01	-0.084
		RbD2	16.0	384230.01	-0.206
		KD1	10.0	389287.0	-0.411
		KD2	13.0	391016.0	-0.823
Alk.Ratio (K:Rb): 4.678(4.751) → at 235°C: 9.532(6.719)					
	100°C	RbD1	17.0	377111.01	-0.057
		RbD2	14.0	384229.94	-0.14
		KD1	10.0	389287.01	-0.304
		KD2	12.0	391016.01	-0.745

Continued on next page

Table B.26 – continued from previous page

			FWHM	Center	Max.Att.
Alk.Ratio (K:Rb): 2.988(3.83) → at 235°C: 5.881(5.417)					
	105°C	RbD1	15.0	377111.0	-0.187
		RbD2	15.0	384230.04	-0.501
		KD1	9.0	389287.02	-1.162
		KD2	15.0	391016.0	-2.261
Alk.Ratio (K:Rb): 3.996(4.029) → at 235°C: 7.604(5.698)					
	110°C	RbD1	15.0	377111.01	-0.113
		RbD2	14.0	384230.0	-0.325
		KD1	9.0	389287.28	-0.966
		KD2	14.0	391016.02	-1.964
Alk.Ratio (K:Rb): 5.711(5.744) → at 235°C: 10.516(8.124)					
→ → Avg. Estimated Alk. Ratio (K:Rb) at 235°C: 6.6(15.939) ← ←					
Run 3	70°C	RbD1	16.333	377111.33	-0.009
		RbD2	17.0	384230.34	-0.02
		KD1	12.667	389287.01	-0.028
		KD2	14.0	391016.01	-0.051
Alk.Ratio (K:Rb): 3.208(5.798) → at 235°C: 7.89(8.2)					
→ → Avg. Estimated Alk. Ratio (K:Rb) at 235°C: 7.89(8.2) ← ←					

Table B.27: Kappa 3 - High Power Spec. Results (Fitted)

			FWHM	Center	Max.Att.	η
Run 1	95°C	RbD1	15.662(3.506)	377108.75(2.13)	-0.05	0.643(0.599)
		RbD2	17.164(0.783)	384229.91(0.39)	-0.112	0.984(0.103)
		KD1	16.318(1.983)	389286.29(0.98)	-0.158	0.934(0.233)
		KD2	18.457(1.096)	391015.73(0.55)	-0.245	1.0(0.132)
Alk.Ratio (K:Rb): 3.363(7.646) → at 235°C: 6.851(10.813)						
	100°C	RbD1	20.643(0.79)	377110.83(0.4)	-0.061	1.0(0.088)
		RbD2	14.508(0.428)	384230.45(0.24)	-0.13	0.599(0.066)
		KD1	14.331(0.231)	389286.72(0.11)	-0.324	1.0(0.036)
		KD2	17.342(0.168)	391016.0(0.09)	-0.473	0.799(0.022)
Alk.Ratio (K:Rb): 3.892(3.902) → at 235°C: 7.66(5.518)						
	105°C	RbD1	16.104(0.634)	377111.15(0.32)	-0.085	0.94(0.089)
		RbD2	14.924(0.263)	384230.37(0.13)	-0.218	0.896(0.039)
		KD1	13.737(0.187)	389286.45(0.09)	-0.467	0.893(0.03)
		KD2	19.007(0.16)	391015.53(0.09)	-0.616	0.728(0.019)
Alk.Ratio (K:Rb): 4.001(4.034) → at 235°C: 7.613(5.705)						
→ → Avg. Estimated Alk. Ratio (K:Rb) at 235°C: 7.375(13.418) ← ←						

Table B.28: Kappa 3 - High Power Spec. Results (Integrated)

			FWHM	Center	Max.Att.
Run 1	95°C	RbD1	15.667	377110.34	-0.052
		RbD2	17.5	384229.5	-0.121
		KD1	14.5	389286.5	-0.162
		KD2	17.0	391016.0	-0.249
Alk.Ratio (K:Rb): 1.194(1.952) → at 235°C: 2.433(2.761)					
	100°C	RbD1	19.0	377111.01	-0.066
		RbD2	15.0	384231.01	-0.13
		KD1	13.0	389287.0	-0.331
		KD2	19.0	391015.01	-0.462
Alk.Ratio (K:Rb): 22.18(29.254) → at 235°C: 43.652(41.371)					
	105°C	RbD1	18.0	377111.0	-0.091
		RbD2	17.0	384231.01	-0.217
		KD1	14.0	389287.0	-0.459
		KD2	21.0	391016.01	-0.596
Alk.Ratio (K:Rb): 3.058(3.244) → at 235°C: 5.819(4.587)					
→ → Avg. Estimated Alk. Ratio (K:Rb) at 235°C: 17.301(45.709) ← ←					

Table B.29: Kappa 3 - Low Power Spec. Results (Fitted)

			FWHM	Center	Max.Att.	η
Run 2	90°C	RbD1	20.824(0.994)	377110.06(0.5)	-0.049	1.0(0.109)
		RbD2	17.027(0.506)	384230.22(0.27)	-0.115	0.749(0.067)
		KD1	12.573(0.521)	389286.35(0.26)	-0.285	0.995(0.094)
		KD2	14.894(0.271)	391016.3(0.14)	-0.579	0.835(0.041)
Alk.Ratio (K:Rb): 3.87(3.895) → at 235°C: 8.17(5.508)						
	95°C	RbD1	18.916(1.035)	377109.82(0.53)	-0.027	1.0(0.124)
		RbD2	16.758(0.536)	384230.33(0.26)	-0.065	1.0(0.071)
		KD1	11.811(0.299)	389286.82(0.15)	-0.167	0.954(0.057)
		KD2	12.958(0.141)	391015.73(0.07)	-0.386	0.937(0.025)
Alk.Ratio (K:Rb): 4.199(4.256) → at 235°C: 8.554(6.018)						
	100°C	RbD1	14.55(0.727)	377110.96(0.43)	-0.078	0.595(0.114)
		RbD2	16.721(0.246)	384230.23(0.12)	-0.169	1.0(0.034)
		KD1	10.727(0.165)	389286.53(0.08)	-0.51	0.945(0.035)
		KD2	12.886(0.092)	391015.89(0.05)	-1.029	0.923(0.016)
Alk.Ratio (K:Rb): 4.479(4.493) → at 235°C: 8.816(6.354)						
	105°C	RbD1	15.982(0.229)	377111.21(0.11)	-0.05	1.0(0.032)
		RbD2	14.613(0.194)	384230.19(0.09)	-0.103	0.952(0.029)
		KD1	9.695(0.068)	389286.62(0.03)	-0.38	0.924(0.013)
		KD2	11.366(0.025)	391015.58(0.01)	-1.094	0.746(0.004)
Alk.Ratio (K:Rb): 6.242(6.49) → at 235°C: 11.878(9.178)						
	110°C	RbD1	15.488(0.14)	377111.06(0.07)	-0.074	1.0(0.021)
		RbD2	13.832(0.058)	384230.47(0.03)	-0.197	1.0(0.009)
		KD1	8.826(0.062)	389286.65(0.03)	-0.886	0.783(0.01)
		KD2	12.178(0.035)	391015.91(0.02)	-1.823	0.582(0.004)
Alk.Ratio (K:Rb): 7.3(7.332) → at 235°C: 13.442(10.369)						
	120°C	RbD1	15.063(0.148)	377111.04(0.07)	-0.183	1.0(0.022)
		RbD2	11.088(0.049)	384230.37(0.02)	-0.541	0.971(0.01)
	130°C	RbD1	10.751(0.045)	377111.42(0.02)	-0.431	1.0(0.009)
		RbD2	9.994(0.024)	384230.41(0.01)	-1.736	0.738(0.004)
→ → Avg. Estimated Alk. Ratio (K:Rb) at 235°C: 10.172(17.41) ← ←						
Run 3	70°C	RbD1	8.173(1.377)	377111.04(0.93)	-0.004	0.0(0.348)
		RbD2	15.624(0.897)	384230.64(0.44)	-0.009	1.0(0.13)
		KD1	11.414(0.828)	389286.92(0.44)	-0.015	0.0(0.166)
		KD2	14.974(0.41)	391015.47(0.2)	-0.041	0.952(0.062)
Alk.Ratio (K:Rb): 3.987(4.267) → at 235°C: 9.806(6.034)						
	75°C	RbD1	13.489(0.668)	377111.07(0.4)	-0.015	0.323(0.111)
		RbD2	22.144(0.606)	384228.43(0.3)	-0.033	1.0(0.062)
		KD1	12.53(0.586)	389286.32(0.3)	-0.065	0.839(0.106)
		KD2	16.151(0.365)	391016.86(0.2)	-0.116	0.688(0.051)
Alk.Ratio (K:Rb): 3.199(3.255) → at 235°C: 7.559(4.603)						

Continued on next page

Table B.29 – continued from previous page

			FWHM	Center	Max.Att.	η
	80°C	RbD1	16.472(1.037)	377111.52(0.51)	-0.011	1.0(0.142)
		RbD2	20.811(0.592)	384229.93(0.29)	-0.022	1.0(0.064)
		KD1	11.414(0.231)	389286.79(0.12)	-0.045	0.661(0.046)
		KD2	17.158(0.18)	391015.19(0.09)	-0.077	0.929(0.024)
Alk.Ratio (K:Rb): 2.865(2.867) → at 235°C: 6.513(4.054)						
	85°C	RbD1	18.384(0.768)	377110.54(0.38)	-0.013	1.0(0.095)
		RbD2	16.145(0.241)	384230.57(0.12)	-0.028	1.0(0.034)
		KD1	11.977(0.241)	389286.76(0.12)	-0.073	0.946(0.046)
		KD2	15.528(0.133)	391016.07(0.07)	-0.152	1.0(0.02)
Alk.Ratio (K:Rb): 4.251(4.329) → at 235°C: 9.309(6.122)						
	90°C	RbD1	16.989(0.545)	377110.54(0.27)	-0.021	1.0(0.073)
		RbD2	16.826(0.222)	384230.42(0.11)	-0.038	1.0(0.029)
		KD1	11.6(0.136)	389286.69(0.07)	-0.102	0.962(0.026)
		KD2	14.692(0.07)	391016.33(0.03)	-0.219	1.0(0.011)
Alk.Ratio (K:Rb): 4.125(4.209) → at 235°C: 8.708(5.952)						
	95°C	RbD1	15.43(0.103)	377111.16(0.05)	-0.062	1.0(0.015)
		RbD2	16.802(0.065)	384230.06(0.03)	-0.14	1.0(0.009)
		KD1	11.661(0.074)	389286.3(0.04)	-0.41	1.0(0.014)
		KD2	14.083(0.037)	391016.13(0.02)	-0.896	0.919(0.006)
Alk.Ratio (K:Rb): 5.005(5.01) → at 235°C: 10.197(7.086)						
	100°C	RbD1	15.173(0.091)	377111.24(0.04)	-0.087	1.0(0.013)
		RbD2	15.772(0.051)	384230.53(0.02)	-0.211	1.0(0.007)
		KD1	10.888(0.319)	389286.55(0.16)	-0.643	0.974(0.066)
		KD2	15.426(0.219)	391013.75(0.11)	-1.086	0.842(0.032)
Alk.Ratio (K:Rb): 4.996(4.997) → at 235°C: 9.832(7.066)						
	105°C	RbD1	17.053(0.317)	377111.12(0.16)	-0.051	1.0(0.042)
		RbD2	14.759(0.084)	384230.57(0.04)	-0.129	1.0(0.013)
		KD1	9.59(0.059)	389286.35(0.03)	-0.537	0.875(0.012)
		KD2	11.206(0.025)	391016.03(0.01)	-1.367	0.802(0.004)
Alk.Ratio (K:Rb): 6.773(6.85) → at 235°C: 12.889(9.688)						
	110°C	RbD1	15.658(0.162)	377111.21(0.08)	-0.072	1.0(0.023)
		RbD2	13.522(0.051)	384230.09(0.02)	-0.207	1.0(0.008)
		KD1	8.527(0.066)	389286.6(0.03)	-1.041	0.777(0.009)
		KD2	12.832(0.04)	391015.77(0.02)	-2.095	0.501(0.003)
Alk.Ratio (K:Rb): 8.523(8.57) → at 235°C: 15.694(12.12)						
→ → Avg. Estimated Alk. Ratio (K:Rb) at 235°C: 10.056(22.24) ← ←						
Run 4	70°C	RbD1	10.133(1.741)	377109.79(0.8)	-0.004	1.0(0.381)
		RbD2	14.684(1.184)	384231.04(0.74)	-0.009	0.221(0.181)
		KD1	14.219(1.018)	389287.17(0.5)	-0.017	1.0(0.164)
		KD2	18.342(0.759)	391016.79(0.38)	-0.026	1.0(0.094)

Continued on next page

Table B.29 – continued from previous page

			FWHM	Center	Max.Att.	η
Alk.Ratio (K:Rb): 4.434(5.203) → at 235°C: 10.903(7.358)						
	80°C	RbD1	15.104(0.865)	377110.52(0.42)	-0.01	1.0(0.129)
		RbD2	17.401(0.348)	384230.08(0.17)	-0.019	1.0(0.045)
		KD1	13.324(0.171)	389286.61(0.08)	-0.044	1.0(0.029)
		KD2	16.566(0.109)	391015.76(0.06)	-0.075	0.911(0.015)
Alk.Ratio (K:Rb): 3.846(3.849) → at 235°C: 8.744(5.443)						
	85°C	RbD1	15.493(0.637)	377110.71(0.33)	-0.019	1.0(0.095)
		RbD2	16.813(0.266)	384230.5(0.13)	-0.041	1.0(0.036)
		KD1	11.942(0.356)	389286.37(0.18)	-0.103	1.0(0.068)
		KD2	15.619(0.21)	391015.71(0.11)	-0.193	0.985(0.031)
Alk.Ratio (K:Rb): 4.164(4.169) → at 235°C: 9.118(5.896)						
	90°C	RbD1	15.961(0.582)	377110.83(0.28)	-0.028	1.0(0.084)
		RbD2	17.074(0.195)	384230.4(0.1)	-0.081	1.0(0.026)
		KD1	11.592(0.107)	389286.63(0.05)	-0.212	1.0(0.021)
		KD2	14.434(0.061)	391016.17(0.03)	-0.414	0.98(0.01)
Alk.Ratio (K:Rb): 4.923(5.069) → at 235°C: 10.393(7.169)						
	95°C	RbD1	21.011(0.864)	377111.01(0.42)	-0.025	1.0(0.092)
		RbD2	16.827(0.128)	384230.17(0.06)	-0.054	1.0(0.017)
		KD1	10.793(0.072)	389286.38(0.04)	-0.161	1.0(0.015)
		KD2	13.211(0.037)	391015.88(0.02)	-0.341	0.93(0.006)
Alk.Ratio (K:Rb): 4.065(4.137) → at 235°C: 8.283(5.85)						
	100°C	RbD1	18.103(0.295)	377110.87(0.14)	-0.038	1.0(0.036)
		RbD2	16.183(0.191)	384230.41(0.1)	-0.071	0.934(0.027)
		KD1	10.388(0.033)	389286.68(0.02)	-0.251	0.952(0.006)
		KD2	12.378(0.016)	391016.21(0.01)	-0.564	0.877(0.002)
Alk.Ratio (K:Rb): 4.847(4.975) → at 235°C: 9.54(7.035)						
	105°C	RbD1	17.428(0.209)	377111.26(0.1)	-0.049	1.0(0.026)
		RbD2	15.474(0.07)	384230.27(0.03)	-0.116	1.0(0.01)
		KD1	9.085(0.068)	389286.38(0.03)	-0.504	0.992(0.016)
		KD2	11.257(0.028)	391015.29(0.01)	-1.302	0.814(0.005)
Alk.Ratio (K:Rb): 6.556(6.707) → at 235°C: 12.475(9.485)						
	110°C	RbD1	15.491(0.173)	377111.22(0.08)	-0.071	1.0(0.025)
		RbD2	14.56(0.045)	384230.38(0.02)	-0.179	1.0(0.007)
		KD1	8.734(0.076)	389286.38(0.04)	-0.894	0.78(0.013)
		KD2	12.023(0.037)	391016.08(0.02)	-2.084	0.567(0.005)
Alk.Ratio (K:Rb): 8.171(8.278) → at 235°C: 15.046(11.707)						
	130°C	RbD1	11.07(0.027)	377111.2(0.01)	-0.822	1.0(0.005)
		RbD2	11.253(0.023)	384230.42(0.01)	-2.698	0.753(0.003)
→ → Avg. Estimated Alk. Ratio (K:Rb) at 235°C: 10.563(22.025) ← ←						

Table B.30: Kappa 3 - Low Power Spec. Results (Integrated)

			FWHM	Center	Max.Att.
Run 2	90°C	RbD1	20.0	377111.0	-0.052
		RbD2	19.0	384231.0	-0.116
		KD1	13.0	389287.0	-0.28
		KD2	16.0	391017.0	-0.576
Alk.Ratio (K:Rb): 3.32(3.334) → at 235°C: 7.008(4.715)					
	95°C	RbD1	17.0	377111.01	-0.03
		RbD2	17.5	384230.51	-0.066
		KD1	11.5	389287.01	-0.165
		KD2	12.5	391016.01	-0.39
Alk.Ratio (K:Rb): 0.946(6.37) → at 235°C: 1.927(9.009)					
	100°C	RbD1	15.0	377111.0	-0.078
		RbD2	17.5	384230.01	-0.176
		KD1	9.5	389287.01	-0.502
		KD2	13.0	391016.0	-1.02
Alk.Ratio (K:Rb): 3.789(4.895) → at 235°C: 7.457(6.923)					
	105°C	RbD1	17.0	377111.0	-0.05
		RbD2	15.0	384229.01	-0.101
		KD1	10.0	389287.0	-0.375
		KD2	12.0	391016.01	-1.117
Alk.Ratio (K:Rb): -0.063(10.134) → at 235°C: -0.119(14.332)					
	110°C	RbD1	16.0	377111.0	-0.075
		RbD2	15.0	384231.01	-0.2
		KD1	10.0	389287.01	-0.866
		KD2	13.0	391015.0	-1.75
Alk.Ratio (K:Rb): 7.313(7.322) → at 235°C: 13.466(10.355)					
	120°C	RbD1	14.0	377111.0	-0.189
		RbD2	13.0	384230.01	-0.555
	130°C	RbD1	12.0	377111.04	-0.441
		RbD2	13.0	384230.0	-1.698
→ → Avg. Estimated Alk. Ratio (K:Rb) at 235°C: 5.948(22.058) ← ←					
Run 3	70°C	RbD1	13.0	377112.0	-0.004
		RbD2	15.0	384230.0	-0.009
		KD1	11.0	389287.0	-0.014
		KD2	15.0	391017.01	-0.042
Alk.Ratio (K:Rb): 0.388(2.294) → at 235°C: 0.955(3.244)					
	75°C	RbD1	15.0	377112.02	-0.014
		RbD2	18.0	384230.0	-0.036
		KD1	12.0	389285.01	-0.067
		KD2	15.0	391016.02	-0.127
Alk.Ratio (K:Rb): 0.331(0.575) → at 235°C: 0.783(0.814)					

Continued on next page

Table B.30 – continued from previous page

			FWHM	Center	Max.Att.
	80°C	RbD1	17.0	377111.97	-0.011
		RbD2	19.0	384230.0	-0.023
		KD1	12.0	389287.01	-0.044
		KD2	15.0	391015.0	-0.08
Alk.Ratio (K:Rb): 0.927(1.259) → at 235°C: 2.108(1.78)					
	85°C	RbD1	18.0	377111.02	-0.015
		RbD2	17.0	384231.01	-0.028
		KD1	12.0	389287.01	-0.072
		KD2	15.0	391016.0	-0.15
Alk.Ratio (K:Rb): 3.675(4.506) → at 235°C: 8.048(6.372)					
	90°C	RbD1	18.0	377111.0	-0.022
		RbD2	18.0	384231.0	-0.038
		KD1	12.0	389287.0	-0.101
		KD2	14.0	391016.01	-0.218
Alk.Ratio (K:Rb): 2.267(3.184) → at 235°C: 4.787(4.502)					
	95°C	RbD1	17.0	377111.02	-0.063
		RbD2	17.0	384230.01	-0.148
		KD1	12.0	389285.01	-0.407
		KD2	14.0	391016.0	-0.886
Alk.Ratio (K:Rb): 4.553(4.652) → at 235°C: 9.277(6.578)					
	100°C	RbD1	16.0	377111.0	-0.088
		RbD2	17.0	384230.01	-0.213
		KD1	12.0	389287.0	-0.639
		KD2	11.0	391016.0	-1.342
Alk.Ratio (K:Rb): 4.957(4.957) → at 235°C: 9.756(7.011)					
	105°C	RbD1	17.0	377111.0	-0.054
		RbD2	16.0	384230.04	-0.131
		KD1	10.0	389285.01	-0.521
		KD2	12.0	391016.01	-1.323
Alk.Ratio (K:Rb): 6.661(7.45) → at 235°C: 12.674(10.536)					
	110°C	RbD1	17.0	377111.01	-0.075
		RbD2	15.0	384229.01	-0.212
		KD1	9.0	389287.01	-1.015
		KD2	14.0	391015.0	-2.008
Alk.Ratio (K:Rb): 7.384(7.631) → at 235°C: 13.596(10.792)					
→ → Avg. Estimated Alk. Ratio (K:Rb) at 235°C: 6.887(20.412) ← ←					
Run 4	70°C	RbD1	12.0	377110.0	-0.004
		RbD2	17.0	384230.01	-0.009
		KD1	13.0	389287.01	-0.017
		KD2	18.0	391019.02	-0.028

Continued on next page

Table B.30 – continued from previous page

			FWHM	Center	Max.Att.
Alk.Ratio (K:Rb): 0.678(0.898) → at 235°C: 1.666(1.27)					
	80°C	RbD1	16.0	377111.0	-0.01
		RbD2	18.0	384231.0	-0.019
		KD1	13.0	389287.01	-0.044
		KD2	17.0	391017.0	-0.074
Alk.Ratio (K:Rb): 1.561(1.626) → at 235°C: 3.55(2.299)					
	85°C	RbD1	15.5	377111.01	-0.02
		RbD2	18.0	384230.51	-0.042
		KD1	11.5	389287.01	-0.103
		KD2	15.0	391015.5	-0.193
Alk.Ratio (K:Rb): 3.601(4.224) → at 235°C: 7.886(5.973)					
	90°C	RbD1	16.5	377111.0	-0.029
		RbD2	18.0	384230.01	-0.082
		KD1	12.0	389287.01	-0.213
		KD2	14.5	391016.01	-0.409
Alk.Ratio (K:Rb): 5.251(5.555) → at 235°C: 11.086(7.856)					
	95°C	RbD1	18.0	377111.03	-0.029
		RbD2	18.0	384230.0	-0.055
		KD1	10.0	389287.01	-0.162
		KD2	14.0	391016.01	-0.338
Alk.Ratio (K:Rb): 3.404(4.133) → at 235°C: 6.936(5.845)					
	100°C	RbD1	16.0	377111.01	-0.04
		RbD2	18.0	384230.0	-0.07
		KD1	11.0	389287.01	-0.248
		KD2	13.0	391016.0	-0.555
Alk.Ratio (K:Rb): 38.572(52.871) → at 235°C: 75.912(74.771)					
	105°C	RbD1	17.0	377111.0	-0.052
		RbD2	16.0	384229.01	-0.119
		KD1	10.0	389287.01	-0.498
		KD2	12.0	391016.01	-1.354
Alk.Ratio (K:Rb): 4.317(4.586) → at 235°C: 8.215(6.485)					
	110°C	RbD1	17.0	377111.01	-0.074
		RbD2	15.0	384230.0	-0.181
		KD1	10.0	389287.0	-0.855
		KD2	14.0	391016.01	-1.978
Alk.Ratio (K:Rb): 6.247(6.676) → at 235°C: 11.503(9.442)					
	130°C	RbD1	13.0	377111.0	-0.83
		RbD2	14.0	384230.01	-2.652
→ → Avg. Estimated Alk. Ratio (K:Rb) at 235°C: 15.844(79.911) ← ←					

Table B.31: Kappa 4 - High Power Spec. Results (Fitted)

			FWHM	Center	Max.Att.	η
Run 1	90°C	RbD1	15.619(0.453)	377110.43(0.22)	-0.23	1.0(0.065)
		RbD2	14.38(0.327)	384229.57(0.16)	-0.619	0.906(0.051)
		KD1	10.952(0.673)	389286.38(0.36)	-0.332	0.643(0.139)
		KD2	14.782(0.413)	391015.48(0.2)	-0.661	1.0(0.063)
Alk.Ratio (K:Rb): 1.02(1.02) → at 235°C: 2.152(1.443)						
	95°C	RbD1	14.675(0.306)	377111.04(0.15)	-0.361	1.0(0.047)
		RbD2	13.295(0.273)	384230.34(0.13)	-0.872	0.984(0.045)
		KD1	11.457(0.238)	389286.53(0.12)	-0.529	0.803(0.047)
		KD2	14.587(0.157)	391016.04(0.08)	-0.914	0.861(0.024)
Alk.Ratio (K:Rb): 1.097(1.097) → at 235°C: 2.236(1.552)						
→ → Avg. Estimated Alk. Ratio (K:Rb) at 235°C: 2.194(2.119) ← ←						
Run 2	90°C	RbD1	12.602(0.376)	377111.5(0.18)	-0.05	1.0(0.066)
		RbD2	15.514(0.201)	384230.8(0.1)	-0.127	0.943(0.029)
		KD1	13.38(0.133)	389286.57(0.06)	-0.13	1.0(0.022)
		KD2	17.592(0.1)	391016.16(0.05)	-0.196	1.0(0.013)
Alk.Ratio (K:Rb): 2.11(2.153) → at 235°C: 4.455(3.045)						
	95°C	RbD1	13.105(1.862)	377110.77(0.84)	-0.101	0.984(0.329)
		RbD2	16.905(1.062)	384230.39(0.52)	-0.223	1.0(0.142)
		KD1	12.759(0.982)	389286.63(0.63)	-0.257	0.94(0.204)
		KD2	17.509(0.53)	391016.21(0.28)	-0.481	0.962(0.085)
Alk.Ratio (K:Rb): 2.134(2.24) → at 235°C: 4.348(3.167)						
	120°C	RbD1	17.706(0.219)	377111.18(0.11)	-0.399	0.928(0.028)
		RbD2	24.535(0.189)	384230.47(0.1)	-0.516	0.903(0.017)
→ → Avg. Estimated Alk. Ratio (K:Rb) at 235°C: 4.402(4.394) ← ←						

Table B.32: Kappa 4 - High Power Spec. Results (Integrated)

			FWHM	Center	Max.Att.
Run 1	90°C	RbD1	16.0	377111.0	-0.233
		RbD2	16.0	384230.02	-0.645
		KD1	10.0	389287.01	-0.341
		KD2	14.0	391016.01	-0.675
Alk.Ratio (K:Rb): 0.729(0.73) → at 235°C: 1.54(1.032)					
	95°C	RbD1	16.0	377111.01	-0.376
		RbD2	15.0	384230.01	-0.877
		KD1	12.0	389286.0	-0.52
		KD2	15.0	391016.01	-0.918
Alk.Ratio (K:Rb): 0.442(0.663) → at 235°C: 0.9(0.937)					
→ → Avg. Estimated Alk. Ratio (K:Rb) at 235°C: 1.22(1.43) ← ←					
Continued on next page					

Table B.32 – continued from previous page

			FWHM	Center	Max.Att.
Run 2	90°C	RbD1	14.0	377111.01	-0.052
		RbD2	17.0	384231.01	-0.128
		KD1	14.0	389287.0	-0.13
		KD2	18.0	391016.0	-0.195
Alk.Ratio (K:Rb): 1.289(1.304) → at 235°C: 2.722(1.845)					
	95°C	RbD1	10.333	377111.34	-0.103
		RbD2	13.333	384230.34	-0.226
		KD1	10.0	389286.67	-0.253
		KD2	13.667	391016.34	-0.473
Alk.Ratio (K:Rb): 1.699(1.792) → at 235°C: 3.461(2.534)					
	120°C	RbD1	20.0	377111.01	-0.397
		RbD2	26.0	384230.01	-0.532
→ → Avg. Estimated Alk. Ratio (K:Rb) at 235°C: 3.091(3.156) ← ←					

Table B.33: Kappa 4 - Low Power Spec. Results (Fitted)

			FWHM	Center	Max.Att.	η
Run 3	95°C	RbD1	18.031(1.229)	377110.81(0.62)	-0.039	0.933(0.149)
		RbD2	15.16(0.205)	384230.22(0.1)	-0.09	0.989(0.03)
		KD1	11.143(0.18)	389286.63(0.09)	-0.138	0.927(0.036)
		KD2	14.546(0.099)	391015.9(0.05)	-0.288	0.907(0.015)
Alk.Ratio (K:Rb): 2.537(2.59) → at 235°C: 5.17(3.662)						
	100°C	RbD1	14.729(0.231)	377111.32(0.11)	-0.149	1.0(0.035)
		RbD2	13.077(0.131)	384230.2(0.06)	-0.417	1.0(0.022)
		KD1	10.872(0.206)	389286.19(0.11)	-0.561	0.76(0.043)
		KD2	14.608(0.107)	391015.9(0.05)	-1.318	1.0(0.017)
Alk.Ratio (K:Rb): 3.004(3.021) → at 235°C: 5.911(4.273)						
→ → Avg. Estimated Alk. Ratio (K:Rb) at 235°C: 5.54(5.64) ← ←						
Run 4	70°C	RbD1	16.892(1.507)	377112.04(0.73)	-0.01	1.0(0.2)
		RbD2	17.031(0.637)	384230.24(0.31)	-0.017	1.0(0.084)
		KD1	13.937(0.456)	389286.12(0.23)	-0.017	1.0(0.074)
		KD2	16.129(0.254)	391014.78(0.13)	-0.032	0.842(0.036)
Alk.Ratio (K:Rb): 1.544(1.561) → at 235°C: 3.796(2.207)						
	80°C	RbD1	15.285(0.807)	377111.21(0.4)	-0.016	1.0(0.12)
		RbD2	15.881(0.377)	384230.48(0.19)	-0.031	0.841(0.053)
		KD1	11.844(0.172)	389286.48(0.09)	-0.037	0.96(0.033)
		KD2	15.659(0.106)	391015.62(0.05)	-0.071	0.998(0.015)
Alk.Ratio (K:Rb): 1.939(1.953) → at 235°C: 4.408(2.762)						
→ → Avg. Estimated Alk. Ratio (K:Rb) at 235°C: 4.102(3.549) ← ←						

Table B.34: Kappa 4 - Low Power Spec. Results (Integrated)

			FWHM	Center	Max.Att.
Run 3	95°C	RbD1	18.333	377111.34	-0.041
		RbD2	16.0	384229.51	-0.09
		KD1	12.0	389286.5	-0.136
		KD2	15.0	391015.0	-0.291
Alk.Ratio (K:Rb): 1.808(2.376) → at 235°C: 3.684(3.36)					
	100°C	RbD1	16.0	377111.0	-0.151
		RbD2	14.0	384231.01	-0.414
		KD1	12.0	389287.0	-0.558
		KD2	15.0	391016.0	-1.312
Alk.Ratio (K:Rb): 2.813(3.374) → at 235°C: 5.537(4.771)					
→ → Avg. Estimated Alk. Ratio (K:Rb) at 235°C: 4.61(5.908) ← ←					
Run 4	70°C	RbD1	17.0	377111.0	-0.01
		RbD2	17.0	384230.0	-0.017

Continued on next page

Table B.34 – continued from previous page

			FWHM	Center	Max.Att.
		KD1	13.0	389287.01	-0.017
		KD2	16.0	391013.01	-0.031
Alk.Ratio (K:Rb): -0.566(0.707) → at 235°C: -1.392(1.0)					
	80°C	RbD1	16.0	377113.99	-0.016
		RbD2	18.0	384230.01	-0.031
		KD1	12.0	389287.0	-0.037
		KD2	16.0	391017.0	-0.072
Alk.Ratio (K:Rb): 15.279(20.84) → at 235°C: 34.739(29.472)					
→ → Avg. Estimated Alk. Ratio (K:Rb) at 235°C: 16.674(34.583) ← ←					

Table B.35: Kappa 5 - Low Power Spec. Results (Fitted)

			FWHM	Center	Max.Att.	η
Run 1	50°C	RbD1	16.378(0.197)	377111.0(0.1)	-0.025	1.0(0.027)
		RbD2	15.385(0.193)	384230.54(0.09)	-0.061	1.0(0.028)
	55°C	RbD1	15.28(0.131)	377110.97(0.06)	-0.04	1.0(0.019)
		RbD2	13.412(0.109)	384230.33(0.05)	-0.105	1.0(0.018)
	60°C	RbD1	15.071(0.124)	377111.13(0.06)	-0.064	1.0(0.019)
		RbD2	13.049(0.073)	384230.43(0.03)	-0.179	1.0(0.013)
	65°C	RbD1	13.928(0.276)	377111.08(0.13)	-0.128	1.0(0.045)
		RbD2	12.509(0.154)	384230.3(0.07)	-0.44	1.0(0.028)
	70°C	RbD1	12.114(0.041)	377111.18(0.02)	-0.189	1.0(0.008)
		RbD2	10.937(0.025)	384230.41(0.01)	-0.666	0.968(0.005)
	75°C	RbD1	10.615(0.055)	377111.19(0.03)	-0.444	1.0(0.012)
		RbD2	9.395(0.035)	384230.36(0.02)	-1.772	0.868(0.008)

Table B.36: Kappa 5 - Low Power Spec. Results (Integrated)

			FWHM	Center	Max.Att.
Run 1	50°C	RbD1	17.0	377111.0	-0.026
		RbD2	16.0	384231.0	-0.062
	55°C	RbD1	16.0	377111.0	-0.041
		RbD2	14.0	384231.01	-0.107
	60°C	RbD1	15.0	377111.0	-0.066
		RbD2	14.0	384231.01	-0.183
	65°C	RbD1	15.0	377111.0	-0.135
		RbD2	14.0	384230.01	-0.447
	70°C	RbD1	13.0	377111.01	-0.193
		RbD2	13.0	384230.01	-0.674
	75°C	RbD1	13.0	377111.01	-0.452
		RbD2	12.0	384231.0	-1.774

Table B.37: Noah - High Power Spec. Results (Fitted)

			FWHM	Center	Max.Att.	η
Run 1	130°C	RbD1	138.876(1.266)	377149.14(0.7)	-0.067	0.839(0.023)
		RbD2	155.517(0.683)	384235.22(0.37)	-0.115	0.914(0.011)
		KD1	108.417(0.227)	389295.22(0.11)	-0.314	0.978(0.005)
		KD2	142.052(0.175)	391020.04(0.09)	-0.479	1.0(0.003)
Alk.Ratio (K:Rb): 3.795(3.797) $\rightarrow$ at 235°C: 6.179(5.37)						
	140°C	RbD1	128.717(1.326)	377151.18(0.72)	-0.086	1.0(0.026)
		RbD2	148.457(0.966)	384236.27(0.53)	-0.17	0.89(0.016)
		KD1	105.269(0.258)	389295.42(0.13)	-0.569	0.956(0.006)
		KD2	134.167(0.183)	391019.8(0.09)	-0.933	1.0(0.003)
Alk.Ratio (K:Rb): 5.31(5.315) $\rightarrow$ at 235°C: 8.166(7.516)						
	145°C	RbD1	134.246(0.602)	377150.63(0.33)	-0.15	0.881(0.011)
		RbD2	154.04(0.413)	384235.65(0.22)	-0.261	0.941(0.007)
		KD1	97.054(0.239)	389295.29(0.12)	-0.942	0.989(0.006)
		KD2	128.519(0.173)	391020.18(0.09)	-1.506	0.911(0.003)
Alk.Ratio (K:Rb): 4.796(4.8) $\rightarrow$ at 235°C: 7.174(6.788)						
$\rightarrow$ $\rightarrow$ Avg. Estimated Alk. Ratio (K:Rb) at 235°C: 7.173(11.492) $\leftarrow$ $\leftarrow$						

Table B.38: Noah - High Power Spec. Results (Integrated)

			FWHM	Center	Max.Att.
Run 1	130°C	RbD1	132.0	377155.01	-0.069
		RbD2	156.0	384235.0	-0.114
		KD1	107.0	389297.0	-0.31
		KD2	134.0	391024.01	-0.495
Alk.Ratio (K:Rb): 4.207(4.221) $\rightarrow$ at 235°C: 6.849(5.969)					
	140°C	RbD1	133.0	377147.0	-0.087
		RbD2	149.0	384236.0	-0.169
		KD1	104.0	389289.01	-0.572
		KD2	129.0	391021.01	-0.945
Alk.Ratio (K:Rb): 5.206(5.212) $\rightarrow$ at 235°C: 8.006(7.371)					
	145°C	RbD1	128.0	377154.01	-0.15
		RbD2	156.0	384229.01	-0.259
		KD1	95.0	389297.03	-0.949
		KD2	129.0	391022.01	-1.485
Alk.Ratio (K:Rb): 5.048(5.058) $\rightarrow$ at 235°C: 7.552(7.153)					
$\rightarrow$ $\rightarrow$ Avg. Estimated Alk. Ratio (K:Rb) at 235°C: 7.469(11.889) $\leftarrow$ $\leftarrow$					

Table B.39: Noah - Low Power Spec. Results (Fitted)

			FWHM	Center	Max.Att.	η
Run 2	130°C	RbD1	183.497(5.176)	377153.26(2.82)	-0.063	1.0(0.074)
		RbD2	138.02(2.302)	384235.87(1.25)	-0.114	0.899(0.041)
		KD1	93.429(1.198)	389295.04(0.61)	-0.586	0.933(0.03)
		KD2	116.043(0.679)	391017.77(0.34)	-1.165	0.914(0.014)
Alk.Ratio (K:Rb): 6.886(7.165) → at 235°C: 11.21(10.132)						
→ → Avg. Estimated Alk. Ratio (K:Rb) at 235°C: 11.21(10.132) ← ←						

Table B.40: Noah - Low Power Spec. Results (Integrated)

			FWHM	Center	Max.Att.
Run 2	130°C	RbD1	151.0	377155.0	-0.076
		RbD2	135.0	384240.01	-0.121
		KD1	89.0	389295.01	-0.629
		KD2	106.0	391010.01	-1.26
Alk.Ratio (K:Rb): 6.654(7.29) → at 235°C: 10.833(10.309)					
→ → Avg. Estimated Alk. Ratio (K:Rb) at 235°C: 10.833(10.309) ← ←					

Table B.41: Sandy II - High Power Spec. Results (Fitted)

			FWHM	Center	Max.Att.	η
Run 1	135°C	RbD1	141.518(1.816)	377147.63(0.99)	-0.206	0.929(0.034)
		RbD2	156.165(2.079)	384231.74(1.15)	-0.368	0.843(0.035)
		KD1	99.623(0.899)	389293.66(0.45)	-0.635	1.0(0.021)
		KD2	128.256(0.593)	391020.32(0.3)	-1.11	1.0(0.011)
Alk.Ratio (K:Rb): 2.37(2.376) → at 235°C: 3.748(3.36)						
	140°C	RbD1	135.491(2.747)	377145.87(1.74)	-0.282	1.0(0.064)
		RbD2	152.609(1.364)	384231.32(0.73)	-0.493	1.0(0.022)
		KD1	93.451(0.519)	389294.99(0.26)	-0.941	0.929(0.013)
		KD2	122.048(0.332)	391019.92(0.17)	-1.681	0.875(0.006)
Alk.Ratio (K:Rb): 2.651(2.658) → at 235°C: 4.077(3.759)						
	145°C	RbD1	133.463(0.901)	377150.2(0.48)	-0.354	0.998(0.017)
		RbD2	140.825(0.883)	384235.47(0.48)	-0.658	0.94(0.015)
		KD1	89.144(0.443)	389294.86(0.22)	-1.426	0.938(0.01)
		KD2	131.149(0.336)	391020.42(0.17)	-2.257	0.729(0.005)
Alk.Ratio (K:Rb): 3.053(3.067) → at 235°C: 4.567(4.338)						
	160°C	RbD1	105.604(0.33)	377150.13(0.17)	-1.275	1.0(0.008)
		RbD2	116.279(0.325)	384235.41(0.18)	-2.773	0.805(0.006)
→ → Avg. Estimated Alk. Ratio (K:Rb) at 235°C: 4.131(6.659) ← ←						
Run 2	135°C	RbD1	141.527(2.801)	377144.08(1.67)	-0.101	1.0(0.074)
		RbD2	167.889(1.748)	384234.26(0.93)	-0.145	0.982(0.027)
		KD1	116.191(1.306)	389294.76(0.65)	-0.222	0.994(0.026)
		KD2	157.214(1.213)	391020.12(0.6)	-0.329	1.0(0.017)
Alk.Ratio (K:Rb): 2.01(2.023) → at 235°C: 3.18(2.86)						
	140°C	RbD1	152.758(2.404)	377150.8(1.32)	-0.13	1.0(0.041)
		RbD2	174.69(1.456)	384234.49(0.79)	-0.186	1.0(0.021)
		KD1	116.462(3.832)	389293.4(2.25)	-0.425	0.805(0.119)
		KD2	121.924(0.254)	391019.56(0.13)	-0.574	1.0(0.005)
Alk.Ratio (K:Rb): 2.101(2.136) → at 235°C: 3.231(3.021)						
	145°C	RbD1	154.405(0.222)	377150.45(0.12)	-0.153	0.987(0.004)
		RbD2	177.866(0.334)	384234.54(0.18)	-0.211	1.0(0.005)
		KD1	96.677(0.345)	389295.24(0.17)	-0.448	1.0(0.008)
		KD2	113.794(0.184)	391020.22(0.09)	-0.904	0.927(0.004)
Alk.Ratio (K:Rb): 2.358(2.408) → at 235°C: 3.528(3.406)						
→ → Avg. Estimated Alk. Ratio (K:Rb) at 235°C: 3.313(5.379) ← ←						

Table B.42: Sandy II - High Power Spec. Results (Integrated)

			FWHM	Center	Max.Att.
Run 1	135°C	RbD1	139.0	377165.01	-0.209
Continued on next page					

Table B.42 – continued from previous page

			FWHM	Center	Max.Att.
		RbD2	140.0	384234.02	-0.382
		KD1	98.0	389298.01	-0.638
		KD2	123.0	391018.0	-1.125
Alk.Ratio (K:Rb): 2.555(2.556) → at 235°C: 4.041(3.614)					
	140°C	RbD1	131.0	377156.49	-0.286
		RbD2	151.0	384232.0	-0.498
		KD1	92.0	389296.0	-0.927
		KD2	123.0	391015.0	-1.664
Alk.Ratio (K:Rb): 2.551(2.556) → at 235°C: 3.923(3.614)					
	145°C	RbD1	137.0	377153.01	-0.357
		RbD2	133.0	384237.0	-0.661
		KD1	87.0	389296.0	-1.425
		KD2	139.0	391018.0	-2.151
Alk.Ratio (K:Rb): 2.963(2.977) → at 235°C: 4.432(4.21)					
	160°C	RbD1	104.0	377154.01	-1.295
		RbD2	121.0	384232.01	-2.719
→ → Avg. Estimated Alk. Ratio (K:Rb) at 235°C: 4.132(6.626) ← ←					
Run 2	135°C	RbD1	138.0	377154.99	-0.101
		RbD2	162.0	384232.5	-0.147
		KD1	110.0	389293.98	-0.229
		KD2	141.0	391020.51	-0.344
Alk.Ratio (K:Rb): 2.313(2.369) → at 235°C: 3.658(3.35)					
	140°C	RbD1	147.0	377154.5	-0.132
		RbD2	167.0	384231.01	-0.184
		KD1	115.0	389296.51	-0.289
		KD2	120.0	391024.01	-0.565
Alk.Ratio (K:Rb): 2.205(2.238) → at 235°C: 3.391(3.165)					
	145°C	RbD1	151.0	377154.01	-0.151
		RbD2	169.0	384235.01	-0.211
		KD1	91.0	389290.01	-0.454
		KD2	116.0	391024.01	-0.905
Alk.Ratio (K:Rb): 2.505(2.539) → at 235°C: 3.748(3.591)					
→ → Avg. Estimated Alk. Ratio (K:Rb) at 235°C: 3.599(5.845) ← ←					

Table B.43: Savior - High Power Spec. Results (Fitted)

			FWHM	Center	Max.Att.	η
Run 1	140°C	RbD1	125.659(1.702)	377148.09(0.94)	-0.044	0.891(0.035)
		RbD2	147.299(1.431)	384235.81(0.77)	-0.103	0.981(0.023)
		KD1	128.032(0.716)	389294.46(0.36)	-0.288	0.914(0.013)
		KD2	199.672(0.867)	391020.12(0.42)	-0.331	0.932(0.01)
Alk.Ratio (K:Rb): 5.678(5.824) → at 235°C: 8.731(8.237)						
→ → Avg. Estimated Alk. Ratio (K:Rb) at 235°C: 8.731(8.237) ← ←						

Table B.44: Savior - High Power Spec. Results (Integrated)

			FWHM	Center	Max.Att.
Run 1	140°C	RbD1	123.0	377164.01	-0.046
		RbD2	140.5	384236.01	-0.107
		KD1	127.0	389299.48	-0.285
		KD2	185.5	391030.99	-0.335
Alk.Ratio (K:Rb): 5.368(5.542) → at 235°C: 8.254(7.838)					
→ → Avg. Estimated Alk. Ratio (K:Rb) at 235°C: 8.254(7.838) ← ←					

Table B.45: Tommy - Low Power Spec. Results (Fitted)

			FWHM	Center	Max.Att.	η
Run 1	130°C	RbD1	149.532(2.334)	377140.82(1.41)	-0.022	1.0(0.05)
		RbD2	147.354(1.504)	384232.79(0.87)	-0.039	0.54(0.025)
		KD1	99.657(0.998)	389295.04(0.51)	-0.19	0.854(0.024)
		KD2	126.159(0.604)	391018.54(0.3)	-0.367	0.976(0.011)
Alk.Ratio (K:Rb): 7.067(7.181) → at 235°C: 11.507(10.155)						
	135°C	RbD1	140.916(0.938)	377151.12(0.52)	-0.026	0.884(0.017)
		RbD2	153.654(0.402)	384234.0(0.22)	-0.052	0.974(0.006)
		KD1	93.411(0.592)	389295.49(0.31)	-0.296	0.849(0.015)
		KD2	119.33(0.336)	391017.59(0.17)	-0.613	0.956(0.007)
Alk.Ratio (K:Rb): 8.634(8.674) → at 235°C: 13.657(12.266)						
	140°C	RbD1	133.393(0.327)	377151.44(0.18)	-0.063	1.0(0.006)
		RbD2	134.707(0.245)	384234.22(0.13)	-0.172	1.0(0.004)
		KD1	89.152(0.481)	389297.16(0.24)	-0.483	0.897(0.013)
		KD2	113.971(0.282)	391018.35(0.14)	-0.958	0.957(0.006)
Alk.Ratio (K:Rb): 5.107(5.111) → at 235°C: 7.853(7.228)						
	160°C	RbD1	94.772(0.174)	377152.06(0.09)	-0.562	0.927(0.004)
		RbD2	98.176(0.251)	384235.46(0.13)	-2.013	0.7(0.004)
→ → Avg. Estimated Alk. Ratio (K:Rb) at 235°C: 11.005(17.651) ← ←						

Table B.46: Tommy - Low Power Spec. Results (Integrated)

			FWHM	Center	Max.Att.
Run 1	130°C	RbD1	141.0	377154.5	-0.022
		RbD2	147.0	384228.5	-0.039
		KD1	98.0	389281.5	-0.196
		KD2	126.0	391032.5	-0.371
Alk.Ratio (K:Rb): 10.993(13.084) → at 235°C: 17.898(18.504)					
	135°C	RbD1	138.0	377145.0	-0.025
		RbD2	150.0	384238.0	-0.054
		KD1	87.0	389284.01	-0.314
		KD2	112.0	391033.0	-0.626
Alk.Ratio (K:Rb): 9.501(9.501) → at 235°C: 15.027(13.436)					
	140°C	RbD1	124.0	377156.01	-0.064
		RbD2	130.0	384226.01	-0.175
		KD1	85.0	389303.0	-0.492
		KD2	111.0	391024.01	-0.973
Alk.Ratio (K:Rb): 5.229(5.241) → at 235°C: 8.04(7.411)					
	160°C	RbD1	96.0	377158.0	-0.564
		RbD2	102.0	384230.01	-1.996

Continued on next page

Table B.46 – continued from previous page

	FWHM	Center	Max.Att.		
→	→	Avg. Estimated Alk. Ratio (K:Rb) at 235°C: 13.655(24.392)		←	←

Table B.47: Wayne - High Power Spec. Results (Fitted)

			FWHM	Center	Max.Att.	η
Run 1	130°C	RbD1	126.714(1.276)	377152.41(0.69)	-0.031	1.0(0.025)
		RbD2	152.371(0.951)	384235.65(0.52)	-0.064	0.885(0.015)
		KD1	109.399(0.465)	389294.65(0.23)	-0.139	0.958(0.01)
		KD2	151.952(0.395)	391019.37(0.2)	-0.2	0.997(0.006)
Alk.Ratio (K:Rb): 3.559(3.576) → at 235°C: 5.794(5.057)						
	135°C	RbD1	115.58(0.636)	377151.28(0.35)	-0.055	0.903(0.014)
		RbD2	139.87(0.587)	384235.19(0.32)	-0.107	0.823(0.01)
		KD1	106.917(0.294)	389295.47(0.15)	-0.189	0.937(0.006)
		KD2	153.31(0.259)	391018.97(0.13)	-0.263	0.922(0.004)
Alk.Ratio (K:Rb): 2.989(2.998) → at 235°C: 4.727(4.239)						
	140°C	RbD1	119.447(0.655)	377149.37(0.36)	-0.078	0.972(0.014)
		RbD2	145.326(0.459)	384235.14(0.25)	-0.151	0.93(0.008)
		KD1	109.154(0.236)	389295.38(0.12)	-0.253	0.966(0.005)
		KD2	157.745(0.211)	391018.81(0.11)	-0.347	0.915(0.003)
Alk.Ratio (K:Rb): 2.813(2.823) → at 235°C: 4.325(3.992)						
	145°C	RbD1	120.655(0.497)	377150.84(0.27)	-0.096	0.872(0.01)
		RbD2	145.981(0.38)	384236.65(0.21)	-0.19	0.894(0.006)
		KD1	112.735(0.226)	389294.64(0.12)	-0.329	0.879(0.004)
		KD2	166.208(0.216)	391019.21(0.11)	-0.434	0.889(0.003)
Alk.Ratio (K:Rb): 2.974(2.988) → at 235°C: 4.45(4.226)						
	150°C	RbD1	119.333(0.483)	377151.53(0.26)	-0.117	0.965(0.01)
		RbD2	149.22(0.366)	384236.43(0.2)	-0.216	0.887(0.006)
	155°C	RbD1	123.418(0.482)	377150.68(0.26)	-0.125	0.899(0.01)
		RbD2	150.985(0.328)	384234.56(0.18)	-0.235	0.889(0.005)
→ → Avg. Estimated Alk. Ratio (K:Rb) at 235°C: 4.824(8.813) ← ←						

Table B.48: Wayne - High Power Spec. Results (Integrated)

			FWHM	Center	Max.Att.
Run 1	130°C	RbD1	109.0	377156.01	-0.034
		RbD2	152.0	384253.01	-0.067
		KD1	108.0	389298.0	-0.137
		KD2	145.0	391018.01	-0.198
Alk.Ratio (K:Rb): 3.537(3.564) → at 235°C: 5.759(5.04)					
	135°C	RbD1	107.0	377149.01	-0.057
		RbD2	138.0	384239.01	-0.105
		KD1	107.0	389296.01	-0.186
		KD2	152.0	391024.01	-0.261
Alk.Ratio (K:Rb): 3.166(3.166) → at 235°C: 5.008(4.478)					
Continued on next page					

Table B.48 – continued from previous page

			FWHM	Center	Max.Att.
	140°C	RbD1	110.0	377148.01	-0.08
		RbD2	140.0	384241.01	-0.153
		KD1	107.0	389297.01	-0.25
		KD2	159.0	391016.01	-0.342
Alk.Ratio (K:Rb): 2.797(2.817) → at 235°C: 4.301(3.983)					
	145°C	RbD1	118.0	377149.01	-0.097
		RbD2	138.0	384241.01	-0.192
		KD1	113.0	389295.01	-0.325
		KD2	170.0	391018.0	-0.422
Alk.Ratio (K:Rb): 2.987(3.007) → at 235°C: 4.468(4.253)					
	150°C	RbD1	120.0	377148.01	-0.116
		RbD2	151.0	384235.01	-0.215
	155°C	RbD1	119.0	377147.01	-0.128
		RbD2	148.0	384234.01	-0.235
→ → Avg. Estimated Alk. Ratio (K:Rb) at 235°C: 4.884(8.929) ← ←					

Table B.49: Wayne - Low Power Spec. Results (Fitted)

			FWHM	Center	Max.Att.	η
Run 2	130°C	RbD1	136.441(2.516)	377152.48(1.36)	-0.026	0.727(0.047)
		RbD2	132.471(1.123)	384230.58(0.62)	-0.056	0.746(0.021)
		KD1	94.304(0.789)	389294.12(0.4)	-0.178	0.937(0.02)
		KD2	115.076(0.41)	391018.14(0.21)	-0.384	0.931(0.009)
Alk.Ratio (K:Rb): 5.301(5.365) → at 235°C: 8.63(7.588)						
	135°C	RbD1	126.735(0.789)	377151.48(0.43)	-0.069	0.993(0.016)
		RbD2	139.051(0.79)	384231.35(0.43)	-0.149	0.919(0.014)
		KD1	89.009(0.506)	389295.96(0.25)	-0.33	0.985(0.013)
		KD2	110.905(0.294)	391020.31(0.15)	-0.628	0.855(0.006)
Alk.Ratio (K:Rb): 3.461(3.461) → at 235°C: 5.475(4.895)						
	140°C	RbD1	119.881(0.485)	377150.8(0.26)	-0.192	1.0(0.01)
		RbD2	133.379(0.371)	384236.34(0.2)	-0.419	0.965(0.007)
		KD1	88.367(0.426)	389295.94(0.22)	-1.056	0.901(0.011)
		KD2	117.627(0.272)	391021.15(0.14)	-1.922	0.854(0.005)
Alk.Ratio (K:Rb): 4.184(4.184) → at 235°C: 6.434(5.917)						
	145°C	RbD1	118.277(0.483)	377149.1(0.26)	-0.278	0.924(0.01)
		RbD2	127.828(0.425)	384234.4(0.23)	-0.643	0.912(0.008)
		KD1	85.656(0.441)	389295.14(0.22)	-1.784	0.857(0.01)
		KD2	128.046(0.346)	391020.42(0.18)	-2.78	0.688(0.005)
Alk.Ratio (K:Rb): 4.656(4.657) → at 235°C: 6.965(6.586)						
	150°C	RbD1	119.741(0.541)	377149.24(0.3)	-0.143	0.943(0.011)
		RbD2	125.379(0.677)	384236.56(0.37)	-0.273	0.782(0.013)
	155°C	RbD1	114.543(0.505)	377148.3(0.27)	-0.162	0.981(0.011)
		RbD2	118.084(0.408)	384233.36(0.21)	-0.444	0.972(0.008)
→ → Avg. Estimated Alk. Ratio (K:Rb) at 235°C: 6.876(12.698) ← ←						

Table B.50: Wayne - Low Power Spec. Results (Integrated)

			FWHM	Center	Max.Att.
Run 2	130°C	RbD1	136.5	377149.0	-0.026
		RbD2	133.0	384227.01	-0.058
		KD1	90.0	389297.01	-0.191
		KD2	105.0	391014.01	-0.412
Alk.Ratio (K:Rb): 6.524(6.524) → at 235°C: 10.622(9.226)					
	135°C	RbD1	121.0	377156.01	-0.069
		RbD2	130.0	384242.01	-0.157
		KD1	85.0	389295.01	-0.328
		KD2	108.0	391017.04	-0.662
Alk.Ratio (K:Rb): 3.384(3.386) → at 235°C: 5.353(4.788)					
Continued on next page					

Table B.50 – continued from previous page

			FWHM	Center	Max.Att.
	140°C	RbD1	114.0	377151.01	-0.196
		RbD2	133.0	384232.01	-0.426
		KD1	86.0	389292.01	-1.063
		KD2	119.0	391025.01	-1.882
Alk.Ratio (K:Rb): 4.262(4.268) → at 235°C: 6.554(6.036)					
	145°C	RbD1	121.0	377158.01	-0.288
		RbD2	119.0	384227.01	-0.664
		KD1	85.0	389296.01	-1.803
		KD2	140.0	391031.03	-2.684
Alk.Ratio (K:Rb): 4.768(4.78) → at 235°C: 7.132(6.76)					
	150°C	RbD1	123.0	377159.01	-0.141
		RbD2	126.0	384235.02	-0.285
	155°C	RbD1	111.0	377156.01	-0.169
		RbD2	111.0	384229.01	-0.448
→ → Avg. Estimated Alk. Ratio (K:Rb) at 235°C: 7.415(13.929) ← ←					

Bibliography

[1]D. Adams, *The restaurant at the end of the universe*, Hitchhiker's Guide (Pan Books, 1980).

[2]S. Stills, *For what it's worth*, Columbia, B-Side: "Do I Have to Come Right Out and Say It?", 1966.

[3]A. Courtesy SLAC National Accelerator Laboratory and H. Office, *Slac history*, (2022) https://www6.slac.stanford.edu/about/slac-history.

[4]M. Breidenbach, J. I. Friedman, H. W. Kendall, E. D. Bloom, D. H. Coward, H. DeStaebler, J. Drees, L. W. Mo, and R. E. Taylor, "Observed behavior of highly inelastic electron-proton scattering", Phys. Rev. Lett. **23**, 935–939 (1969).

[5]E. D. Bloom, D. H. Coward, H. DeStaebler, J. Drees, G. Miller, L. W. Mo, R. E. Taylor, M. Breidenbach, J. I. Friedman, G. C. Hartmann, and H. W. Kendall, "High-energy inelastic $e-p$ scattering at 6° and 10°", Phys. Rev. Lett. **23**, 930–934 (1969).

[6]M. Gell-Mann, "A schematic model of baryons and mesons", Physics Letters **8**, 214–215 (1964).

[7]F. Close, "On the transformation between current and constituent quarks and consequences for polarised electroproduction structure functions", Nuclear Physics B **80**, 269–298 (1974).

[8]R. Adair, "Vernon willard hughes, a biographical memoir", The National Academies Press Memoirs **84**, 11 (2004).

[9]M. J. Alguard, W. W. Ash, G. Baum, J. E. Clendenin, P. S. Cooper, D. H. Coward, R. D. Ehrlich, A. Etkin, V. W. Hughes, H. Kobayakawa, K. Kondo, M. S. Lubell, R. H. Miller, D. A. Palmer, W. Raith, N. Sasao, K. P. Schüler, D. J. Sherden, C. K. Sinclair, and P. A. Souder, "Deep inelastic scattering of polarized electrons by polarized protons", Phys. Rev. Lett. **37**, 1261–1265 (1976).

[10]G. Baum, M. R. Bergström, P. R. Bolton, J. E. Clendenin, N. R. DeBotton, S. K. Dhawan, Y. .-. Guo, V. .-. Harsh, V. W. Hughes, K. Kondo, M. S. Lubell, Z. .-. Mao, R. H. Miller, S. Miyashita, K. Morimoto, U. F. Moser, I. Nakano, R. F. Oppenheim, D. A. Palmer, L. Panda, W. Raith, N. Sasao, K. P. Schüler, M. L. Seely, P. A. Souder, S. J. S. Lorant, K. Takikawa, and M. Werlen, "New measurement of deep-inelastic $e-p$ asymmetries", Phys. Rev. Lett. **51**, 1135–1138 (1983).

[11]R. Carlitz and J. Kaur, "Chiral substructure of the nucleon", Phys. Rev. Lett. **38**, 673–676 (1977).

[12]T. Sloan, "History of the european muon collaboration (emc)", in Cern yellow reports: monographs, Vol. CERN-2019-005 (2019).

[13]J. Ashman, B. Badelek, G. Baum, J. Beaufays, C. Bee, C. Benchouk, I. Bird, S. Brown, M. Caputo, H. Cheung, J. Chima, J. Ciborowski, R. Clifft, G. Coignet, F. Combley, G. Court, G. D'Agostini, J. Drees, M. Düren, N. Dyce, A. Edwards, M. Edwards, T. Ernst, M. Ferrero, D. Francis, E. Gabathuler, J. Gajewski, R. Gamet, V. Gibson, J. Gillies, P. Graftström, K. Hamacher, D. Von Harrach, P. Hayman, J. Holt, V. Hughes, A. Jacholkowska, T. Jones, E. Kabuss, B. Korzen, U. Krüner, S. Kullander, U. Landgraf, D. Lanske, F. Lettenström, T. Lindqvist, J. Loken, M. Matthews, Y. Mizuno, K. Mönig, F. Montanet, J. Nassalski, T. Niinikoski, P. Norton, G. Oakham, R. Oppenheim, A. Osborne, V. Papavassiliou, N. Pavel, C. Peroni, H. Peschel, R. Piegaia, B. Pietrzyk, U. Pietrzyk, B. Povh, P. Renton, J. Rieubland, A. Rijllart, K. Rith, E. Rondio, L. Ropelewski, D. Salmon, A. Sandacz, T. Schröder, K. Schüler, K. Schultze, T.-A. Shibata, T. Sloan, A. Staiano, H. Stier, J. Stock, G. Taylor, J. Thompson, T. Walcher, S. Wheeler, W. Williams, S. Wimpenny, R. Windmolders, W. Womersley, and K. Ziemons, "A measurement of the spin asymmetry and determination of the structure function g1 in deep inelastic muon-proton scattering", Physics Letters B **206**, 364–370 (1988).

[14]X. Zheng, K. Aniol, D. S. Armstrong, T. D. Averett, W. Bertozzi, S. Binet, E. Burtin, E. Busato, C. Butuceanu, J. Calarco, A. Camsonne, G. D. Cates, Z. Chai, J.-P. Chen, S. Choi, E. Chudakov, F. Cusanno, R. De Leo, A. Deur, S. Dieterich, D. Dutta, J. M. Finn, S. Frullani, H. Gao, J. Gao, F. Garibaldi, S. Gilad, R. Gilman, J. Gomez, J.-O. Hansen, D. W. Higinbotham, W. Hinton, T. Horn, C. W. de Jager, X. Jiang, L. Kaufman, J. Kelly, W. Korsch, K. Kramer, J. LeRose, D. Lhuillier, N. Liyanage, D. J. Margaziotis, F. Marie, P. Markowitz, K. McCormick, Z.-E. Meziani, R. Michaels, B. Moffit, S. Nanda, D. Neyret, S. K. Phillips, A. Powell, T. Pussieux, B. Reitz, J. Roche, R. Roché, M. Roedelbronn, G. Ron, M. Rvachev, A. Saha, N. Savvinov, J. Singh, S. Širca, K. Slifer, P. Solvignon, P. Souder, D. J. Steiner, S. Strauch, V. Sulkosky, A. Tobias, G. Urciuoli, A. Vacheret, B. Wojtsekhowski, H. Xiang, Y. Xiao, F. Xiong, B. Zhang, L. Zhu, X. Zhu, and P. A. Żołnierczuk (Jefferson Lab Hall A Collaboration), "Precision measurement of the neutron spin asymmetries and spin-dependent structure functions in the valence quark region", Phys. Rev. C **70**, 065207 (2004).

[15]Y. Hatta, Y. Nakagawa, B. Xiao, F. Yuan, and Y. Zhao, "Gluon orbital angular momentum at small x", Phys. Rev. D **95**, 114032 (2017).

[16]S. Xu, C. Mondal, X. Zhao, Y. Li, and J. P. Vary (BLFQ Collaboration), "Quark and gluon spin and orbital angular momentum in the proton", Phys. Rev. D **108**, 094002 (2023).

[17]B. Povh, K. Rith, C. Scholz, F. Zetsche, and W. Rodejohann, *Particles and nuclei: an introduction to the physical concepts*, Graduate Texts in Physics (Springer Berlin Heidelberg, 2015).

[18]J. Becker, H. Andresen, J. Annand, K. Aulenbacher, K. Beuchel, J. Blume–Werry, T. Dombo, P. Drescher, M. Ebert, D. Eyl, A. Frey, P. Grabmayr, T. Großmann, P. Hartmann, T. Hehl, W. Heil, C. Herberg, J. Hoffmann, J. Kellie, F. Klein, K. Livingston, M. Leduc, M. Meyerhoff, H. Möller, C. Nachtigall, A. Natter, M. Ostrick, E. Otten, R. Owens, S. Plützer, E. Reichert, D. Rohe, M. Schäfer, H. Schmieden, R. Sprengard, M. Steigerwald, K.-H. Steffens, R. Surkau, T. Walcher, R. Watson, and E. Wilms, "Determination of the neutron electric form factor from the reaction 3he(e,e'n) at medium momentum transfer", The European Physical Journal A - Hadrons and Nuclei **6**, 10.1007/s100500050351 (1999).

[19]M. K. Jones, K. A. Aniol, F. T. Baker, J. Berthot, P. Y. Bertin, W. Bertozzi, A. Besson, L. Bimbot, W. U. Boeglin, E. J. Brash, D. Brown, J. R. Calarco, L. S. Cardman, C.-C. Chang, J.-P. Chen, E. Chudakov, S. Churchwell, E. Cisbani, D. S. Dale, R. De Leo, A. Deur, B. Diederich, J. J. Domingo, M. B. Epstein, L. A. Ewell, K. G. Fissum, A. Fleck, H. Fonvieille, S. Frullani, J. Gao, F. Garibaldi, A. Gasparian, G. Gerstner, S. Gilad, R. Gilman, A. Glamazdin, C. Glashausser, J. Gomez, V. Gorbenko, A. Green, J.-O. Hansen, C. R. Howell, G. M. Huber, M. Iodice, C. W. de Jager, S. Jaminion, X. Jiang, W. Kahl, J. J. Kelly, M. Khayat, L. H. Kramer, G. Kumbartzki, M. Kuss, E. Lakuriki, G. Lavessière, J. J. LeRose, M. Liang, R. A. Lindgren, N. Liyanage, G. J. Lolos, R. Macri, R. Madey, S. Malov, D. J. Margaziotis, P. Markowitz, K. McCormick, J. I. McIntyre, R. L. J. van der Meer, R. Michaels, B. D. Milbrath, J. Y. Mougey, S. K. Nanda, E. A. J. M. Offermann, Z. Papandreou, C. F. Perdrisat, G. G. Petratos, N. M. Piskunov, R. I. Pomatsalyuk, D. L. Prout, V. Punjabi, G. Quéméner, R. D. Ransome, B. A. Raue, Y. Roblin, R. Roche, G. Rutledge, P. M. Rutt, A. Saha, T. Saito, A. J. Sarty, T. P. Smith, P. Sorokin, S. Strauch, R. Suleiman, K. Takahashi, J. A. Templon, L. Todor, P. E. Ulmer, G. M. Urciuoli, P. Vernin, B. Vlahovic, H. Voskanyan, K. Wijesooriya, B. B. Wojtsekhowski, R. J. Woo, F. Xiong, G. D. Zainea, and Z.-L. Zhou (The Jefferson Lab Hall A Collaboration), "G_{E_p}/G_{M_p} Ratio by polarization transfer in $\vec{e}\ p \to e\ \vec{p}$", Phys. Rev. Lett. **84**, 1398–1402 (2000).

[20]D. Flay, M. Posik, D. S. Parno, K. Allada, W. R. Armstrong, T. Averett, F. Benmokhtar, W. Bertozzi, A. Camsonne, M. Canan, G. D. Cates, C. Chen, J.-P. Chen, S. Choi, E. Chudakov, F. Cusanno, M. M. Dalton, W. Deconinck, C. W. de Jager, X. Deng, A. Deur, C. Dutta, L. E. Fassi, G. B. Franklin, M. Friend, H. Gao, F. Garibaldi, S. Gilad, R. Gilman, O. Glamazdin, S. Golge, J. Gomez, L. Guo, O. Hansen, D. W. Higinbotham, T. Holmstrom, J. Huang, C. Hyde, H. F. Ibrahim, X. Jiang, G. Jin, J. Katich, A. Kelleher, A. Kolarkar, W. Korsch, G. Kumbartzki, J. J. LeRose, R. Lindgren, N. Liyanage, E. Long, A. Lukhanin, V. Mamyan, D. McNulty, Z.-E. Meziani, R. Michaels, M. Mihovilovi č, B. Moffit, N. Muangma, S. Nanda, A. Narayan, V. Nelyubin, B. Norum, Nuruzzaman, Y. Oh, J. C. Peng, X. Qian, Y. Qiang, A. Rakhman, R. D. Ransome, S. Riordan, A. Saha, B. Sawatzky, M. H. Shabestari, A. Shahinyan, S. Širca, P. Solvignon, R. Subedi, V. Sulkosky, W. A. Tobias, W. Troth, D. Wang, Y. Wang, B. Wojtsekhowski, X. Yan, H. Yao, Y. Ye, Z. Ye, L. Yuan, X. Zhan, Y. Zhang, Y.-W. Zhang, B. Zhao, and X. Zheng (Jefferson Lab Hall A Collaboration), "Measurements of d_2^n and A_1^n: probing the neutron spin structure", Phys. Rev. D **94**, 052003 (2016).

[21]R. J. Fries, *Higher twist effects in nuclei*, 2002.

[22]K. Paschke, private communication, July 2024.

[23]J. L. Friar, B. F. Gibson, G. L. Payne, A. M. Bernstein, and T. E. Chupp, "Neutron polarization in polarized ^{3}He targets", Phys. Rev. C **42**, 2310–2314 (1990).

[24]M. Anselmino, A. Efremov, and E. Leader, "The theory and phenomenology of polarized deep inelastic scattering", Physics Reports **261**, 1–124 (1995).

[25]P. L. Anthony, R. G. Arnold, H. R. Band, H. Borel, P. E. Bosted, V. Breton, G. D. Cates, T. E. Chupp, F. S. Dietrich, J. Dunne, R. Erbacher, J. Fellbaum, H. Fonvieille, R. Gearhart, R. Holmes, E. W. Hughes, J. R. Johnson, D. Kawall, C. Keppel, S. E. Kuhn, R. M. Lombard-Nelsen, J. Marroncle, T. Maruyama, W. Meyer, Z.-E. Meziani, H. Middleton, J. Morgenstern, N. R. Newbury, G. G. Petratos, R. Pitthan, R. Prepost, Y. Roblin, S. E. Rock, S. H. Rokni,

G. Shapiro, T. Smith, P. A. Souder, M. Spengos, F. Staley, L. M. Stuart, Z. M. Szalata, Y. Terrien, A. K. Thompson, J. L. White, M. Woods, J. Xu, C. C. Young, and G. Zapalac, "Determination of the neutron spin structure function", Phys. Rev. Lett. **71**, 959–962 (1993).

[26]K. Abe, T. Akagi, B. D. Anderson, P. L. Anthony, R. G. Arnold, T. Averett, H. R. Band, C. M. Berisso, P. Bogorad, H. Borel, P. E. Bosted, V. Breton, M. J. Buenerd, G. D. Cates, T. E. Chupp, S. Churchwell, K. P. Coulter, M. Daoudi, P. Decowski, R. Erickson, J. N. Fellbaum, H. Fonvieille, R. Gearhart, V. Ghazikhanian, K. A. Griffioen, R. S. Hicks, R. Holmes, E. W. Hughes, G. Igo, S. Incerti, J. R. Johnson, W. Kahl, M. Khayat, Y. G. Kolomensky, S. E. Kuhn, K. Kumar, M. Kuriki, R. Lombard-Nelsen, D. M. Manley, J. Marroncle, T. Maruyama, T. Marvin, W. Meyer, Z.-E. Meziani, D. Miller, G. Mitchell, M. Olson, G. A. Peterson, G. G. Petratos, R. Pitthan, R. Prepost, P. Raines, B. Raue, D. Reyna, L. S. Rochester, S. E. Rock, M. V. Romalis, F. Sabatie, G. Shapiro, J. Shaw, T. B. Smith, L. Sorrell, P. A. Souder, F. Staley, S. St. Lorant, L. M. Stuart, F. Suekane, Z. M. Szalata, Y. Terrien, A. K. Thompson, T. Toole, X. Wang, J. W. Watson, R. C. Welsh, F. Wesselmann, T. Wright, C. C. Young, B. Youngman, H. Yuta, W.-M. Zhang, and P. Zyla (E154 Collaboration), "Precision determination of the neutron spin structure function g_1^n", Phys. Rev. Lett. **79**, 26–30 (1997).

[27]K. Ackerstaff, A. Airapetian, I. Akushevich, N. Akopov, M. Amarian, E. Aschenauer, R. Avakian, H. Avakian, A. Avetissian, B. Bains, S. Barrow, M. Beckmann, S. Belostotski, J. Belz, T. Benisch, S. Bernreuther, N. Bianchi, S. Blanchard, J. Blouw, H. Böttcher, A. Borissov, J. Brack, B. Braun, B. Bray, W. Brückner, A. Brüll, E. Bruins, H. Bulten, G. Capitani, P. Carter, E. Cisbani, G. Court, P. Delheij, E. Devitsin, C. de Jager, E. De Sanctis, D. De Schepper, P. de Witt Huberts, M. Düren, A. Dvoredsky, G. Elbakian, J. Emerson, A. Fantoni, A. Fechtchenko, M. Ferstl, D. Fick, K. Fiedler, B. Filippone, H. Fischer, H. Fortune, J. Franz, S. Frullani, M.-A. Funk, N. Gagunashvili, P. Galumian, H. Gao, Y. Gärber, F. Garibaldi, P. Geiger, V. Gharibyan, A. Golendoukhin, G. Graw, O. Grebeniouk, P. Green, L. Greeniaus, C. Grosshauser, A. Gute, V. Gyurjyan, J. Haas, W. Haeberli, J.-O. Hansen, D. Hasch, O. Häusser, R. Henderson, T. Henkes, R. Hertenberger, Y. Holler, R. Holt, H. Ihssen, M. Iodice, A. Izotov, H. Jackson, A. Jgoun, C. Jones, R. Kaiser, E. Kinney, M. Kirsch, A. Kisselev, P. Kitching, N. Koch, K. Königsmann, M. Kolstein, H. Kolster, W. Korsch, V. Kozlov, L. Kramer, B. Krause, V. Krivokhijine, M. Kückes, G. Kyle, W. Lachnit, W. Lorenzon, A. Lung, N. Makins, S. Manaenkov, F. Martens, J. Martin, A. Mateos, K. McIlhany, R. McKeown, F. Meissner, D. Mercer, A. Metz, N. Meyners, O. Mikloukho, C. Miller, M. Miller, R. Milner, V. Mitsyn, A. Most, R. Mozzetti, V. Muccifora, A. Nagaitsev, Y. Naryshkin, A. Nathan, F. Neunreither, M. Niczyporuk, W.-D. Nowak, M. Nupieri, P. Oelwein, H. Ogami, T. O'Neill, R. Openshaw, V. Papavassiliou, S. Pate, M. Pitt, S. Potashov, D. Potterveld, B. Povh, G. Rakness, R. Redwine, A. Reolon, R. Ristinen, K. Rith, G. Röper, H. Roloff, P. Rossi, S. Rudnitsky, M. Ruh, D. Ryckbosch, Y. Sakemi, I. Savin, K. Schüller, A. Schwind, T.-A. Shibata, T. Shin, A. Simon, K. Sinram, W. Smythe, J. Sowinski, M. Spengos, E. Steffens, J. Stenger, J. Stewart, F. Stock, U. Stoesslein, M. Sutter, H. Tallini, S. Taroian, A. Terkulov, D. Thiessen, B. Tipton, A. Trudel, M. Tytgat, G. Urciuoli, R. Van de Vyver, J. van den Brand, G. van der Steenhoven, M. Vetterli, E. Volk, W. Wander, T. Welch, S. Williamson, T. Wise, T. Wölfel, K. Zapfe-Düren, H. Zohrabian, and R. Zurmühle, "Measurement of the neutron spin structure function g_1^n with a polarized ^{3}He internal target", Physics Letters B **404**, 383–389 (1997).

[28]P. Solvignon, N. Liyanage, J.-P. Chen, S. Choi, K. Aniol, T. Averett, W. Boeglin, A. Camsonne, G. D. Cates, C. C. Chang, E. Chudakov, B. Craver, F. Cusanno, A. Deur, D. Dutta, R. Ent, R. Feuerbach, S. Frullani, H. Gao, F. Garibaldi, R. Gilman, C. Glashausser, V. Gorbenko, O. Hansen, D. W. Higinbotham, H. Ibrahim, X. Jiang, M. Jones, A. Kelleher, J. Kelly, C. Keppel, W. Kim, W. Korsch, K. Kramer, G. Kumbartzki, J. J. LeRose, R. Lindgren, B. Ma, D. J. Margaziotis, P. Markowitz, K. McCormick, Z.-E. Meziani, R. Michaels, B. Moffit, P. Monaghan, C. Munoz Camacho, K. Paschke, B. Reitz, A. Saha, R. Sheyor, J. Singh, K. Slifer, V. Sulkosky, A. Tobias, G. M. Urciuoli, K. Wang, K. Wijesooriya, B. Wojtsekhowski, S. Woo, J.-C. Yang, X. Zheng, and L. Zhu (Jefferson Lab E01-012 Collaboration), "Quark-hadron duality in neutron (^{3}He) spin structure", Phys. Rev. Lett. **101**, 182502 (2008).

[29]D. Flay, M. Posik, D. S. Parno, K. Allada, W. R. Armstrong, T. Averett, F. Benmokhtar, W. Bertozzi, A. Camsonne, M. Canan, G. D. Cates, C. Chen, J.-P. Chen, S. Choi, E. Chudakov, F. Cusanno, M. M. Dalton, W. Deconinck, C. W. de Jager, X. Deng, A. Deur, C. Dutta, L. E. Fassi, G. B. Franklin, M. Friend, H. Gao, F. Garibaldi, S. Gilad, R. Gilman, O. Glamazdin, S. Golge, J. Gomez, L. Guo, O. Hansen, D. W. Higinbotham, T. Holmstrom, J. Huang, C. Hyde, H. F. Ibrahim, X. Jiang, G. Jin, J. Katich, A. Kelleher, A. Kolarkar, W. Korsch, G. Kumbartzki, J. J. LeRose, R. Lindgren, N. Liyanage, E. Long, A. Lukhanin, V. Mamyan, D. McNulty, Z.-E. Meziani, R. Michaels, M. Mihovilovi č, B. Moffit, N. Muangma, S. Nanda, A. Narayan, V. Nelyubin, B. Norum, Nuruzzaman, Y. Oh, J. C. Peng, X. Qian, Y. Qiang, A. Rakhman, R. D. Ransome, S. Riordan, A. Saha, B. Sawatzky, M. H. Shabestari, A. Shahinyan, S. Širca, P. Solvignon, R. Subedi, V. Sulkosky, W. A. Tobias, W. Troth, D. Wang, Y. Wang, B. Wojtsekhowski, X. Yan, H. Yao, Y. Ye, Z. Ye, L. Yuan, X. Zhan, Y. Zhang, Y.-W. Zhang, B. Zhao, and X. Zheng (Jefferson Lab Hall A Collaboration), "Measurements of d_2^n and A_1^n: probing the neutron spin structure", Phys. Rev. D **94**, 052003 (2016).

[30]P. Solvignon, N. Liyanage, J.-P. Chen, S. Choi, K. Slifer, K. Aniol, T. Averett, W. Boeglin, A. Camsonne, G. D. Cates, C. C. Chang, E. Chudakov, B. Craver, F. Cusanno, A. Deur, D. Dutta, R. Ent, R. Feuerbach, S. Frullani, H. Gao, F. Garibaldi, R. Gilman, C. Glashausser, V. Gorbenko, O. Hansen, D. W. Higinbotham, H. Ibrahim, X. Jiang, M. Jones, A. Kelleher, J. Kelly, C. Keppel, W. Kim, W. Korsch, K. Kramer, G. Kumbartzki, J. J. LeRose, R. Lindgren, B. Ma, D. J. Margaziotis, P. Markowitz, K. McCormick, Z.-E. Meziani, R. Michaels, B. Moffit, P. Monaghan, C. Munoz Camacho, K. Paschke, B. Reitz, A. Saha, R. Shneor, J. Singh, V. Sulkosky, A. Tobias, G. M. Urciuoli, K. Wang, K. Wijesooriya, B. Wojtsekhowski, S. Woo, J.-C. Yang, X. Zheng, and L. Zhu (Jefferson Lab E01-012 Collaboration), "Moments of the neutron g^2 structure function at intermediate Q^2", Phys. Rev. C **92**, 015208 (2015).

[31]E. Leader, A. Sidorov, and D. Stamenov, "A new evaluation of polarized parton densities in the nucleon", The European Physical Journal C - Particles and Fields **23**, 479–485 (2002).

[32]M. Chen, "Precision measurement of the neutron asymmetry a1n at large bjorken x at 12 gev jefferson lab", PhD thesis (University of Virginia, Oct. 2023).

[33]M. Roy, "Extraction of deep inelastic cross sections using a 10.4 gev electron beam and a polarized helium-3 target", PhD thesis (University of Kentucky, May 2022).

[34]P. L. Anthony, R. G. Arnold, H. R. Band, H. Borel, P. E. Bosted, V. Breton, G. D. Cates, T. E. Chupp, F. S. Dietrich, J. Dunne, R. Erbacher, J. Fellbaum, H. Fonvieille, R. Gearhart, R. Holmes, E. W. Hughes, J. R. Johnson, D. Kawall, C. Keppel, S. E. Kuhn, R. M. Lombard-

Nelsen, J. Marroncle, T. Maruyama, W. Meyer, Z. E. Meziani, H. Middleton, J. Morgenstern, N. R. Newbury, G. G. Petratos, R. Pitthan, R. Prepost, Y. Roblin, S. E. Rock, S. H. Rokni, G. Shapiro, T. Smith, P. A. Souder, M. Spengos, F. Staley, L. M. Stuart, Z. M. Szalata, Y. Terrien, A. K. Thompson, J. L. White, M. Woods, J. Xu, C. C. Young, and G. Zapalac, "Deep inelastic scattering of polarized electrons by polarized ^{3}He and the study of the neutron spin structure", Phys. Rev. D **54**, 6620–6650 (1996).

[35]P. Solvignon, "Meausrement of the helium-3 spin structure functions in the resonance region: a test of quark-hardon duality on the neutron", PhD thesis (Temple University, Aug. 2006).

[36]M. Meyerhoff, D. Eyl, A. Frey, H. Andresen, J. Annand, K. Aulenbacher, J. Becker, J. Blume-Werry, T. Dombo, P. Drescher, J. Ducret, H. Fischer, P. Grabmayr, S. Hall, P. Hartmann, T. Hehl, W. Heil, J. Hoffmann, J. Kellie, F. Klein, M. Leduc, H. Möller, C. Nachtigall, M. Ostrick, E. Otten, R. Owens, S. Plützer, E. Reichert, D. Rohe, M. Schäfer, L. Schearer, H. Schmieden, K.-H. Steffens, R. Surkau, and T. Walcher, "First measurement of the electric formfactor of the neutron in the exclusive quasielastic scattering of polarized electrons from polarized 3he", Physics Letters B **327**, 201–207 (1994).

[37]D. Rohe, P. Bartsch, D. Baumann, J. Becker, J. Bermuth, K. Bohinc, R. Böhm, S. Buttazzoni, T. Caprano, N. Clawiter, A. Deninger, S. Derber, M. Ding, M. Distler, A. Ebbes, M. Ebert, I. Ewald, J. Friedrich, J. M. Friedrich, R. Geiges, T. Großmann, M. Hauger, W. Heil, A. Honegger, P. Jennewein, J. Jourdan, M. Kahrau, A. Klein, M. Kohl, K. W. Krygier, G. Kubon, A. Liesenfeld, H. Merkel, K. Merle, P. Merle, M. Mühlbauer, U. Müller, R. Neuhausen, E. W. Otten, T. Petitjean, T. Pospischil, M. Potokar, G. Rosner, H. Schmieden, I. Sick, S. Širca, R. Surkau, A. Wagner, T. Walcher, G. Warren, M. Weis, H. Wöhrle, and M. Zeier, "Measurement of the neutron electric form factor G_{en} at $0.67(\mathrm{GeV}/c)2$ via $^3\vec{\mathrm{He}}$ $(\vec{e}, e'n)$", Phys. Rev. Lett. **83**, 4257–4260 (1999).

[38]J. Bermuth, P. Merle, C. Carasco, D. Baumann, R. Böhm, D. Bosnar, M. Ding, M. Distler, J. Friedrich, J. Friedrich, J. Golak, W. Glöckle, M. Hauger, W. Heil, P. Jennewein, J. Jourdan, H. Kamada, A. Klein, M. Kohl, B. Krusche, K. Krygier, H. Merkel, U. Müller, R. Neuhausen, A. Nogga, C. Normand, E. Otten, T. Pospischil, M. Potokar, D. Rohe, H. Schmieden, J. Schmiedeskamp, M. Seimetz, I. Sick, S. Širca, R. Skibiński, G. Testa, T. Walcher, G. Warren, M. Weis, H. Witała, H. Wöhrle, and M. Zeier, "The neutron charge form factor and target analyzing powers from 3he(e,en) scattering", Physics Letters B **564**, 199–204 (2003).

[39]H. Presley, private communication, June 2024.

[40]S. Riordan, S. Abrahamyan, B. Craver, A. Kelleher, A. Kolarkar, J. Miller, G. D. Cates, N. Liyanage, B. Wojtsekhowski, A. Acha, K. Allada, B. Anderson, K. A. Aniol, J. R. M. Annand, J. Arrington, T. Averett, A. Beck, M. Bellis, W. Boeglin, H. Breuer, J. R. Calarco, A. Camsonne, J. P. Chen, E. Chudakov, L. Coman, B. Crowe, F. Cusanno, D. Day, P. Degtyarenko, P. A. M. Dolph, C. Dutta, C. Ferdi, C. Fernandez-Ramirez, R. Feuerbach, L. M. Fraile, G. Franklin, S. Frullani, S. Fuchs, F. Garibaldi, N. Gevorgyan, R. Gilman, A. Glamazdin, J. Gomez, K. Grimm, J.-O. Hansen, J. L. Herraiz, D. W. Higinbotham, R. Holmes, T. Holmstrom, D. Howell, C. W. de Jager, X. Jiang, M. K. Jones, J. Katich, L. J. Kaufman, M. Khandaker, J. J. Kelly, D. Kiselev, W. Korsch, J. LeRose, R. Lindgren, P. Markowitz, D. J. Margaziotis, S. M.-T. Beck, S. Mayilyan, K. McCormick, Z.-E. Meziani, R. Michaels, B. Moffit, S. Nanda, V. Nelyubin, T. Ngo, D. M. Nikolenko, B. Norum, L. Pentchev, C. F. Perdrisat,

E. Piasetzky, R. Pomatsalyuk, D. Protopopescu, A. J. R. Puckett, V. A. Punjabi, X. Qian, Y. Qiang, B. Quinn, I. Rachek, R. D. Ransome, P. E. Reimer, B. Reitz, J. Roche, G. Ron, O. Rondon, G. Rosner, A. Saha, M. M. Sargsian, B. Sawatzky, J. Segal, M. Shabestari, A. Shahinyan, Y. Shestakov, J. Singh, S. Sfirca, P. Souder, S. Stepanyan, V. Stibunov, V. Sulkosky, S. Tajima, W. A. Tobias, J. M. Udias, G. M. Urciuoli, B. Vlahovic, H. Voskanyan, K. Wang, F. R. Wesselmann, J. R. Vignote, S. A. Wood, J. Wright, H. Yao, and X. Zhu, "Measurements of the electric form factor of the neutron up to q2=3.4 gev2 using the reaction 3he to e,e'npp", Phys. Rev. Lett. **105**, 262302 (2010).

[41]T. G. Walker, J. H. Thywissen, and W. Happer, "Spin-rotation interaction of alkali-metal–he-atom pairs", Phys. Rev. A **56**, 2090–2094 (1997).

[42]A. Ben-Amar Baranga, S. Appelt, M. V. Romalis, C. J. Erickson, A. R. Young, G. D. Cates, and W. Happer, "Polarization of ^{3}He by spin exchange with optically pumped rb and k vapors", Phys. Rev. Lett. **80**, 2801–2804 (1998).

[43]I. JOHANSSON, "Spectra of the alkali metals in the lead-sulphide region", English, ARKIV FOR FYSIK **20**, 135–& (1961).

[44]A. Corney, *Atomic and laser spectroscopy*, Oxford science publications (Clarendon Press, 1977).

[45]J. Singh, "Alkali-hybrid spin-exchange optically-pumped polarized ^{3}he targets used for studying neutron structure", PhD thesis (University of Virginia, Dec. 2010).

[46]I. I. Rabi, N. F. Ramsey, and J. Schwinger, "Use of rotating coordinates in magnetic resonance problems", Rev. Mod. Phys. **26**, 167–171 (1954).

[47]K. Kaiser, *Electromagnetic compatibility handbook*, Electrical engieering handbook series (Taylor & Francis, 2004).

[48]M. V. Romalis and G. D. Cates, "Accurate 3he polarimetry using the rb zeeman frequency shift due to the rb-3he spin-exchange collisions", Phys. Rev. A **58**, 3004–3011 (1998).

[49]S. Katugampola, C. Jantzi, D. A. Keder, W. G. Miller, V. Nelyubin, H. Nguyen, S. Tafti, W. A. Tobias, and G. D. Cates, "Frequency shifts in the epr spectrum of 39k due to spin-exchange collisions with polarizaed 3he and precise 3he polarimetry", arXiv **58**, 3004–3011 (2021).

[50]E. Babcock, I. A. Nelson, S. Kadlecek, and T. G. Walker, "3he polarization-dependent epr frequency shifts of alkali-metal–3he pairs", Phys. Rev. A **71**, 013414 (2005).

[51]K. Coulter, A. McDonald, G. Cates, W. Happer, and T. Chupp, "Measurement of 3he depolarization rates during bombardment with a 4he beam", Nuclear Instruments and Methods in Physics Research Section A: Accelerators, Spectrometers, Detectors and Associated Equipment **276**, 29–34 (1989).

[52]S. Riordan, C. Keppel, K. Aniol, J. Annand, J. Arrington, T. Averett, C. A. Gayoso, E. Brash, G. D. Cates, J. .-. Chen, E. Chudakov, D. Flay, G. B. Franklin, M. Friedman, O. Glamazdin, J. Gomez, C. Hanretty, J. .-. Hansen, C. Hyde, M. K. Jones, I. Korover, J. J. LeRose, R. A. Lindgren, N. Liyanage, E. Long, V. Mamyan, M. Mihovilovic, N. Muangma, S. Nanda, D. Parno, C. F. Perdrisat, R. Pomatsalyuk, M. Posik, V. Punjabi, G. Rosner, J. Sjögren, S. Sirca, L. C. Smith, P. Solvignon, N. F. Sparveris, V. Sulkosky, V. Vereshchaka, B. Wojtsekhowski, Z. Ye, J. Zhang, Y. W. Zhang, X. Zheng, R. Zielinski, and the Hall A Collaboration, *Hall a annual report 2012*, 2013.

[53]J. T. Singh, P. A. M. Dolph, W. A. Tobias, T. D. Averett, A. Kelleher, K. E. Mooney, V. V. Nelyubin, Y. Wang, Y. Zheng, and G. D. Cates, "Development of high-performance alkali-hybrid polarized ^{3}He targets for electron scattering", Phys. Rev. C **91**, 055205 (2015).

[54]T. N. B.I.G., P. Daddy, and Mase, *Mo money mo problems*, Bad Boy Records, "Life After Death" Track 10, 1997.

[55]R. E. Jacob, J. Teter, B. Saam, W. C. Chen, and T. R. Gentile, "Low-field orientation dependence of 3he relaxation in spin-exchange cells", Phys. Rev. A **69**, 021401 (2004).

[56]B. Chann, E. Babcock, L. W. Anderson, T. G. Walker, W. C. Chen, T. B. Smith, A. K. Thompson, and T. R. Gentile, "Production of highly polarized 3He using spectrally narrowed diode laser array bars", Journal of Applied Physics **94**, 6908–6914 (2003).

[57]J. Schmiedeskamp, H.-J. Elmers, W. Heil, E. W. Otten, Y. Sobolev, W. Kilian, H. Rinneberg, T. Sander-Thömmes, F. Seifert, and J. Zimmer, "Relaxation of spin polarized 3he by magnetized ferromagnetic contaminants", The European Physical Journal D - Atomic, Molecular, Optical and Plasma Physics **38**, 10.1140/epjd/e2006-00052-0 (2006).

[58]J. Schmiedeskamp, W. Heil, E. W. Otten, R. K. Kremer, A. Simon, and J. Zimmer, "Paramagnetic relaxation of spin polarized 3he at bare glass surfaces", The European Physical Journal D - Atomic, Molecular, Optical and Plasma Physics **38**, 10.1140/epjd/e2006-00050-2 (2006).

[59]J. Korringa, "Nuclear magnetic relaxation and resonnance line shift in metals", Physica **16**, 601–610 (1950).

[60]D. Matyas, S. Katugampola, Y. Wang, M. Kaluarachchi, P. A. M. Dolph, V. Nelyubin, W. A. Tobias, and G. D. Cates, "Nuclear spin relaxation of 3he in glass and metal containers used for spin-exchange optical pumping", Unpublished (2018).

[61]R. Brueggemann, private communication, June 2024.

[62]A. Kelleher, "A measurement of the neutron electric form factor at very large momentum transfer using polarized electrons scattering from a polarized helium-3 target", PhD thesis (College of William and Mary, Jan. 2010).

[63]J. Huang, "Double spin asymmetry A_{LT} in charged pion production from deep inelastic scattering on a transversely polarized 3he target", PhD thesis (Massachusetts Institute of Technology, Feb. 2012).

[64]J. Katich, "Measurement of the target-normal single-spin asymmetry any in the deep inelastic region from the reaction 3he(e,e')", PhD thesis (College of William and Mary, Jan. 2011).

[65]D. V. Vertyanov, I. A. Belyakov, S. P. Timoshenkov, A. V. Borisova, and V. N. Sidorenko, "Effects of gold-aluminum intermetallic compounds on chip wire bonding interconnections reliability", in 2020 ieee conference of russian young researchers in electrical and electronic engineering (eiconrus) (2020), pp. 2216–2220.

[66]M. Born and E. Wolf, *Principles of optics: electromagnetic theory of propagation, interference and diffraction of light (7th edition)*, 7th (Cambridge University Press, 1999).

[67]A. Tobias, *Ge180 aluminosilicate glass properties*, (2012) http://galileo.phys.virginia.edu/research/groups/spinphysics/glass_properties.html.

[68]W. Demtröder, *Laser spectroscopy: vol. 1: basic principles*, Laser Spectroscopy (Springer Berlin Heidelberg, 2008).

[69]M. V. Romalis, E. Miron, and G. D. Cates, "Pressure broadening of rb D_1 and D_2 lines by ^{3}he, ^{4}he, n_2, and xe: line cores and near wings", Phys. Rev. A **56**, 4569–4578 (1997).

[70]R. Walkup, B. Stewart, and D. E. Pritchard, "Collisional line broadening due to van der waals potentials", Phys. Rev. A **29**, 169–173 (1984).

[71]D. A. Steck, *Rubidium 85 d line data*, (2023) http://steck.us/alkalidata.

[72]D. A. Steck, *Rubidium 87 d line data*, (2023) http://steck.us/alkalidata.

[73]T. G. Tiecke, *Properties of potassium*, (2019) https://www.tobiastiecke.nl/archive/PotassiumProperties.pdf.

[74]K. A. Kluttz, T. D. Averett, and B. A. Wolin, "Pressure broadening and frequency shift of the D_1 and D_2 lines of rb and k in the presence of ^{3}he and n_2", Phys. Rev. A **87**, 032516 (2013).

[75]D. K. Nandy, Y. Singh, B. P. Shah, and B. K. Sahoo, "Transition properties of a potassium atom", Phys. Rev. A **86**, 052517 (2012).

[76]B. E. Poling, J. M. Prausnitz, and J. P. O'Connell, *The properties of gases and liquids*, 5th (McGraw-Hill Education, 2001).

[77]D. Ambrose and J. Walton, "Vapour pressures up to their critical temperatures of normal alkanes and 1-alkanols", Pure and Applied Chemistry **61**, 1395–1403 (1989).

[78]P. A. M. Dolph, J. Singh, T. Averett, A. Kelleher, K. E. Mooney, V. Nelyubin, W. A. Tobias, B. Wojtsekhowski, and G. D. Cates, "Gas dynamics in high-luminosity polarized ^{3}he targets using diffusion and convection", Phys. Rev. C **84**, 065201 (2011).

[79]M. Himsworth and T. Freegarde, "Rubidium pump-probe spectroscopy: comparison between ab initio theory and experiment", Phys. Rev. A **81**, 023423 (2010).

[80]X. Zheng, "Precision measurement of neutron spin asymmetry A_1^n at large x_{Bj} using cebaf at 5.7 gev", PhD thesis (Massachusetts Institute of Technology, Dec. 2002).